Effect of Ta, Hf, and Si on the High Humidity Oxidation Resistance of MCrAlY Bond Coat Materials

Katerina Luiza Monea

A thesis submitted in partial fulfillment of the requirements for the
Master's degree in Mechanical Engineering

Faculty of Engineering
University of Ottawa

© Katerina Luiza Monea, Ottawa, Canada, 2024

Abstract

The continued focus to include high hydrogen fuels such as Syngas in aircraft operation to reduce emissions and increase engine efficiency has led to an ongoing investigation into bond coat materials capable of withstanding unfavourable oxidation in high temperature humid environments. The increased presence of water in the engine exhaust leads to increased oxygen activity in the hot section of the engine.

In this work, four commercially available MCrAlY bond coat materials were oxidized in high temperature environments with various humidities to understand the behaviours of different reactive element inclusions in resisting high temperature oxidation. Oxidation tests were done at 0%, 18%, and 33% water by volume at 1100°C in a 1atm environment to simulate conditions expected in engines using high hydrogen fuels. Oxidation was done for 2h and 20h to observe transient oxide formation behaviour.

The surfaces and cross sections of the specimens were examined using SEM and EDS analysis, along with XRD analysis. The progression of surface oxides, TGO thickness, and element depletion zones were observed.

Two opposing mechanisms are observed: the upward diffusion of metal cations to the free surface and the inward diffusion of oxygen to the alloy. The presence of water is shown to increase internal oxidation of the bond coat alloy and delay the formation of a protective alumina TGO.

Tantalum inclusion in the alloy composition is shown to produce the most stable alumina TGO with the least internal oxidation after 20h exposure in 33% H_2O (%vol); the most hostile oxidation environment tested.

Acknowledgments

I would like to sincerely thank my supervisor, Dr. Arnaud Weck for his patience, support, and understanding throughout this project. A special thanks to Dr. Linruo Zhao and Dr. Vladimir Pankov of the NRC for their guidance and expertise in meaningful discussions, and for providing the materials for this study.

Thank you to the people in my lab group, especially Leon Guo for always finding a solution and to Graham Rivers-Killaire for always having a story. Thank you to Spyros Ntais and to Howard Northfield of the CRPUO for their help with the Gemini and ongoing encouragement.

Thank you to my mom, Liliana Monea for forging the path and letting me find my place on it.

Table of Contents

Table of Contents iv

List of Figures viii

Chapter 1 Introduction 1

1.1 Thesis Outline 1

Chapter 2 Literature Review 3

2.1 Gas Turbine System and Materials 3

2.1.1 Gas Turbine High-Temperature Environment 3

2.1.2 Nickel-Based Superalloys 4

2.1.3 Environmental Barrier Coatings (EBCs) 7

2.1.4 Diffusion Coatings 9

2.1.5 Overlay Coatings 9

2.1.6 Thermal Barrier Coatings 12

2.1.7 Metallic Bond Coat 13

2.1.8 Ceramic Top Coat 15

2.1.9 Thermally Grown Oxide 18

2.1.10 Oxidation Kinetics 19

2.2 Oxidation Behaviour in Dry and Humid Environments 22

2.2.1 Dry air oxidation behaviour 22

2.2.2 Humid air oxidation behaviour 23

2.2.3 Spinel Formation 29

2.2.4 Void formation 32

2.3 Reactive Element Addition Influences on Oxidation 34
2.3.1 Effect of Yttrium 34
2.3.2 Effect of Tantalum 35
2.3.3 Effect of Hafnium 36
2.3.4 Effect of Silicon 38
2.3.5 Doping Element Summary 39
2.4 Motivation and Research Objectives 39
Chapter 3 Procedure and Methodology 42
3.1 Materials 42
3.2 Sample Preparation 42
3.3 Vacuum annealing 43
3.4 Sample Mounting 45
3.5 Polishing 45
3.6 Oxidation Treatments 45
3.6.1 Humidification Set-up 45
3.6.2 Calibration of Temperature and Humidity 47
3.7 Characterization 49
Chapter 4 Results 53
4.1 Bulk Microstructure Characterization 53
4.2 Oxidation in Dry Air 55
4.2.1 Sample A 55
4.2.2 Sample B 58
4.2.3 Sample C 61
4.2.4 Sample D 64

4.3 Humid Environment Oxidation 18% H_2O (%vol) 67
4.3.1 Sample A 67
4.3.2 Sample B 70
4.3.3 Sample C 73
4.3.4 Sample D 75
4.4 Humid Environment Oxidation 33% H_2O (%vol) 78
4.4.1 Sample A 78
4.4.2 Sample B 81
4.4.3 Sample C 84
4.4.4 Sample D 87
4.5 Summary of Results 90
4.5.1 Sample A 90
4.5.2 Sample B 93
4.5.3 Sample C 96
4.5.4 Sample D 99
Chapter 5 Discussion of Results 105
5.1 Effect of Humidity of Oxidation 105
5.1.1 Dry air oxidation 105
5.1.2 Air + 18% H_2O (%vol) 106
5.1.3 Air + 33% H_2O (%vol) 107
5.2 Effect of Composition on Oxidation 108
5.2.1 Base Composition 108
5.2.2 Effect of Cobalt 108
5.2.3 Effect of Tantalum 109

5.2.4 Effect of Hafnium and Silicon 109
Chapter 6 Conclusions 112
6.1 Novelty 112
6.2 Main Conclusions 112
6.3 Future Work 113
References 115
Appendix A: EDS Cross-Section Element Maps and Line Scans 120
Appendix B: Thermodynamic Tables for Saturated Water 141

List of Figures

Figure 2.1 General diagram of a gas turbine engine core [3] 3

Figure 2.2 {001} plane γ/γ′ microstructure of the single crystal superalloy DD6 [10] 5

Figure 2.3 γ (left) and γ' (right) unit cells for Ni-Al [7] 5

Figure 2.4 Creep strength of common turbine disc alloys as a function of the γ′ and γ′′ strengthening phases [8] 6

Figure 2.5 History of nickel-based superalloy development relative to temperature capability from 1940-2010 [8] 7

Figure 2.6 Schematic sketches of the general configuration of the three different types of coatings used for high-temperature applications (from left to right): diffusion coatings, metal overlay coatings, and thermal barrier coatings [11] 8

Figure 2.7 (a) EB-PVD deposited CoCrAlY coating on nickel-based superalloy (MarM002) [5], (b) Argon-shrouded plasma sprayed NiCoCrAlY coating on nickel-based superalloy [5] 11

Figure 2.8 Oxidative degradation of EB-PVD and PS overlay coatings showing benefit of active element additions [8] 11

Figure 2.9 Cross-section diagram of TBC system with EB-PVD ceramic top coat [12] 12

Figure 2.10 Standard APS and EB-PVD deposited zirconia top-coat morphologies. APS TBC is deposited on sprayed MCrAlY bond coat and EB-PVD TBC is deposited on pack cemented diffusion bond coat [11] 13

Figure 2.11 Comparison between thermal reduction and coating life of three general protective coating systems [8] 14

Figure 2.12 Phase diagram for $ZrO_2 – Y_2O_3$ [8] 16

Figure 2.13 Rumpling of the TGO as a result of thermal cycling [2] 19

Figure 2.14 (a) TGO cross-section showing columnar alumina structure (b) Diagram illustrating flux paths [15] 21

Figure 2.15 BSE image of vacuum cast CoNiCrAlHf bond coat alloy [17]..... 22

Figure 2.16 Fractured cross-sectional BSE images of the TGO formed on the NiCoCrAlY prepared in (a) air, (b) Ar + water vapor, and (c) air +water vapor after cyclic oxidation at 1050 ◦C for 150 h [20]..... 25

Figure 2.17 Different crystal morphologies developed on the sample surfaces oxidized in (a) air and (b) air + 25% H_2O at 1050 ◦C [20]..... 26

Figure 2.18 Surface morphologies of three high entropy alloys after oxidation at 1100 ℃ for 650h [30]..... 27

Figure 2.19: SEM observations of Crofer22APU oxidized in H_2/10%H_20 at 800°C for 100h [7]. 29

Figure 2.20: SEM of TBC bond coat cross section taken from field tests of industrial turbine blade material systems. (a) High water content syngas (b) Low water content natural gas [36]..... 30

Figure 2.21: Before and after SEM images of cast NiCoCrAlY TGO grown in 0% H_2O (a)(d), 5% H_2O (b)(e), and 15% H_2O (c)(f) after thermal cycling at 1125°C [7],[13]..... 31

Figure 2.22: Spinel surface coverage as a function of water vapor percentage for cast CoNiCrAlY and NiCoCrAlY exposed to 1125°C [7]..... 31

Figure 2.23 Schematic illustration of the oxidation mechanism for the TGO-formed 7YSZ TBCs at (a) low (Ar + water vapour) and (b) high (Air + water vapor) Po [20]. 33

Figure 2.24 Cross-sectional morphologies of a high entropy alloy after oxidation at 1100 ◦C for 620 h [30]..... 36

Figure 2.25 Surface SEM images of CoNiCrAlHf alloys after oxidation at 1050 C. (a) 1 h, air, (b) 24 h, air, (c) 1 h, air + water vapor, (d) 24 h, air + water vapor [17]..... 37

Figure 2.26 Bond coat composition effects for coatings on X4 alloy substrate in dry O2 vs. 10% H2O environments comparing TBC lifetimes in 1h cycles [31] 38

Figure 3.1 Processed MCrAlY (a) target material (d=60 mm) (b) polished bulk samples (10x10x2 mm)..... 43

Figure 3.2 High-Vacuum Tube Furnace Set-up used for Vacuum Annealing Treatments 43

Figure 3.3 Alumina Card Sample Holder 44

Figure 3.4 Schematic of Humidification Set-up. Dry air gas bottle (1), pressure gage (2,) thermometer (3), saturators (4), heating tapes (5), in-line humidity meter (6), specimen loading position (7), furnace (8), alumina tube (9), gas outlet (10). 46

Figure 3.5 Furnace Heating Curve for 20h Oxidation Treatment 47

Figure 3.6 Furnace calibration temperature profile at 1100°C in air 48

Figure 3.7 BSE SEM Sample A 0% H_2O 2h oxidation TGO and Al-depleted zone measurement 49

Figure 3.8 Example of rumpling, void identification, Al-depleted zone, and oxide pegs in sample B, 18% H_2O, 20h oxidation cross-section 50

Figure 3.9 Example of internal oxidation in sample D, 18% H_2O, 20h oxidation cross-section . 50

Figure 3.10 Example of surface voids and transient species on sample A, 18% H_2O, 2h oxidation specimen. 51

Figure 3.11 EDS element map Sample A 0% H_2O 2h oxidation TGO, Al-depleted zone, and Y-depleted zone measurement 51

Figure 3.12 Grey value plot of Al element map Sample A 0% H_2O 2h oxidation for Al-depletion zone measurement 52

Figure 4.1 BSD SEM of polished bulk material surfaces (a) sample A, (b) sample B, (c) sample C, (d) Sample D 53

Figure 4.2 XRD surface characterization of bulk material surface (a) sample A (b) sample B (c) sample C (d) sample D 54

Figure 4.3 GI XRD of sample A surface after oxidation in dry air for 2h at 1100°C 55

Figure 4.4 BSD SEM of sample A (a) surface (b) cross-section, after oxidation in dry air for 2h at 1100°C 56

Figure 4.5 GI XRD of sample A surface after oxidation in dry air for 20h at 1100°C 57

Figure 4.6 BSD SEM of sample A (a) surface (b) cross-section, after oxidation in dry air for 20h at 1100°C 58

Figure 4.7 GI XRD of sample B surface after oxidation in dry air for 2h at 1100°C..... 58

Figure 4.8 BSD SEM of sample B (a) surface (b) cross-section, after oxidation in dry air for 2h at 1100°C 59

Figure 4.9 GI XRD of sample B surface after oxidation in dry air for 20h at 1100°C..... 60

Figure 4.10 BSD SEM of sample B (a) surface (b) cross-section, after oxidation in dry air for 20h at 1100°C 60

Figure 4.11 GI XRD of sample C surface after oxidation in dry air for 2h at 1100°C..... 61

Figure 4.12 BSD SEM of sample C (a) surface (b) cross-section, after oxidation in dry air for 2h at 1100°C 62

Figure 4.13 GI XRD of sample C surface after oxidation in dry air for 20h at 1100°C..... 63

Figure 4.14 BSD SEM of sample C (a) surface (b) cross-section, after oxidation in dry air for 20h at 1100°C 63

Figure 4.15 GI XRD of sample D surface after oxidation in dry air for 2h at 1100°C 64

Figure 4.16 BSD SEM of sample D (a) surface (b) cross-section, after oxidation in dry air for 2h at 1100°C 65

Figure 4.17 GI XRD of sample D surface after oxidation in dry air for 20h at 1100°C 66

Figure 4.18 BSD SEM of sample D (a) surface (b) cross-section, after oxidation in dry air for 20h at 1100°C 66

Figure 4.19 GI XRD of sample A surface after oxidation in air 18% H_2O for 2h at 1100°C 67

Figure 4.20 BSD SEM of sample A (a) surface (b) cross-section, after oxidation in air 18% H_2O for 2h at 1100°C..... 68

Figure 4.21 GI XRD of sample A surface after oxidation in air 18% H2O for 20h at 1100°C.... 69

Figure 4.22 BSD SEM of sample A (a) surface (b) cross-section, after oxidation in air 18% H_2O for 20h at 1100°C..... 69

Figure 4.23 GI XRD of sample B surface after oxidation in air 18% H2O for 2h at 1100°C..... 70

Figure 4.24 BSD SEM of sample B (a) surface (b) cross-section, after oxidation in air 18% H_2O for 2h at 1100°C..... 71

Figure 4.25 GI XRD of sample B surface after oxidation in air 18% H2O for 20h at 1100°C.... 72

Figure 4.26 BSD SEM of sample B (a) surface (b) cross-section, after oxidation in air 18% H_2O for 20h at 1100°C..... 72

Figure 4.27 GI XRD of sample C surface after oxidation in air 18% H2O for 2h at 1100°C..... 73

Figure 4.28 BSD SEM of sample C (a) surface (b) cross-section, after oxidation in air 18% H_2O for 2h at 1100°C..... 74

Figure 4.29 GI XRD of sample C surface after oxidation in air 18% H2O for 20h at 1100°C.... 74

Figure 4.30 BSD SEM of sample C (a) surface (b) cross-section, after oxidation in air 18% H_2O for 20h at 1100°C..... 75

Figure 4.31 GI XRD of sample D surface after oxidation in air 18% H2O for 2h at 1100°C..... 76

Figure 4.32 BSD SEM of sample D (a) surface (b) cross-section, after oxidation in air 18% H_2O for 2h at 1100°C..... 76

Figure 4.33 GI XRD of sample D surface after oxidation in air 18% H2O for 20h at 1100°C.... 77

Figure 4.34 BSD SEM of sample D (a) surface (b) cross-section, after oxidation in air 18% H_2O for 20h at 1100°C..... 78

Figure 4.35 GI XRD of sample A surface after oxidation in air 33% H2O for 2h at 1100°C..... 79

Figure 4.36 BSD SEM of sample A (a) surface (b) cross-section, after oxidation in air 33% H_2O for 2h at 1100°C..... 80

Figure 4.37 GI XRD of sample A surface after oxidation in air 33% H2O for 20h at 1100°C.... 80

Figure 4.38 BSD SEM of sample A (a) surface (b) cross-section, after oxidation in air 33% H_2O for 20h at 1100°C..... 81

Figure 4.39 GI XRD of sample B surface after oxidation in air 33% H2O for 2h at 1100°C..... 82

Figure 4.40 BSD SEM of sample B (a) surface (b) cross-section, after oxidation in air 33% H_2O for 2h at 1100°C 82

Figure 4.41 GI XRD of sample B surface after oxidation in air 33% H2O for 20h at 1100°C 83

Figure 4.42 BSD SEM of sample B (a) surface (b) cross-section, after oxidation in air 33% H_2O for 20h at 1100°C 84

Figure 4.43 GI XRD of sample C surface after oxidation in air 33% H2O for 2h at 1100°C 85

Figure 4.44 BSD SEM of sample C (a) surface (b) cross-section, after oxidation in air 33% H_2O for 2h at 1100°C 85

Figure 4.45 GI XRD of sample C surface after oxidation in air 33% H2O for 20h at 1100°C 86

Figure 4.46 BSD SEM of sample C (a) surface (b) cross-section, after oxidation in air 33% H_2O for 20h at 1100°C 87

Figure 4.47 GI XRD of sample D surface after oxidation in air 33% H2O for 2h at 1100°C 88

Figure 4.48 BSD SEM of sample D (a) surface (b) cross-section, after oxidation in air 33% H_2O for 2h at 1100°C 88

Figure 4.49 GI XRD of sample D surface after oxidation in air 33% H2O for 20h at 1100°C 89

Figure 4.50 BSD SEM of sample D (a) surface (b) cross-section, after oxidation in air 33% H_2O for 20h at 1100°C 90

Figure 4.51 BSD SEM of surface and cross-section of sample A in dry air (a) (d), 18% H_2O humidity (b) (e), and 33% H_2O humidity (c) (f) after 2h oxidation exposure 91

Figure 4.52 BSD SEM of surface and cross-section of sample A in dry air (a) (d), 18% H_2O humidity (b) (e), and 33% H_2O humidity (c) (f) after 20h oxidation exposure 92

Figure 4.53 Effect of Humidity on TGO Thickness (a) and Al-depletion (b) in sample A for 0%, 18% and 33% H_2O in 2h and 20h oxidation 92

Figure 4.54 BSD SEM of surface and cross-section of sample B in dry air (a) (d), 18% H_2O humidity (b) (e), and 33% H_2O humidity (c) (f) after 2h oxidation exposure 94

Figure 4.55 BSD SEM of surface and cross-section of sample B in dry air (a) (d), 18% H_2O humidity (b) (e), and 33% H_2O humidity (c) (f) after 20h oxidation exposure 95

Figure 4.56 Effect of Humidity on TGO Thickness (a) and Al-depletion (b) in sample B for 0%, 18% and 33% H_2O in 2h and 20h oxidation 95

Figure 4.57 BSD SEM of surface and cross-section of sample C in dry air (a) (d), 18% H_2O humidity (b) (e), and 33% H_2O humidity (c) (f) after 2h oxidation exposure 97

Figure 4.58 BSD SEM of surface and cross-section of sample C in dry air (a) (d), 18% H_2O humidity (b) (e), and 33% H_2O humidity (c) (f) after 2h oxidation exposure 98

Figure 4.59 Effect of Humidity on TGO Thickness (a) and Al-depletion (b) in sample C for 0%, 18% and 33% H_2O in 2h and 20h oxidation 98

Figure 4.60 BSD SEM of surface and cross-section of sample D in dry air (a) (d), 18% H_2O humidity (b) (e), and 33% H_2O humidity (c) (f) after 2h oxidation exposure 101

Figure 4.61 BSD SEM of surface and cross-section of sample D in dry air (a) (d), 18% H_2O humidity (b) (e), and 33% H_2O humidity (c) (f) after 2h oxidation exposure 102

Figure 4.62 Effect of Humidity on TGO Thickness (a) and Al-depletion (b) in sample D for 0%, 18% and 33% H_2O in 2h and 20h oxidation 103

Figure 5.1 Intergranular voids in sample A (a) and sample B (b) after 20h oxidation in dry air 106

Figure 5.2 Intergranular voids in sample A (a), sample B (b), and sample D (c) after 20h oxidation in air + 18% H_2O 107

Figure 5.3 Composition Effects on TGO Thickness (a) and Al-depletion (b) at 0% H_2O for 2h and 20h oxidation 110

Figure 5.4 Composition Effects on TGO Thickness (a) and Al-depletion (b) at 18% H_2O for 2h and 20h oxidation 111

Figure 5.5 Composition Effects on TGO Thickness(a) and Al-depletion (b) at 33% H_2O for 2h and 20h oxidation 111

Figure 0.1 EDS Element Map A-0%-2h 120

Figure 0.2 EDS Element Line Scan A-0%-2h 120

Figure 0.3 EDS Element Map B-0%-2h 121
Figure 0.4 EDS Element Line Scan B-0%-2h 121
Figure 0.5 EDS Element Map C-0%-2h 122
Figure 0.6 EDS Element Line Scan C-0%-2h 122
Figure 0.7 EDS Element Map D-0%-2h 122
Figure 0.8 EDS Element Line Scan D-0%-2h 123
Figure 0.9 EDS Element Map A-0%-20h 123
Figure 0.10 EDS Element Line Scan A-0%-20h 124
Figure 0.11 EDS Element Map B-0%-20h 124
Figure 0.12 EDS Element Line Scan B-0%-20h 124
Figure 0.13 EDS Element Map C-0%-20h 125
Figure 0.14 EDS Element Line Scan C-0%-20h 125
Figure 0.15 EDS Element Map D-0%-20h 126
Figure 0.16 EDS Element Line Scan D-0%-20h 126
Figure 0.17 EDS Element Map A-18%-2h 127
Figure 0.18 EDS Element Line Scan A-18%-2h 127
Figure 0.19 EDS Element Map B-18%-2h 128
Figure 0.20 EDS Element Line Scan B-18%-2h 128
Figure 0.21 EDS Element Map C-18%-2h 129
Figure 0.22 EDS Element Line Scan C-18%-2h 129
Figure 0.23 EDS Element Map D-18%-2h 129
Figure 0.24 EDS Element Line Scan D-18%-2h 130
Figure 0.25 EDS Element Map A-18%-20h 130
Figure 0.26 EDS Element Line Scan A-18%-20h 131

Figure 0.27 EDS Element Map B-18%-20h 131
Figure 0.28 EDS Element Line Scan B-18%-20h 131
Figure 0.29 EDS Element Map C-18%-20h 132
Figure 0.30 EDS Element Line Scan C-18%-20h 132
Figure 0.31 EDS Element Map D-18%-20h 133
Figure 0.32 EDS Element Line Scan D-18%-20h 133
Figure 0.33 EDS Element Map A-33%-2h 134
Figure 0.34 EDS Element Line Scan A-33%-2h 134
Figure 0.35 EDS Element Map B-33%-2h 135
Figure 0.36 EDS Element Line Scan B-33%-2h 135
Figure 0.37 EDS Element Map C-33%-2h 136
Figure 0.38 EDS Element Line Scan C-33%-2h 136
Figure 0.39 EDS Element Map D-33%-2h 136
Figure 0.40 EDS Element Line Scan D-33%-2h 137
Figure 0.41 EDS Element Map A-33%-20h 137
Figure 0.42 EDS Element Line Scan A-33%-20h 138
Figure 0.43 EDS Element Map B-33%-20h 138
Figure 0.44 EDS Element Line Scan B-33%-20h 138
Figure 0.45 EDS Element Map C-33%-20h 139
Figure 0.46 EDS Element Line Scan C-33%-20h 139
Figure 0.47 EDS Element Map D-33%-20h 140
Figure 0.48 EDS Element Line Scan D-33%-20h 140

List of Tables

Table 1 Composition by weight % of common and prototype MCrAlY overlay coatings [8]..... 10

Table 2 Elemental constituents of metallic coatings, their functions, and effects [7] 15

Table 3 Properties of 7-YSZ Top Coat Thermal Barrier Coatings at Room Temperature [5], [12] 17

Table 4 PBR Values for Common Oxide Scales [7]..... 20

Table 5 Review of oxidation parameters found in literature 28

Table 6 Summary of Reactive Element Effects on Oxidation..... 39

Table 7 Summary of Bond Coat Material Composition 42

Table 8 EDS surface results of bulk materials [wt%]..... 54

Table 9 XRD results for sample A in 0%, 18%, and 33% H_2O (%vol) in 2h and 20h oxidation with differences in identified species bolded..... 93

Table 10 XRD results for sample B in 0%, 18%, and 33% H_2O (%vol) in 2h and 20h oxidation with differences in identified species bolded..... 95

Table 11 XRD results for sample C in 0%, 18%, and 33% H_2O (%vol) in 2h and 20h oxidation with differences in identified species bolded..... 99

Table 12 XRD results for sample D in 0%, 18%, and 33% H_2O (%vol) in 2h and 20h oxidation with differences in identified species bolded..... 104

Table 13 Thermodynamic properties of Water Temperature Entry..... 141

Table 14 Thermodynamic Properties of Water Pressure Entry 142

Chapter 1 Introduction

Enhancing efficiency and performance of jet turbine engines has been an ongoing objective of the aerospace industry since its inception. In line with Canada's 2030 Emissions Reduction Plan, the aerospace sector is actively pursuing strategies to reduce emissions and enhance the efficiency of jet turbine engines [1]. The present approach involves increasing the engine's operating temperatures to achieve more complete combustion and utilizing high hydrogen fuels like syngas to produce more water vapor in the exhaust [1].

Higher operating temperatures in the turbine section of the engine have been shown to improve efficiency, reduce emissions, and increase the thrust to weight ratio in operation [2]. However, the present material systems used in the industry may be highly susceptible to water vapor corrosion, which can lead to a shortened engine lifespan [3]. Higher temperatures and water vapor create a harsh and demanding environment for working materials, which can accelerate oxidation and degradation. Gaining a better understanding of how different elements contribute to the oxidation behavior of aerospace materials in a high-water-vapor environment is crucial for developing more resilient and durable material systems that can withstand the challenges posed by these conditions.

In this study, four commercially available bond coat alloys were isothermally heat treated under three humidity conditions to investigate and isolate the roles of different elemental inclusions. The treatments were done at 1atm for 2h and 20h to investigate the initial and prolonged oxidation behaviours and make predictions as to which materials would best perform in humid environment applications.

1.1 Thesis Outline

Chapter 1 summarizes the application context used to define the scope of the research. The proposed materials and investigation parameters are presented.

Chapter 2 is a literature review of existing TBC technologies highlighting the effects of different alloying elements on oxidation in dry and humid air environments.

Chapter 3 describes information on the specimen materials, sample preparation, oxidation treatments, and characterization techniques.

Chapter 4 is a presentation of the results including the characterization of the bulk materials and the oxidation treatments.

Chapter 5 is a discussion of the results highlighting the different mechanisms present in dry and humid oxidation conditions.

Chapter 6 is a summary conclusion of the work, including future areas of study.

Chapter 2 Literature Review

2.1 Gas Turbine System and Materials

2.1.1 Gas Turbine High-Temperature Environment

Gas turbine engines are critical components of power generation, marine, and aviation systems [11]; each with their own performance priorities. Power generation emphasizes high durability, marine applications focuses on corrosion resistance, and aviation prioritizes weight reduction [11]. A general schematic of a gas turbine engine core is seen in Figure 2.1.

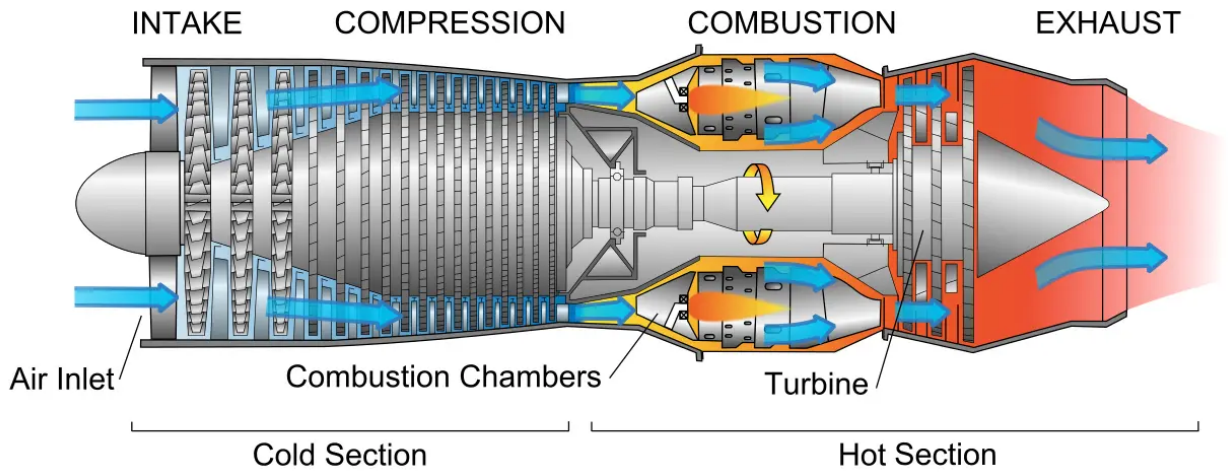

Figure 2.1 General diagram of a gas turbine engine core [3]

The engine core comprises of an intake fan, compression stage, combustor, and turbine, each of which performs a specific function in the operation of the engine. The intake fan determines how much air enters the engine core. In the compression stage, stationary vanes are paired with rotating vanes to produce compression. A higher compression ratio results in better combustion and increased propulsion from the engine [4]. In the combustor, fuel and air are ignited with excess air before the exhaust gases pass through the turbine. The turbine is powered by exhaust gases and the spinning of the vanes powers the compressor and intake fan. The velocity of the exhaust and the shape of the nozzle determine propulsion power.

Temperatures in the hot section can exceed the melting point of the working materials. In 2003, the mean turbine blade temperature for aircraft engines was 1050°C with a maximum temperature of 1150°C [5]. Current efficiencies for simple cycle combustion is around 40% [6] with achievable

turbine inlet temperatures of 1650°C [7]. As continued efforts are made to improve the efficiency of gas turbine engines, the inlet temperatures will also rise, bringing with them harsher environments and more opportunities for oxidation, hot-corrosion, creep, and fatigue to shorten the lives of working components [5], [7]. In high temperature environments, materials' resistance to oxidation and corrosion is the primary factor in setting the service temperature limit [5].

To address this issue, high-temperature superalloys are used in the manufacture of turbine blades and other components, and Thermal Barrier Coatings (TBCs) are applied to reduce the temperature seen by these working parts.

In the following section, nickel-base superalloys are discussed. Nickel-based superalloys are the industry standard for working parts in turbine engines due to their superior strength and creep resistance at high temperatures [8].

2.1.2 Nickel-Based Superalloys

Superalloys are a class of materials capable of being used in load-bearing applications at temperatures within 80% of their melting point. Nickel and chromium are used as base materials, due to their high melting points and ability to be considerably alloyed. Superalloys typically have an excess of ten alloying elements [7] and high configurational entropy is responsible for the stability of superalloys [9]. Nickel is the fifth most abundant element on earth and has an fcc (γ') crystal structure. It is found in the first row of the d block of transition metals [8]. Single crystal nickel-based superalloys have two typical phases present which can be seen in

Figure 2.2. Smaller precipitates are spherical and larger gamma prime segments, such as those seen below, are cuboidal [7].

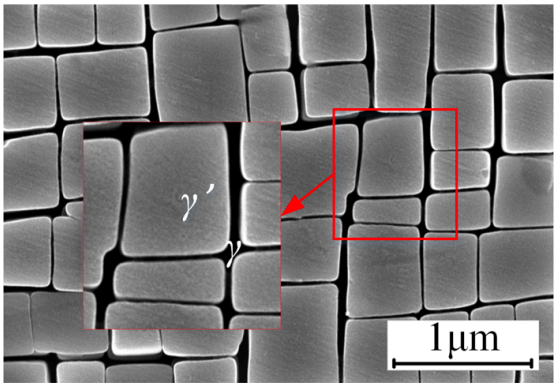

Figure 2.2 {001} plane γ/γ' microstructure of the single crystal superalloy DD6 [10]

The gamma phase contains mostly nickel, cobalt, iron, chromium, ruthenium, molybdenum, rhenium, and tungsten; these elements stabilize the gamma phase as they have atomic radii similar to that of nickel. The gamma phase forms a continuous matrix that the other phases reside in. Ruthenium and rhenium are also responsible for significant improvement in strength at high temperatures [8].

The gamma prime phase contains mostly, aluminum, titanium, niobium, and tantalum; these have atomic radii larger than that of nickel and promote ordered phases such as Ni_3(Al, Ta, Ti). This phase is a precipitate phase which is coherent with the γ-matrix [8]. Coherent interfaces have low energy, and the precipitates have little driving force to grow. The fine and hard precipitates impede dislocation motion, significantly increasing strength over a wide temperature range [7]. A simplified unit cell of the γ and γ' phases are seen in Figure 2.3.

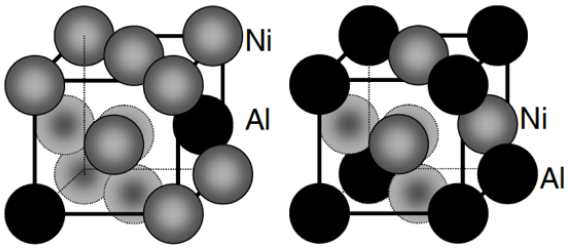

Figure 2.3 γ (left) and γ' (right) unit cells for Ni-Al [7]

The gamma prime phase is credited with high temperature resistance. The size and volume fraction of the gamma prime phases affect the creep and fatigue strength of the alloy (Figure 2.4).

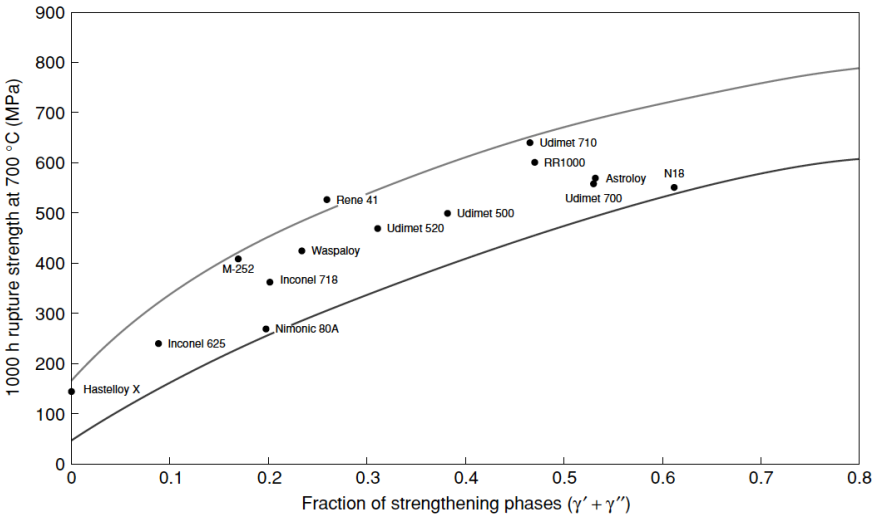

Figure 2.4 Creep strength of common turbine disc alloys as a function of the γ′ and γ″ strengthening phases [8]

To improve resistance to creep and thermal fatigue, superalloys can be manufactured as single crystals that remove grain boundaries, reducing atomic diffusion processes. These alloys do not need grain boundary strengthening elements such as carbon, boron, and zirconium. However, the alloys do have phase boundaries. A lack of grain boundaries affects oxidation behaviour as there are no grain boundaries to diffuse to.

First-generation single crystal superalloys contain appreciable quantities of the γ hardening elements Al, Ti, and Ta. The grain-boundary-strengthening elements C and B are no longer present [7], [8]. Second-generation alloys are characterized by a 3 wt% concentration of Re, which is increased to about 6 wt% for the third-generation alloys. Generally, the modern alloys are characterized by significantly lower concentrations of Cr and higher concentrations of Al and Re. Concentrations of Ti and Mo are now at very low levels [7], [8]. The period since 2000 has seen the emergence of the fourth-generation single-crystal superalloys, which are characterized by additions of ruthenium [7], [8]. A historical overview of nickel-based superalloy development and the enhanced performance over time is shown in Figure 2.5.

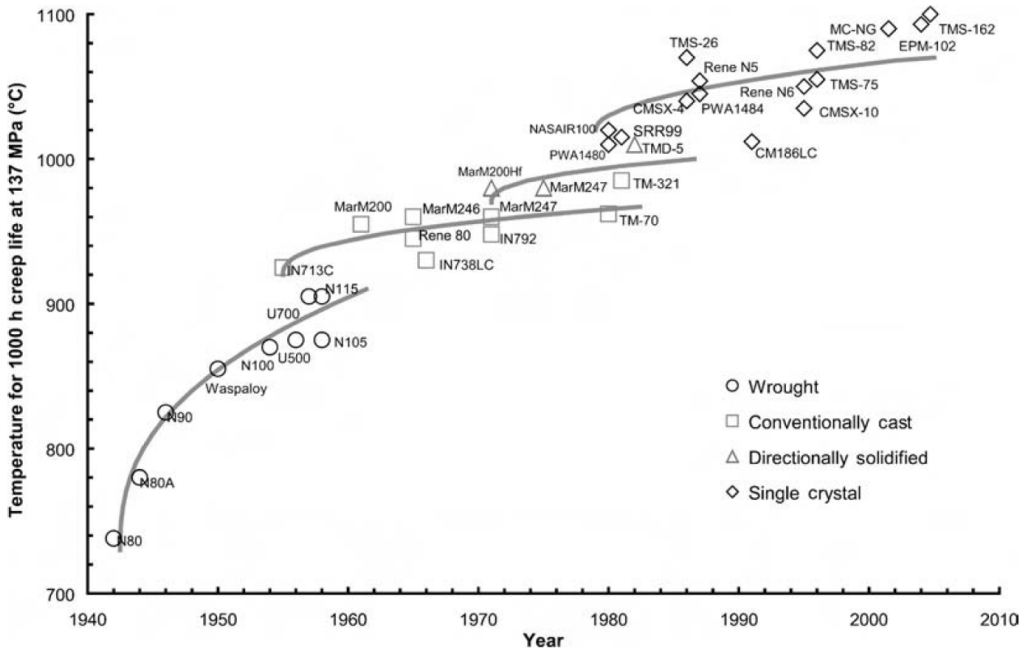

Figure 2.5 History of nickel-based superalloy development relative to temperature capability from 1940-2010 [8]

While nickel-based superalloys have proven to be excellent materials for high-temperature applications, they do have limitations. As turbine inlet temperatures rise, resistance to oxidation, hot-corrosion, creep, and fatigue, is imperative. These processes modify the superalloy composition, compromising the desired mechanical properties. To overcome these limitations and extend the temperature range of these alloys, environmental barrier coatings (EBCs) have been developed. These coatings are used to protect the underlying nickel-based superalloy from harsh environments, allowing them to operate at even higher temperatures without losing their mechanical properties [7].

2.1.3 Environmental Barrier Coatings (EBCs)

Environmental barrier coatings aim to reduce the temperature, oxidation, and hot-corrosion of the substrate material through the growth of a protective oxide scale. An effective environmental barrier coating should have the following properties [7]:

Oxidation/Corrosion Resistance

- Thermodynamically stable, protective surface scale of uniform thickness
- Slow growth rate of protective surface scale

- Adherent surface scale
- High concentration of scale former

Stability

- No undesired phase changes within the coating
- Low diffusion rate across interface at use temperature
- Adequate compositional stability across interface
- Minimized brittle phase formation

Adhesion

- Good adherence of coating to substrate
- Matched coating/substrate properties to reduce thermal stress
- Minimized growth stresses
- Optimized surface condition (rough or smooth)

Structural Properties

- Can withstand service-related creep, fatigue, and impact loading of surface without failure of function

The primary types of environmental barrier coatings for high temperature applications are diffusion coatings and overlay coatings. Diagrams of both systems are shown in Figure 2.6 along with a diagram of the TBC system that can be made with either bond coat system [11].

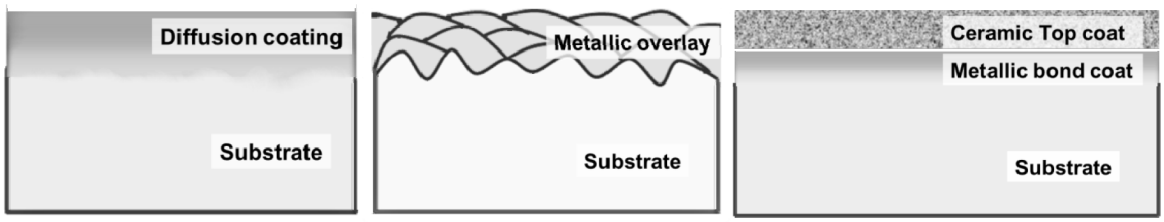

Figure 2.6 Schematic sketches of the general configuration of the three different types of coatings used for high-temperature applications (from left to right): diffusion coatings, metal overlay coatings, and thermal barrier coatings [11]

2.1.4 Diffusion Coatings

Diffusion coatings consist of a substrate alloy and an oxide scale forming compound such as aluminium, chromium, or silicon. Through exposure to high temperatures, the scale forming compounds diffuse into the substrate and form an intermetallic layer 10-100 μm deep. Diffusion coatings are capable of coating complex geometries and require temperatures within the range of conventional furnaces, reducing the capital investment of the technique. For oxidation resistance, aluminide coatings have been found to be superior [7]. For the purpose of this thesis, more attention is given to overlay coatings.

2.1.5 Overlay Coatings

Overlay coatings do not involve any elements from the substrate in the coating process. This allows for the deposition of completely different alloy compositions from the substrate, optimizing coating properties for corrosion resistance, mechanical and thermal compatibility with the substrate, and oxidation behaviour.

The microstructure of overlay coatings is composed of β and γ phases. The ratio of each dictates the phase stability, oxidation and corrosion resistance, ductility, and strength of the coating [7], [8]. This feature makes overlay coatings more customizable based on intended application.

MCrAlY type coatings joined the group of EBCs in the ‘70s and offered enhanced customizability and corrosion-resistance [5]. For gas turbine engine applications, MCrAlY bond coat materials are the most widely used form of overlay coating. M stands for “metal”, typically nickel, cobalt, iron, or a combination thereof; chromium and aluminum are added in varying ratios; Y stands for yttrium, though other transition metal and metalloid elements are sometimes added as well, this is sometimes represented as MCrAlX, though the two can be used interchangeably in the literature [2], [5]. The MCrAl portion of the system provides the corrosion resistance and desired ductility, and the reactive elements improve the oxide scale adhesion and reduce the oxidation rate [5].

Overlay coatings have a lower aluminum content compared to diffusion coatings at 10-15%. This is possible due to the selective oxidation of aluminum instigated by higher chromium contents [11]. Coating compositions by weight are within the range of 15-25% Cr, 10-15% Al, and 0.2-0.5% Y [2], [12]. Table 1 summarizes the compositions of some common and prototype MCrAlY systems.

Table 1 Composition by weight % of common and prototype MCrAlY overlay coatings [8]

	Ni	Co	Cr	Al	Y	Ti	Si	Hf	Others
NiCrAlY	Bal		25	6	0.4				
NiCrAlY	Bal		22	10	1.0				
NiCrAlY	Bal		31	11	0.6				
NiCrAlY	Bal		35	6	0.5				
CoNiCrAlY	32	Bal	21	8	0.5				
CoCrAlY	—	Bal	25	14	0.5				
NiCoCrAlTaY	Bal	23	20	8.5	0.6				4 Ta
NiCoCrAlYSi	Bal	0–40	12.5–20	2–8	0–0.25	0–10	2–10		0–4 Nb 0–4 Mo 0–20 Fe 0–5 Mn
NiCrAlTi	Bal		30–40	1–10		1–5			
NiCoCrAlHf	Bal	0–40	10–45	6–25				0–10	

MCrAlY coatings are based on the two-phase β+γ microstructure. The aluminum forms an intermetallic β-NiAl or CoAl phase and is surrounded by a Ni or Co based γ solid solution matrix [13], [2], [11]. This combination of β and γ phases is responsible for increasing the ductility and thereby the thermal fatigue resistance of the coating [8]. The high chromium content compared to diffusion coatings is responsible for the increased oxidation and corrosion resistance [11]. Overlay coatings can also have γ′-Ni_3Al, α-Cr, and σ-(Co,Cr) phases present [12].

In practice, NiCrAlY and NiCoCrAlY coatings have superior high-temperature oxidation resistance than cobalt-based coatings [5], however NiCrAlY systems undergo an unfavourable phase transformation above 1000°C, making NiCoCrAlY the standard composition used in high temperature application [11]. Examples of CoCrAlY and NiCoCrAlY overlay coatings deposited by electron beam physical vapor deposition (EB-PVD) and argon shrouded plasma spray respectively can be seen in Figure 2.7 (a) and (b).

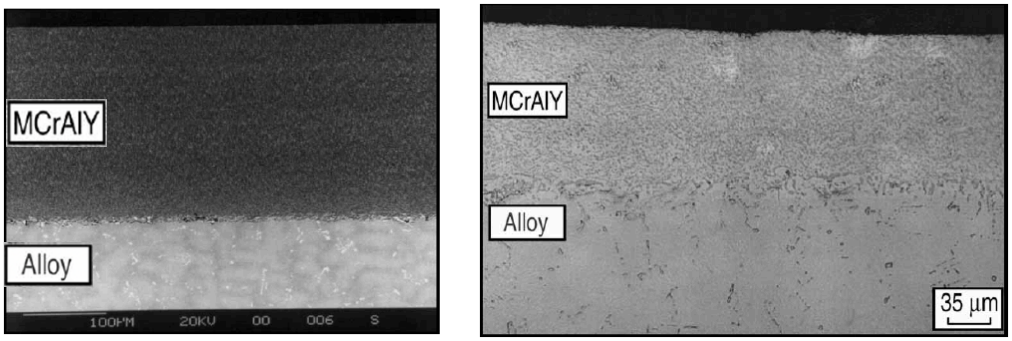

Figure 2.7 (a) EB-PVD deposited CoCrAlY coating on nickel-based superalloy (MarM002) [5], (b) Argon-shrouded plasma sprayed NiCoCrAlY coating on nickel-based superalloy [5]

Air plasma spray is another common deposition method for overlay bond coats. The process produces a thick coating and is less expensive than EB-PVD. However, this method is typically used for stationary parts such as combustor liners where coating thickness is less important and is unsuitable for moving parts such as turbine blades [2]. The addition of reactive elements such as yttrium, hafnium, and silicon have been shown to improve cyclic oxidation performance as seen in Figure 2.8.

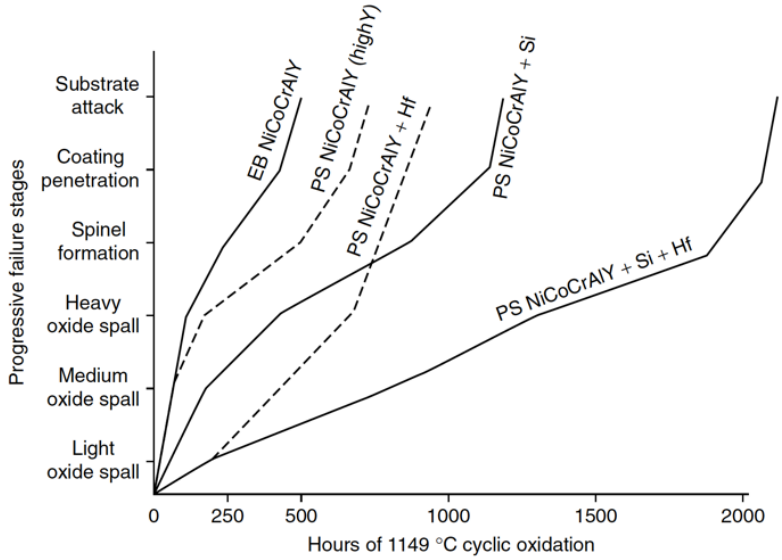

Figure 2.8 Oxidative degradation of EB-PVD and PS overlay coatings showing benefit of active element additions [8]

Overlay coatings are within the range of 100-200 µm thick [2], and cost 2-4 times as much as diffusion coatings. MCrAlY systems however, offer better control of the mechanical and

thermodynamic properties, and are less prone to spall under cyclic oxidation conditions compared to diffusion coatings [2], [14].

2.1.6 Thermal Barrier Coatings

Thermal barrier coatings (TBCs) are multi-material systems used to improve the efficiency of gas turbines. They were first introduced for static parts in high temperature environments in the '70s [5], [2]. TBCs enable higher operating temperatures by reducing the substrate temperatures by over 100°C [2]. When used in conjunction with internal cooling, these systems can allow for operation 250°C above the substrate melting temperature of the superalloy components [12]. An overview of a typical turbine blade TBC system is shown in Figure 2.9.

Cooling air flows through pinholes in the coating from hollow channels in the vanes. The ceramic top coat (between 100-400 µm) is responsible for the majority of the temperature resistance, however, provides no oxidative protection. The oxidation resistance is seen in the thin thermally grow oxide (TGO) (1-10 µm), for which the bond coat (~60 µm) acts as an elemental reservoir. The bond coat material must have good adhesion to the superalloy substrate, and an elemental composition that allows for the quick formation and slow growth of the TGO.

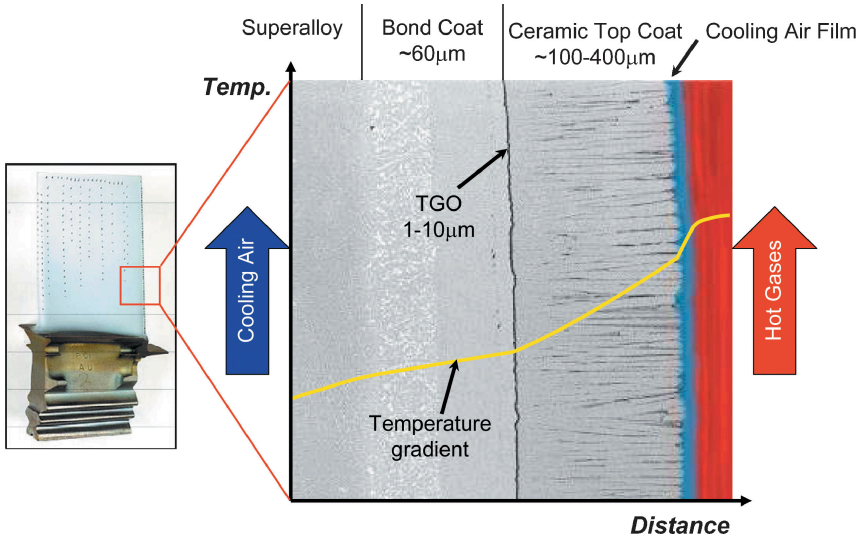

Figure 2.9 Cross-section diagram of TBC system with EB-PVD ceramic top coat [12]

Stationary components like combustor liners and nozzles use air plasma spray deposited systems achieving thicknesses of 250-500 µm. As these parts do not move, thickness is less important, and

the low thermal conductivity of APS systems can be capitalized on. Aeroturbine blades in the high-pressure turbine section employ electron-beam physical vapor deposition (EB-PVD) techniques to achieve smaller thicknesses of 100-250 µm, minimizing rotational inertia [2]. The microstructure of the two systems are highlighted in Figure 2.10.

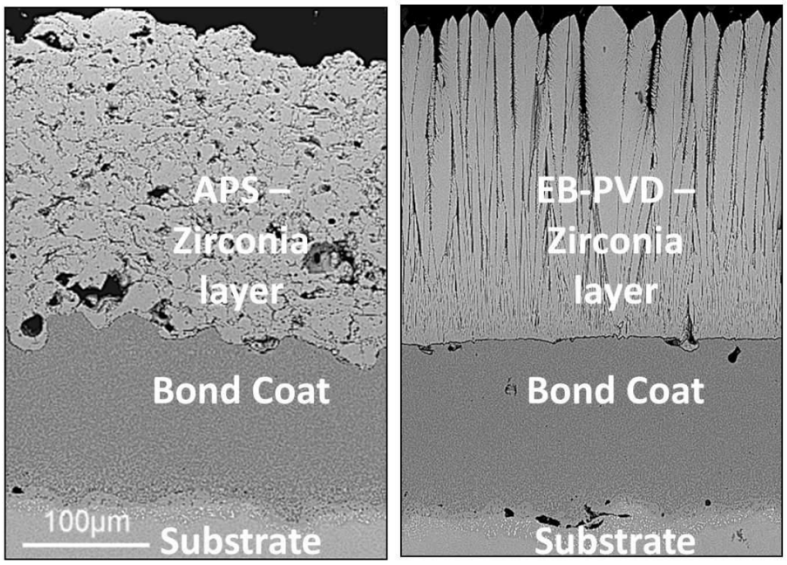

Figure 2.10 Standard APS and EB-PVD deposited zirconia top-coat morphologies. APS TBC is deposited on sprayed MCrAlY bond coat and EB-PVD TBC is deposited on pack cemented diffusion bond coat [11]

During service, the microstructures and compositions of the TBC layers are constantly changing. The layers of the TBC systems interact with each other chemically and mechanically, determining the durability of the system through these relationships [2].

2.1.7 Metallic Bond Coat

The primary role of the metallic bond coat is to act as a reservoir of elements needed in the formation of a stable, slow growing, and adhesive TGO [2], [12], [11]. Bond coat oxidation is largely influential in TBC durability and should be thermo-chemically compatible with the substrate such that the superalloy retains its properties in service, and compatible with the vastly different properties of the ceramic top coat [5], [15].

In the high-temperature oxidative environments, two main mechanisms govern the degradation of the TBC system: oxidation and interdiffusion between the substrate and the bond coat [16]. The bond coat should minimize diffusion with the substrate resulting in aluminum depletion and

upward diffusion of refractory elements like sulfur, which result in compromised creep and rupture properties in the bond coat alloy [2]. Aluminum diffusion from coating to substrate reduces the aluminum available for alumina scale formation. Interdiffusion results in the development of a β-phase depletion zone in the coating and a γ′-phase depletion zone in the substrate [16]. With increased oxidation exposure, the depth of the β-depleted zone below the TGO increases; affecting the properties of the underlying alloy phase, and altering the TGO's strain state such that cracking and spallation is increased during cyclic heating and cooling [17].

Aluminum based and MCrAlY overlay EBCs have been repurposed as bond coats, as they have proven to be reliable oxide formers and are designed to be compatible with the substrate. A comparison of bond coat influence on TBC life can be seen in Figure 2.11.

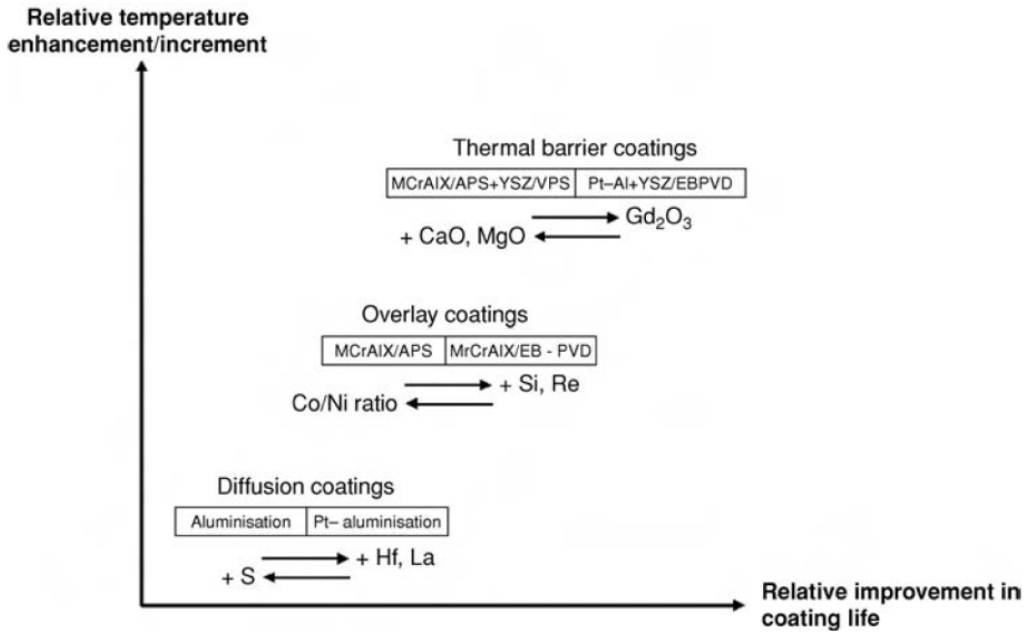

Figure 2.11 Comparison between thermal reduction and coating life of three general protective coating systems [8]

The failure modes associated with bond coats are heavily influenced by the deposition method and subsequent microstructure. Spallation is due to microstructural instability at the bond coat TGO or TGO ceramic interfaces. This is generated by bond coat oxidation and by thermal mismatch between components [5]. APS coatings tend to fail from delamination cracking from in-plane compressive stress that cause out-of-plane tensile stresses. The rough surface first helps adherence because of mechanical interlocking but later drives delamination, highlighting the benefits of slow

growing TGOs [5]. EB-PVD coatings fail at the TGO bond coat interface, unless there is a lot of rumpling due to progressive adhesion reduction from microcrack formation and growth [5]. Spallation and cracking of the TGO is the ultimate failure mechanism of TBC systems, particularly EB-PVD TBCs [12]. Table 2 summarizes the different constituents of overlay coatings and their functions and effects [7].

Table 2 Elemental constituents of metallic coatings, their functions, and effects [7]

Elemental Constituent	Beneficial Aspects	Detrimental Aspects
Ni	Major constituent of substrate alloy. Provides strength.	Prone to destructive interaction with sulfur.
Co	Major constituent of substrate alloy. Provides microstructural stability and strength.	Prone to destructive interaction with sulfur.
Al	Constituent of substrate alloy. Major contributor to providing strength. Contributes to oxidation resistance.	Large concentration lowers melting point.
Cr	Constituent of substrate alloy. Contributes to oxidation resistance to 1500°F (816°C). Reduces Al requirement for formation of alumina scale. Imparts resistance to hot corrosion.	Lowers creep strength.
Ta	Enhances hot corrosion and oxidation resistance. Improves strength.	
Si	Enhances oxidation and type II hot corrosion resistance.	Large concentration leads to formation of brittle phases.
Hf, Y, Y_2O_3, oxides of other reactive elements	Improves adherence of alumina and chromia scales.	Large amounts are detrimental.
Pt	Improves oxidation and hot corrosion resistance.	

2.1.8 Ceramic Top Coat

The ceramic top coat is responsible for the drastic temperature difference between the hot exhaust gas and the superalloy. Its main purpose is insulation, and it does not provide any oxidation protection [15]. Small spalls in the coating are negligible due to the internal cooling and boundary

layer influences of the ceramic coating that allow small defects to be protected by the surrounding coating. Large spalls are preceded by cracks that form along delamination planes inside the coating or at the interface with the TGO [15].

Yttria stabilized zirconia is most notable for having a high melting point, low thermal conductivity, high oxygen permeability, a large thermal expansion coefficient, and stability at the operating temperatures within the turbine engine [2]. Without the yttrium addition, pure zirconia undergoes a brittle phase transformation during cooling from the tetragonal phase to the monoclinic phase [18]. A phase diagram for yttria stabilized zirconia shows the main cubic, tetragonal, monoclinic, and non-transformable tetragonal phases (Figure 2.12).

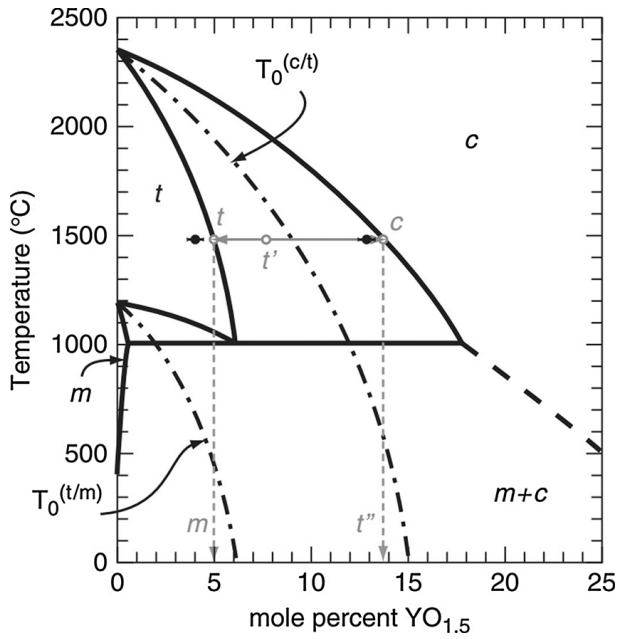

Figure 2.12 Phase diagram for ZrO_2 – Y_2O_3 [8]

The cubic phase is brittle and does not perform well against erosion. For lower yttria content, the tetragonal phase shows improved toughness, however it experiences a martensitic transformation to the monoclinic phase upon cooling associated with a 3-5% volume increase [2], [12]. The tetragonal phase transforms into the monoclinic upon cooling and reforms upon subsequent heating, resulting in microcracking and early spallation [2]. The monoclinic phase is also associated with an increase in thermal conductivity in the ceramic [5]. Between 5-10% Y_2O_3 additions the non-transformable (t′) phase is obtained, which does not undergo a phase change between ambient and operating temperature. Through extensive experimentation 7wt%- Y_2O_3

stabilized ziroconia (7-YSZ) was found to have the best balance of thermal and mechanical properties. Higher yttria content was shown to result in lowered fracture toughness and reduced erosion resistance [12], [15].

The t' phase has large grains on the order of 100 microns when deposited by EB-PVD, and has a porosity on the order of 10-25% [2]. 7-YSZ allows for component lives upwards of 20,000h [5]. The non-transformable tetragonal structure is created by the quenching of liquid or cubic phase YSZ from high temperatures [18], this is possible with APS and EB-PVD due to the high cooling rates of both processes. Thermodynamically, the system would want to become stable with tetragonal (t) and cubic (c) constituents, however from Figure 2.12 the t' phase does not easily transform under 1200°C [12]. When t' is aged above 1200°C, the material experiences a phase separation by diffusion which then allows for the t→m transition to occur [18]. The decomposition of t' increases by an order of magnitude for every 100°C [14].

Of the two deposition techniques used in industry, the thermal conductivity of EB-PVD deposited top coats is larger than that of APS deposited top coats, making them less effective at reducing the underlying metal temperature. However, EB-PVD topcoats show superior erosion resistance and adhesion to the TGO resulting in a longer lifespan. EB-PVD offers smoother coatings, better thickness control, and minimum cooling hole closure for holes 0.25-0.5mm in diameter, making it preferable for blades and vanes [8]. A summary of coating properties based on deposition method is found in Table 3.

Table 3 Properties of 7-YSZ Top Coat Thermal Barrier Coatings at Room Temperature [5], [12]

	Deposition Method	
Property/Characteristic	**EB-PVD**	**Plasma Spray**
Thermal conductivity (W m^{-1} K^{-1})	1.5–1.9	0.8–1.1
Surface roughness (μm)	1.0	10.0
Adhesive strength (MPa)	400	20–40
Young's modulus (GPa)	90	200
Erosion rate (normalized to PVD)	1	7

Although the thermal conductivity of EB-PVD coatings is larger than that of APS, it remains the industry standard due to the other desirable properties, with research being done to lower the thermal conductivity coefficient [2].

2.1.9 Thermally Grown Oxide

The thermally grown oxide (TGO) forms at the interface between the bond coat and the ceramic top coat. This protective oxide scales should aim to have uniform thickness, a slow growth rate, minimal internal stresses, and a similar thermal expansion to the substrate material [7]. The TGO forms when the bond coat reacts with the combustion gas to form a thermo-chemically protective oxide, typically α-Al_2O_3 [13], [15]. When the alumina scale first starts to form, it goes through transient phases which are faster growing than α-Al_2O_3. γ-Al_2O_3, δ-Al_2O_3, or θ-Al_2O_3 typically grow as undesirable brittle whiskers and the transformation of transient phases to α-Al_2O_3 results in an 8-13% volume reduction and a 75 MPa residual compressive stress in the TGO [12]. Critical alumina scale thickness is on the order of 5 μm for EB-PVD coatings and 10 μm for APS coatings [12].

The scale should have a low oxygen ingress at operating temperature, and low counter-diffusion of metallic elements. TGO formation is controlled by the bond coat microstructure and microchemistry, but can be largely influenced by impurities, water vapor, and dopants [15]. α-Al_2O_3 can be considered to be dehydrated, as temperature rise drives water out of the structure's interstitial sites [13].

The necessary amount of aluminum required to grow a protective scale is determined by kinetics, and is more than thermodynamic estimates based on equilibrium [12]. During the thermal cycling and subsequent growth of the alumina layer, internal compressive stresses of up to 4 GPa can develop at room temperature. Even though the film is thin, a large amount of internal energy is stored within, which can lead to delamination from the bond coat [15]. The position of the TGO in the TBC system is shown in Figure 2.13, where rumpling of the TGO due to the internal compressive stresses and resultant delamination from the ceramic top coat is visible.

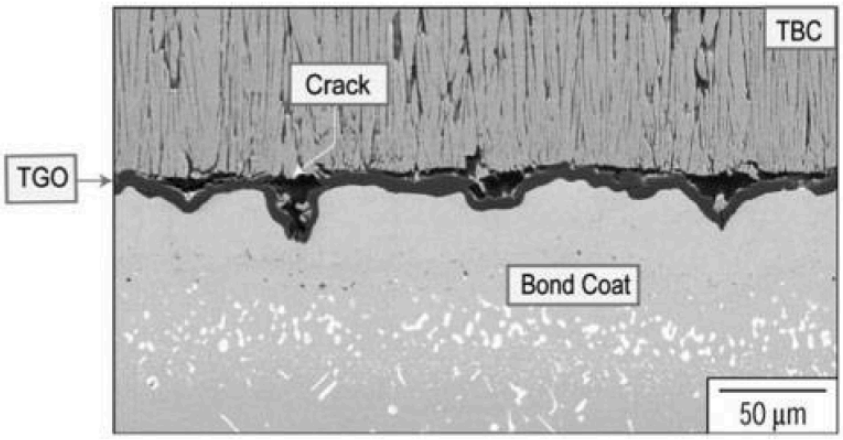

Figure 2.13 Rumpling of the TGO as a result of thermal cycling [2]

2.1.10 Oxidation Kinetics

Kinetics describes the speed at which a transformation occurs. The rate of oxidation for a component is described by the oxidation kinetics, which depend on the composition, real surface to geometric area ratio, temperature, gas composition, and oxidation cycling conditions. Isothermal tests are used to study oxidation kinetics. Samples are polished and held at the desired temperature inside a furnace for upwards of 20h [7]. The gas composition and temperature are maintained as close to application conditions as possible, however the gas velocities found in gas turbine engines cannot be recreated inside a furnace.

2.1.10.1 Parabolic Growth

Protective scales such as alumina are characterized by a parabolic growth rate which is thermally activated and grows by diffusion through the oxide scale. The oxide scale thickness is described as x through the function,

$$x^2 = kt$$

where k is the rate constant and t is exposure time usually given in seconds [7].

MCrAlY and diffusion coatings obey the parabolic rate law, gaining more weight under cyclic oxidation than isothermal. In overlay coatings NiO, Cr_2O_3, and α-Al_2O_3 initially form simultaneously, through continued oxidation the Ni atoms are replaced by Cr atoms and the stable form of the oxide is mainly Cr_2O_3, and α-Al_2O_3 [14].

2.1.10.2 Linear Growth

Non-protective scales result in a linear oxide growth rate controlled by metal-oxygen reactions on the surface [7]. As the scale is porous, the growth rate is not scale thickness dependent and can be described as,

$$x = x_{\circ} + kt$$

where $x_{\circ}$ is a constant.

2.1.10.3 Pilling-Bedworth Ratio

The Pilling-Bedworth Ratio (PBR) is used to determine the protective nature of an oxide scale. It is a ratio of the volume of oxide formed to the volume of metal consumed. When the PBR is much smaller than unity, the volume of oxide formed is less than the volume of metal consumed which requires a porous structure to cover the surface of the metal. Porous scales are not protective. If the PBR is much greater than unity, large compressive forces will develop in the quickly growing scale which lead to spallation and expose the substrate to further oxidation. Table 4 gives PBR values for common oxide scales, showing that a value close to unity is desired as it is non-porous and slow growing [7], [11].

Table 4 PBR Values for Common Oxide Scales [7]

System	PBR	Protectiveness
Al/Al_2O_3	1.28	P
Cr/Cr_2O_3	1.99	P
Si/SiO_2	2.15	P
Ca/CaO	0.64	NP
Ta/Ta_2O_5	2.47	NP

P, protective; NP, nonprotective

Common exceptions to the PBR are geometry effects such as edges, the volatility of the oxide scale, and chemical interactions with the substrate.

2.1.10.4 TGO Formation

Between 1000°C-1125°C, the alumina oxide grows through the counter-diffusion of oxygen and aluminum along the alumina grain boundaries which are shown in Figure 2.14 (a). The parabolic growth rate is determined by the alumina grain size and the presence of impurities. Inter-diffusion

along the grain boundaries controls the TGO thickness and elongation. The grain boundaries in the alumina layer are found to be clean and without amorphous interphases [15].

Once the TGO layer has formed, continuing growth is due predominantly to the inward diffusion of oxygen, however in practice the counter-flux of cations is the driving force. The literature does not address the counter-diffusion mechanisms and how they determine elongation strain [15]. The flux paths are along the alumina grain boundaries [20]. A schematic of the paths is found in Figure 2.14 (b).

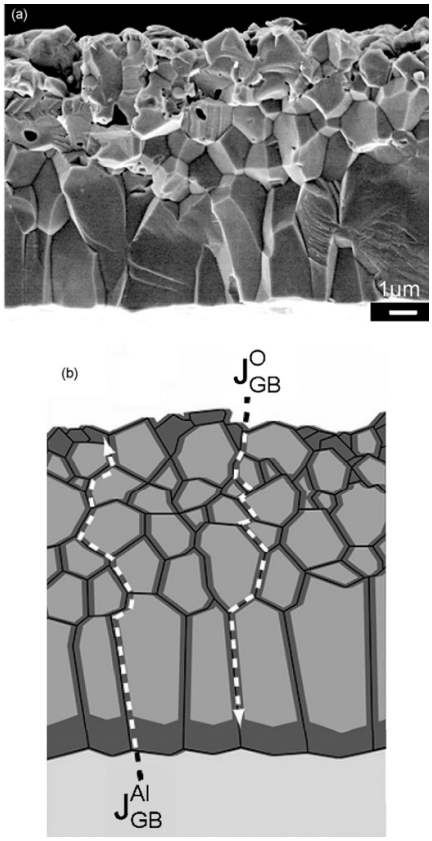

Figure 2.14 (a) TGO cross-section showing columnar alumina structure (b) Diagram illustrating flux paths [15]

Oxide scales spall once they reach a critical thickness, which is followed by the reformation of the scale. Aluminum in the alloy diffuses to the oxide–alloy interface to reform the scale. As this process continues, an aluminum depleted zone forms in the alloy below the oxide scale. The thickness of the depleted zone is dependent on the aluminum content of the alloy. Isothermal oxidation of NiCoCrAlY with 12 wt % Al, exhibits depleted zone thickness 3 times the thickness of the alumina scale [2]. The nucleation of α-Al_2O_3 can be instigated by crystalline seed layers

such as α-Cr_2O_3 [21], leading to the faster formation of a uniform and stable protective oxide scale. Good adhesion between the top coat and the bond coat is a desirable quality, as it slows the oxidation growth responsible for buckling and spall. This being a major failure mechanism of TBCs [2].

2.2 Oxidation Behaviour in Dry and Humid Environments

2.2.1 Dry air oxidation behaviour

In TBC systems the ceramic top coat is oxygen blind. Oxidation resistance is the responsibility of the bond coat. The process by which oxidation occurs begins with the adsorption of oxygen molecules onto the metal surface where the oxygen dissociates into its atomic form and migrates to low-energy spots. Here, the oxygen ionizes to bond with the metal. As these reactions continue, oxides form over the low-energy sites, eventually overlapping to form a coherent layer of transient oxide film. Oxygen and metal then diffuse through the film, stabilizing the layer and continuing the growth process [7]. The factors governing the extent and speed of this reaction are thermodynamics and kinetics [22]. A common phase distribution in MCrAlY bond coat materials is seen in Figure 2.15, showing a vacuum cast CoNiCrAlHf alloy with four distinguishable areas.

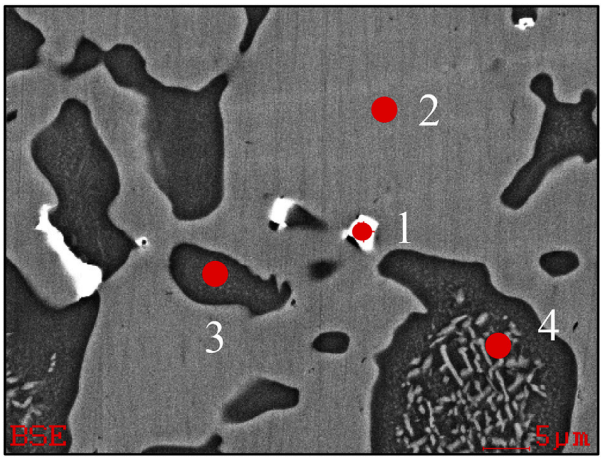

Figure 2.15 BSE image of vacuum cast CoNiCrAlHf bond coat alloy [17]

The light area in the microstructure (1) corresponds to the Y-rich phase. Yttrium (Y) is added at low concentrations to improve the adhesion of the TGO. At 0% H_2O, the Y-rich phase yields outcrops of NiO that are surrounded by spinel. Y increases the O_2 dissociation rate, and thereby, the surface concentration of atomic O resulting in quick-forming TGO.

The grey area in the microstructure (2) corresponds to the $\gamma + \gamma'$ phases, has an FCC lattice, and contains a random distribution of different species of atoms such as Cr and Co. It is mainly composed of a Ni_3Al matrix and yields α-alumina that is faintly dotted with spinel at the onset of oxidation.

The dark area in the microstructure (3) corresponds to the β phase and has a BCC crystal structure. It is predominantly composed of NiAl and serves as the main source of Al for the thermally grown oxide (TGO). Initially, the dark area forms alumina.

Point 4 is a CoNiCr rich intermetallic phase also present in some of the materials selected for this study. In specimens where hafnium is present, Hf-rich precipitates congregate around the γ′-β phase boundaries [17].

In the first hours of oxidation TGO growth is mainly dependent on upward Al diffusion, causing a rapid mass increase as the TGO forms. Oxygen reacts with Al, Cr, and Ni to form θ-Al_2O_3, Cr_2O_3, and NiO. Transient θ-Al_2O_3 forms before undergoing a phase transformation to α-Al_2O_3 once a depth of approximately 300 nm is achieved. θ-Al_2O_3 has a blade-like morphology and provides channels for oxygen to penetrate the oxide layer, lending poor oxidation resistance to the TGO [23].

As oxidation exposure time increases, an Al-depleted γ+γ′ phase forms under the TGO. Cr_2O_3 undergoes a phase transformation to CrO_3 which can evaporate, creating voids in TGO. The lack of Al availability leads to solid state reactions between Al_2O_3 and CrO_3 with NiO to form (Ni, Co)(Cr, Al)$_2O_4$ spinels. These spinels provide fast diffusion paths for oxygen, accelerating local oxidation [23], [24].

2.2.2 Humid air oxidation behaviour

The turbine exhaust from the combustion zone of a gas turbine engine can be expected to be 12-14% water vapor when burning natural gas and up to 15-30% for high hydrogen fuels [25]. Water vapor can significantly alter the oxidation rate, microstructure, oxide-alloy adhesion, and corrosion resistance of the TGO in TBCs, which in turn reduces the life of the system [25]–[27]. The presence of water vapor has been found to alter the phase transformation rate of the growing alumina scale [28], promoting the growth of metastable or transition aluminas (γ-Al_2O_3, δ-Al_2O_3, or θ-Al_2O_3) in β–NiAl bond coatings [8]. Water vapor has been reported to promote cracks

formation and oxide spallation at high temperature. Stress corrosion cracking in the TGO can lead to oxide spallation in humid environments, decreasing the coating lifetime.

In dry and wet air, the oxidation process follows the parabolic rate law. However, in H_2/10%H_2O the parabolic rate constant is larger, leading to a faster oxidation rate [27]. The water vapor is thought to stabilize the faster growing metastable γ,θ-Al_2O_3 phases resulting in a thicker TGO compared to scales grown in dry air [26]. However, other studies have hypothesized that the presence of water promotes internal oxidation of the alloy, delaying surface oxidation and resulting in a thinner scale [17]. Li et al. [20] found that cyclic oxidation in 25% H_2O resulted in a thinner oxide layer than in dry air.

For chromia scales, the grain size of the TGO is reduced by the presence of water, increasing plasticity and relieving stress in the TGO layer, which helps to prevent local cracking [27]. The effect of water on chromia and alumina scales does not appear to be the same. For chromia scales, water improves adhesion at the alloy-scale interface delaying spallation compared to dry air samples under the same test conditions, which showed severe buckling under cyclic oxidation at 950°C [27]. However, although the scale was less prone to spall, the oxide formed on the surface of the alloy was more porous and less protective of the substrate [27]. In alumina forming TGOs water increases scale spallation [26], [28].

Zhou et al. [29] found that outward diffusion of nickel and chromium increased in humid oxidation, studying low-pressure plasma-sprayed NiCrAlY coating in O2 + 5% H2O. Li et al found that the diffusion of aluminum from the coating was too slow to maintain a minimum concentration of Al at the alloy-oxide interface to form Y_2O_3 and Al_2O_3 in initial oxidation, leading to more spinels. Other researchers showed that water vapor can improve the oxidation resistance of alloys through other mechanisms, such as promoting the formation of Cr_2O_3 hexagonal oxides that act similarly in protecting the alloy as α-Al_2O_3 [20].

MCrAlY alloys form a TGO of two layers shown in Figure 2.16; a dense, columnar grain alumina at the alloy-oxide interface, and a porous equiaxed grain layer on the surface. In air, the alumina forms large columnar grains, where cracks in the TGO and voids at the alloy-oxide interface are easily identified (a). In Ar + 25% H_2O many voids are visible in the columnar and equiaxed grains (b), while in 25% H_2O, very fine oxide grains are observed with no visible voids (c). Water vapor at the oxide grain boundaries hindered their movement and as a result, grain growth. Y_2O_3 particles

were found at the interface between the columnar and equiaxed grains, HfO_2 was found in the middle of the TGO [20].

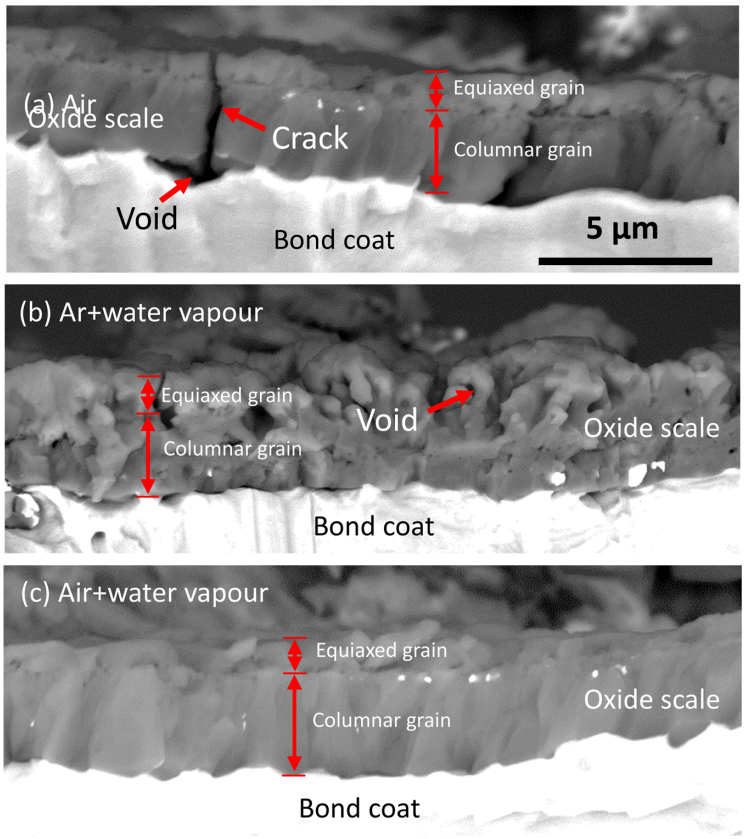

Figure 2.16 Fractured cross-sectional BSE images of the TGO formed on the NiCoCrAlY prepared in (a) air, (b) Ar + water vapor, and (c) air +water vapor after cyclic oxidation at 1050 ◦C for 150 h [20].

In air, the surface equiaxed oxide has a hexagonal structure, corresponding with α-Al_2O_3 (Figure 2.17(a)). In 25% H_2O, plate-like tetragonal alumina was identified, corresponding with γ-Al_2O_3 ((Figure 2.17 (b)). This endorses the theory that water vapor delays the transformation of transient aluminas [20].

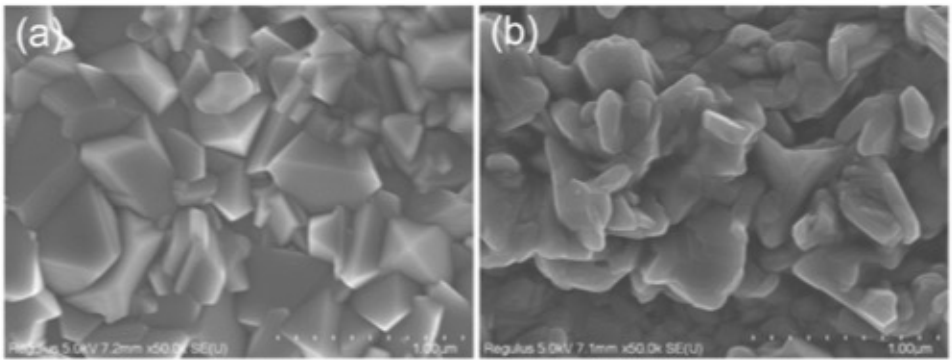

Figure 2.17 Different crystal morphologies developed on the sample surfaces oxidized in (a) air and (b) air + 25% H_2O at 1050 ◦C [20].

D.J Young et al describe the oxygen flux across the TGO (J_O) as:

$$J_O = \frac{C\mu_O}{RT}\frac{D_{eff}}{\delta x}$$

$$\mu_O = \mu_O^0 + RTlnP_O$$

Where C is the concentration of diffusing species, μ_O is the oxygen chemical potential, x is the distance from the scale/gas interface, R is the universal gas constant, T is the oxidation temperature in Kelvin, and D_{eff} is the diffusion coefficient. μ_O is the chemical potential of pure oxygen and P_O is the oxygen partial pressure. Typically, μ_O does not change [17].

Studies have used ^{18}O tracer technology to prove that reactive element doped alumina mainly grows by the inward diffusion of oxygen at the grain boundaries. It can be concluded that the growth of the oxide scale is governed by the diffusion of oxygen. Therefore, the rate of oxygen diffusion is directly influenced by the size of the grain boundaries. Roger B. Bagwell et al. showed that water vapor increases the diffusion coefficient by a factor of 50% at 950°C, and Jesse P. Angle et al. showed that the apparent kinetic rate constant for oxygen diffusion in the presence of water was 79% higher than in dry air at 1300°C [17].

At the same diffusion depth, the solubility of oxygen in the oxide formed with water vapor is considerably greater than that obtained in air. This can be explained by the fact that $(OH)^-$ ions are smaller and more polarizable than O_2, facilitating faster diffusion [17]. The dissociation of H_2O leads to a higher P_H that can affect atomic defects in α-Al2O3 [20].

Detrimental internal oxidation is heightened in the presence of oxide defects such as cracks and voids. A dense α-Al_2O_3 leads to a low P_O at the alloy-oxide interface. A large oxygen potential gradient exists across the TGO, as is the driving force for the outward diffusion of reactive element ions. The consumption of aluminum and oxygen decreases as the TGO thickness increases. The diffusion coefficients of Al and O in Al_2O_3 are near equal at 700°C and 1000°C, indicating that temperature is not the main influence. Water vapor aides in the transport of oxygen ions through the thin Al_2O_3 scale to the bond coat, inducing rapid TGO growth in early oxidation [20].

Figure 2.18 highlights the surface morphologies of three Y, Ta, Hf co-doped MCrAlY (high entropy) alloys after dry air oxidation at 1100°C for 650h. In Figure 2.18 (c) whisker-like θ-Al_2O_3 is found on the surface of the oxide layer, not having transformed into α-Al_2O_3 in the earlier stages of oxidation. The volume contraction associated with the θ-Al_2O_3 to α-Al_2O_3 transformation leads to the formation of voids on the surface of the oxide layer (Figure 2.18(f)). In the presence of water, void formation is expected to be more prevalent as transient oxide transformation to α-Al_2O_3 is delayed. Y/Hf oxides are also visible on the surface in Figure 2.18 (i) and are further discussed in the next section. Unlike other reactive elements (Y, Hf, Si), Ta or Ta oxides were not found in the oxide scale [30].

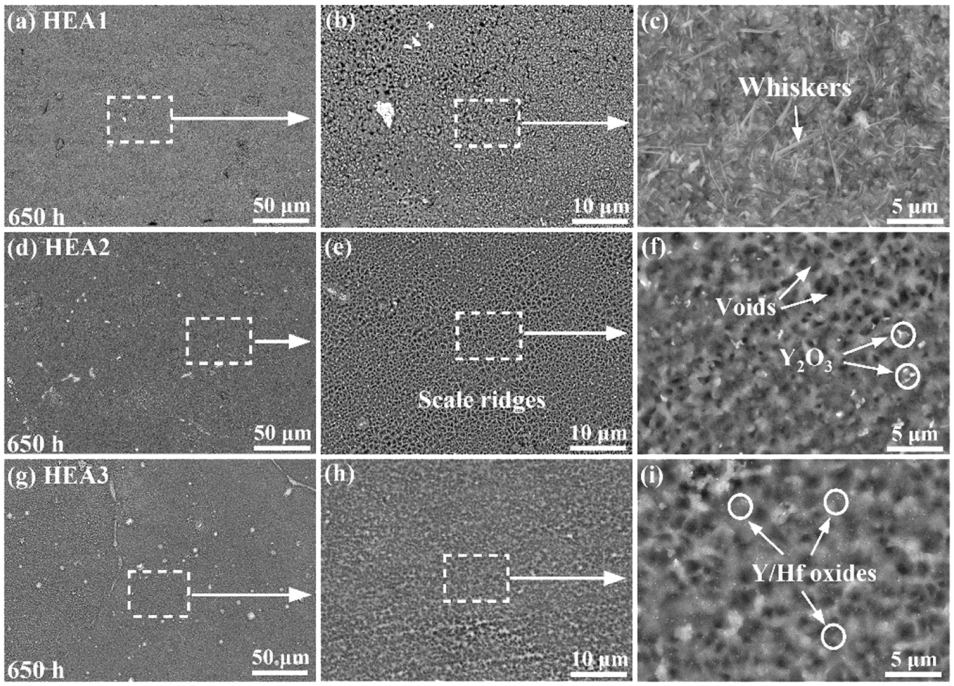

Figure 2.18 Surface morphologies of three high entropy alloys after oxidation at 1100 °C for 650h [30].

A summary table of the test conditions used in the literature for the study of MCrAlY alloy oxidation behaviour in humid environments is seen in Table 5.

Table 5 Review of oxidation parameters found in literature

Authors	Material	Temperature (°C)	Oxidation Environment	Oxidation Time
Li et al. [17], [20]	NiCoCrAlY	1050	Air + 25% H_2O (%vol) Ar + 25% H_2O (%vol)	150h cyclic
	CoNiCrAlHf	1050	Air + 25% H_2O (%vol)	1/24/300/600h cyclic
Haynes et al. [31]	NiCoCrAlYHfSi	1100	Air + 10% H_2O (%vol) Air + 50% H_2O (%vol)	100h cyclic
Fontana et al. [32]	FeCrMnAlTiLaPCS	800	H_2 + 10% H_2O (%vol)	100h isothermal
Zhou et al. [29]	NiAl	950	(20% O_2 + 80% Ar) + 15% H_2O (%vol)	16h isothermal
Sullivan et al. [13]	NiCoCrAlYHfSi CoNiCrAlY	1125	(20% O_2 + 80% N_2) + 0/5/10/15/20/30/40/50% H_2O (%vol)	0-5h isothermal
Hu et al. [30]	NiFeCoCrAlYTa	1100	Air	6h isothermal 620h cyclic
Huang et al. [33]	NiCoCrAlY+$TaSi_2$	1100	Air + 25% H_2O (%vol)	400/1500h cyclic

Shuting et al. [34]	CoCrAlYSi	1050	Air	300h isothermal

2.2.3 Spinel Formation

When exposed to dry air, alumina forming bond coats oxidize to create a uniform, thermochemically protective α-Al_2O_3 scale on the order of around 5 mm [25]. As α-Al_2O_3 can be thought of as being dehydrated, the presence of higher water vapor means more time is required to remove the water from the scale structure, allowing for the prolonged transient phases γ, δ, and θ. The temporary stabilization of the γ, δ and θ alumina phases in the presence of water promotes diffusion of Cr, Co, and Ni cations from the substrate to the TGO interface where they form unwanted oxides. The solid state reaction of these oxides with the alumina forms spinels [25]. The brittle whisker-like spinel is associated with reduced TGO life as it is brittle and leads to cracking in the TGO [27]. Figure 2.19 shows growth of spinels in a chromium-based superalloy under wet air conditions.

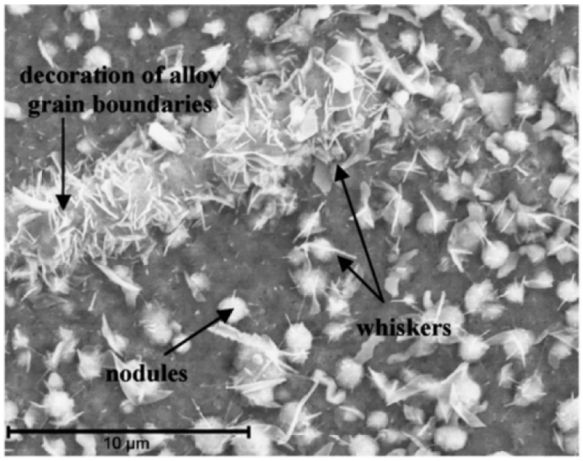

Figure 2.19: SEM observations of Crofer22APU oxidized in H_2/10%$H_2$0 at 800°C for 100h [7].

Figure 2.20 highlights the promotion of spinel formation in the TGO when burning high water-vapor forming syngas versus low water forming natural gas [25], [35]. The formation of spinel also results in volume expansion, weakening the TGO and top coat interface [25]. Sullivan et al. observed spinel on the order of 30 µm thick. The larger the spinel, the less stable the TBC will be

over the course of thermal cycling [25]. In all cases, water content was found to significantly reduce corrosion resistance in chromia and alumina TGOs [26], [27].

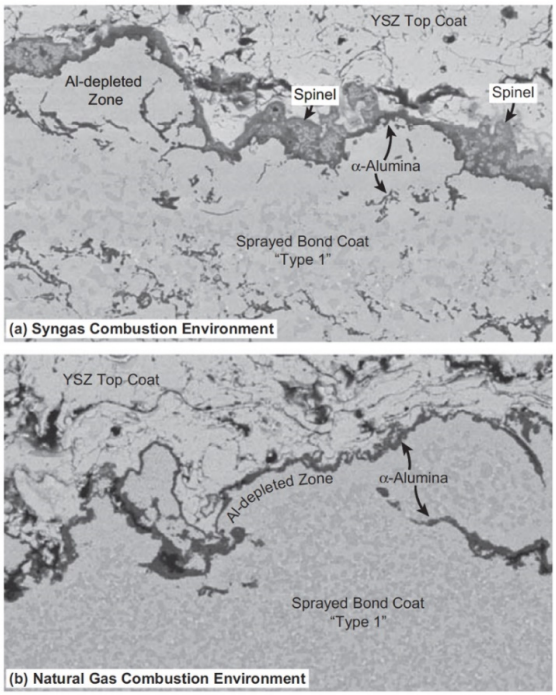

Figure 2.20: SEM of TBC bond coat cross section taken from field tests of industrial turbine blade material systems. (a) High water content syngas (b) Low water content natural gas [36].

The amount of spinel observed in the TGO is directly related to the water vapor content in the air. Figure 2.21 illustrates how an increase in spinel and NiO coverage of the substrate after thermal loading increases with water vapor content, with darker areas being the desirable α-Al_2O_3, the grey areas being spinel, and the bright white spots being NiO [13]. Initial alloy phases with large amounts of Ni, Co, and or Cr produce oxide products that contain a large quantity of those elements as well. From the comparison of (a), (b), and (c) to (d), (e), and (f) it is shown that high Al β phase becomes α-Al_2O_3, low Al γ phase becomes α-Al_2O_3 with spinel, and M, Y-rich phases become areas of NiO encircled by spinel [25]. As the water content increases, the amount of unwanted oxide increases until 15% H_2O when the surface is almost completely covered in spinel and NiO.

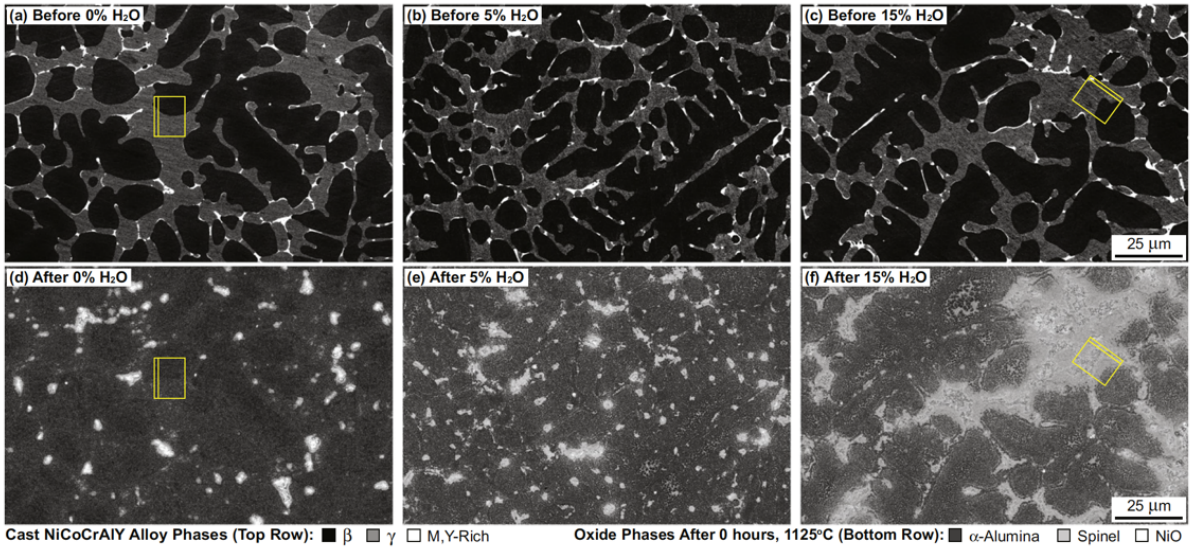

Figure 2.21: Before and after SEM images of cast NiCoCrAlY TGO grown in 0% H_2O (a)(d), 5% H_2O (b)(e), and 15% H_2O (c)(f) after thermal cycling at 1125°C [7],[13].

After 0% H_2O exposure, needle-like metastable alumina has been converted to α-alumina in the β phase, and after 15% H_2O exposure, the metastable alumina has transitioned to alumina/spinel towards the center of the β phase [13]. The surface coverage of spinel increases with water vapor content before plateauing at around 15-30% H_2O and falling slightly after 50% H_2O, which was the highest value tested by Sullivan et al. This is illustrated in Figure 2.22.

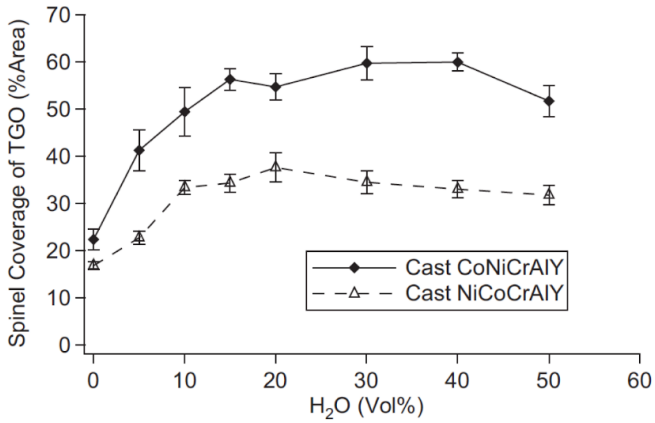

Figure 2.22: Spinel surface coverage as a function of water vapor percentage for cast CoNiCrAlY and NiCoCrAlY exposed to 1125°C [7]

2.2.4 Void formation

Provenzano et al [37] studied void formation in 4-5% (wt%) Y and Hf ion implanted Co-22Cr-11Al (wt%) MCrAl alloy at 700°C and 1000°C. The formation and growth of voids occurs at the alloy-oxide interface and is associated with a Kirkendall-type mechanism. The size and number of voids is dependent on temperature, and oxidation exposure time. Rapid diffusion of metal ions from the bulk to the oxide-gas interface creates a mass imbalance, followed by diffusion of the ions through the growing oxide scale. This creates cation vacancies at the oxide-gas interface, which then diffuse inwards through the oxide scale to the alloy-oxide interface to counterbalance the upward mass flow, depositing once the concentration exceeds the equilibrium concentration [37]. This mechanism is dependent on the faster diffusion of aluminum, chromium, and cobalt in their corresponding oxides than oxygen in the same oxides. At high temperature, the diffusion of oxygen in yttria and hafnia is much higher than the diffusion coefficients of yttrium and hafnium, suggesting that yttria and hafnia form before other oxide species in the early stages of oxidation. These oxides allow for the fast inward diffusion of oxygen and reduce the outward diffusion of metal ions. The inward diffusion of oxygen reverses the flow of vacancies to the oxide-gas interface where they are annihilated [37].

Void size increases with temperature and exposure time, while the number of voids decreases. This implies that voids coalesce with prolonged oxidation. Voids are detrimental to TGO adhesion, reducing the contact area between the alloy and oxide and increasing stress by behaving as cracks at the interface [37]. The literature on the influence of water on defects of alumina-forming alloys is contradictory. Theories of how test atmosphere affects void formation within the TGO also differ. Some researchers claim that water vapor accelerates oxidation in TBC, and others claim it has little effect. Li et al. [20] investigated the effect of water vapor on the oxidation behaviour of NiCoCrAlY TBCs at 1050 ◦C by thermal cycling. Air and argon with 25% H_2O were achieved in a tube furnace with a flow rate of 5L/min. Li et al found that the position and number of voids within the TGO was affected by the oxidation atmosphere. In dry air, voids were found within the TGO. In air + 25% H_2O, fewer defects were formed inside the TGO, reducing the inward flux of oxygen after 150h.

Internal oxidation of the Al-depleted zone below the TGO can significantly affect the formation of voids. Karabela et al. saw microvoid formation at the alloy-oxide interface reportedly from the

outward diffusion of Ni, Cr, and Ti to the surface, and Smialek showed that void growth happens by vapor transport of Al from the void surface to the oxide. Li et al. observed that oxygen ingress was most notable in dry air oxidation. In the air + 25% H_2O environment, a continuous and protective TGO was observed, with no voids inside the TGO. This suppressed the formation of internal oxides. Voids were dispersed throughout the TGO in dry air, while microvoids were seen at the TGO/top coat interface in air + 25% H_2O.

There are two theories on void formation: one considers the growth of stress within the oxide scale, and the other considers transient stages of oxidation. A proposed mechanism for void formation and propagation is seen in Figure 2.23 for low P_O in Ar + 25% H_2O and high P_O in air + 25% H_2O.

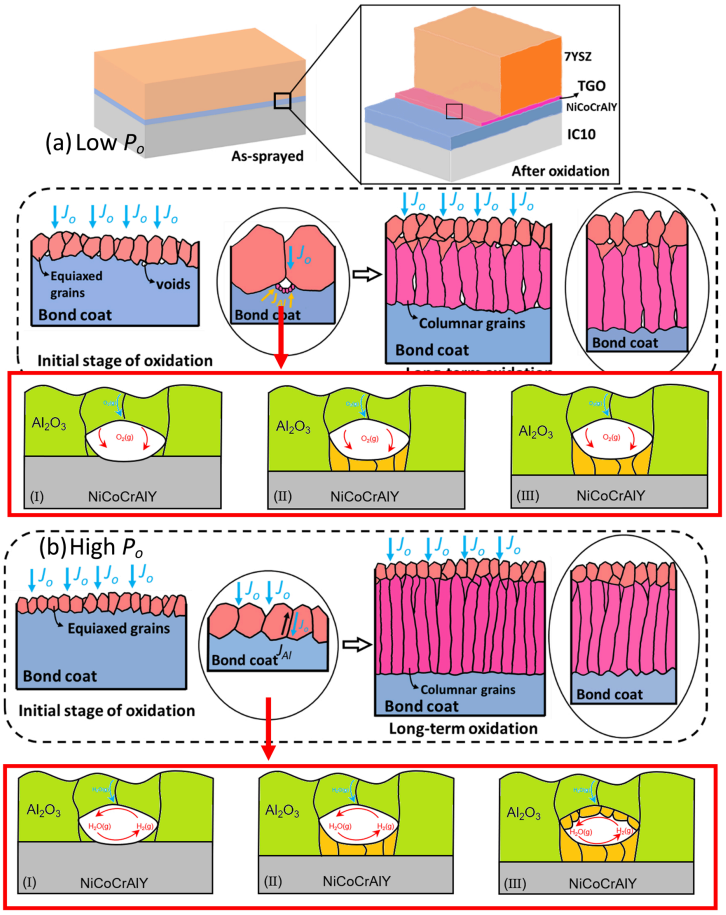

Figure 2.23 Schematic illustration of the oxidation mechanism for the TGO-formed 7YSZ TBCs at (a) low (Ar + water vapour) and (b) high (Air + water vapor) Po [20].

The alumina phase transformation from θ-α results in a 14.3% volume contraction, which create internal stresses between the alloy and oxide during thermal cycling, forming interfacial voids. In

the Ar + 25% H_2O environment, slow nucleation and heterogeneous alumina growth leads to faster aluminum diffusion fluxes towards the oxide surface through the grain boundaries, creating vacancies at the alloy-oxide interface (Figure 2.23 (a)).

Voids were identified in the dry air 150h cyclic oxidation, while the air + 25% H_2O condition did not show voids present in the TGO microstructure. In the FeCrAl coating, the flux of vacancies was opposite to the flux of FeCr, meaning vacancies accumulated at the interface. The rate of oxidation increases with vacancy content as they act as diffusion paths for ions (Figure 2.23 (a-I)). Voids become trapped in the equiaxed/columnar grain interface as inward columnar alumina grows in Ar + 25% H_2O (Figure 2.23 (a-II and -III)).

In the air + 25% H_2O condition, the interface diffusion of oxygen is faster than the rate of oxygen transport to the interface by the grain boundary, driving the nucleation of oxide grains (Figure 2.23 (b)). Compressive stress at the grain boundary and tensile stress at the grain centre drive inward diffusion of oxygen. Oxygen transport through the scale leads to new oxide formation at the alloy-oxide interface (Figure 2.23 (b-I and -II)), which can form on the ceiling of the void due to aluminum evaporation across the void. This reaction occurs near the grain boundaries where diffusing oxygen comes into contact with evaporating aluminum (Figure 2.23 (b-III)). This would explain why voids are only identified on the TGO surface.

Void distribution was lower in the air + 25% H_2O condition than the Ar + 25% H_2O oxidation treatment. Higher P_O and faster nucleation of alumina grains in initial oxidation result in uniform stresses in the TGO. As the TGO grows, the dense equiaxed grains reduce the outward diffusion of aluminum, providing enough aluminum to react with oxygen at the alloy-oxide interface [20].

2.3 Reactive Element Addition Influences on Oxidation

The addition of reactive elements affects the oxide scale growth rate, phase transformation, and vacancy formation. Voids at the alloy-oxide interface and the formation of Ni/Co-rich spinels by internal oxidation lead to failure in the TBC system [20].

2.3.1 Effect of Yttrium

Yttrium and hafnium are known as reactive elements because their oxides are more stable than the oxide scales formed on most alloys in high-temperature oxidation. Yttrium has been shown to slow

the upward diffusion of Al and Cr in MCrAlY coatings, and can act as a vacancy sink, suppressing the formation of voids at the oxide-alloy interface [7].

By supressing the upward diffusion of Al and Cr, the growth mechanisms of alumina and chromia are altered; reducing the lateral growth of the oxides and the residual stresses found in the TGO upon cooling. This phenomenon was observed by Pint et al. and by Jedlinkski and Mowec in a cyclic oxidation study on Y ion-implanted NiAl where Al_2O_3 scale spallation was significantly decreased with increasing Y content [7].

In high-temperature environments, yttrium segregates at the oxide-alloy interface and promote the formation of oxide pegs [30]. Oxide pegs are formed between the oxide and alloy as a result of internal oxidation; a phenomenon that is accelerated by the presence of water vapor. Oxide pegs can improve adhesion between the two layers and are comprised of Y/Hf oxides that form in the substrate near the interface wrapped by alumina [7],[30].

2.3.2 Effect of Tantalum

In MCrAlY bond coats, Ta is mainly dissolved into the β-NiAl phase [30], and reduces the diffusivity of Al to the surface [7]. In dry air oxidation, Ta doping of bond coat materials was found to increase the generation speed of α-Al_2O_3 in early oxidation, delay the outward diffusion of Al, thereby increasing the oxidation resistance at high temperatures, and enhance oxide-alloy adhesion through the formation of oxide pegs (Figure 2.24). Ta was found to promote the formation of Cr_2O_3 in early oxidation which has been found to be a beneficial oxide in the formation of a continuous and dense Al_2O_3 TGO [33]. In this context, the speed of upward diffusion of Al to the oxide alloy interface is measured by the thickness of the Al-depleted γ'-Ni_3Al phase below the TGO, with a thinner Al-depletion zone corresponding to a slower consumption of Al in TGO formation, and improved oxidation resistance. When using XRD as a characterization technique, the relative peak intensities of γ'-Ni_3Al to other identified oxides can explain the oxide scale thickness on the surface [30].

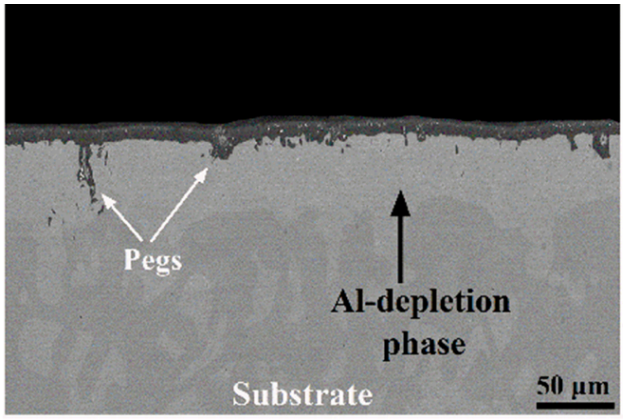

Figure 2.24 Cross-sectional morphologies of a high entropy alloy after oxidation at 1100 ◦C for 620 h [30]

Figure 2.24 also highlights the phenomenon of interfacial undulations or rumpling at the TGO alloy interface. This is attributed to rapid consumption of Al in the bond coat and inhomogeneous oxidation. The inclusion of Ta has been shown to reduce this effect by slowing the upward diffusion of Al [30].

2.3.3 Effect of Hafnium

Hafnium is seen to segregate in precipitates along the β-γ phase boundaries. Figure 2.25 shows the surface of a CoNiCrAlHf alloy during the initial stages of oxidation in dry and humid air. In humid conditions (Figure 2.25 c and d) HfO_2 particles are found forming on the β-NiAl phase and are not as prevalent on the dry air condition samples (Figure 2.25 a and b). It was observed by Kai Yan et al. [17] that water vapor promotes the formation and outward movement of interfacial voids, accelerating spallation of the oxide scale in NiAl alloys at 1100°C. The diffusion capacity of oxygen ions was improved by the interfacial voids in the humid atmosphere, and void formation was linked to the distribution of HfO_2 observed in the experiments.

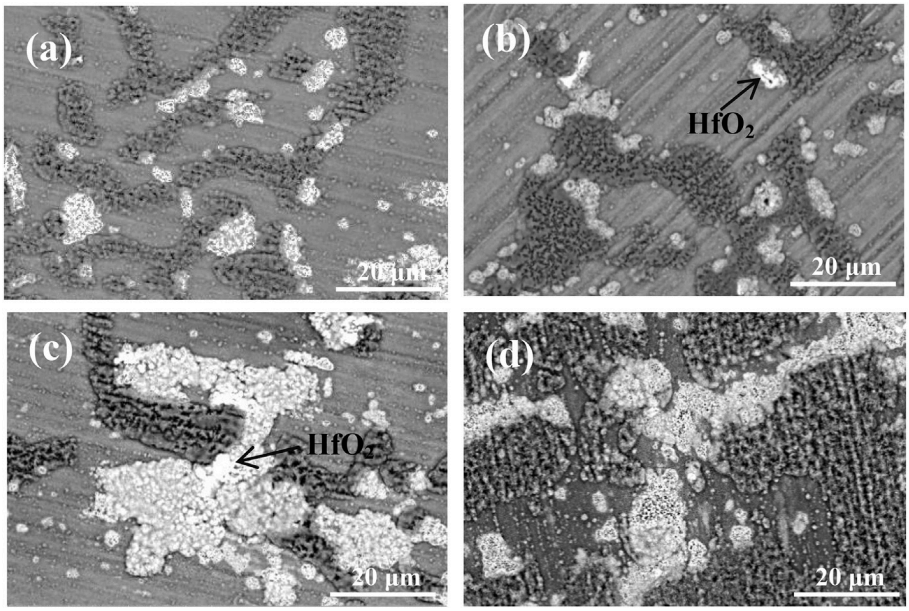

Figure 2.25 Surface SEM images of CoNiCrAlHf alloys after oxidation at 1050 C. (a) 1 h, air, (b) 24 h, air, (c) 1 h, air + water vapor, (d) 24 h, air + water vapor [17]

In coating materials where Hf is present, voids can form at the bond coat and TGO interface. One proposed mechanism for this behaviour is the segregation of HfO_2 particles at this interface during oxidation. The volume changes coming from the growth of HfO_2 create stresses between the alloy and oxide. In dry air, HfO_2 is not uniform and promotes an uneven stress distribution, leading to TGO spallation [17].

In dry air, the diffusion rate of Hf is lower than that of Al, resulting in fine HfO_2 pegs forming at the oxide alloy interface (Figure 2.25 a and b) because the inward diffusion of oxygen is slower than the outward segregation of Hf. In humid conditions, the concentration of oxygen is higher at the interface, promoting Hf segregation, which rapidly oxidizes to form an Hf rich layer. In the presence of water vapor, the HfO_2 interlayer is more uniform, reducing the number of defects in the oxide layer. Li et al. found that the oxygen flux J_O decreased significantly after a HfO_2-rich layer forms within the oxide layer [17].

Li et al. concluded that the even distribution of HfO_2 at the alloy oxide interface in the presence of water contributes to a slower oxidation rate and better adhesion.

2.3.4 Effect of Silicon

Silicon is mainly distributed in the β phase of MCrAlY bond coat alloys, and much like the other doping elements, slows the upward diffusion of Al from the bond coat and reduces internal oxidation of the alloy [7]. Shuting et al. [34] observed that the Si content is directly related to the volume fraction and distribution of the β phase within the alloy, with increasing Si content leading to increased β phase volume fraction. The β phase is where alumina initially forms during oxidation and acts as the primary source of Al for TGO growth.

In bond coat materials, Si first diffuses to the surface to form silicides. Over long-term oxidation, these silicides decompose and form SiO_2. As the presence of water reduces the density of the oxide scale, it allows for an increased inward diffusion of water into the bond coat. This accelerates the SiO_2 formation [33]. SiO_2 may be beneficial for oxidation resistance, but in large quantities it can make the TGO brittle and promote spallation. For an α-Al_2O_3 oxide scale, the Pilling-Bed worth ratio (PBR) is 1.28 [7]. However, Shuting et al. calculated that the PBR of CoCrAlSiY coatings with 2% and 5% Si were 2.51 and 3.05, respectively. From section 2.1.10, having a PBR much greater than unity causes greater residual strain in the oxide during thermal cycling, leading to cracking and spallation of the TGO, exposing the bond coat to further oxidation [7], [34]

Figure 2.26 highlights the differences in TBC lifetimes for bond coat compositions with Y and YHfSi applied to an X4 alloy substrate in dry O2 and 10% H2O environments. One standard deviation for three TBCs of each type tested to failure is shown by the error bars.

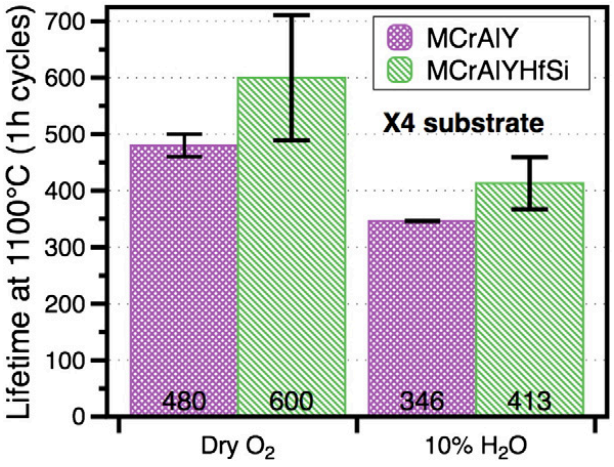

Figure 2.26 Bond coat composition effects for coatings on X4 alloy substrate in dry O2 vs. 10% H2O environments comparing TBC lifetimes in 1h cycles [31]

TBCs on X4/YHfSi showed a 25% higher average life compared to X4/Y. Despite the large standard deviation for X4/YHfSi, it was still considered a statistically significant result [31].

2.3.5 Doping Element Summary

Table 6 summarizes the effects of doping elements on oxidation behaviour found in literature.

Table 6 Summary of Reactive Element Effects on Oxidation

Element	Location in Bulk Material	Dry Air Oxidation	Mechanisms	Detrimental Aspects
Y	Y-rich phase inside of γ phase	Slows upward diffusion of Al Aides phase transition of θ-Al_2O_3 to α-Al_2O_3 Void suppression Improved adhesion	Forms Y-rich oxides in early oxidation Forms $AlYO_3$ and $Al_5Y_3O_{12}$ oxide pegs	-
Ta	Distributed in the β phase and Ta-rich precipitates along the β-γ phase boundaries	Slows upward diffusion of Al Reduces rumpling Improves adhesion	Forms beneficial oxides in early oxidation Promotes oxide pegs	-
Hf	Precipitates along the β-γ phase boundaries	Slows upward diffusion of Al Improves adhesion	HfO_2 formation between alloy and TGO slows internal oxidation Promotes oxide pegs	HfO_2 formation can promote voids and spalling
Si	Distributed in the β phase	Slows upward diffusion of Al	Increases alumina-forming β phase in alloy SiO_2 formation above TGO slows internal oxidation	Large amounts of SiO_2 can lead to spallation of TGO

2.4 Motivation and Research Objectives

Previous studies investigating the effects of water vapor on high-temperature isothermal oxidation behavior in MCrAlY bond coat materials have produced conflicting results, in part due to the variability in experimental conditions used across different studies. Specifically, the studies have not been conducted at the same temperature, for the same duration, or with the same water vapor

content, making it difficult to compare and understand the effects of each alloying element and the overall oxidation mechanisms at work. The studies have also differed in studying the bulk bond coat material versus depositing it onto a substrate with various deposition methods. As a result, there is a need for a comprehensive investigation that controls for these variables to better understand the oxidation mechanisms involved and their effectiveness.

The research presented in this thesis is conducted in collaboration with the National Research Council of Canada and aims to investigate the effect of specific alloys element on the high-temperature behaviour of various bond coat materials and their resistance to isothermal humid-environment oxidation. This study focuses on comparing the behaviour of four commercially available Oerlikon Metco MCrAlY bond coat alloys [4]: Amdry 962, Amdry 365-2, Amdry 997, and Amdry 386. The composition of the selected materials differs by one to two elements, which allows for the comparison and isolation of different behaviours based on the reactive element inclusions. In addition to investigating the effects of alloying elements on high temperature oxidation resistance, this study also aims to characterize the phases present during oxidation and to understand the impact of water vapor content on the formation and evolution of these phases.

In this work, the substrate and ceramic top coat are excluded so that the oxidation behavior of the bond coat material can be examined in isolation. The study of the bond coat in isolation allows for the observation of the intrinsic properties and performance of the bond coats and gives a more accurate evaluation of the effects of alloying elements on high-temperature oxidation resistance. By controlling the water vapor content, the study aims to investigate the specific influence of this parameter on the formation and evolution of different phases and oxides present in the oxidation process.

Trends found on the effects of elemental additions and humidity on the bond coat alloy oxide formation and initial oxidation will be valuable in making predictions for the behaviour of complete TBC systems. Interdiffusion effects between the substrate and bond coat are negated as the study focuses on the early oxidation stages of TGO formation. In further oxidation, the results may diverge from what would be seen in application with a substrate.

To achieve this objective:

- Industry standards and thermodynamic first principles are used to design and calibrate the treatments and experiments used to quantify the humid environment oxidation behaviours.

- Specimens are subjected to isothermal high temperature humid environments of 0%, 18%, and 33% water by volume for 2h and 20h at 1100°C and 1atm. This temperature is shown to be comparable with previous literature and industry expectations of the temperatures seen by the bond coat [38], [39], [40], [41], [17], [36], [42], [43].
- Specimens are analysed using scanning electron microscopy (SEM), energy-dispersive spectroscopy (EDS), and x-ray diffraction (XRD) to identify the microstructure and composition of different phases and oxides.
- Specimen surfaces are analysed to determine oxide coverage and spinel growth, and cross-sections were examined to determine element depletion, oxide layer thickness, and oxygen penetration.

Chapter 3 Procedure and Methodology

3.1 Materials

The materials for this study were procured from Oerlikon Metco, a supplier of aerospace coating materials. The targets are made using thermal spray and are intended for EBPVD deposition [44]. A table summarizing the four bond coat compositions is shown in Table 7 [44], with the alloying element variations highlighted. The material labels will be used to identify the specimens in this work.

Table 7 Summary of Bond Coat Material Composition

Commercial Name	**Material Label**	**Composition (wt%)**
Amdry 962	A	67Ni-22Cr-10Al-1.0Y
Amdry 365-2	B	47.5Ni-**23Co**-17Cr-12Al-0.5Y
Amdry 997	C	43.9Ni-**23Co**-20Cr-8.5Al-**4Ta**-0.6Y
Amdry 386	D	47.6Ni-**22Co**-17Cr-12Al-**0.5Hf**-0.5Y-**0.4Si**

3.2 Sample Preparation

Specimens were pre-cut from targets (*60mm diameter)* (Figure 3.1 a) to *10x10x2mm* squares (Figure 3.1 b) using EDM wire cutting.

EDS done on bulk samples to confirm the manufacturer's listed composition (Section 4.1).

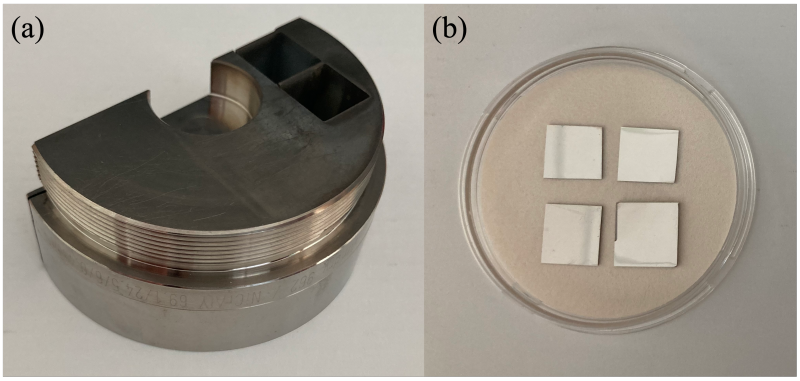

Figure 3.1 Processed MCrAlY (a) target material (d=60 mm) (b) polished bulk samples (10x10x2 mm)

3.3 Vacuum annealing

Samples were annealed in a high vacuum furnace for 2h at 1100°C to homogenize the bulk materials and remove any defects from the target manufacturing and EDM wire cutting.

An alumina tube furnace shown in Figure 3.2 was used in conjunction with a Watlow 96 temperature controller, and a Pfeiffer HiCube 80 vacuum pump capable of achieving a vacuum of $7.00e^{-6}$ torr at room temperature and $5.00e^{-4}$ torr at 1100°C.

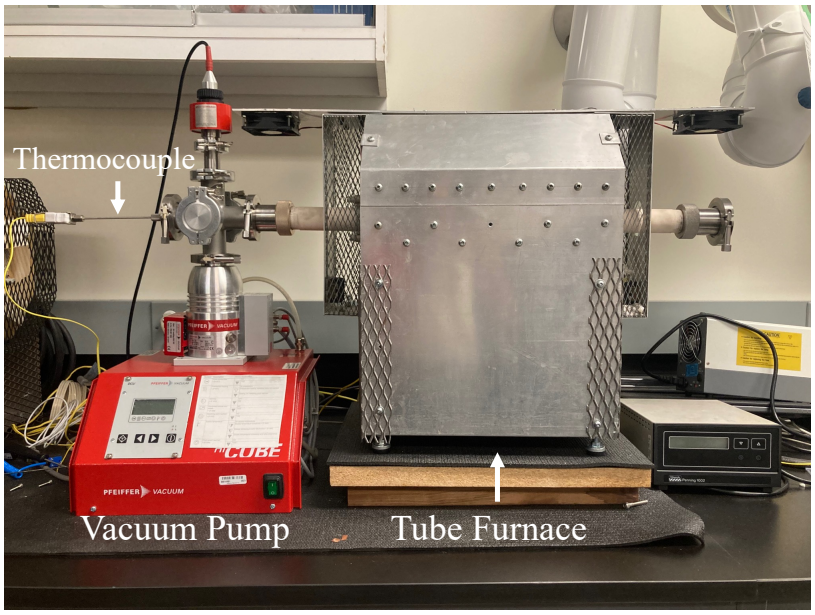

Figure 3.2 High-Vacuum Tube Furnace Set-up used for Vacuum Annealing Treatments

Samples were loaded into the furnace with the use of a pre-measured guide, to ensure the sample holder was placed in the same position at the centre of the furnace for each treatment.

An alumina card (Figure 3.3) was cut to *25x40x4mm* to serve as a sample holder during heat treatments. The sample holder held the specimens directly below a stationary thermocouple (Figure 3.2) positioned in the center of the furnace, to ensure the specimens were exposed to the furnace set temperature.

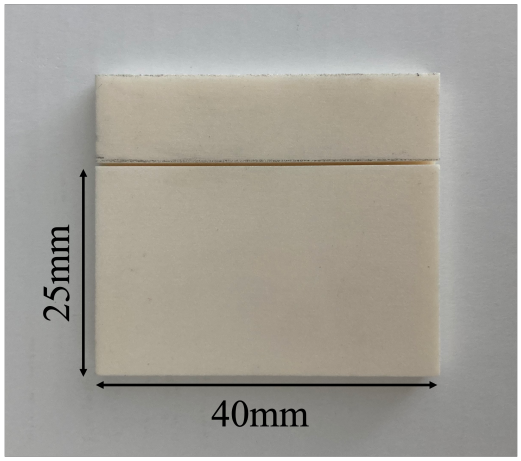

Figure 3.3 Alumina Card Sample Holder

Alumina was chosen for the tube and sample holder as it is non-reactive at the temperatures used in treatment. After heat treatment, the vacuum annealed samples were double mounted, and the cross-section was analysed to confirm that the bulk showed a consistent phase distribution with the manufacturer's composition. This was confirmed with EDS and can be found in Appendix A: EDS Cross-Section Element Maps and Line Scans

A YO_2 oxide layer was seen on the surface of the specimens after vacuum annealing. This would have to be removed to return the specimen surface to the bulk composition. BSD imaging and EDS were used to measure the depth of the Y-depleted zone. The analysis of TGO thickness and element depletion zones is seen in Section 3.7.

Samples were then polished to remove the 15µm Y-depleted area, returning the surface of the specimens to bulk composition, and to provide a smooth surface to observe the oxidation reaction. More information on polishing is found in Section 3.5.

EDS element maps and line scans of the specimen cross-sections is found in Appendix A: EDS Cross-Section Element Maps and Line Scans.

3.4 Sample Mounting

Cross-section analysis was done to characterize and measure the TGO, Al-depleted zone, and Y-depleted zone after oxidative treatments.

Samples were double cold mounted to preserve the brittle oxide layer on the specimen surface. The double cold mounting process is detailed as follows: a resin (Allied High Tech 145-10010) and hardener (Allied High Tech 145-10015) were used in a 10:3 ratio to mount the samples. This epoxy was chosen for its short cure time (2h) and ability to be dissolved if the specimens needed to be retrieved.

The samples were first mounted flat in epoxy and then cut in half using a thin blade saw (Struers Secotom-10), before being mounted again with the cut edge at the bottom of the mould. The cut edge was then polished to a mirror finish using the same procedure as the sample surface polishing.

3.5 Polishing

Samples were polished to 0.05 μm beginning with 800 grit silicon carbide paper and moving incrementally through 1000, 1200, and 2500 grit papers and then 3 μm , 1 μm diamond suspension solutions and 0.05 μm colloidal silica. Bulk and double cold mounted samples were sonically rinsed for 5 minutes between suspensions.

3.6 Oxidation Treatments

3.6.1 Humidification Set-up

Samples were oxidized in the same tube furnace (Section 3.3) on an alumina card with dry air (H_2O < 10ppm) [45] passing through a humidification set-up at a controlled rate of 2 bubbles/sec (~0.9mL/s). The slow flow rate ensures that the supply of humid air in the chamber is replenished, and the air spends enough time in the humidification set-up to pick up the required water content. One specimen of each composition was prepared per oxidative condition, as the experiments were time intensive.

For dry air oxidation, air from the bottle is passed directly to the furnace with a constant pressure of 1atm (101.3 kPa).

For humid air treatments, air from the bottle passes through two saturators (Figure 3.4 (1)) set to the correct temperature before entering the furnace. The saturators consist of two closed-system

double boilers filled with distilled water. The tubes are heated with heating tape (Figure 3.4 (5)) set above the dew point to ensure that water does not condense out of the gas before entering the furnace tube. An in-line humidity sensor (Figure 3.4 (6)) measures the relative humidity in the gas at the entrance of the furnace.

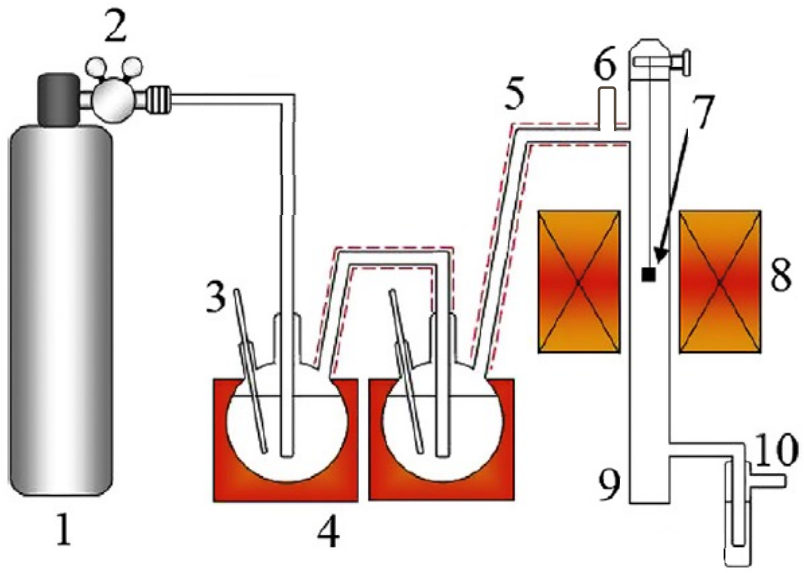

Figure 3.4 Schematic of Humidification Set-up. Dry air gas bottle (1), pressure gage (2,) thermometer (3), saturators (4), heating tapes (5), in-line humidity meter (6), specimen loading position (7), furnace (8), alumina tube (9), gas outlet (10).

Thermodynamic first principles were used to set the saturator temperatures. Humidity was measured in %vol H_2O using partial pressures and the thermodynamic steam tables (Appendix B: Thermodynamic Tables for Saturated Water) [46].

A sample calculation to determine the saturator temperatures for 33% H_2O (%vol) is seen below: From the ideal gas equation, the percent volume in the line is proportional to the partial vapor pressure. The total pressure in the system is atmospheric pressure (*101.3kPa*) giving a needed partial vapor pressure of *33.4kPa*. In the steam tables, we interpolate between *30 kPa* and *40 kPa* to obtain the gas temperature required to achieve 33% H_2O. The saturators should be set to 71°C.

This calculation was repeated for 18% H_2O, giving a saturator set temperature of 60°C.

3.6.2 Calibration of Temperature and Humidity

Furnace Temperature

The furnace heating curve for a 20h oxidation treatment can be seen in Figure 3.5.

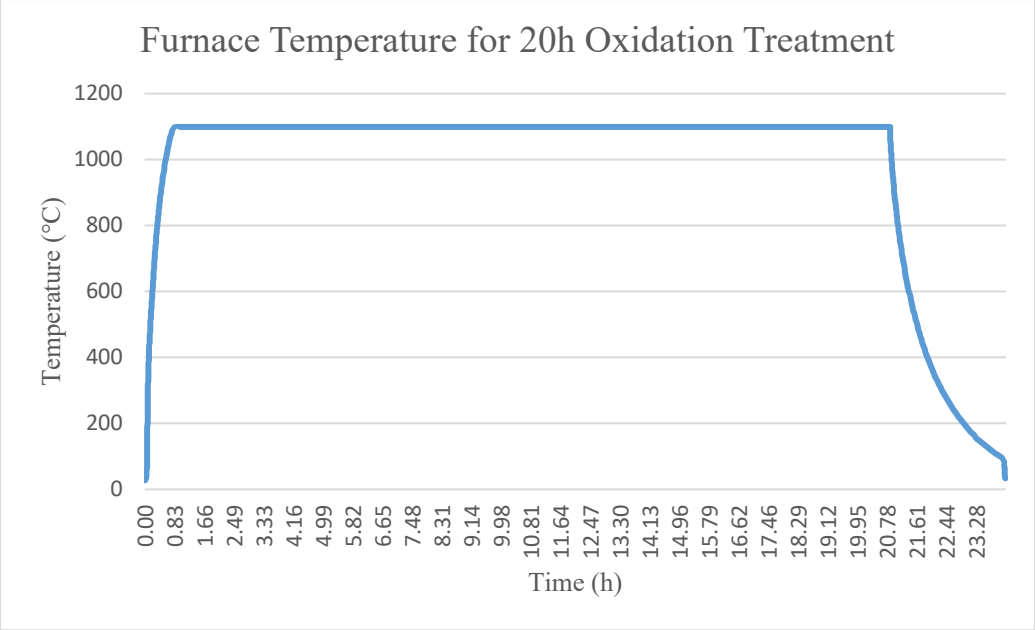

Figure 3.5 Furnace Heating Curve for 20h Oxidation Treatment

The furnace profile was measured by press fitting a drilled sample to the end of a k-type thermocouple which is notched at 1cm intervals for accuracy of repetition. A stationary thermocouple, positioned at the centre of the furnace, is connected to the Watlow temperature controller to set the furnace temperature. Once the stationary thermocouple has reached the desired furnace temperature, the notched probe is moved from the centre of the furnace towards the end and held at each position until steady state is reached. The thermal profile can be seen in Figure 3.6.

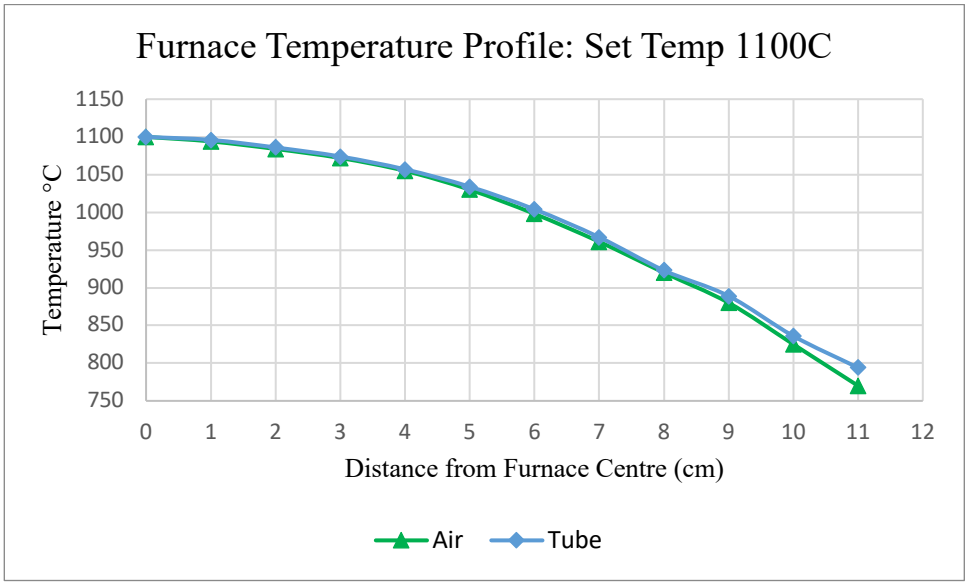

Figure 3.6 Furnace calibration temperature profile at 1100°C in air

At 1cm from the centre of the furnace, the measured temperature was 1094°C in open air. With the chosen specimen loading configuration, this means that the edges of the 1cm samples were held within 6°C of the set temperature.

The test was repeated at the bottom of the alumina tube to ensure that the thermal gradient along the vertical axis would not affect treatment, as the alumina card holds the samples just below the vertical center of the furnace.

3.6.2.1 Humidity

To ensure that the desired water content is entering the furnace tube, an in-line humidity sensor was placed at the entrance of the furnace. The sensor measured temperature and relative humidity (ϕ), which is a ratio of the water vapor partial pressure to P_{sat} , the amount of water air can hold at a given temperature before beginning to condense.

$$\phi = \frac{P_v}{P_{sat}}$$

For the case of 33% H_2O (%vol), the humidity sensor gives the values: $T = 71.5℃$ and $\phi = 99.1\%$ From the steam tables (Appendix B: Thermodynamic Tables for Saturated Water), the saturation pressure at this temperature is $P_{sat} = 33.41\ kPa$. Rearranging the above equation we see,

$$P_v = \phi P_{sat}$$

$$P_v = 33.1\ kPa$$

The same calculation was done for 18% H_2O (%vol), where the sensor showed $T = 60.1\,℃$ and $\phi = 99.1\%$. This confirms that the gas entering the furnace has the correct amount of water vapor for our experiments.

3.7 Characterization

Scanning Electron Microscopy (SEM)

A Gemini Zeiss 500 SEM was used at 20 keV for in-lens and backscattered imaging of the specimen surface and cross-section. This energy was used to be able to image and take EDS scans simultaneously. The in-lens (SE1) detector, located inside the electron column of the SEM, provides more contrast than the conventional SE2 detector. Backscattered electrons are electrons from the microscope beam that penetrate the specimen surface and re-emerge through the same surface. In this process, the electrons lose energy through interactions with the specimen atoms and can give us information about the sample composition.

The TGO was measured using the BSE detector. Sample A 0% H_2O 2h oxidation is used as an example in Figure 3.7 to show the TGO and Al-depletion zone measurements. These values were also cross-referenced with the measurements taken from the EDS element maps seen in the next section.

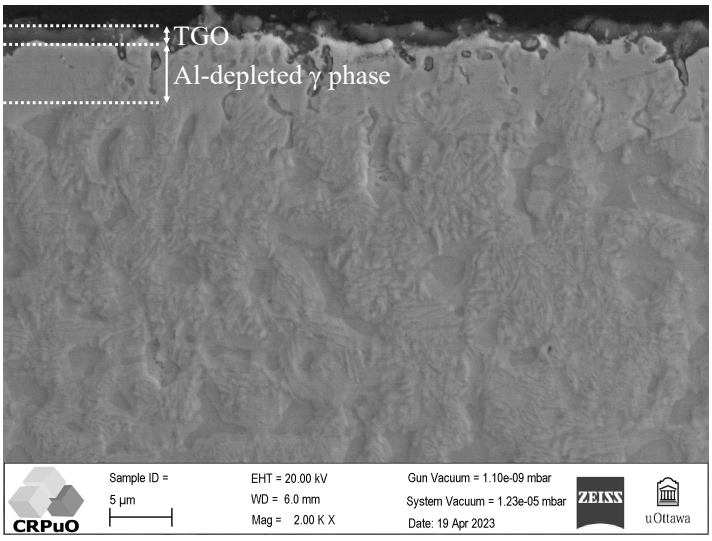

Figure 3.7 BSE SEM Sample A 0% H_2O 2h oxidation TGO and Al-depleted zone measurement

From high magnification images of the specimen cross sections, as seen in Figure 3.8, voids at the equiaxed/columnar grain boundaries can be identified. Rumpling and oxide peg size and density are also visually qualified.

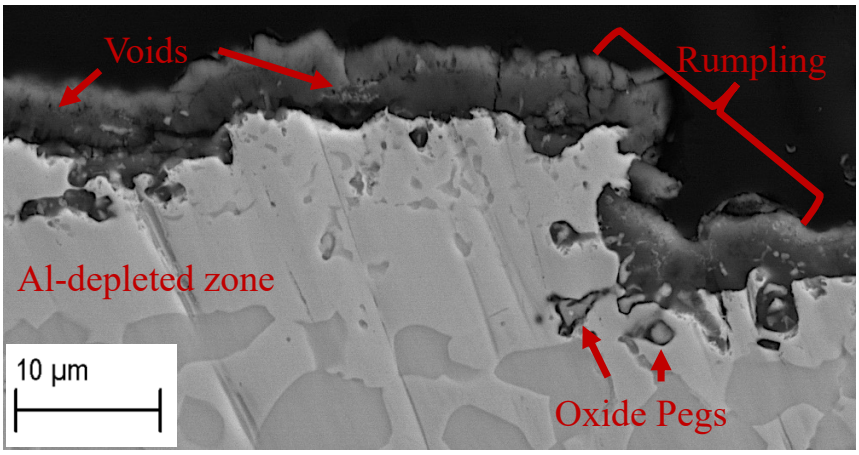

Figure 3.8 Example of rumpling, void identification, Al-depleted zone, and oxide pegs in sample B, 18% H_2O, 20h oxidation cross-section

In Figure 3.9, internal oxidation is identified using backscatter SEM as bright areas in the alloy.

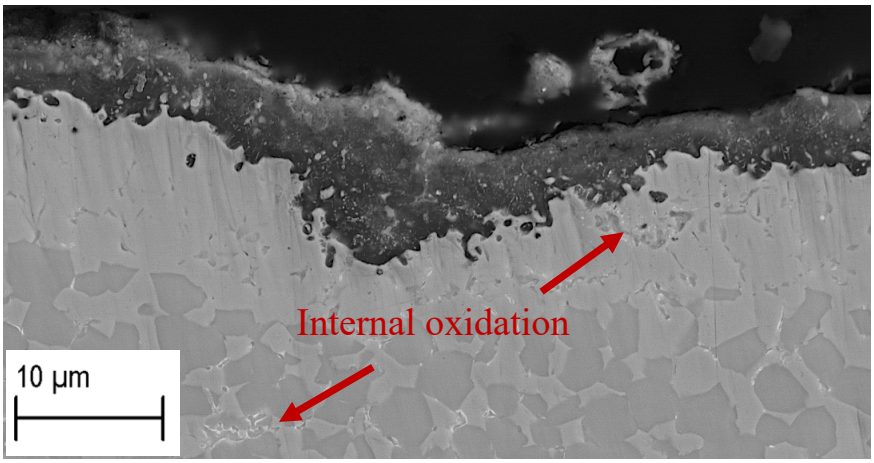

Figure 3.9 Example of internal oxidation in sample D, 18% H_2O, 20h oxidation cross-section

Figure 3.10 highlights surface voids and the visual qualification of surface spinels and transient species, which are later confirmed with XRD.

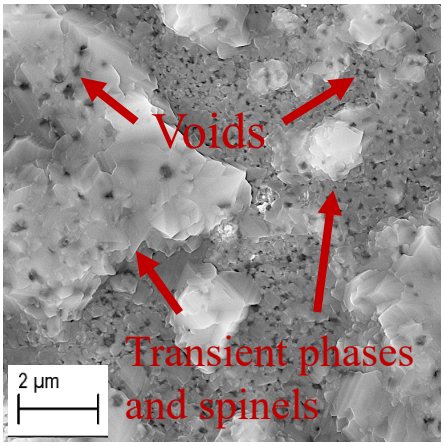

Figure 3.10 Example of surface voids and transient species on sample A, 18% H_2O, 2h oxidation specimen.

3.7.1.1 Energy Dispersive Spectroscopy (EDS)

A Bruker XFlash 6160 EDX detector is used in conjunction with the Gemini Zeiss 500 for quantitative x-ray analysis. Sample A 0% H_2O 2h oxidation is again used in Figure 3.11 to show how the TGO, Al-depleted zone, and Y-depleted zone were measured.

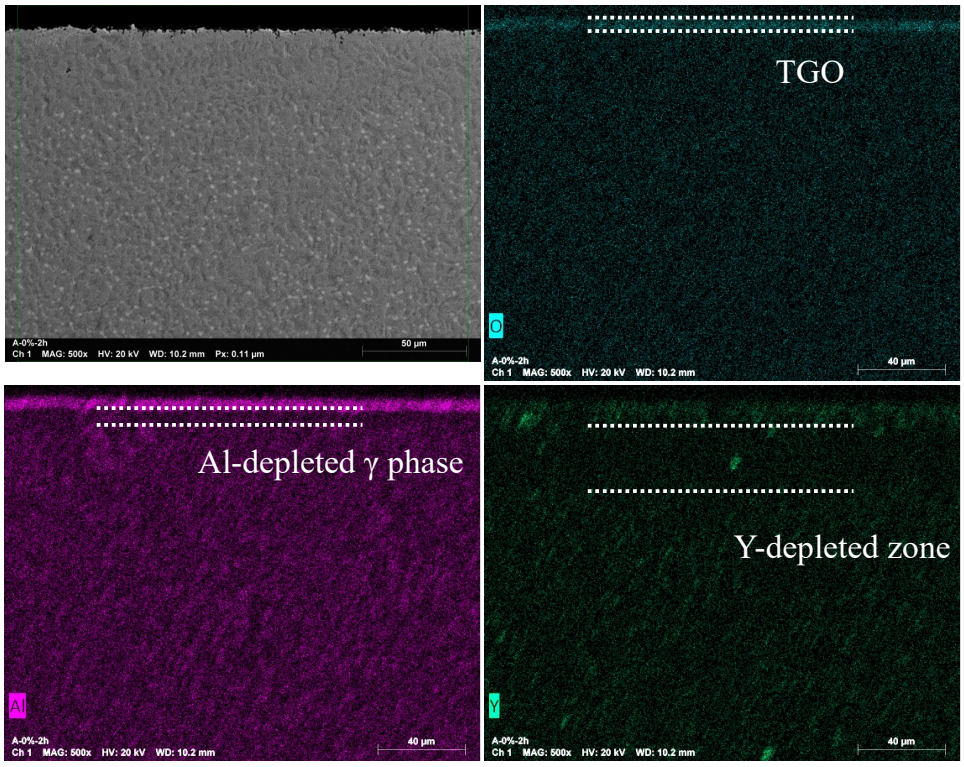

Figure 3.11 EDS element map Sample A 0% H_2O 2h oxidation TGO, Al-depleted zone, and Y-depleted zone measurement

To measure the aluminum depletion zones from the EDS maps, Fiji analysis software is used to plot the grey values across the image. Figure 3.12 shows the element depletion zone plot for Al, using sample A-0%-2h as an example.

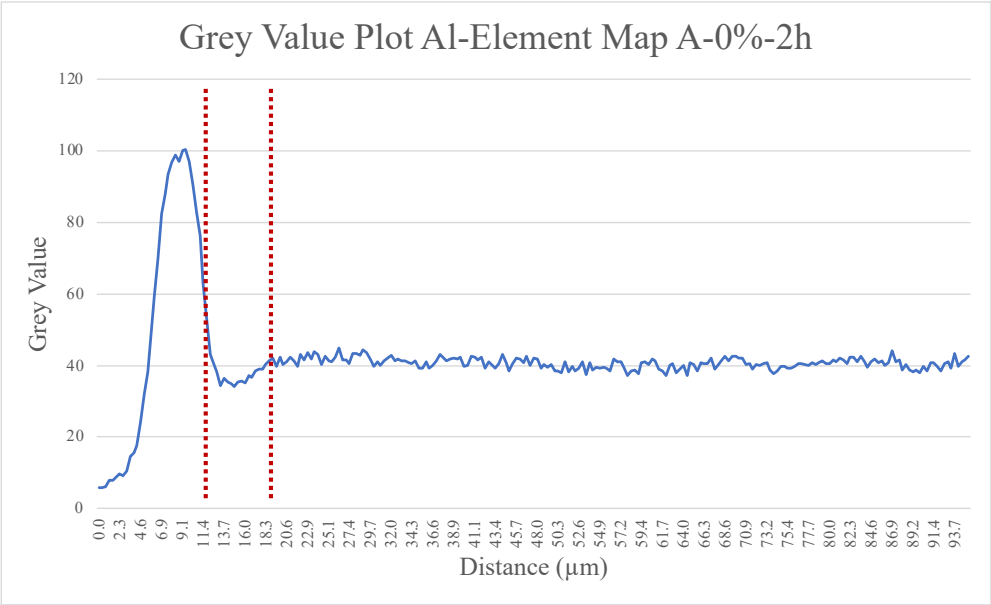

Figure 3.12 Grey value plot of Al element map Sample A 0% H_2O 2h oxidation for Al-depletion zone measurement

3.7.1.2 X-Ray Diffraction (XRD)

A Rigaku Ultima XRD was used in parallel beam mode, grazing incidence (GIXRD) to characterize the surface compounds of the TGO. Parallel beam mode was used to avoid a roughness effect from the surfaces of the specimens. GIXRD is a technique for looking at thin films and specimen surfaces that uses small incident angles (typically between 0-3°) to limit the penetration depth of the x-rays and graze the surface without collecting bulk specimen information. Acquisition time was optimized to obtain a good signal to noise ratio and ranges between two and four hours. HighScore and MDI Jade were used to identify peaks and match them with compounds in the software database.

Chapter 4 Results

In this section, the bulk material characterization is presented to confirm the compositions and phases expected from the manufacturer and literature. The oxidation results are then shown by sample in order of water vapor content.

4.1 Bulk Microstructure Characterization

Figure 4.1 displays the BSD SEM images of specimen surfaces after heat treatment and polishing. All samples display the characteristic γ, β and Y-rich phases. The Y-rich phase is most obvious in sample A (Figure 4.1(a)), which also shows a NiCr-rich intermetallic phase. Ta-rich precipitates can be seen on the γ-β phase boundary in Figure 4.1 (c) and Hf-rich precipitates can be seen on the γ-β phase boundary in (Figure 4.1 (d)).

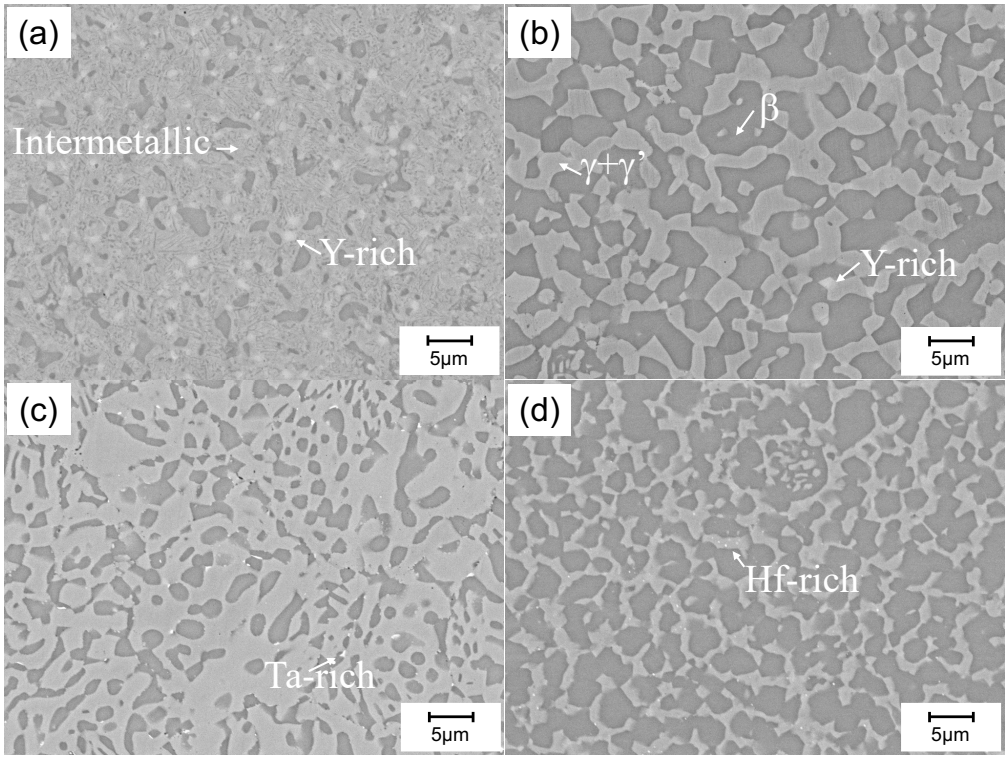

Figure 4.1 BSD SEM of polished bulk material surfaces (a) sample A, (b) sample B, (c) sample C, (d) Sample D

The surfaces were analysed using EDS to confirm that the element distribution was similar to the listed compositions given by the supplier. The results in Table 8 confirm that the prepared samples are within 1% [wt%] of the listed compositions given by the manufacturer in Table 7 [44].

Table 8 EDS surface results of bulk materials [wt%]

Element	Al	Cr	Co	Ni	Y	Ta	Hf	Si
A	9.59	20.85	-	68.5	1.05	-	-	-
B	13.92	18.37	22.76	44.95	0.00	-	-	-
C	8.81	20.32	23.4	43.22	0.89	3.36	-	-
D	14.62	17.15	23.2	43.5	0.35	-	0.67	0.51

XRD analyses show that all samples have the characteristic γ′-Ni_3Al, β-NiAl, and a Cr,Co,Ni intermetallic phase (Figure 4.2).

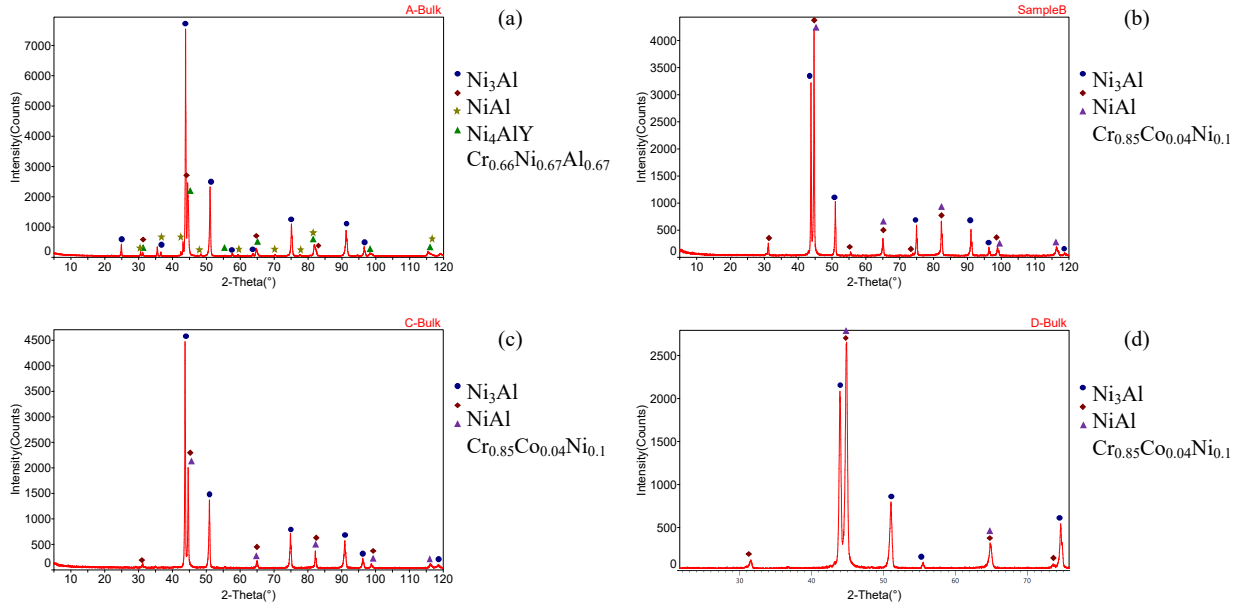

Figure 4.2 XRD surface characterization of bulk material surface (a) sample A (b) sample B (c) sample C (d) sample D

From the relative peak heights, Figure 4.2 (a) and (c) show that samples A and C have a higher amounts of γ′-Ni_3Al than β-NiAl by volume. In sample A a small but notable Y-rich Ni_4AlY is identified. Samples B and D (Figure 4.2 (b), (d)) show more β-NiAl than γ′-Ni_3Al by volume. The XRD phase identification corroborates what is seen in the BSD SEM images of the bulk

material specimens Figure 4.1. The Y, Ta, and Hf-rich phases are not identified with XRD. This is because their volume fraction is relatively insignificant to the β and γ+γ′ phases.

4.2 Oxidation in Dry Air

In this section, the results of dry air oxidation exposures for 2h and 20h are presented by sample. A summary of results is given at the end of the section.

4.2.1 Sample A

4.2.1.1 2h Oxidation Exposure

After 2h oxidation in dry air, XRD analysis of sample A (Figure 4.3) shows that an α-Al_2O_3 layer does form. This is identified in Figure 4.4 (a). However, the relative peak heights of $NiAl_2O_4$ and NiO, (both spinels) show significant surface coverage. This is corroborated by in Figure 4.4 (a).

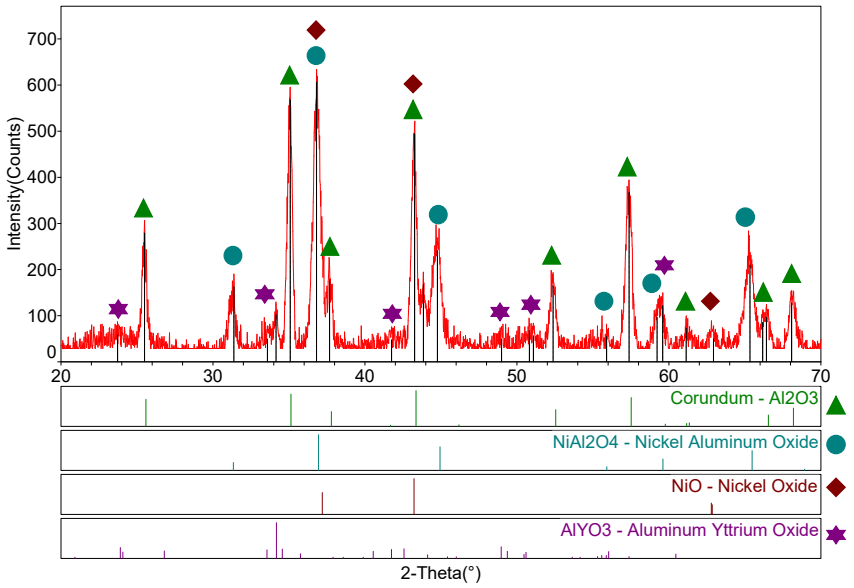

Figure 4.3 GI XRD of sample A surface after oxidation in dry air for 2h at 1100℃

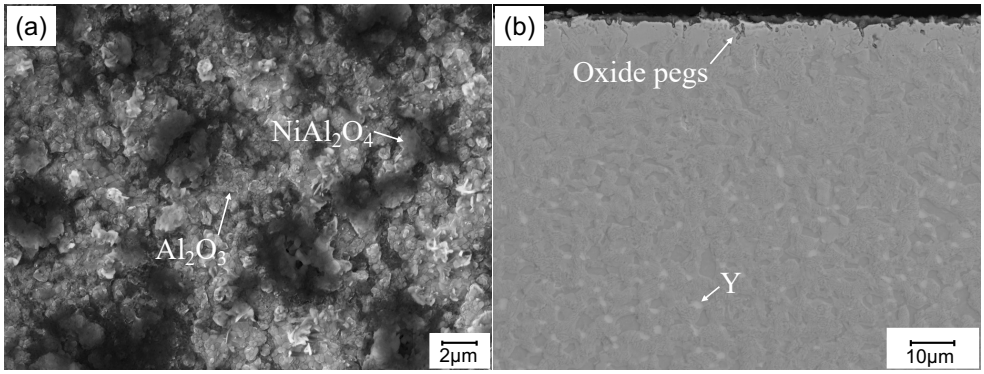

Figure 4.4 BSD SEM of sample A (a) surface (b) cross-section, after oxidation in dry air for 2h at 1100℃

From the cross-section analysis (Figure 4.4 (b)), a thick spinel accounts for the majority of the 1.29 μm TGO. An Al-depleted zone of 6.8 μm (5.3x the TGO thickness) seen in EDS mapping (0), indicates that aluminum consumption is moderate in the initial formation of the TGO. Oxide pegs form in the Al-depleted γ+γ′-phase, confirming internal oxidation of the alloy. Minor voids in the alloy point to rapid upward diffusion of aluminum in the early stages of oxidation. Little rumpling of the alloy is observed, however, and TGO adhesion is poor with cracks visible in the cross-section.

4.2.1.2 20h Oxidation Exposure

XRD analysis of sample A after 20h oxidation in dry air (Figure 4.5) shows predominantly α-Al_2O_3 growth on the surface with notable amount of transient Ni_2Y and minimal $NiAl_2O_4$ spinel.

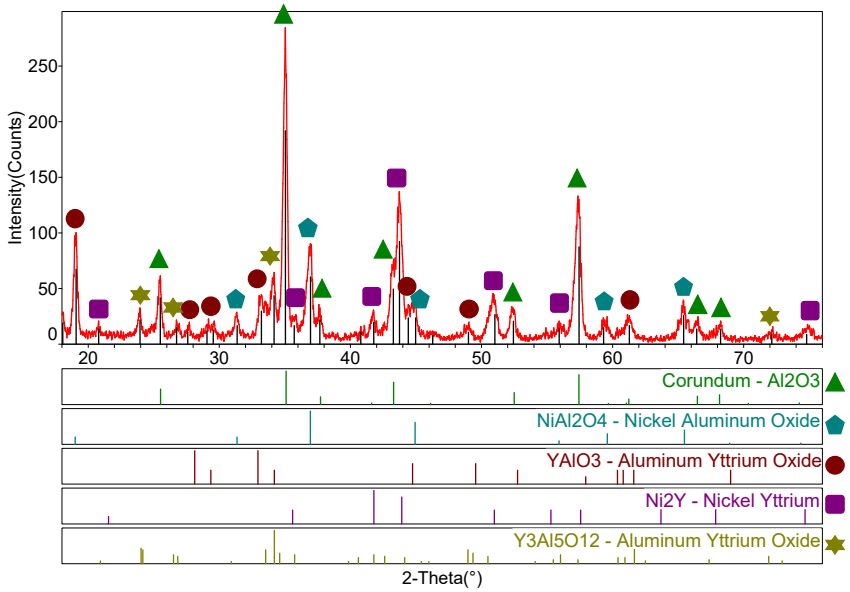

Figure 4.5 GI XRD of sample A surface after oxidation in dry air for 20h at 1100℃

After 20h exposure, Figure 4.6 (a) shows a reduction in surface spinel coverage as well as a more pronounced α-Al_2O_3 layer in the TGO. $AlYO_3$ and $Al_5Y_3O_{12}$ oxides are found at the alloy-oxide interface as oxide pegs in Figure 4.6 (b). From the cross-section, the TGO is 4.67 μm and the Al-depletion zone is 17.1 μm. There is better adhesion of the TGO with less cracking than in 2h oxidation, though the cross-section shows moderate rumpling of the alloy. A continuous TGO layer is observed. With prolonged exposure, the depletion zone reduces to 3.7x the TGO thickness. This indicates that a stable α-Al_2O_3 has formed, slowing internal oxidation. Transient Ni_2Y is seen in the XRD, implying that the spinel has undergone a solid-state reaction to form Al_2O_3 and Ni_2Y on the surface. This transformation would lead to a volume change at the TGO and top coat interface in application that would lead to spallation of the top coat. Spinel still decorates the surface after 20h with large outcrops visible.

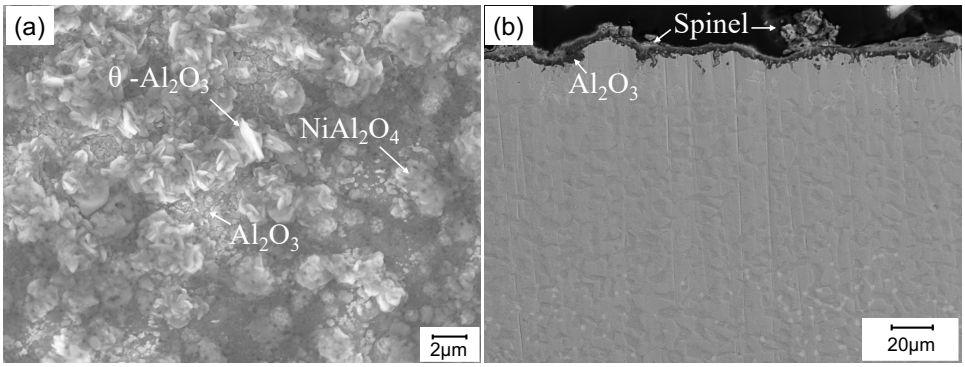

Figure 4.6 BSD SEM of sample A (a) surface (b) cross-section, after oxidation in dry air for 20h at 1100℃

4.2.2 Sample B

4.2.2.1 2h Oxidation Exposure

After 2h oxidation in dry air, XRD analysis of sample B (Figure 4.7) predominantly forms α-Al_2O_3 on the β-phase. The bright areas in Figure 4.8 (a) correspond to $CoAl_2O_4$ spinel in the XRD.

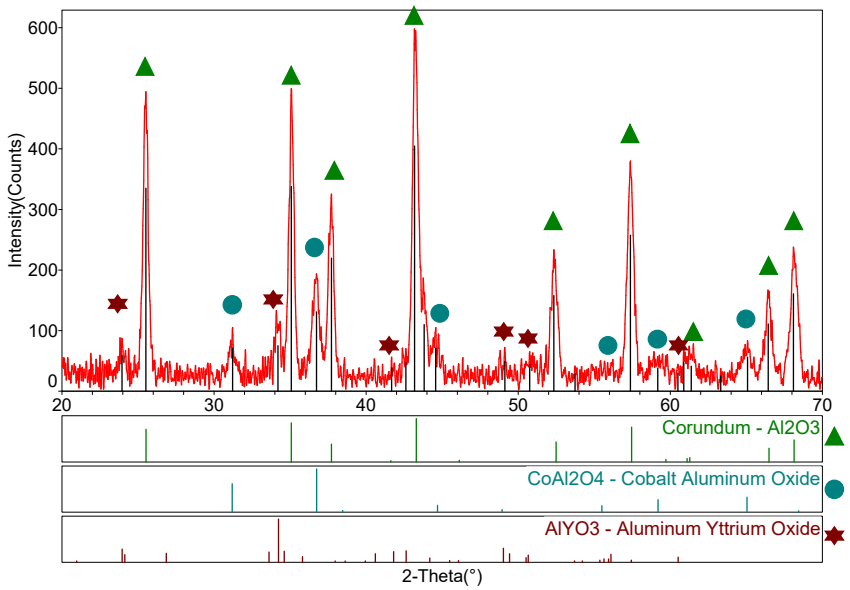

Figure 4.7 GI XRD of sample B surface after oxidation in dry air for 2h at 1100℃

After 2h oxidation in dry air, Figure 4.8 (a) shows the surface of sample B begins α-Al_2O_3 formation on the β-phase, and $AlYO_3$ and $CoAl_2O_4$ spinel decorate the $\gamma+\gamma'$-phase and voids are visible on the TGO surface.

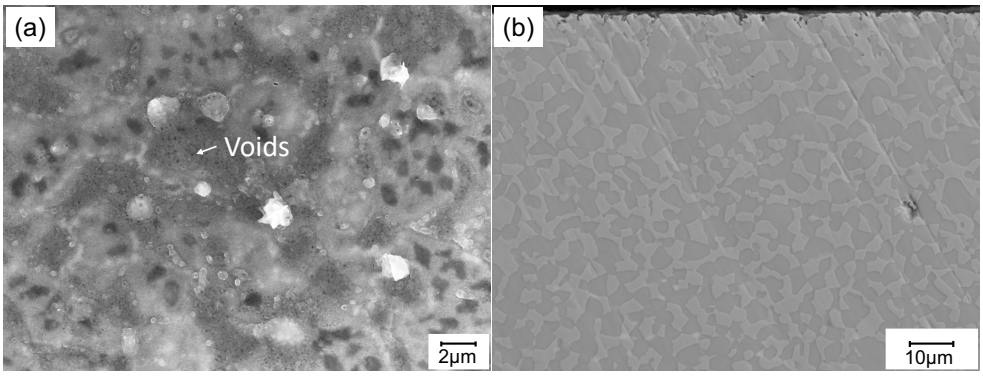

Figure 4.8 BSD SEM of sample B (a) surface (b) cross-section, after oxidation in dry air for 2h at 1100℃

In Figure 4.8 (b), the cross section shows a thin 0.97 μm TGO and the beginnings of oxide pegs are visible in the alloy. The TGO appears continuous and minimal rumpling of the alloy is observed, indicating uniform oxidation and low upward diffusion of aluminum during TGO formation. An Al-depleted zone of approximately 2.1 μm suggests that α-Al_2O_3 is slow to form with minimal spinel formation.

4.2.2.2 20h Oxidation Exposure

After 20h of oxidation exposure, the XRD results of sample B in Figure 4.9 show more α-Al_2O_3 growth with moderate spinel growth.

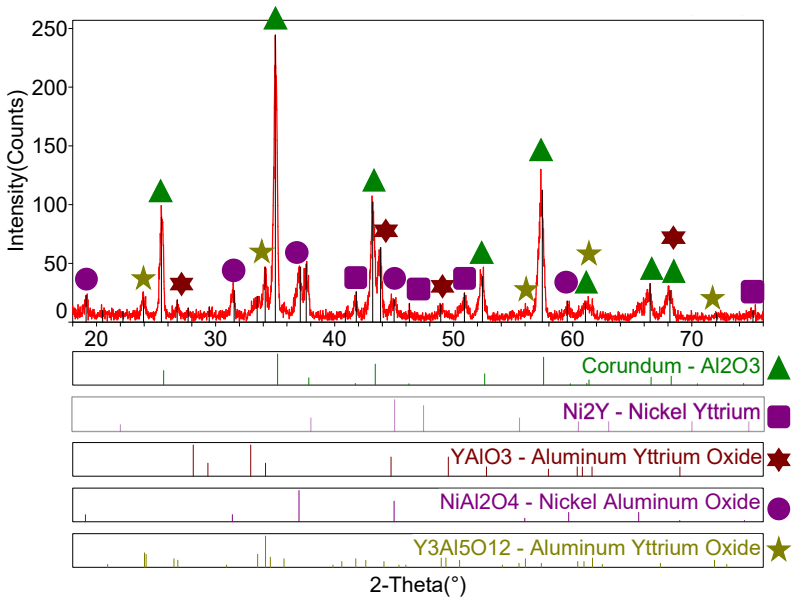

Figure 4.9 GI XRD of sample B surface after oxidation in dry air for 20h at 1100℃

After 20h oxidation, Figure 4.10 (a) shows a significant increase in spinel surface coverage and trace amounts of transient Ni_2Y and θ-Al_2O_3. No voids are seen on the surface and there is a slight increase in oxygen pegs. Spall is observed on the surface of the TGO.

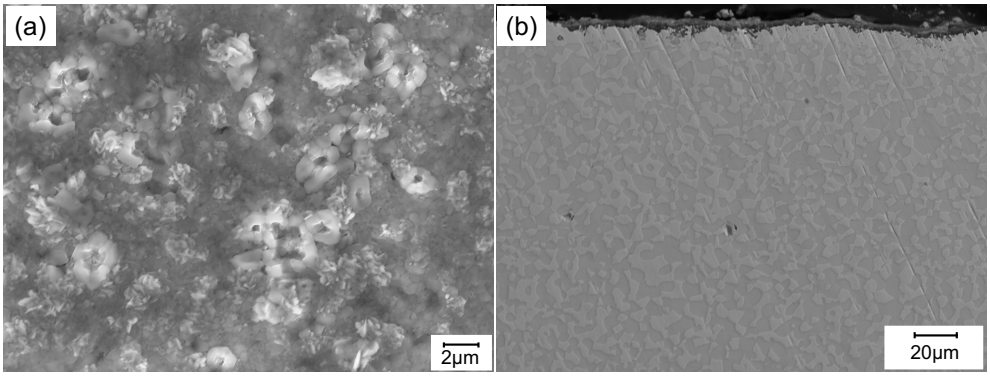

Figure 4.10 BSD SEM of sample B (a) surface (b) cross-section, after oxidation in dry air for 20h at 1100℃

The cross-section in Figure 4.10 (b) shows a dense α-Al_2O_3 base layer with spinel covering the surface of the TGO and no significant alloy rumpling. A TGO thickness of 4.0 μm and an Al-depleted zone of 8.9 μm is observed. The rate of Al-depletion to TGO growth is marginally higher

than in 2h oxidation and is explained by the formation of more spinels. This shows the benefits of Cr in the alloy composition for forming a stable and uniform α-Al_2O_3 TGO in the initial stages of oxidation.

4.2.3 Sample C

4.2.3.1 2h Oxidation Exposure

From Figure 4.11, sample C forms an α-Al_2O_3 layer dotted with $NiCo_2O_4$ spinel after 2h exposure in dry air.

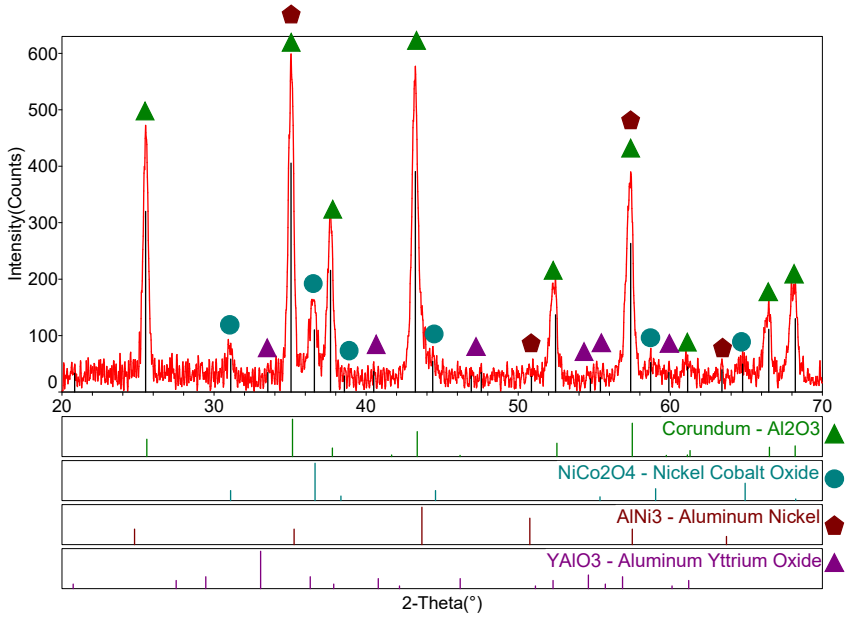

Figure 4.11 GI XRD of sample C surface after oxidation in dry air for 2h at 1100℃

In Figure 4.12 (a), sample C forms an inconsistent α-Al_2O_3 layer dotted with $NiCo_2O_4$ spinel after 2h exposure in dry air. The alloy is still visible, and large outcrops of yttria are also observed. No voids are visible on the sample surface.

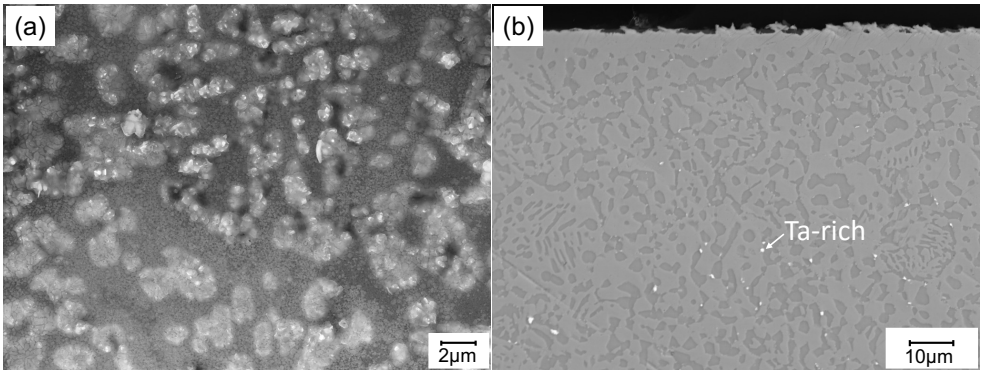

Figure 4.12 BSD SEM of sample C (a) surface (b) cross-section, after oxidation in dry air for 2h at 1100℃

In Figure 4.12 (b), the cross section confirms an non-continuous TGO of 0.71 μm forming on the alloy β-phase. An Al-depleted zone of 5.3 μm (of 6.5x the TGO thickness) suggests large aluminum consumption in TGO formation, though no transient θ-Al_2O_3 is seen on the surface. Less spinel coverage is observed compared to other compositions in dry air after 2h. The slow growth rate of the TGO can be attributed to tantalum slowing the upward diffusion of aluminum in the alloy.

4.2.3.2 20h Oxidation Exposure

After 20h oxidation exposure, sample C shows less spinel compared to the 2h oxidation exposure (Figure 4.13), though the substrate is more prevalent. The identifiable spinel species is $NiAl_2O_4$.

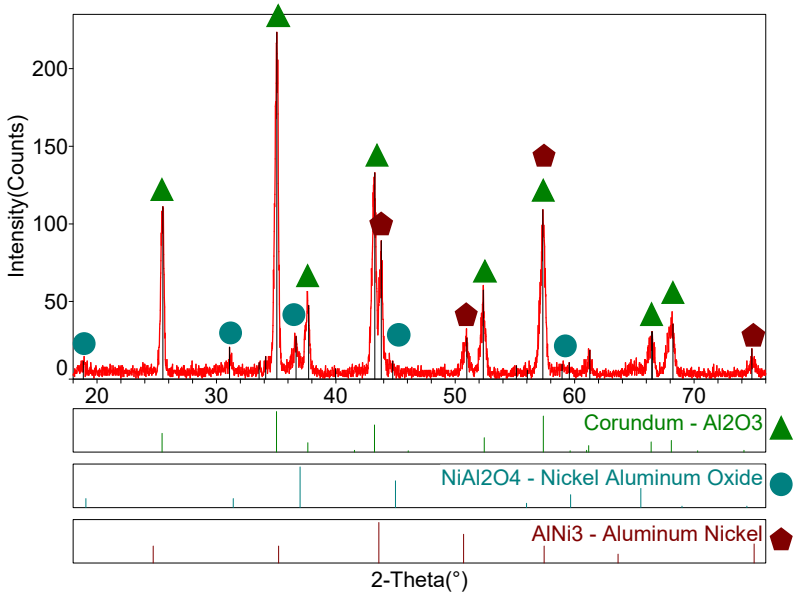

Figure 4.13 GI XRD of sample C surface after oxidation in dry air for 20h at 1100℃

After 20h oxidation, sample C shows more spinel surface coverage and an increase in α-Al_2O_3 in Figure 4.14 (a). Spallation also allows for visible pockets of the alloy. No voids are visible in the TGO.

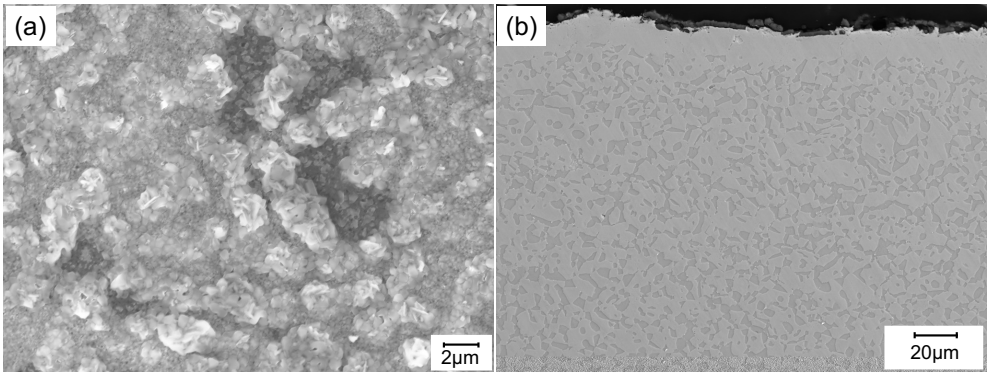

Figure 4.14 BSD SEM of sample C (a) surface (b) cross-section, after oxidation in dry air for 20h at 1100℃

Very poor adhesion of the 2.33 μm TGO is seen in Figure 4.14 (b) and Al-depletion at a depth of 15.3 μm confirms that a continuous, protective TGO has not formed. Little rumpling is seen in the alloy, confirming that tantalum slows the upward diffusion of aluminum and may be responsible

for the slow formation of the TGO. Some oxide pegs form in the Al-depleted γ+γ′-phase, showing an increase in internal oxidation with time.

4.2.4 Sample D

4.2.4.1 2h Oxidation Exposure

XRD results of sample D after 2h oxidation exposure in dry air show predominant spinel surface coverage with small amounts of beneficial HfO_2 and identifiable α-Al_2O_3 (Figure 4.15).

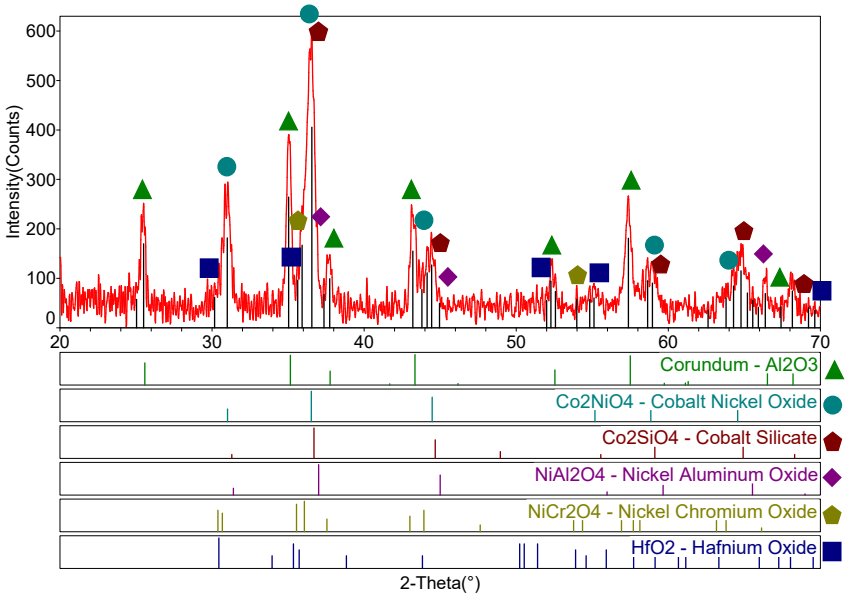

Figure 4.15 GI XRD of sample D surface after oxidation in dry air for 2h at 1100℃

Figure 4.16 (a) shows α-Al_2O_3 formation with small amounts of beneficial HfO_2 and spinel on the surface of sample D after 2h oxidation exposure in dry air. Significant spall in the TGO is observed, however it was not picked up with XRD.

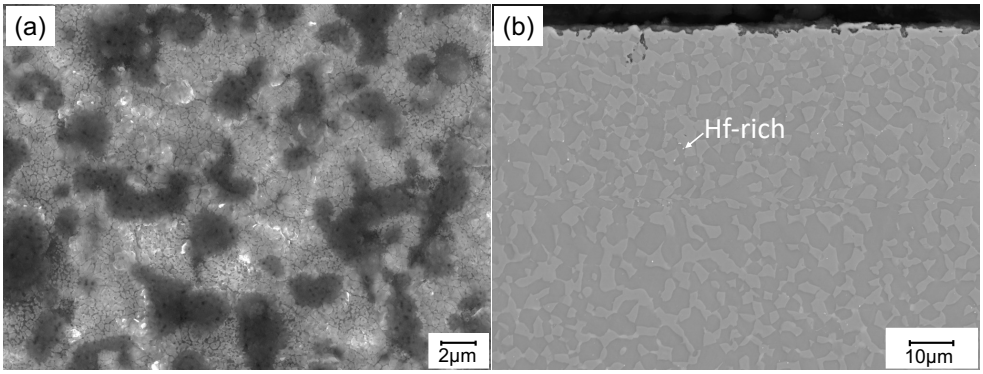

Figure 4.16 BSD SEM of sample D (a) surface (b) cross-section, after oxidation in dry air for 2h at 1100℃

In Figure 4.16 (b), the TGO measures 1.0 μm with an almost indetectable Al-depletion of 0.7 μm, showing that silicon and hafnium effectively reduce the upward diffusion of aluminum, as stated in the literature. Hf-oxide pegs are seen in the TGO and no rumpling of the alloy is observed.

4.2.4.2 20h Oxidation Exposure

After 20h oxidation exposure in dry air, sample D shows fewer spinel species on the TGO surface (Figure 4.17). There is an increase in HfO_2, with silicides and SiO_2 is also identifiable in small relative quantities. The substrate is identified with moderate relative peak heights showing spallation of the TGO.

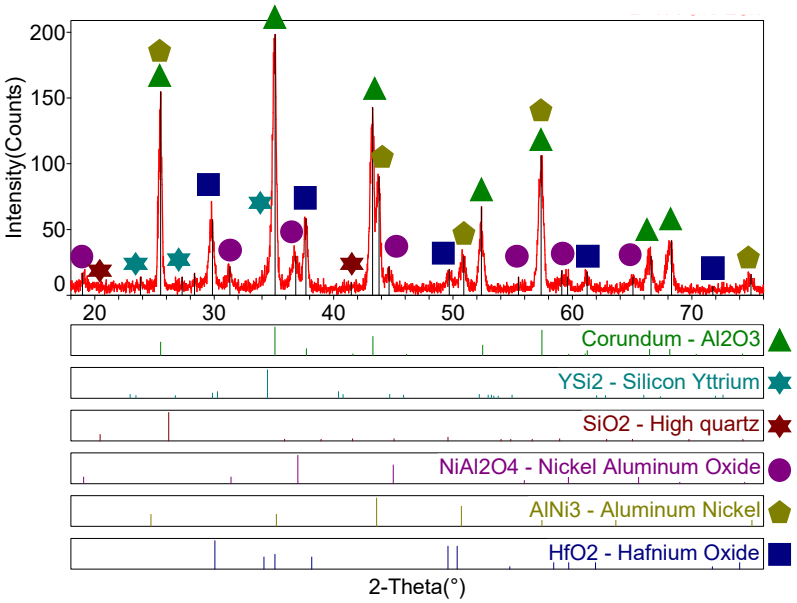

Figure 4.17 GI XRD of sample D surface after oxidation in dry air for 20h at 1100℃

In 20h oxidation exposure, sample D shows less spall and more spinel surface coverage on the surface (Figure 4.18 (a)).

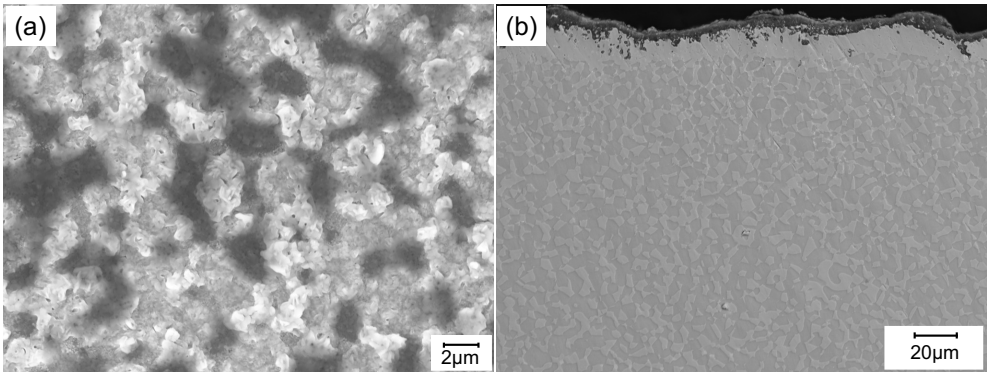

Figure 4.18 BSD SEM of sample D (a) surface (b) cross-section, after oxidation in dry air for 20h at 1100℃

From Figure 4.18 (b), the TGO measures 5.33 μm, 3.8x larger than after 2h, indicating that the oxide layer is not dense and protective to slow growth. An Al-depleted zone of 13.3 μm confirms that aluminum continues to diffuse to the surface as the TGO spalls. Yttria and hafnia peg

formation also increases at the alloy-oxide interface. Rumpling is seen in the alloy, which would cause spallation of the TGO.

4.3 Humid Environment Oxidation 18% H_2O (%vol)

In this section, the results of dry air oxidation exposures for 2h and 20h are presented by sample. A summary of results is given at the end of the section.

4.3.1 Sample A

4.3.1.1 2h Oxidation Exposure

After oxidation in air 18% H_2O for 2h, sample A XRD results show a large amount of transient Ni_2Y (Figure 4.19). $NiAl_2O_4$ spinel is also significant in comparison to the α-Al_2O_3 peaks.

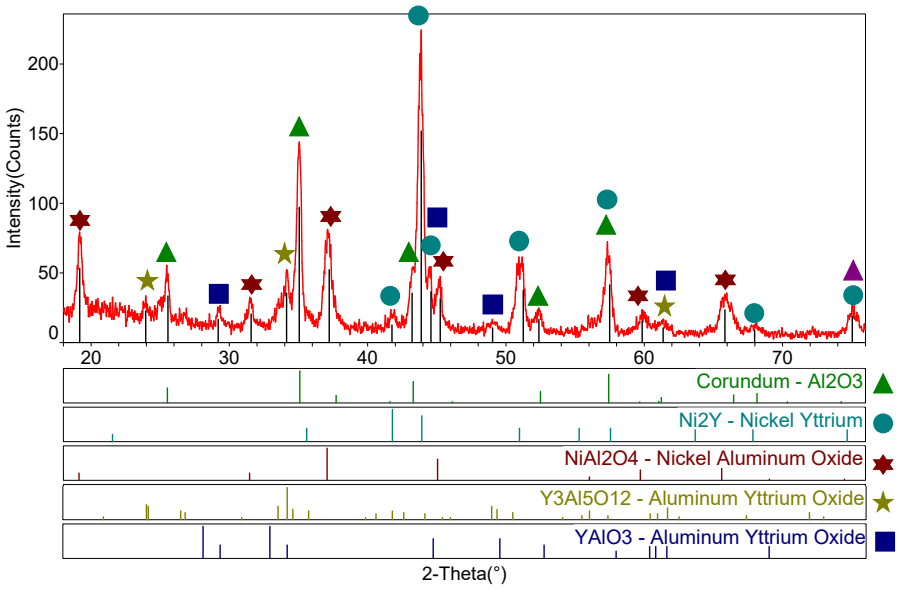

Figure 4.19 GI XRD of sample A surface after oxidation in air 18% H_2O for 2h at 1100℃

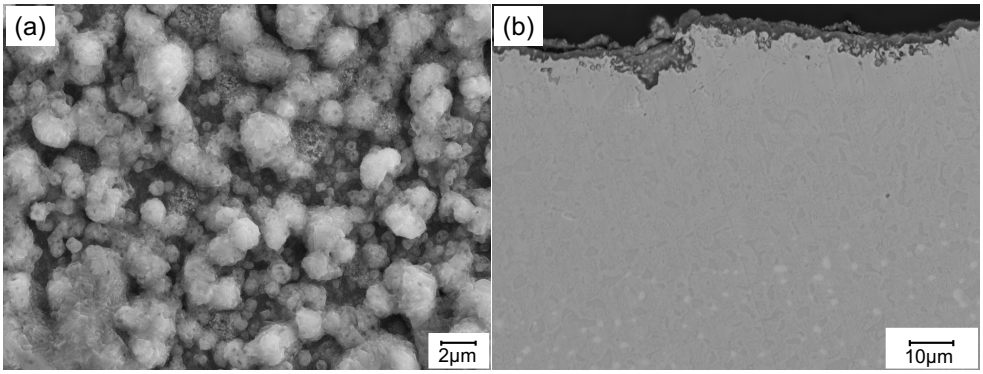

Figure 4.20 BSD SEM of sample A (a) surface (b) cross-section, after oxidation in air 18% H_2O for 2h at 1100℃

Figure 4.20 (a) and (b) highlight the surface and cross-section of sample A in 18% H_2O 2h oxidation. The 2.74 μm TGO is 2x thicker than that grown in dry air and is comprised of large amounts of spinel and transient Ni_2Y that cover the sample surface, as well as a non-uniform layer of α-Al_2O_3 at the alloy-oxide interface. This would indicate that the presence of water delays the formation of stable alumina and increases the undesirable oxidation of Ni, leading to the increased formation of spinels and transient species. Y-oxides are present as oxide pegs. Rumpling, visible voids, and an Al-depletion zone of 11.4 μm indicate an increase in rapid upward diffusion of metal cations to the surface where they react to form predominantly spinel.

4.3.1.2 20h Oxidation Exposure

XRD results for sample A after oxidation in air 18% H_2O for 2h shows significantly more alumina growth compared to the 2h exposure. Spinel and transient Ni_2Y are also significant (Figure 4.21).

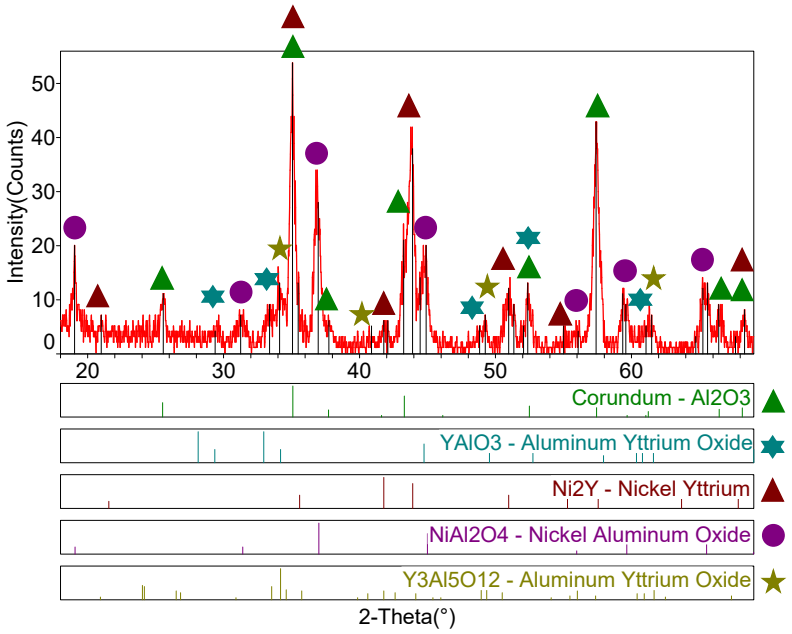

Figure 4.21 GI XRD of sample A surface after oxidation in air 18% H2O for 20h at 1100℃

From Figure 4.22 (a) we can see a reduction in surface spinel coverage. Voids are present on the oxide surface, indicating that initially aluminum rapidly diffused upward creating voids within the alloy. The penetration of oxygen into the alloy then forced the voids to migrate upwards to the oxide-gas interface.

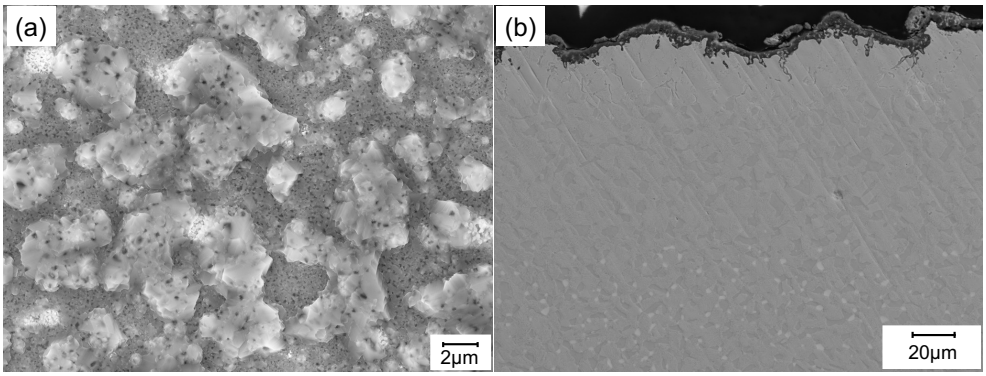

Figure 4.22 BSD SEM of sample A (a) surface (b) cross-section, after oxidation in air 18% H_2O for 20h at 1100℃

The cross-section in Figure 4.22 (b) shows a dense and continuous TGO with a thickness of 5.0 μm and an Al-depletion of 21.7 μm, both double that in 2h oxidation. This confirms that after 2h

sample A does not form a protective TGO. Rumpling increases in the alloy from 2h to 20h oxidation exposure.

4.3.2 Sample B

4.3.2.1 2h Oxidation Exposure

For 2h oxidation in air 18% H_2O, sample B shows significant spinels and Ni2Y in XRD (Figure 4.23). This is also seen in Figure 4.24 (a) on the specimen surface where Ni_2Y and (Co, Ni)Al_2O_4 + Al_2O_3 intermix oxide are identified.

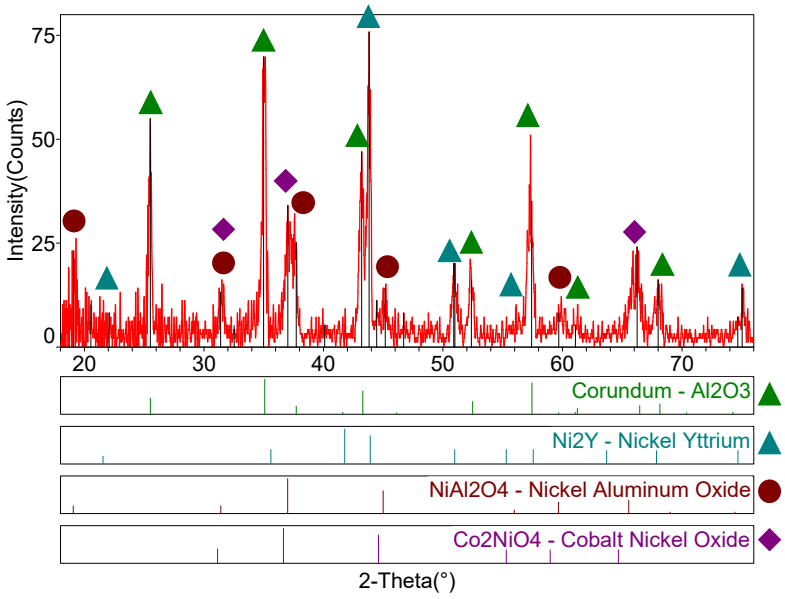

Figure 4.23 GI XRD of sample B surface after oxidation in air 18% H2O for 2h at 1100℃

The cross-section in Figure 4.24 (b) shows some rumpling and voids in the alloy indicating an increase in upward diffusion of alumina during initial oxidation compared to dry air. The TGO is continuous, measuring 1.94 µm with an Al-depletion zone of 5.32 µm, both double that in dry air. Some rumpling of the alloy and the beginnings of oxide peg formation are seen at the alloy-oxide interface. Adhesion is diminished in the TGO with spallation visible at the inflection points in the alloy.

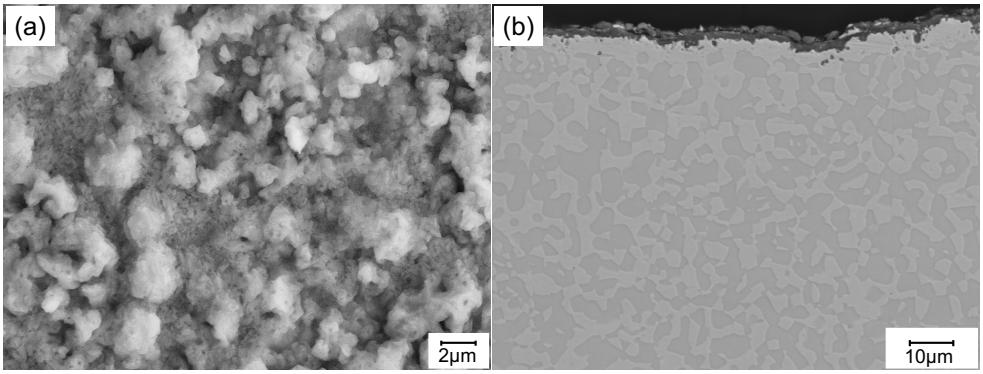

Figure 4.24 BSD SEM of sample B (a) surface (b) cross-section, after oxidation in air 18% H_2O for 2h at 1100℃

4.3.2.2 20h Oxidation Exposure

Sample B 20h oxidation exposure in air + 18% H_2O XRD in Figure 4.25 shows more alumina growth and significantly less spinel than 2h exposure. However, in Figure 4.26 (a) shows reduced spinel surface coverage and increased alumina growth, much like sample A. Identified spinel is predominantly $CoAl_2O_4$. A high concentration of voids is seen on the oxide surface, indicating rapid upward diffusion during early oxidation, followed by an increase in oxygen penetration, forcing the voids to the surface. Ni_2Y coats the surface, meaning the alumina forms below this layer. Voids are visible in the Ni_2Y top layer.

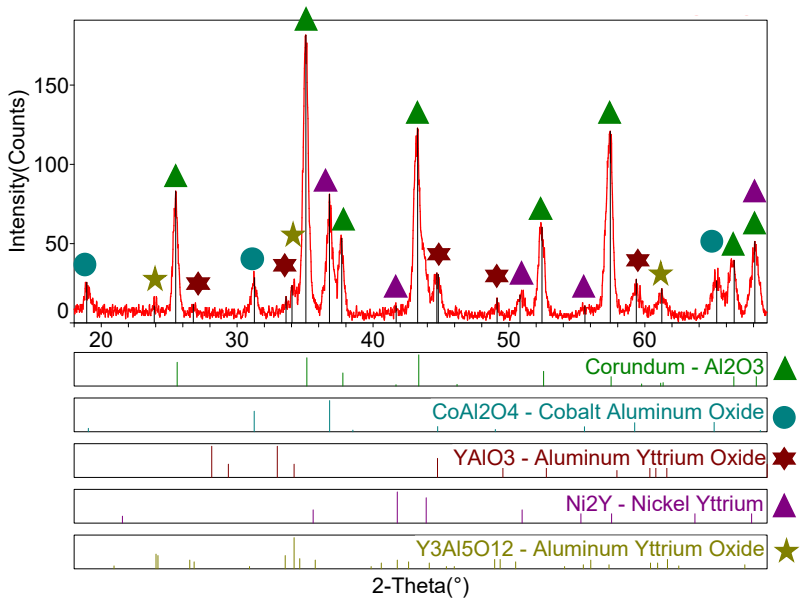

Figure 4.25 GI XRD of sample B surface after oxidation in air 18% H2O for 20h at 1100℃

Figure 4.26 (b) shows an increase in alloy rumpling compared to the 2h exposure and dry air condition. The 3.67 µm TGO has poor adhesion, with cracks and spall at the alloy inflection points. An Al-depletion zone of 9.99 µm forms under the TGO. the Al-depleted zone to TGO thickness remains 2.7x, as with the 2h exposure, indicating a similar aluminum consumption in the TGO growth. Further oxide peg formation is also observed.

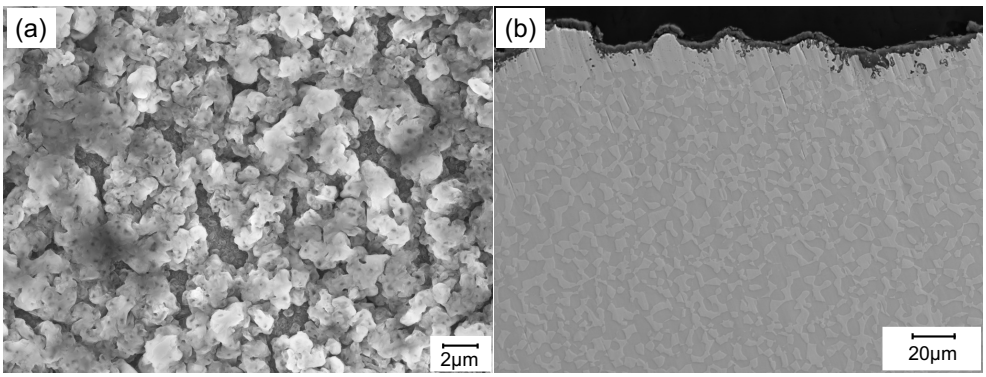

Figure 4.26 BSD SEM of sample B (a) surface (b) cross-section, after oxidation in air 18% H_2O for 20h at 1100℃

4.3.3 Sample C

4.3.3.1 2h Oxidation Exposure

XRD of sample C 2h oxidation exposure in air 18% H_2O (Figure 4.27) shows predominantly alumina, spinel, and alloy.

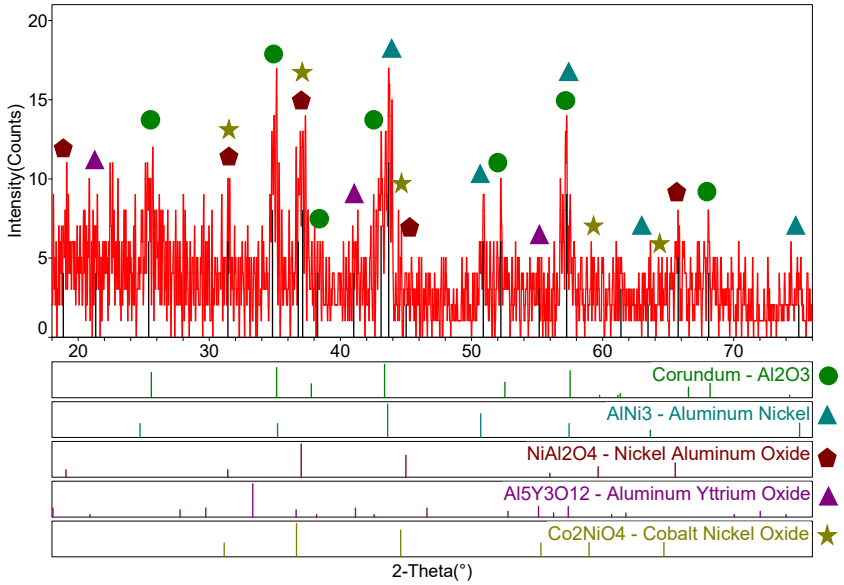

Figure 4.27 GI XRD of sample C surface after oxidation in air 18% H2O for 2h at 1100℃

After 2h oxidation in 18% H_2O Figure 4.28 (a) shows an increase in spinel surface coverage with pockets of alloy still visible, indicating that the 0.81 μm TGO is not continuous. This is also seen in the cross-section in Figure 4.28 (b) where there is significant spall. Oxide pegs are more prevalent than in dry air suggesting more oxygen penetration of the alloy during oxidation. The TGO thickness is similar to the dry air exposure, suggesting that tantalum is effective at slowing the upward diffusion of aluminum in the presence of water. The Al-depletion zone is 5.3 μm, also similar to the dry air condition, indicating the preferential formation of α-Al_2O_3 in early oxidation in the presence of water vapor.

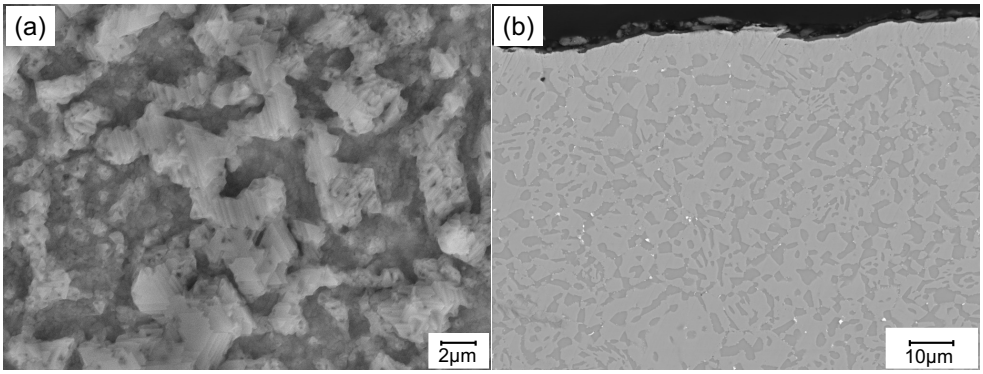

Figure 4.28 BSD SEM of sample C (a) surface (b) cross-section, after oxidation in air 18% H_2O for 2h at 1100℃

4.3.3.2 20h Oxidation Exposure

After 20h oxidation exposure in air 18% H_2O, XRD of sample C (Figure 4.29) shows good alumina growth with minimal spinel compared to the 2h exposure. However, the alloy is still identified.

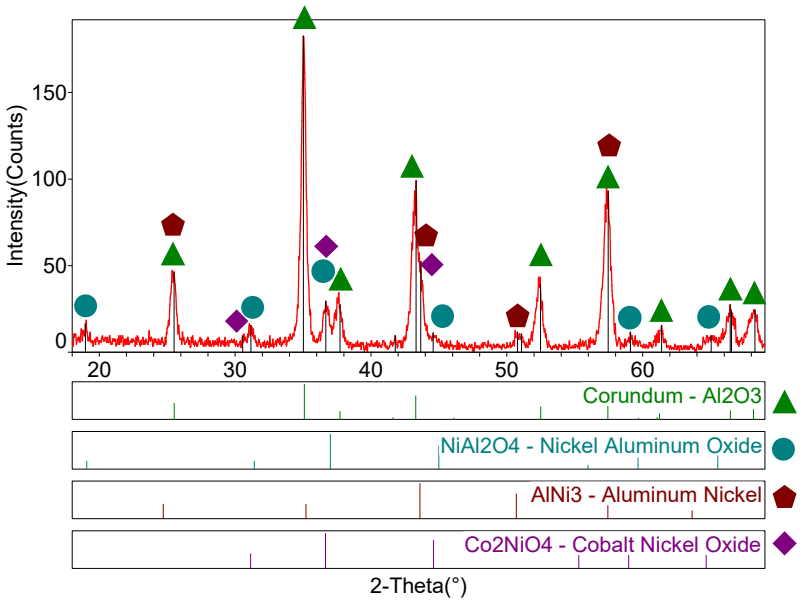

Figure 4.29 GI XRD of sample C surface after oxidation in air 18% H2O for 20h at 1100℃

Figure 4.30 (a) shows enhanced α-Al_2O_3 coverage and reduced spinel, as well as spall in the TGO.

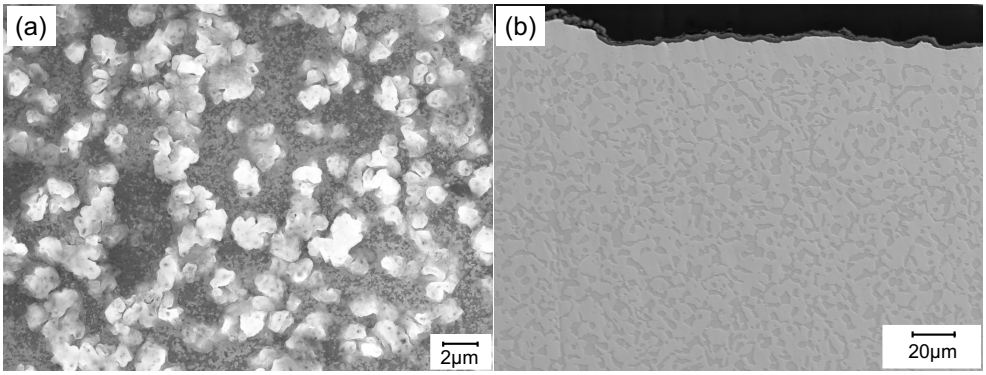

Figure 4.30 BSD SEM of sample C (a) surface (b) cross-section, after oxidation in air 18% H_2O for 20h at 1100℃

Large sections of TGO delimitation are still visible on the surface pointing to poor adhesion of the 2.67 μm TGO in Figure 4.30 (b). Al Al-depletion of 11.1 μm is less than in dry air as α-Al_2O_3 grows preferentially to spinels.

4.3.4 Sample D

4.3.4.1 2h Oxidation Exposure

XRD of sample D after 2h oxidation exposure in air 18% H_2O (Figure 4.31) shows significant spinel growth compared to alumina. Relative peak heights indicate a large amount of HfO_2 also.

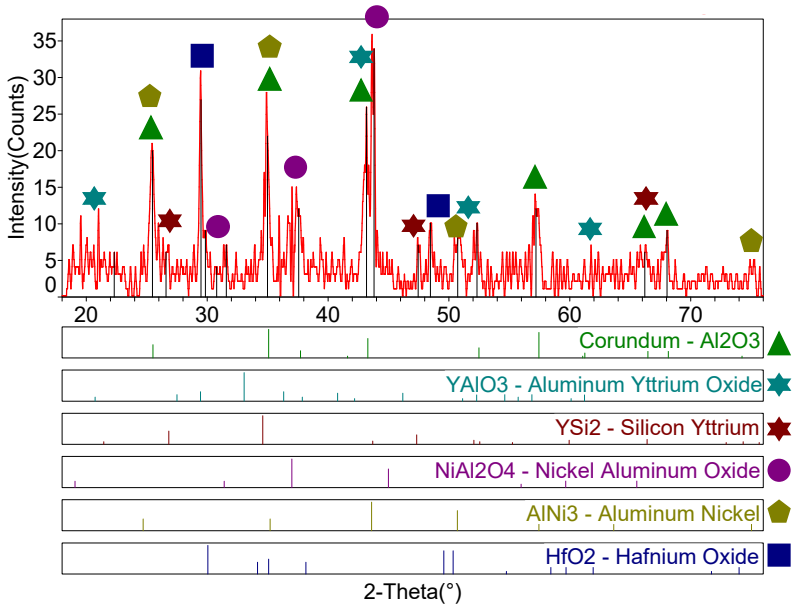

Figure 4.31 GI XRD of sample D surface after oxidation in air 18% H2O for 2h at 1100℃

Figure 4.32 (a) shows complete spinel surface coverage of the specimen. A continuous TGO is formed with no visible spallation. Large HfO_2 particles are also identified.

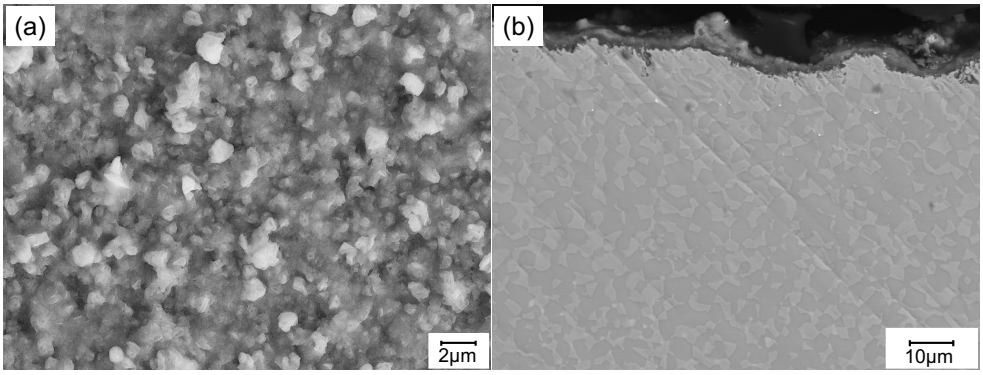

Figure 4.32 BSD SEM of sample D (a) surface (b) cross-section, after oxidation in air 18% H_2O for 2h at 1100℃

Figure 4.32 (b) shows a TGO of 3.55 μm, 3.5x thicker than in dry air. This may be due to the delay in transformation from θ-Al_2O_3 to α-Al_2O_3. Al-depletion of 7.6 μm is 11.5x more than in dry air, showing large aluminum consumption in the TGO formation, which corroborates the theory that non-protective θ-Al_2O_3 takes longer to transform to α-Al_2O_3 in the presence of water. Rumpling

of the alloy is moderate, and the alloy is identified with XRD indicating spall. Rumpling and oxide peg formation also increase compared to dry air.

4.3.4.2 20h Oxidation Exposure

After 20h oxidation exposure in air 18% H_2O, Figure 4.33 shows XRD of sample D where alumina and transient Ni_2Y are most notable. Less HfO_2 is observed than in the 2h exposure, and the alloy is still identified which implies spallation.

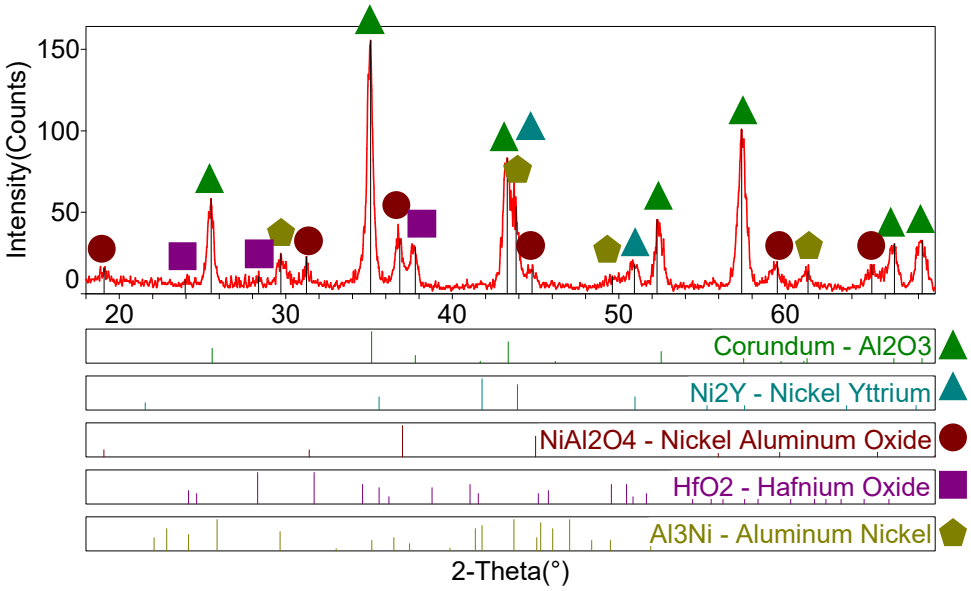

Figure 4.33 GI XRD of sample D surface after oxidation in air 18% H2O for 20h at 1100℃

Figure 4.34 (a) shows more alumina growth and a reduction in surface spinels. Visible spallation of the TGO is seen and confirmed with XRD. More voids are seen on the surface than the dry air and 2h exposures showing more oxygen ingress.

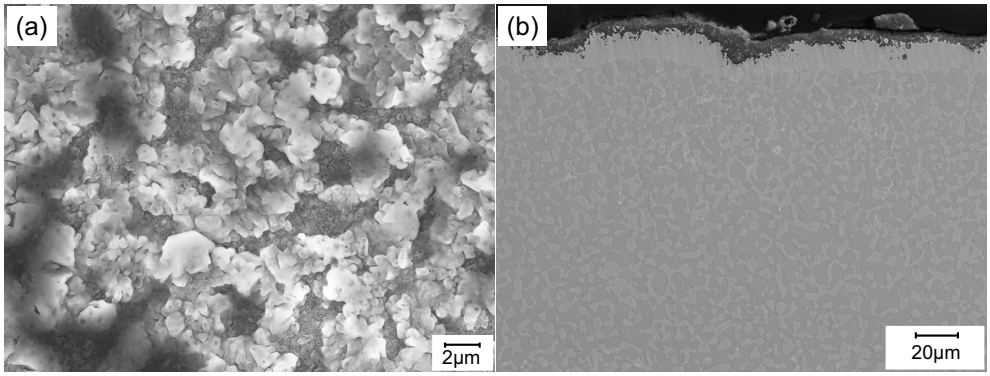

Figure 4.34 BSD SEM of sample D (a) surface (b) cross-section, after oxidation in air 18% H_2O for 20h at 1100℃

In Figure 4.34 (b) we see HfO_2 pegs embedded in the 7.67 μm TGO. The Al-depletion of 13.3 μm shows that an α-Al_2O_3 layer is formed with prolonged exposure, slowing the upward diffusion of aluminum. Rumpling of the alloy and oxide peg formation have both increased from the 2h exposure.

4.4 Humid Environment Oxidation 33% H_2O (%vol)

In this section, the results of dry air oxidation exposures for 2h and 20h are presented by sample. A summary of results is given at the end of the section.

4.4.1 Sample A

4.4.1.1 2h Oxidation Exposure

Sample A oxidation exposure in air 33% H_2O for 2h shows good alumina growth in XRD (Figure 4.35). Transient Ni_2Y and $YCrO_4$ are present as well as $NiAl_2O_4$ spinel.

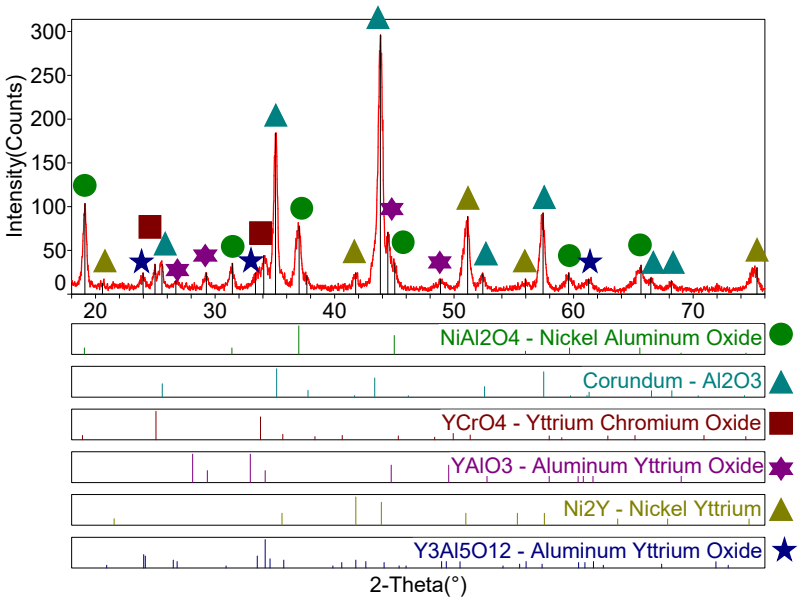

Figure 4.35 GI XRD of sample A surface after oxidation in air 33% H2O for 2h at 1100℃

Figure 4.36 (a) shows complete Ni_2Y and $NiAl_2O_4$ surface coverage of the specimen. The cross-section in Figure 4.36 (b) shows an α-Al_2O_3 layer with Y-rich oxide pegs at the alloy-oxide interface. No alloy rumpling is observed, and oxide peg formation is seen in the 1.81 µm TGO. The Al-depletion of 8.0 µm is 4.4x the TGO thickness, a similar ratio to the 18% humidity exposure, however, the TGO is 1.5x thinner than at 18% H_2O. More voids are seen on the oxide surface suggesting that increased oxygen penetration forces more voids to the surface from the alloy-oxide interface.

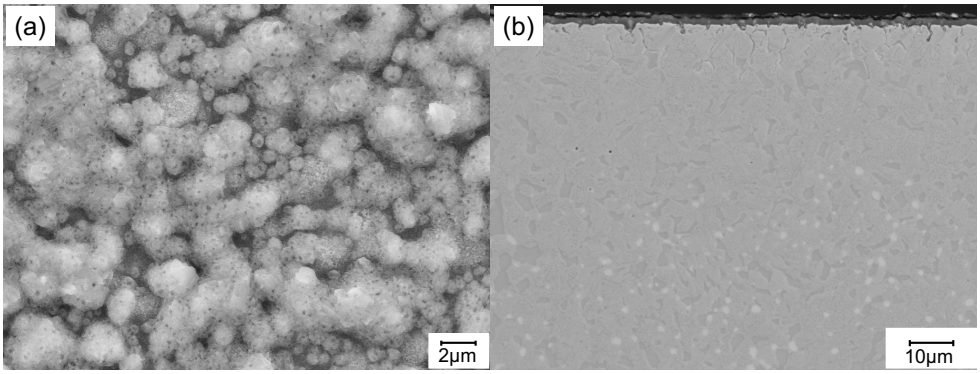

Figure 4.36 BSD SEM of sample A (a) surface (b) cross-section, after oxidation in air 33% H_2O for 2h at 1100℃

4.4.1.2 20h Oxidation Exposure

After 20h oxidation exposure in air 33% H_2O, sample A has more Ni_2Y and $NiAl2O_4$ spinel observed with XRD (Figure 4.37) than after 2h exposure.

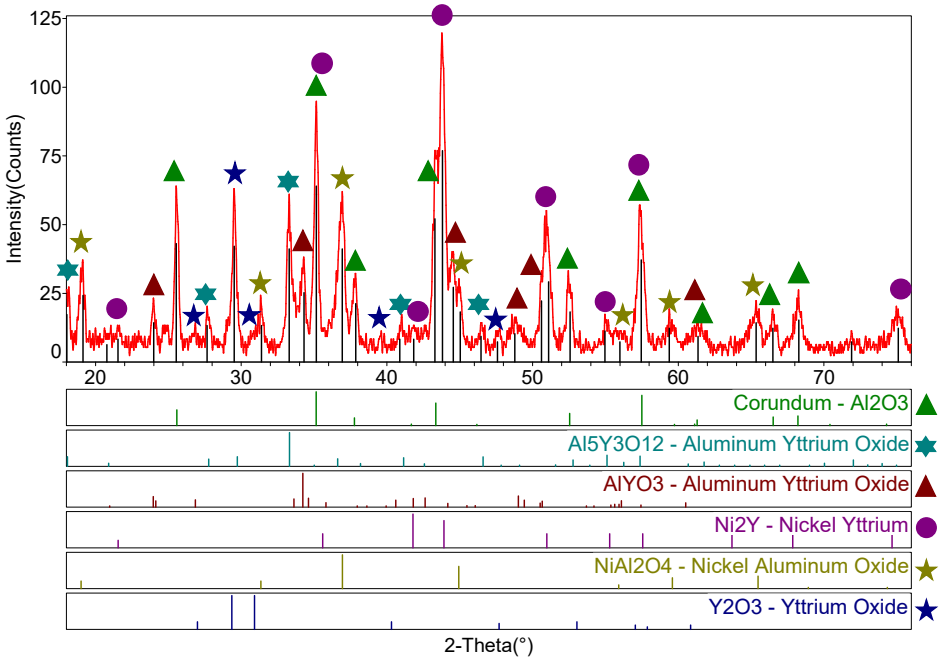

Figure 4.37 GI XRD of sample A surface after oxidation in air 33% H2O for 20h at 1100℃

From the specimen surface (Figure 4.38 (a)), large voids are seen in the TGO, which act as quick diffusion path into the alloy, with complete surface coverage of spinel and Ni_2Y.

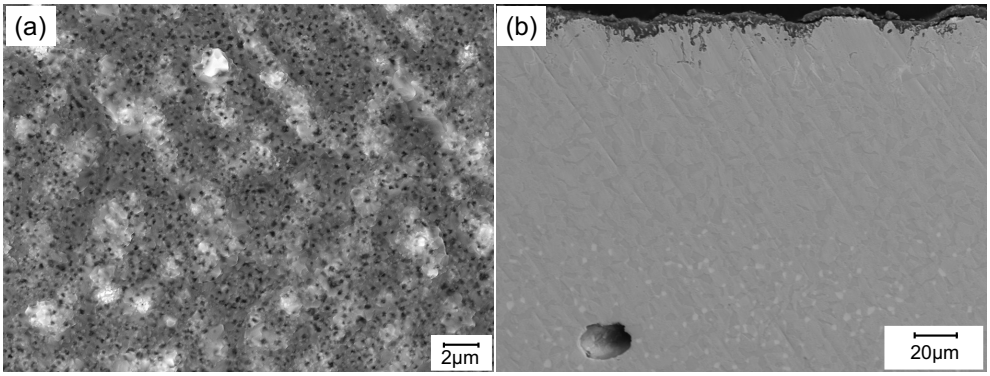

Figure 4.38 BSD SEM of sample A (a) surface (b) cross-section, after oxidation in air 33% H_2O for 20h at 1100℃

In Figure 4.38 (b) the specimen cross-section shows rumpling of the alloy with spallation of the TGO at the inflection points. Significant oxide pegs are formed at the alloy-oxide interface, and the TGO is not consistent or uniform. The TGO measures 4.0 μm and the Al-depletion zone measures 22.9 μm. After 20h oxidation, the Al-depleted zone remains fairly linear with TGO growth compared to 18% H_2O 20h, at 4.8x the TGO thickness. The TGO shows significant spall and the oxide pegs have increased with exposure time.

4.4.2 Sample B

4.4.2.1 2h Oxidation Exposure

Sample B oxidation exposure in air 33% H_2O for 2h XRD results show alumina growth with significant Ni_2Y and spinel (Figure 4.39).

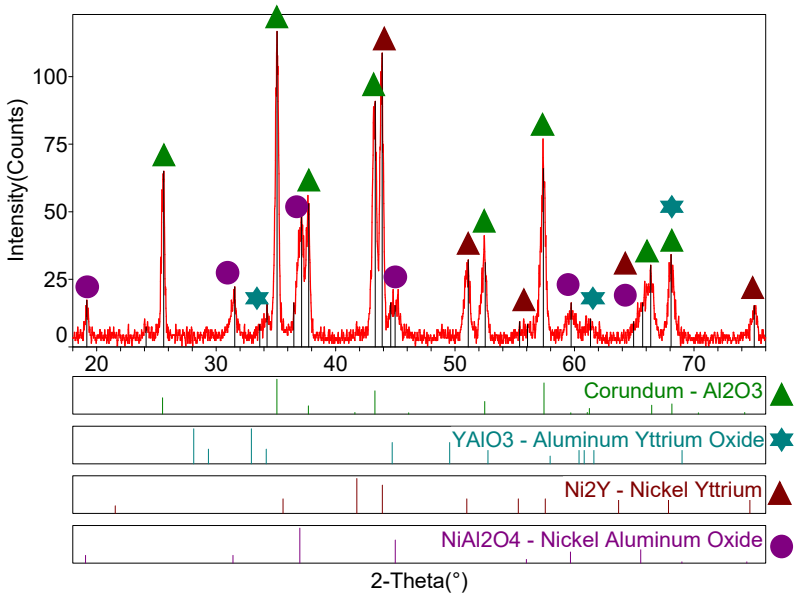

Figure 4.39 GI XRD of sample B surface after oxidation in air 33% H2O for 2h at 1100℃

Figure 4.40 (a) shows the specimen complete surface coverage of spinel and Ni_2Y.

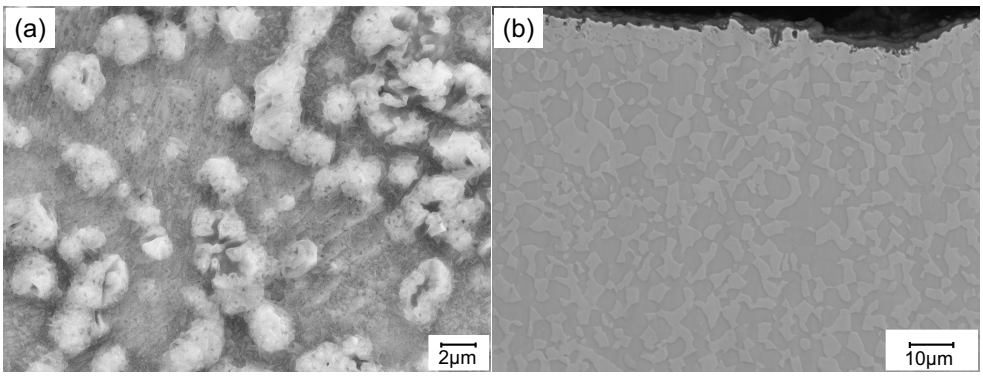

Figure 4.40 BSD SEM of sample B (a) surface (b) cross-section, after oxidation in air 33% H_2O for 2h at 1100℃

From Figure 4.42 (b) fewer voids are noted on the surface than in 18% H_2O, indicating slower upward diffusion of aluminum during TGO formation. An Al-depletion of 6.7 μm corroborates that more alumina forms on the surface, though the presence of water delays the transition to α-Al_2O_3. The TGO is thinner than in 18% H_2O at 1.85 μm, and oxide pegs increase. Broad rumpling

of the alloy is observed with oxide pegs in the alloy-oxide interface. The TGO has better adhesion that in 18% H_2O.

4.4.2.2 20h Oxidation Exposure

After 20h oxidation exposure in air 33% H_2O, sample B XRD results (Figure 4.41) shows less Ni2Y and more spinel ($CoAl_2O_4$, $NiAl_2O_4$).

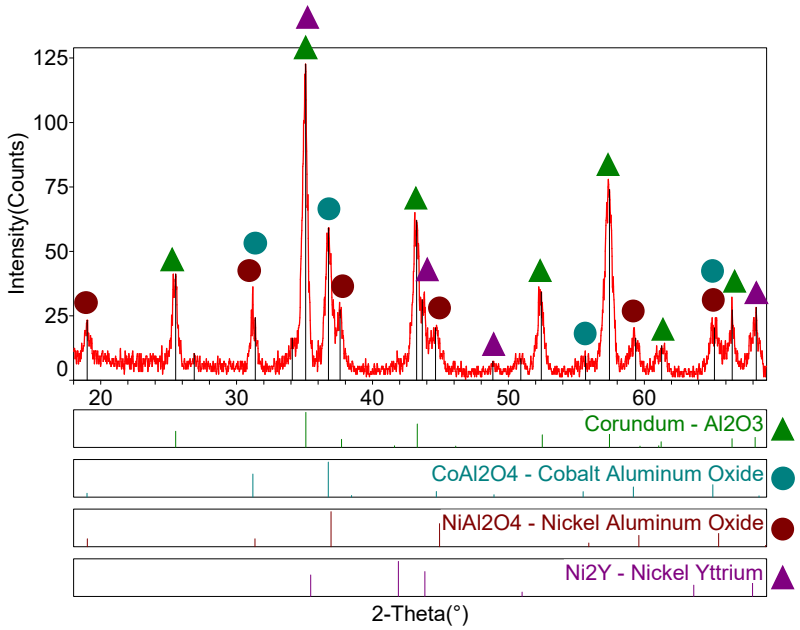

Figure 4.41 GI XRD of sample B surface after oxidation in air 33% H2O for 20h at 1100℃

Figure 4.42 (a) shows a dense α-Al_2O_3 covered in $CoAl_2O_4$ and $NiAl_2O_4$ spinels with less transient Ni2Y detected. Large yttrium oxides are seen on the surface and fewer voids provide channels for diffusion through the TGO.

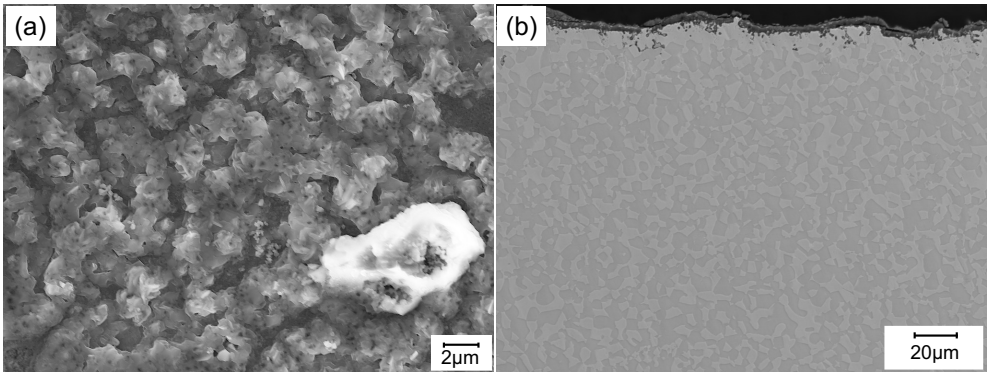

Figure 4.42 BSD SEM of sample B (a) surface (b) cross-section, after oxidation in air 33% H_2O for 20h at 1100℃

In Figure 4.42 (b) the cross-section shows a 4.0 μm TGO. Increased oxide peg formation shows more internal oxidation than the 18% H_2O 20h condition. Less rumpling of the alloy and an Al-depletion of 7.0 μm confirms that less aluminum is consumed in the formation of the TGO compared to the 18% H_2O 20h condition and that the θ-Al_2O_3 has converted to α-Al_2O_3, creating a protective oxide layer. However, the delay in this transformation due to the increased presence of water allows for the upward diffusion of cobalt and nickel to form more unwanted oxides. The significantly thicker TGO compared to Al-depletion would confirms that the TGO contains more spinel, with a new $CoAl_2O_4$ species identified.

4.4.3 Sample C

4.4.3.1 2h Oxidation Exposure

Sample C oxidation exposure in air 33% H_2O for 2h shows alumina and spinel growth with large alloy peaks (Figure 4.43). Transient Ni_2Y is not identified.

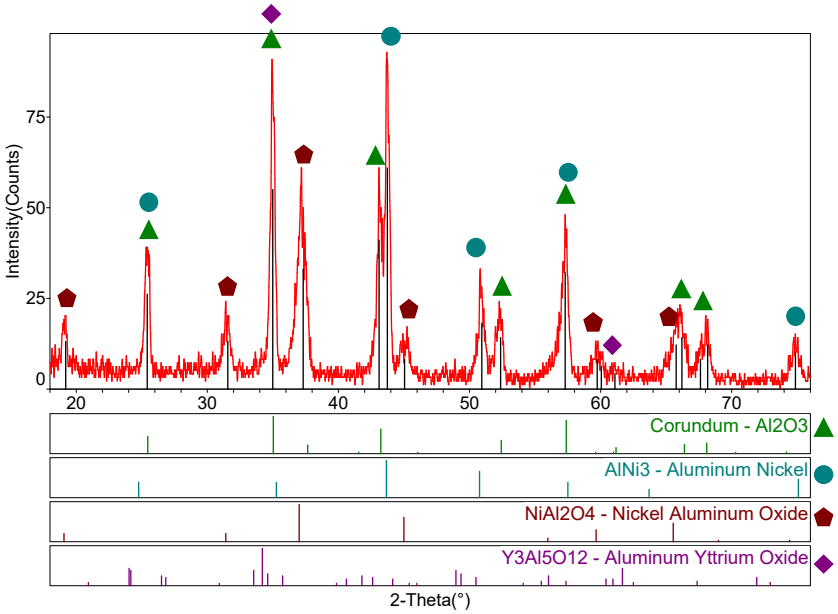

Figure 4.43 GI XRD of sample C surface after oxidation in air 33% H2O for 2h at 1100℃

From the specimen surface, Figure 4.44 (a) shows more spinel coverage than the other two humidity conditions with α-Al_2O_3 visible beneath. Transient Ni_2Y is not identified.

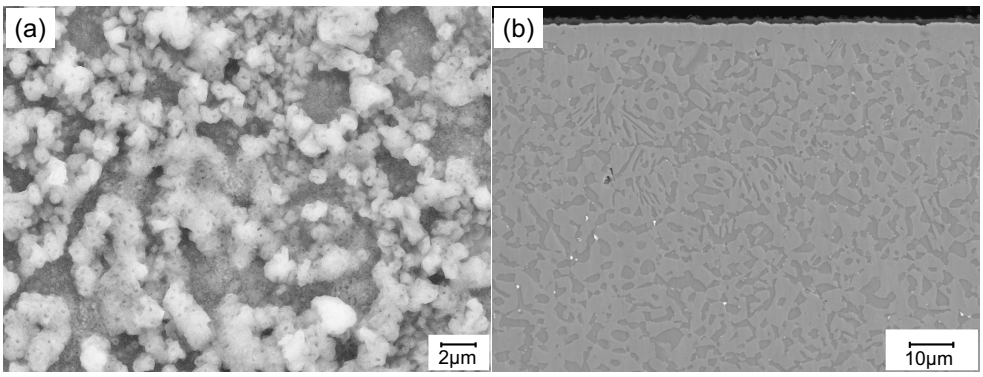

Figure 4.44 BSD SEM of sample C (a) surface (b) cross-section, after oxidation in air 33% H_2O for 2h at 1100℃

In Figure 4.44 (b), no rumpling and a thin 1.29 μm TGO is observed. The substrate is the dominant identified compound in XRD, indicating a non-uniform TGO growth. The Al-depleted zone is 8.12 μm, 6.3x the TGO thickness, much like the other two humidity conditions after 2h, suggesting that sample C is the least affected by the presence of water during TGO formation. Voids are pushed

to the surface with increasing oxygen penetration, explaining the increase from 18% humidity. After 20h these voids are annihilated.

4.4.3.2 20h Oxidation Exposure

After 20h oxidation exposure in air 33% H_2O, sample C XRD results (Figure 4.45) show more alumina growth and the formation of an additional spinel species; $NiCo_2O_4$.

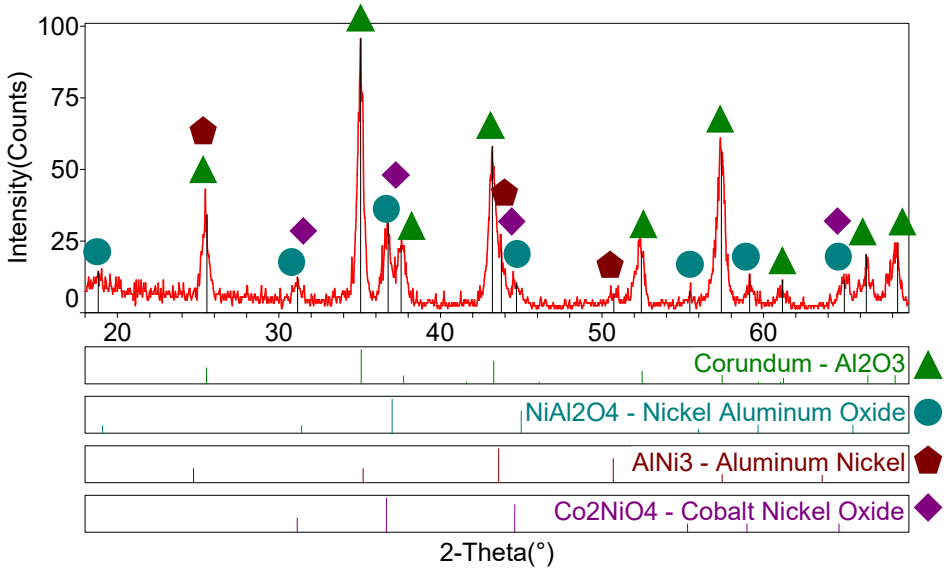

Figure 4.45 GI XRD of sample C surface after oxidation in air 33% H2O for 20h at 1100℃

From the surface imaging, Figure 4.46 (a) shows more alumina growth and the formation of an additional spinel species; $NiCo_2O_4$. A reduction is surface spinel is seen after 20h, much like the 18% H_2O exposure.

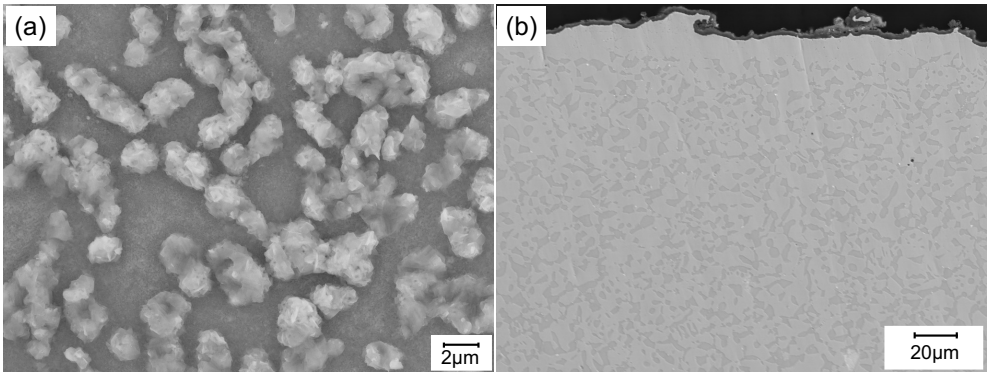

Figure 4.46 BSD SEM of sample C (a) surface (b) cross-section, after oxidation in air 33% H_2O for 20h at 1100℃

From the specimen cross-section, Figure 4.46 (b) shows a TGO of 2.40 µm, the smallest difference in TGO growth between 2h and 20h of all the humidity exposures for this composition. Oxide peg formation increased from the 18% H_2O 20h exposure, indicating that a protective α-Al_2O_3 has formed. Al-depletion is 8.6 µm and rumpling of the alloy is minimal. Minimal spallation of the TGO is observed and improved adhesion is seen in the TGO compared to the 2h exposure.

4.4.4 Sample D

4.4.4.1 2h Oxidation Exposure

Sample D oxidation exposure in air 33% H_2O for 2h Figure 4.47 XRD results show alumina, spinel, and alloy peaks with some transient Si_2Y.

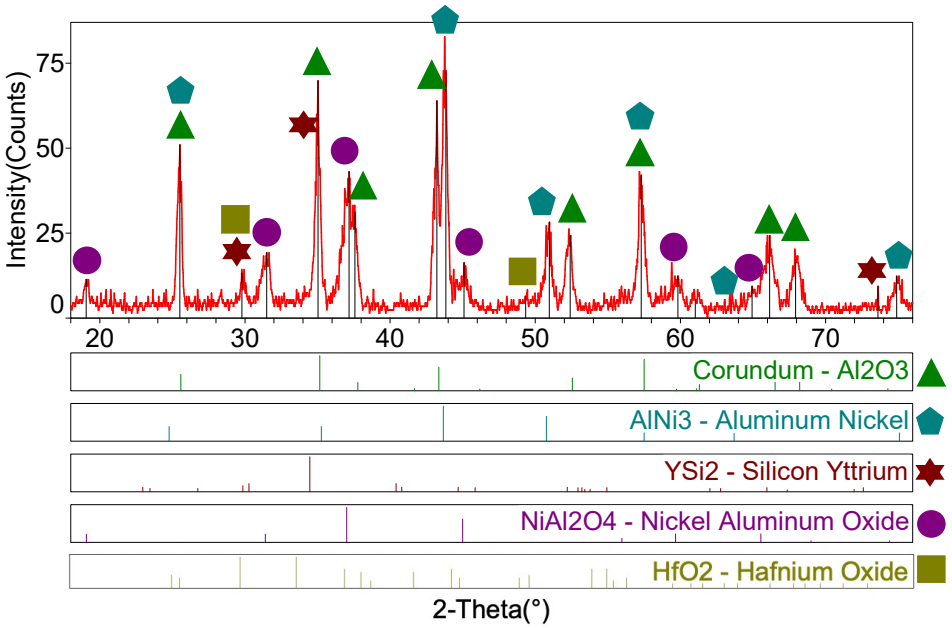

Figure 4.47 GI XRD of sample D surface after oxidation in air 33% H2O for 2h at 1100℃

From Figure 4.48 (a) we see complete spinel surface coverage of the specimen, as well as transient Si_2Y, and yttria particles. Spall is visible in the TGO.

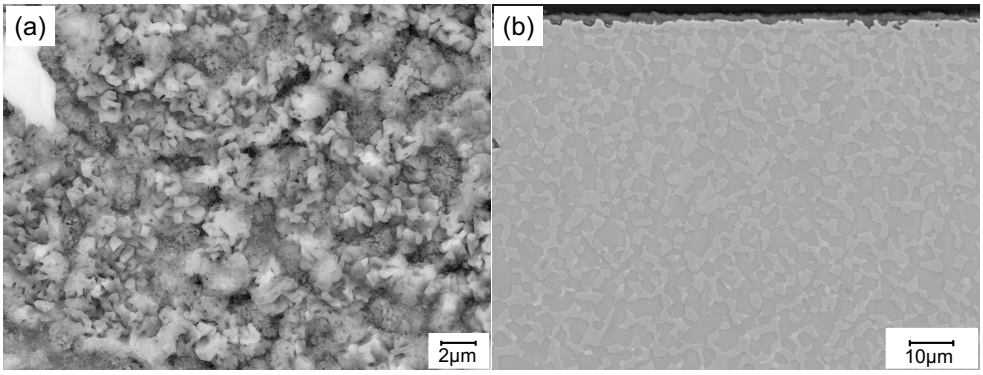

Figure 4.48 BSD SEM of sample D (a) surface (b) cross-section, after oxidation in air 33% H_2O for 2h at 1100℃

In Figure 4.48 (b), we observe a 2.75 μm TGO of mixed spinel and alumina. An Al-depletion of 1.9 μm suggests that oxide nucleation happens quickly in early oxidation, reducing the diffusion flux of elements from the bond coat. This may also explain the reduction in HfO_2 compared to the

18% humidity exposure. Identification of the alloy in XRD suggests that the TGO is not uniform after 2h.

4.4.4.2 20h Oxidation Exposure

After 20h oxidation exposure in air 33% H_2O, sample D XRD results (Figure 4.49) show a majority of alumina growth with some transient Si_2Y and minimal spinel. HfO_2 is also identified.

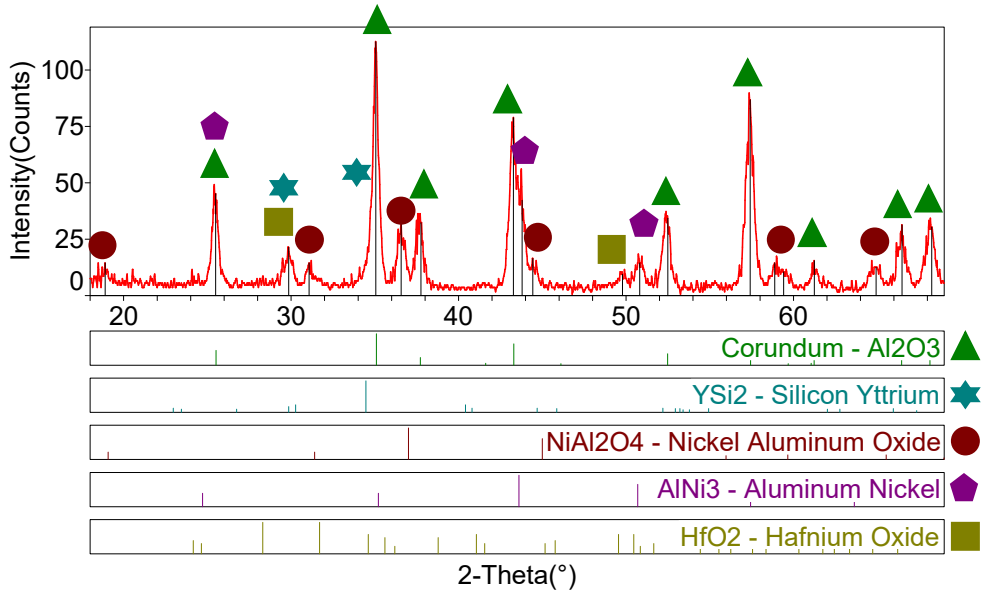

Figure 4.49 GI XRD of sample D surface after oxidation in air 33% H2O for 20h at 1100℃

From Figure 4.50 (a) we see that the surface of the specimen is completely covered in spinel with some transient Si_2Y, HfO_2. The TGO is not uniform, with pockets of the alloy visible.

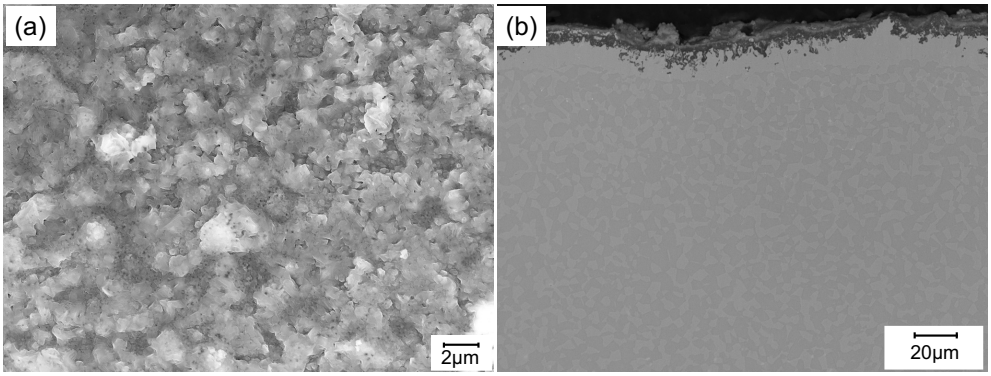

Figure 4.50 BSD SEM of sample D (a) surface (b) cross-section, after oxidation in air 33% H_2O for 20h at 1100℃

Less rumpling of the alloy is seen in Figure 4.50 (b), and oxygen peg formation has increased from the 2h exposure and the 18% H_2O condition. An α-Al_2O_3 layer is visible at the alloy-oxide interface with an intermix oxide on the surface. The TGO is 5.0 μm thick following the same pattern as the other compositions. The Al-depletion remains constant at 13.3 μm. Broad rumpling of the alloy is visible as well as lots of oxide pegs at the alloy-oxide interface. HfO_2 particles are seen in the alumina layer of the TGO. The TGO is the thickest of all four compositions, with large spinel outcrops that would lead to spall in the ceramic top coat in application.

4.5 Summary of Results

In this section, the effect of increasing humidity is presented by composition and oxidation exposure time to better show trends. These results are then discussed and compared with existing literature in section 0.

4.5.1 Sample A

Sample A has the simplest alloy composition Figure 4.51 highlights the surfaces and cross-sections of sample A after 2h exposure in the three humid air conditions. In Figure 4.51 (a), (b) and (c) transient species surface coverage increases with humidity. Figure 4.52 highlights the surfaces and cross-sections of sample A after 20h exposure in the three humid air conditions. Figure 4.52 (a), (b), and (c) show an increase in alumina on the surface of the specimens in all humidities compared to 2h exposure. Voids are most prevalent in Figure 4.52 (b) and (c) indicating the fast upward diffusion of aluminum to the surface during prolonged oxidation. In the dry air condition, surface

voids are minimal, but voids at the equiaxed/columnar alumina grain boundaries can be seen in Figure 4.52 (a).

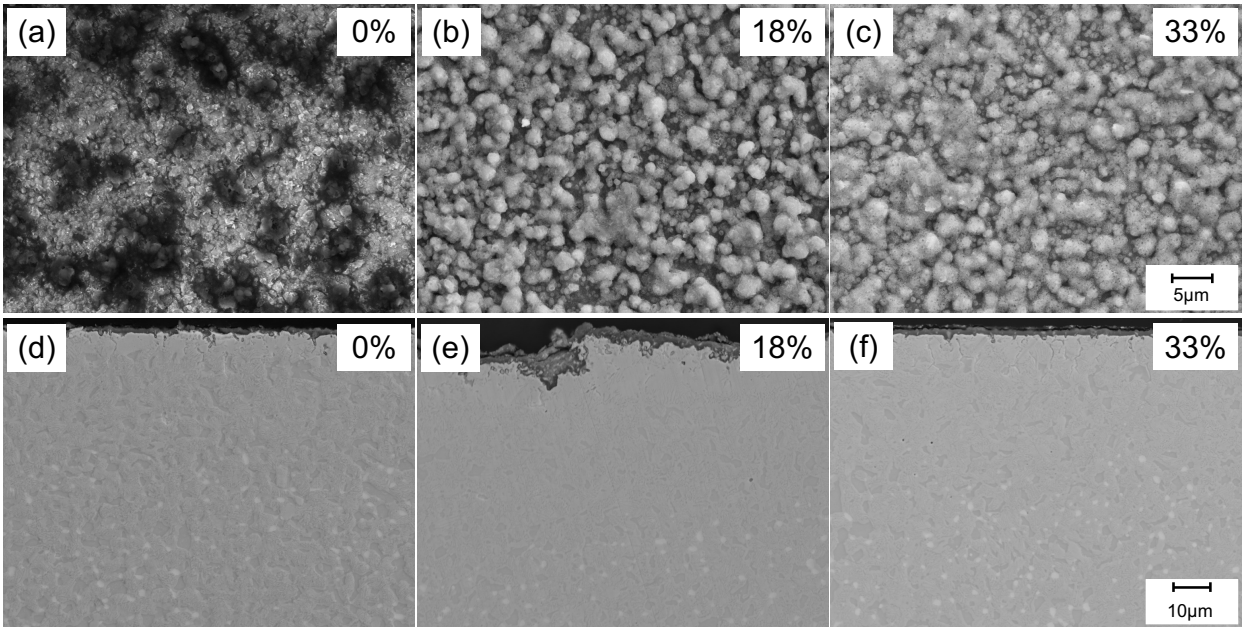

Figure 4.51 BSD SEM of surface and cross-section of sample A in dry air (a) (d), 18% H_2O humidity (b) (e), and 33% H_2O humidity (c) (f) after 2h oxidation exposure

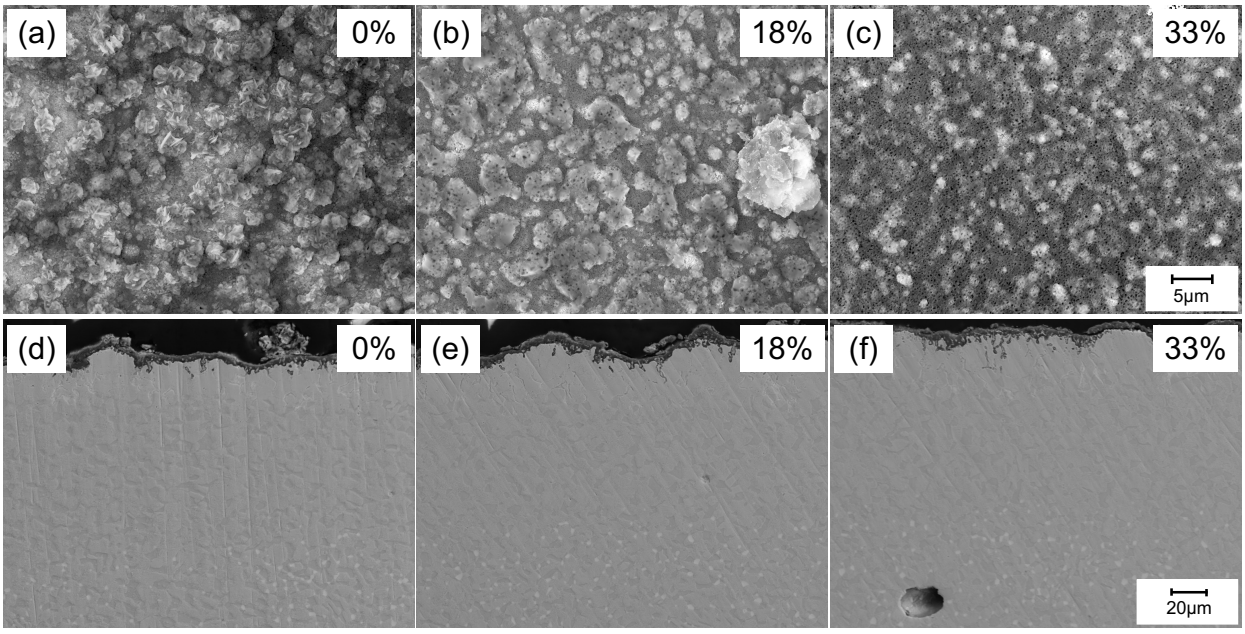

Figure 4.52 BSD SEM of surface and cross-section of sample A in dry air (a) (d), 18% H_2O humidity (b) (e), and 33% H_2O humidity (c) (f) after 20h oxidation exposure

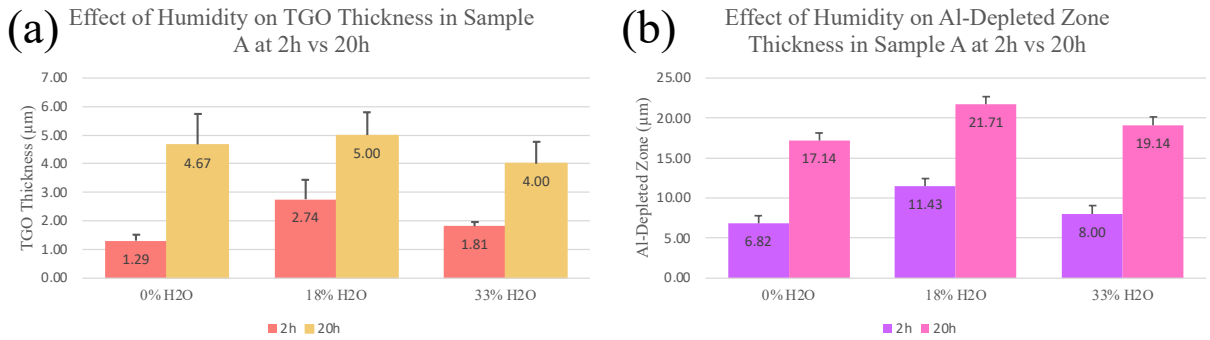

Figure 4.53 Effect of Humidity on TGO Thickness (a) and Al-depletion (b) in sample A for 0%, 18% and 33% H_2O in 2h and 20h oxidation

Figure 4.53 summarises the effect of humidity on TGO thickness (a) and Al-depletion (b) in sample A over 2h and 20h oxidation exposures. From the results, TGO thickness increases with time. In dry air, Figure 4.51 (a) shows sample A does not form a continuous TGO after 2h. The 18% H_2O environment produces the thickest TGO (Figure 4.51 (e), Figure 4.52 (e)), and the oxides grown in all conditions initially consist of majority spinel and transient species after 2h exposure as seen in Table 9. Table 9 summarizes the XRD results of sample A in all oxidation conditions. The identified compounds are ordered from highest to lowest in terms of relative peak height, which gives an idea of the relative amount of each compound found on the surface. The differences in compounds identified between the 2h and 20h oxidation exposure are bolded between specimens.

After 20h oxidation, alumina formation increases across all oxidation conditions. Significant rumpling is observed across all humidities compared to 2h exposure (Figure 4.52). Adhesion of the TGO is worst in 18% H_2O (Figure 4.51 (e), Figure 4.52 (e)). TGO thickness and rumpling are the largest in 18% H_2O oxidation for both 2h and 20h oxidation and also shows the greatest Al-depletion (Figure 4.53). Oxide peg formation increases with increasing humidity in Figure 4.51 and Figure 4.52. This indicates an increase in internal oxidation and creates unwanted stresses in the alloy-oxide interface during thermal cycling. From Table 9 we see that spinel coverage decreases in the presence of humidity and extended oxidation time. After 20h, transient species are identified on all samples after the TGO has formed, indicating ongoing oxidation of the alloy.

Table 9 XRD results for sample A in 0%, 18%, and 33% H_2O (%vol) in 2h and 20h oxidation with differences in identified species bolded

0%	18%	33%
2h		
$NiAl_2O_4$	Ni_2Y	Al_2O_3
Al_2O_3	Al_2O_3	$NiAl_2O_4$
$AlYO_3$	$NiAl_2O_4$	Ni_2Y
NiO	$Y_3Al_5O_{12}$	**$CrYO_4$**
	$AlYO_3$	$AlYO_3$
		$Y_3Al_5O_{12}$
20h		
Al_2O_3	Al_2O_3	Ni_2Y
Ni_2Y	Ni_2Y	Al_2O_3
$NiAl_2O_4$	$NiAl_2O_4$	$NiAl_2O_4$
$Y_3Al_5O_{12}$	$Y_3Al_5O_{12}$	$Y_3Al_5O_{12}$
$AlYO_3$	$AlYO_3$	**Y_2O_3**
		$AlYO_3$

4.5.2 Sample B

Sample B introduces cobalt in the alloy composition. Figure 4.54 highlights the surfaces and cross-sections of sample B after 2h exposure in the three humid air conditions. In Figure 4.54 (a), a uniform α-Al_2O_3 layer has not formed after 2h exposure, however from Table 10 we see that the emerging TGO is primarily alumina, highlighting influence of cobalt in preferential alumina formation. Figure 4.54 (b) shows that the 18% humidity condition shows the largest transient species surface coverage after 2h, indicating that the transformation to stable alumina is delayed. In 33% humidity, Figure 4.54 (c) and Table 10 show a smaller percentage of spinel formation. However, the transition form θ-Al_2O_3 to α-Al_2O_3 is delayed in the presence of water, creating a thicker TGO than in dry air.

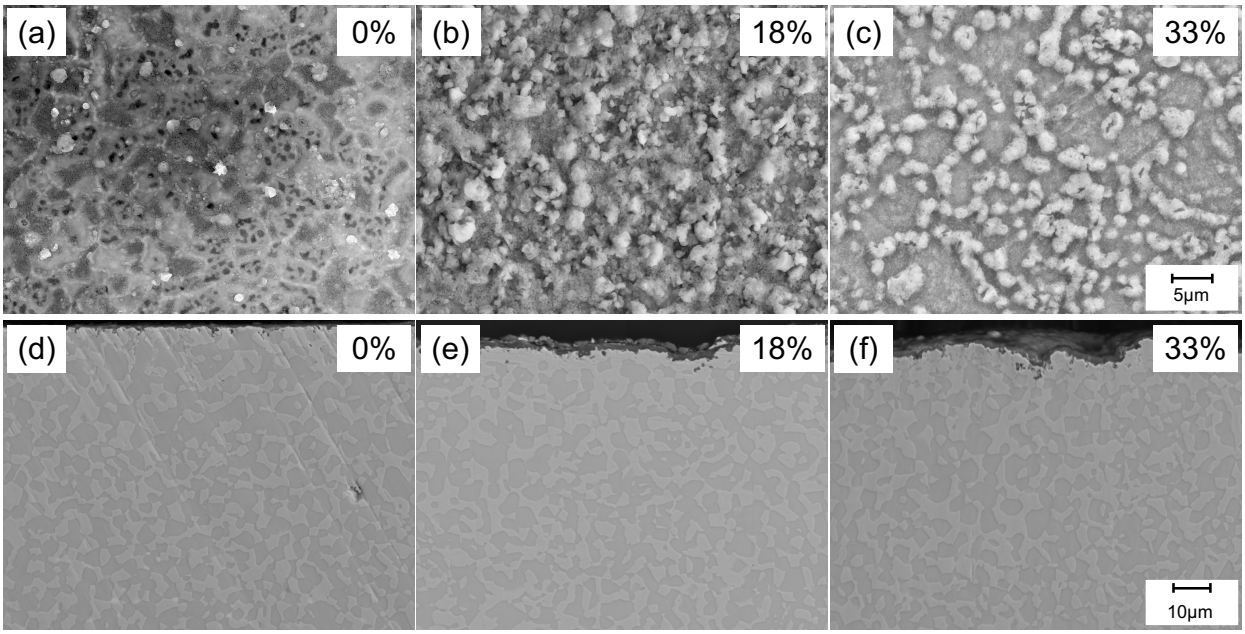

Figure 4.54 BSD SEM of surface and cross-section of sample B in dry air (a) (d), 18% H_2O humidity (b) (e), and 33% H_2O humidity (c) (f) after 2h oxidation exposure

Figure 4.55 highlights the surfaces and cross-sections of sample B after 20h exposure in the three humid air conditions.

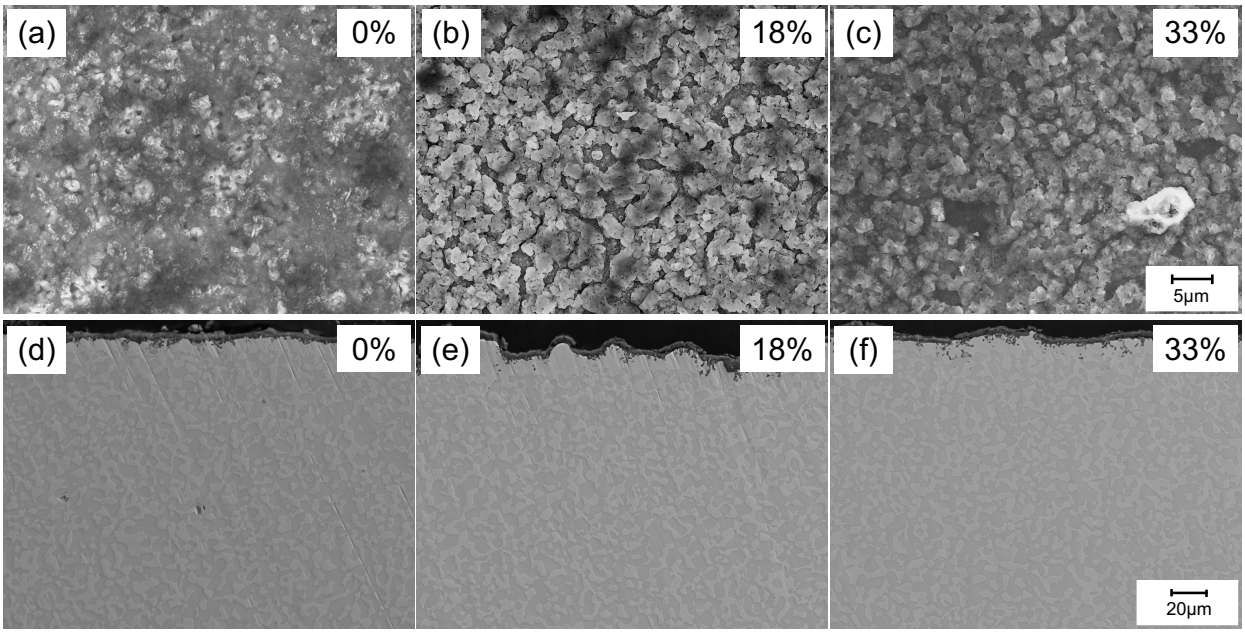

Figure 4.55 BSD SEM of surface and cross-section of sample B in dry air (a) (d), 18% H_2O humidity (b) (e), and 33% H_2O humidity (c) (f) after 20h oxidation exposure

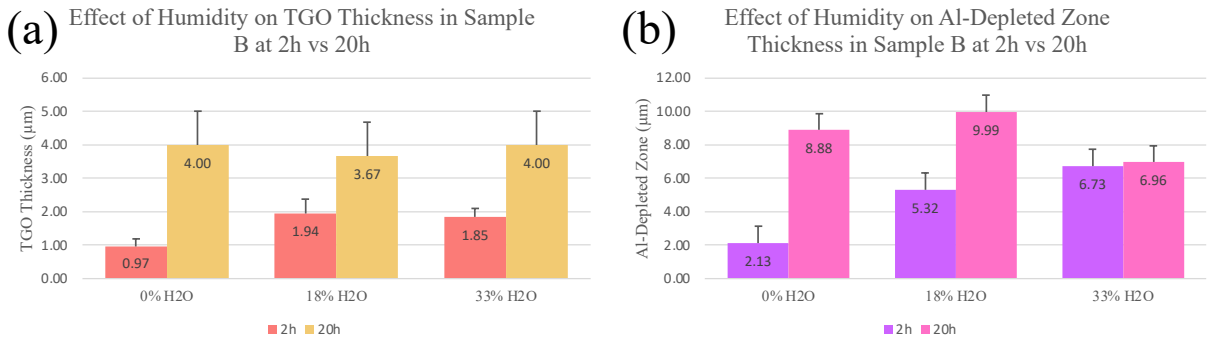

Figure 4.56 Effect of Humidity on TGO Thickness (a) and Al-depletion (b) in sample B for 0%, 18% and 33% H_2O in 2h and 20h oxidation

Figure 4.56 summarises the effect of humidity on TGO thickness (a) and Al-depletion (b) in sample B over 2h and 20h oxidation exposures. In 2h exposure, Figure 4.54 (e) and (f), and Figure 4.56 show the TGO thickness doubles in the presence of water compared to dry air as more transient oxides form before a transforming into protective α-Al_2O_3 (Table 10).

After 20h oxidation, Figure 4.56 (a) shows the TGO thicknesses across the humidity conditions is comparable, indicating that after initial TGO formation, α-Al_2O_3 forms, and growth is stable. While aluminum consumption is initially highest in the 33% humidity condition after 2h, the preferential formation of alumina that undergoes a phase transformation protects the alloy from further oxidation after 20h while the dry air and 18% humidity TGOs are less protective. Adhesion of the TGO decreases in the presence of humidity with delamination seen in 18% H_2O and 33% H_2O 20h oxidation. In Figure 4.56 (b), we see that the difference in aluminum consumption between the two exposure times is smallest in 33% H_2O, indicating that this condition formed the most dense and protective alumina layer, slowing the continued oxidation of the alloy. As with sample A, Table 10 shows that transient species on the surface of the TGO decrease with prolonged exposure and are most pronounced in 18% humidity.

Table 10 XRD results for sample B in 0%, 18%, and 33% H_2O (%vol) in 2h and 20h oxidation with differences in identified species bolded

0%	18%	33%
2h		
Al_2O_3	Ni_2Y	Al_2O_3
$CoAl_2O_4$	Al_2O_3	Ni_2Y
$AlYO_3$	$CoAl_2O_4$	**$NiAl_2O_4$**
	$NiAl_2O_4$	$AlYO_3$
20h		
Al_2O_3	Al_2O_3	Al_2O_3
$NiAl_2O_4$	Ni_2Y	**$CoAl_2O_4$**
$AlYO_3$	$CoAl_2O_4$	$NiAl_2O_4$
$Y_3Al_5O_{12}$	**$AlYO_3$**	Ni_2Y
Ni_2Y	**$Y_3Al_5O_{12}$**	

4.5.3 Sample C

Sample C introduces tantalum to the alloy composition. Figure 4.57 highlights the surfaces and cross-sections of sample C after 2h exposure in the three humid air conditions. In Figure 4.57 (a) and (d) we see that a uniform TGO has not formed in dry air after 2h exposure. Sample C has a slower growing TGO compared to samples A and B, but grows more α-Al_2O_3 than the other two compositions as seen in Table 11.

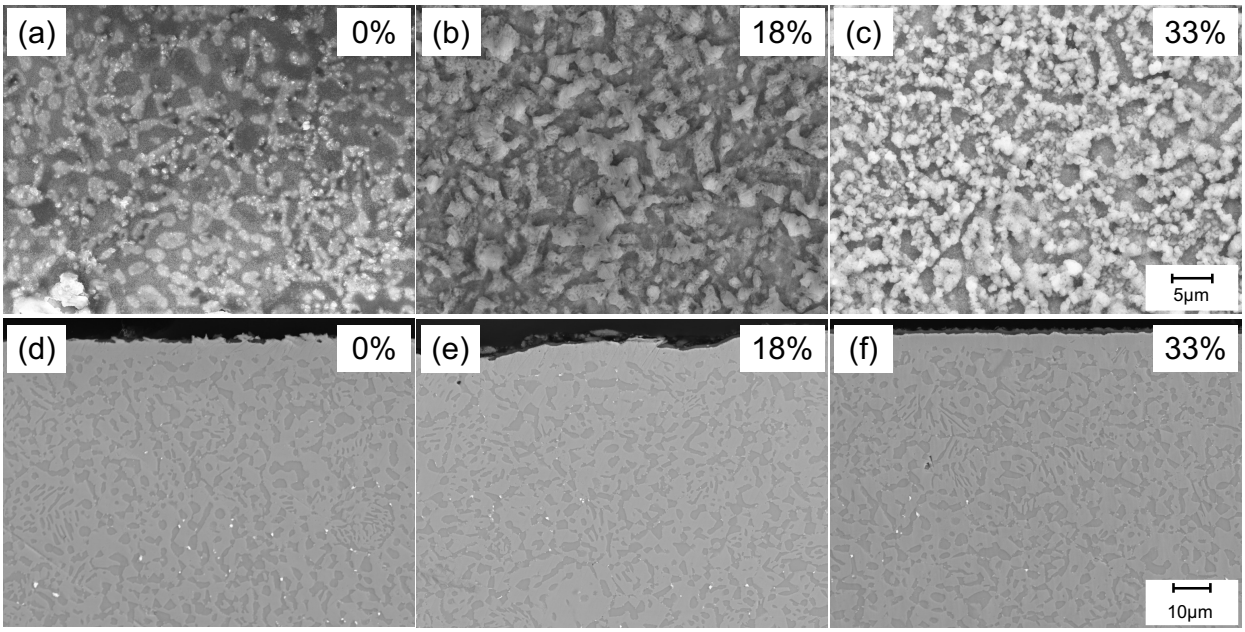

Figure 4.57 BSD SEM of surface and cross-section of sample C in dry air (a) (d), 18% H_2O humidity (b) (e), and 33% H_2O humidity (c) (f) after 2h oxidation exposure

Figure 4.58 highlights the surfaces and cross-sections of sample C after 20h exposure in the three humid air conditions. Spinel coverage of the surface reduces with extended exposure in Figure 4.58, undergoing a solid-state transformation on the surface as a protective TGO forms between the alloy and the free surface, reducing the upward diffusion of nickel, cobalt, and chromium. TGO adhesion is poor in this composition, but improves with increasing humidity and oxidation time from Figure 4.58 (d), (e), and (f). Oxide peg formation increases with increasing humidity and oxidation time. In Table 11 no transient species are identified in any of the specimens, highlighting the effect of tantalum in producing a stable alumina early in oxidation.

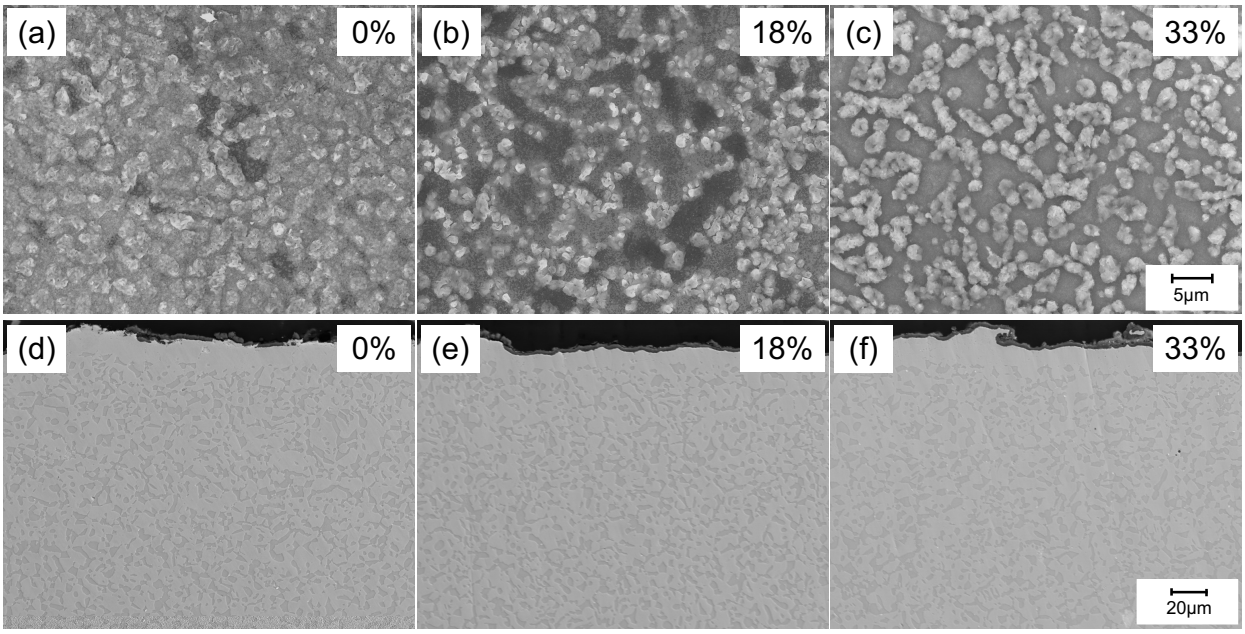

Figure 4.58 BSD SEM of surface and cross-section of sample C in dry air (a) (d), 18% H_2O humidity (b) (e), and 33% H_2O humidity (c) (f) after 20h oxidation exposure

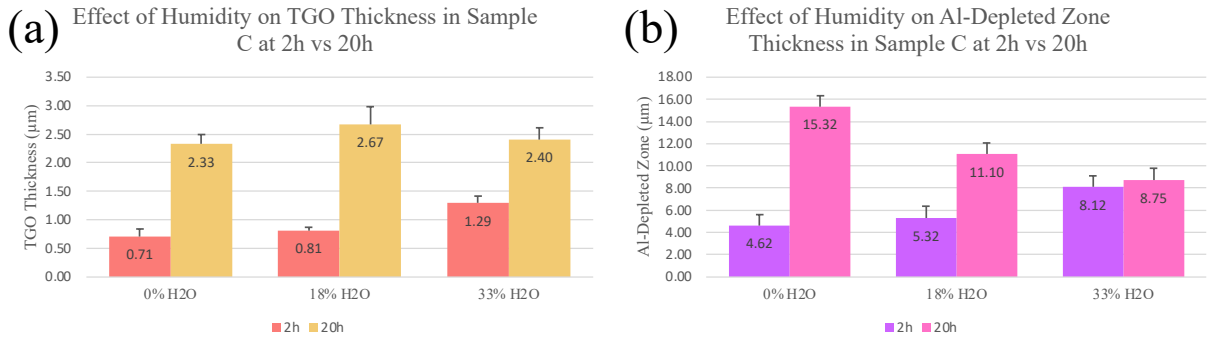

Figure 4.59 Effect of Humidity on TGO Thickness (a) and Al-depletion (b) in sample C for 0%, 18% and 33% H_2O in 2h and 20h oxidation

Figure 4.59 summarises the effect of humidity on TGO thickness (a) and Al-depletion (b) in sample C over 2h and 20h oxidation exposures. TGO thickness increases with time, with 18% H_2O environment producing the thickest TGO after extended exposure in Figure 4.58 (e). The rate of TGO growth remains constant between 0% and 18% humidity, as neither grow a uniform protective oxide as seen in Figure 4.58 (a) and (b) where spallation is visible on the surface. This is seen as well in Figure 4.59 (b) where the Al-depletion is highest in the 20h exposures. In 33%

H_2O, a similar trend to the previous compositions is seen in Figure 4.59 (b), where the rate of aluminum consumption is lowest between the two exposure times, indication that the most protective oxide scale is formed in 33% H_2O.

Table 11 XRD results for sample C in 0%, 18%, and 33% H_2O (%vol) in 2h and 20h oxidation with differences in identified species bolded

0%	18%	33%
2h		
Al_2O_3	Al_2O_3	Ni_3Al
Co_2NiO_4	Ni_3Al	Al_2O_3
$AlYO_3$	$NiAl_2O_4$	$NiAl_2O_4$
Ni_3Al	Co_2NiO_4	**$Y_3Al_5O_{12}$**
	$Y_3Al_5O_{12}$	
20h		
Al_2O_3	Al_2O_3	Al_2O_3
Ni_3Al	$NiAl_2O_4$	$NiAl_2O_4$
$NiAl_2O_4$	Ni_3Al	**Co_2NiO_4**
	Co_2NiO_4	Ni_3Al

4.5.4 Sample D

Sample D excludes tantalum and introduces hafnium and silicon to the alloy composition.

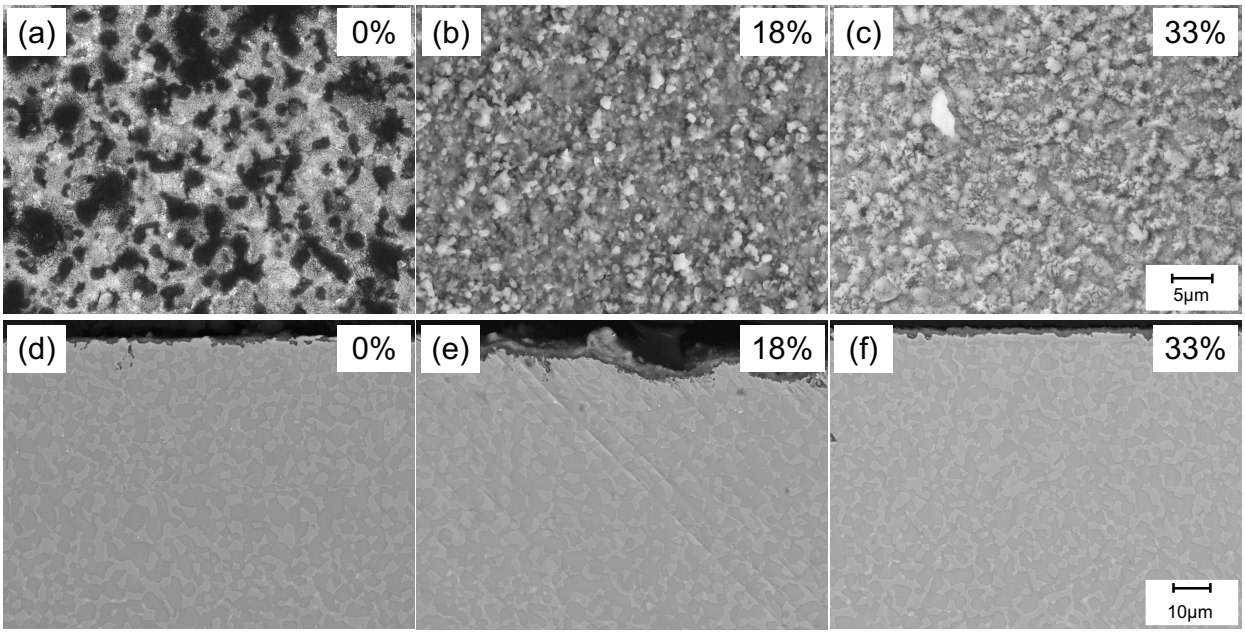

Figure 4.60 highlights the surfaces and cross-sections of sample D after 2h exposure in the three humid air conditions. Table 12 also shows large spinel coverage as seen in Figure 4.60 (a) and (b) for the 0% and 18% humidity treatments after 2h exposure, and preferential alumina formation in 33% H_2O. Fewer transient species are identified on the surface than other compositions, highlighting the benefits of hafnium and silicon additions to alumina phase transformation. Table 12 shows an increase in hafnia formation in 18% and 33% H_2O, indicating that the alumina formation is delayed in the presence of water in this composition.

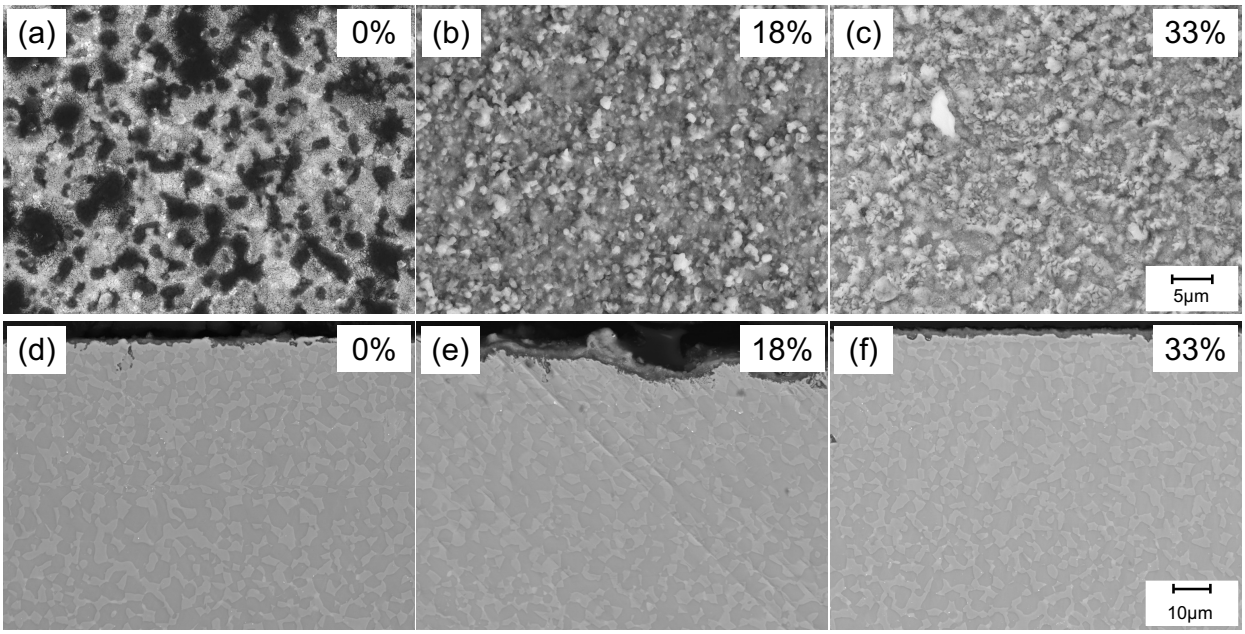

Figure 4.60 BSD SEM of surface and cross-section of sample D in dry air (a) (d), 18% H_2O humidity (b) (e), and 33% H_2O humidity (c) (f) after 2h oxidation exposure

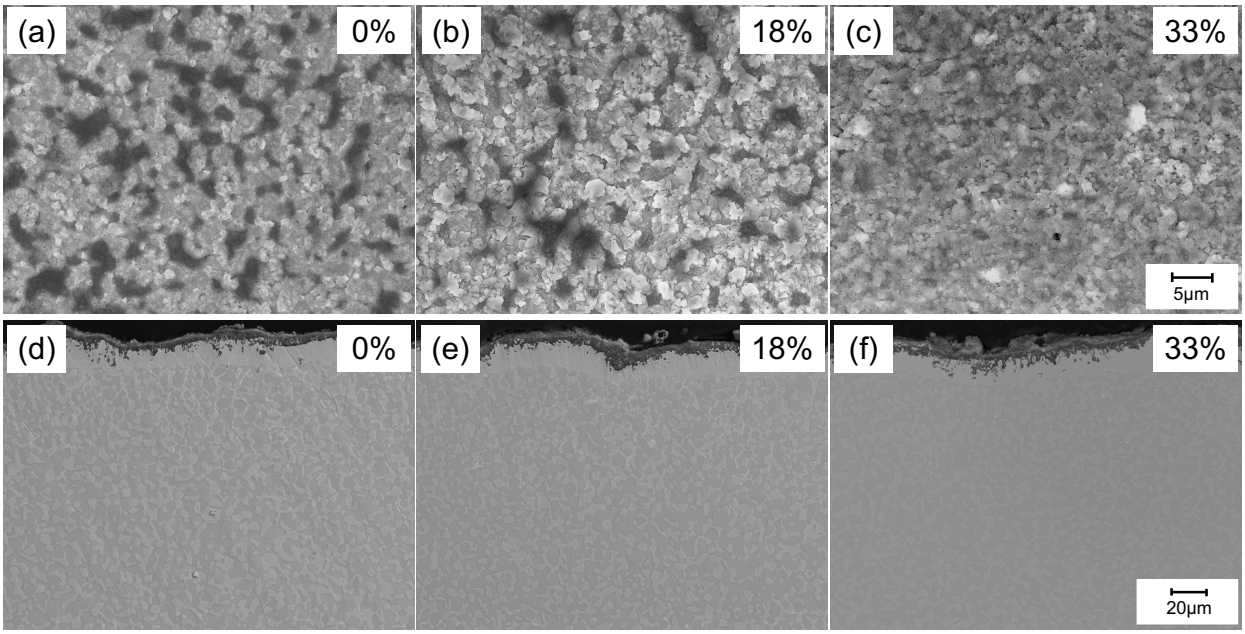

Figure 4.61 highlights the surfaces and cross-sections of sample D after 20h exposure in the three humid air conditions. Sample D follows the same trends in TGO growth in the presence of water vapor as the other compositions, however, spall in the TGO is present in all conditions (Figure 4.61 (a), (b), and (c)), indicating poor adhesion. This is confirmed with XRD in Table 12 where the substrate is identified in all conditions. This may be due to increased stresses between the oxide and alloy as a result of hafnium and silicon oxides within the TGO. Transient species are identified in the 18% H_2O condition in Table 12. Void formation in the TGO and on the surface in

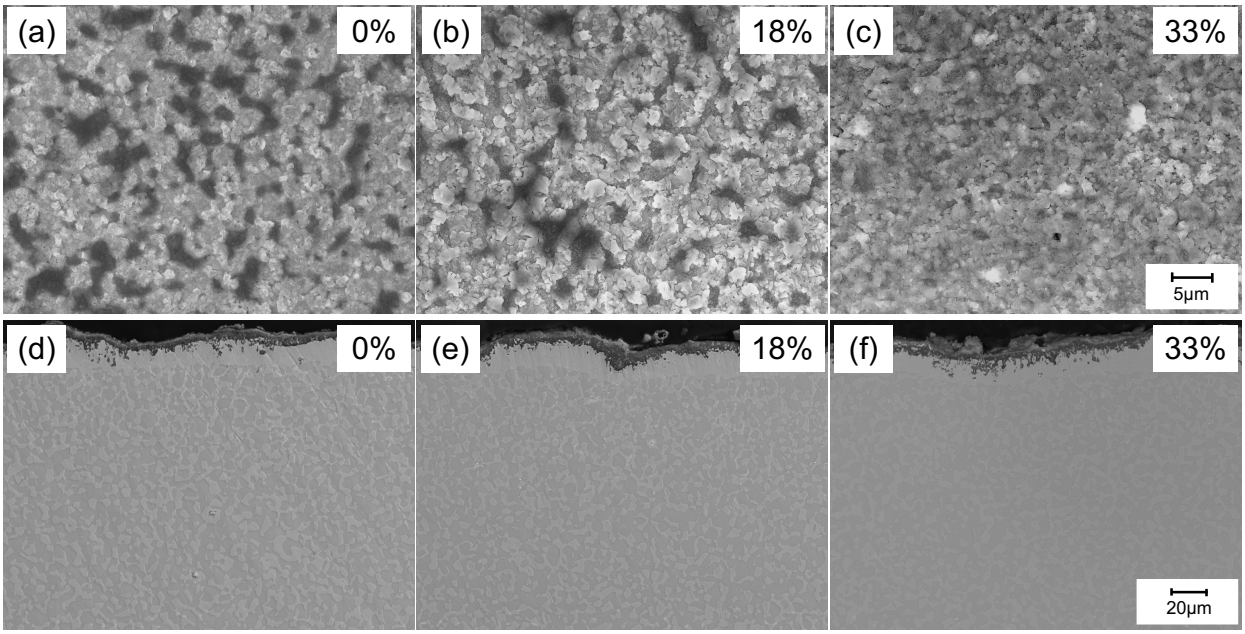

Figure 4.61 (a), (b), and (c) is considerably less than in samples A and B, highlighting the benefits of hafnium and silicon in uniform alumina formation.

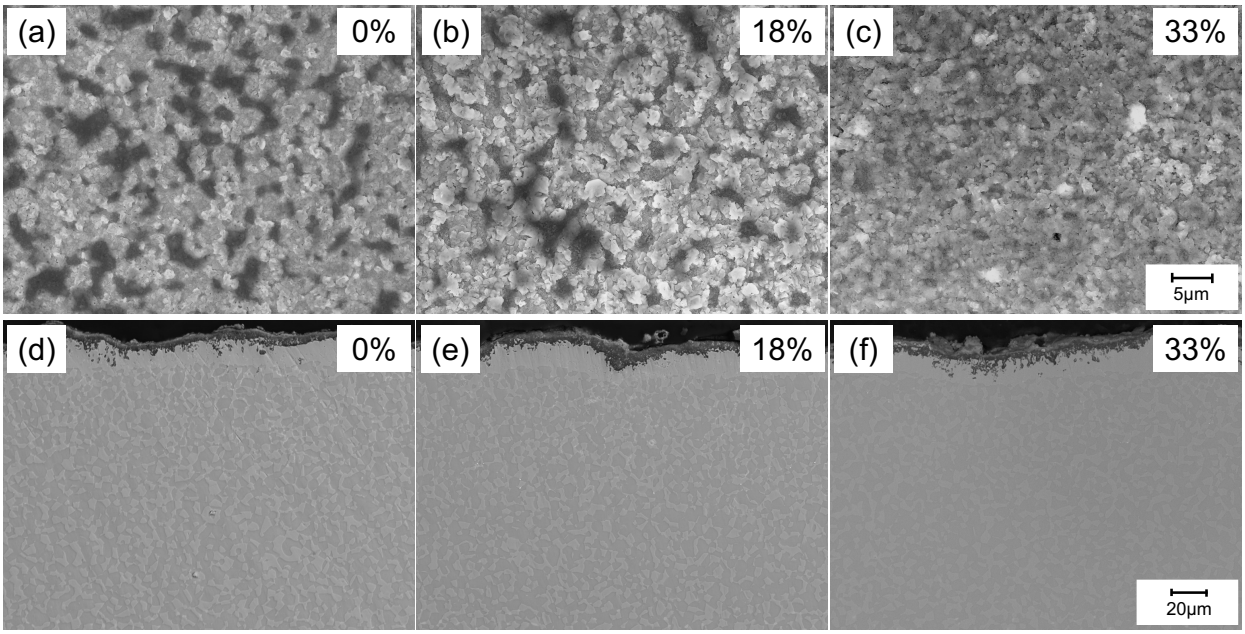

Figure 4.61 BSD SEM of surface and cross-section of sample D in dry air (a) (d), 18% H_2O humidity (b) (e), and 33% H_2O humidity (c) (f) after 2h oxidation exposure

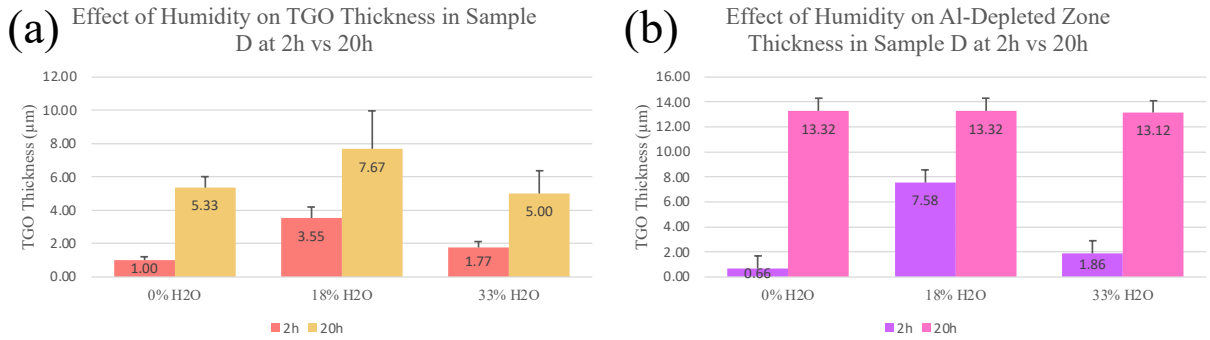

Figure 4.62 Effect of Humidity on TGO Thickness (a) and Al-depletion (b) in sample D for 0%, 18% and 33% H_2O in 2h and 20h oxidation

Figure 4.62 summarises the effect of humidity on TGO thickness (a) and Al-depletion (b) in sample D over 2h and 20h oxidation exposures. Trends in Al-depletion follow those of the other compositions for 2h oxidation exposure. The low aluminum consumption in dry air indicates that protective oxide formation is slower than in the other compositions. After 20h oxidation, alumina formation increases across all oxidation conditions. In Figure 4.62 (b) we see a large rate of aluminum consumption in the 33% H_2O condition, unlike the other compositions, indicating that the TGO is less protective. Significant rumpling is observed across all humidities compared to 2h exposure in

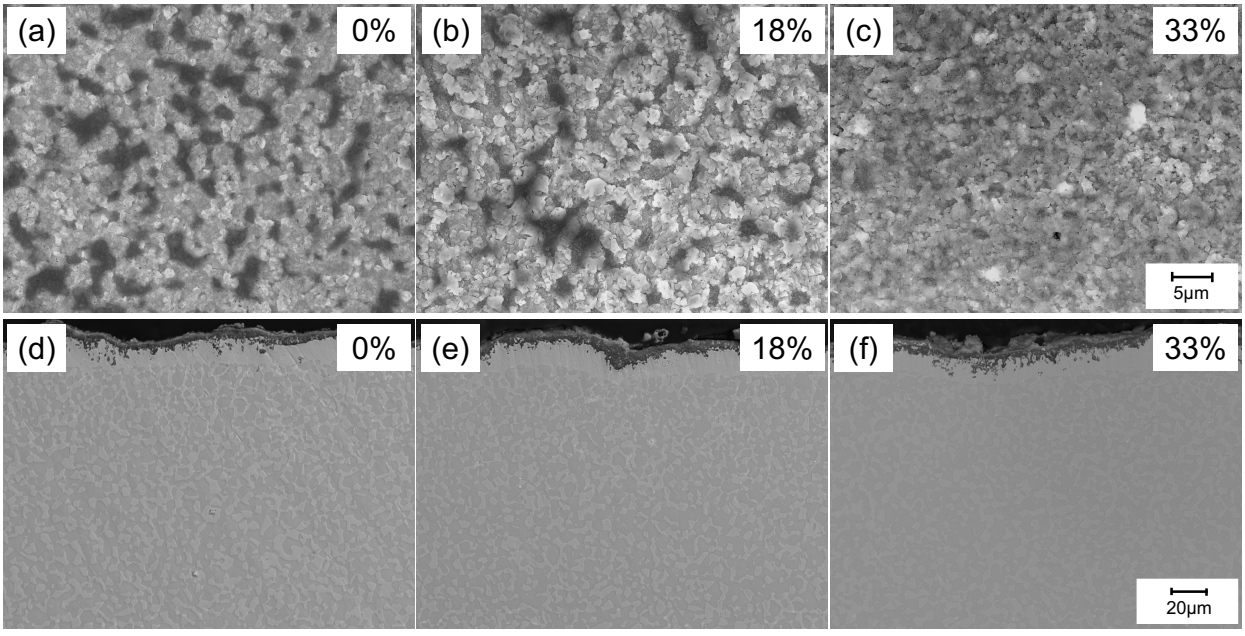

Figure 4.61 (d), (e), and (f). TGO thickness and rumpling are the largest in 18% H_2O oxidation for both 2h and 20h oxidation and also shows the greatest Al-depletion after 2h. Oxide peg formation increases with increasing humidity and oxidation exposure in Figure 4.61.

Table 12 XRD results for sample D in 0%, 18%, and 33% H_2O (%vol) in 2h and 20h oxidation with differences in identified species bolded

0%	18%	33%
2h		
$NiCo_2O_4$	$NiAl_2O_4$	Ni_3Al
Al_2O_3	Al_2O_3	Al_2O_3
$SiCo_2O_4$	HfO_2	$NiAl_2O_4$
$NiAl_2O_4$	Ni_3Al	HfO_2
$NiCr_2O_4$	**$AlYO_3$**	YSi_2
HfO_2	**YSi_2**	
20h		
Al_2O_3	Al_2O_3	Al_2O_3
Ni_3Al	$NiAl_2O_4$	Ni_3Al
HfO_2	**Ni_2Y**	$NiAl_2O_4$
$NiAl_2O_4$	HfO_2	HfO_2
YSi_2	Ni_3Al	YSi_2
SiO_2		

Chapter 5 Discussion of Results

In this section, results are further discussed to highlight the trends in oxidation behaviour between humid environments and alloy compositions. Oxidation mechanisms are proposed and conclusions regarding alloy performance are drawn. The parameters of discussion are quick and uniform α-Al_2O_3 TGO formation, spinel coverage and thickness, internal oxidation of the bond coat alloy, aluminum consumption in TGO formation, TGO adhesion, void presence, and alloy rumpling. α-Al_2O_3 TGO formation, adhesion, and spinel formation are quantified by SEM imaging and XRD relative peak height. Internal oxidation and aluminum consumption in the TGO formation is quantified using EDS mapping of the element depletion zones. Rumpling and void formation are also indicators of high aluminum consumption in TGO formation and inhomogeneous oxidation, and are observed with SEM imaging.

5.1 Effect of Humidity of Oxidation

5.1.1 Dry air oxidation

In all compositions, the dry air condition forms the thinnest TGO after 2h (Figure 4.51 (d), Figure 4.54 (d), Figure 4.57 (d), and Figure 4.60 (d)), indicating that oxide formation is the slowest of the three humidity conditions. However, α-Al_2O_3 is the dominant alumina species on the surface from Figure 4.51 (a), Figure 4.54 (a), Figure 4.57 (a), and Figure 4.60 (a). After 20h, the dry air samples show the largest TGO growth rates, meaning that the oxide formed in the initial stages of oxidation is not protective. This is corroborated by the large presence of spinels seen on the surface and from XRD analysis in Table 9, Table 10, Table 11, and Table 12. Oxide spall is seen in all samples (Figure 4.52 (a), Figure 4.55 (a), Figure 4.58 (a), and Figure 4.61 (a)), as well as large Al-depleted zones after 20h. Voids are seen between the equiaxed and columnar alumina grains in samples A and B in Figure 5.1 as found by Li et al [20] after 150h of thermal cycling at 1050 °C for NiCoCrAlY bond coat alloy. Voids may not have been seen in the other compositions after a comparatively short exposure compared to Li et al. due to the beneficial effects of Ta, Hf, and Si in slowing the upward diffusion of Al to the surface. The oxides formed in dry conditions show dense spinel coverage on the surface after 20h.

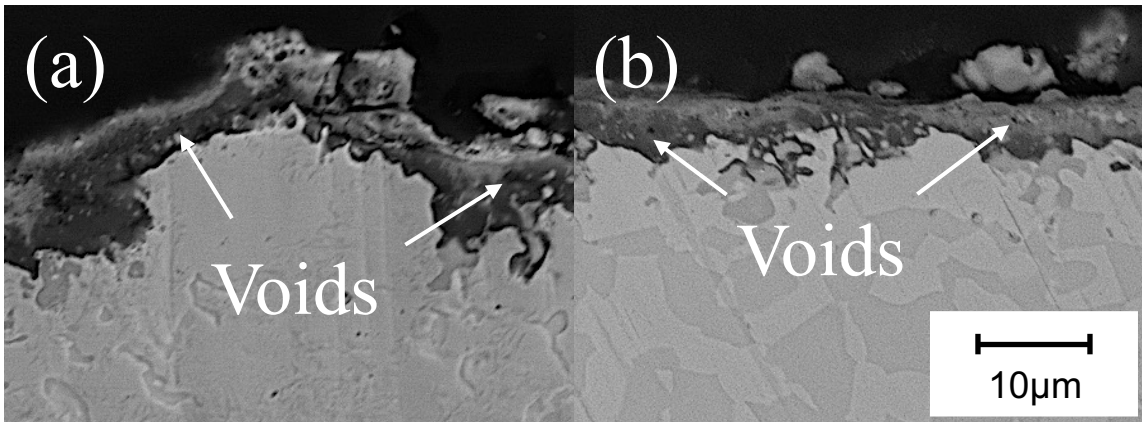

Figure 5.1 Intergranular voids in sample A (a) and sample B (b) after 20h oxidation in dry air

5.1.2 Air + 18% H_2O (%vol)

In 18% H_2O, all samples show an increase in initial oxide formation compared to dry air from Figure 4.53, Figure 4.56, Figure 4.59, and Figure 4.62. This confirms the findings from Haynes et al. [43] who studied the effect of air + 10% H_2O on NiCoCrAlYHfSi alloy at 1100 °C in cyclic oxidation, and Fontana et al. [32] who studied H_2 + 10% H_2O on FeCrAlRe alloy at 800 °C. Surface aluminas are identified as θ and γ phases after 2h, corroborating the findings of Gleeson and Reed [8], [12] that water vapor delays the phase transformation of transient aluminas to protective α-Al_2O_3. After 20h, the alumina has undergone the phase transformation to α-Al_2O_3, creating large stresses at the alloy-oxide interface due to volume contraction and causing spall in all samples (Figure 4.52 (b), Figure 4.55 (b), Figure 4.58 (b), and Figure 4.61 (b)). The aluminum depletion is highest in this condition for 2h and 20h exposures, corroborating the delay in phase transformation, and allowing more oxygen to penetrate the non-protective oxide layer. More spinel is seen on the surface than in dry air, as reported by Zhou et al. for NiAl with air + 15% H_2O at 950 °C, and Sullivan et al. for NiCoCrAlYHfSi in humid air at 1125 °C [29], [47]. Li et al. [20] showed that alumina nucleation is slowed in lower oxygen partial pressure (P_O) leading to faster aluminum diffusion fluxes through the oxide grain boundaries to the surface, creating vacancies and voids at the alloy-oxide interface in NiCoCrAlY alloy. In this condition, voids were seen on the surface of the TGO (Figure 4.52 (e), Figure 4.55 (e), Figure 4.58 (e), and Figure 4.61 (e)) and at the equiaxed/columnar grain boundaries in Figure 5.2, acting as fast diffusion paths for the continued oxidation of the bond coat [20]. The fast and continued upward diffusion of aluminum results in

more rumpling of the bond coat alloy, which leads to spall of the TGO and ceramic top coat in application. Alloy rumpling was the worst in the 18% H_2O.

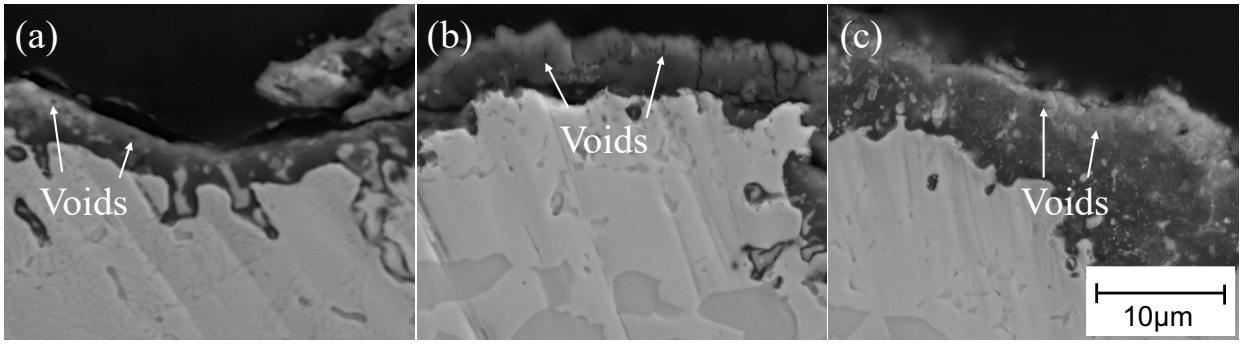

Figure 5.2 Intergranular voids in sample A (a), sample B (b), and sample D (c) after 20h oxidation in air + 18% H_2O

5.1.3 Air + 33% H_2O (%vol)

In the 33% H_2O condition, spinel coverage increases with humidity in the 2h oxidation exposures seen in Figure 4.51 (c), Figure 4.54 (c), Figure 4.57 (c), and Figure 4.60 (c). This is in-line with what was found by Sullivan et al. [47] when studying air with 0%, 18%, 30% and 50% H_2O in CoNiCrAlY and NiCoCrAlY bond coats for 0-5h isothermal oxidation at 1125 °C. Fewer surface voids were seen after 20h compared to the 18% H_2O condition for all compositions, and a reduction in spinel surface coverage was seen for all samples in Figure 4.52 (c), Figure 4.55 (c), Figure 4.58 (c), and Figure 4.61 (c). Li et al. [20] proposed that higher levels of water vapor resulted in higher P_O, where interface diffusion of oxygen is faster than the rate of oxygen transport to the interface, driving the nucleation of oxide grains. The oxygen transport through the TGO leads to new columnar alumina forming at the alloy-oxide interface, protecting the alloy from further oxidation. This is seen in all compositions, where the TGO is thinner at initial formation than the 18% H_2O condition and remains thinner after 20h for compositions that do not experience significant spall (Figure 4.53, Figure 4.56, Figure 4.59, and Figure 4.62). Li et al. observed this behaviour in two studies on NiCoCrAlY and CoNiCrAlHf in air + 25% H_2O at 1050 °C [20], [17]. The faster nucleation of alumina grains results in uniform stresses in the TGO which result in less cracking of the oxide and rumpling of the alloy as protective alumina is quick to slow the upward diffusion of aluminum. The dense equiaxed alumina top layer reduces the outward diffusion of aluminum compared to 18% H_2O. Fewer voids are seen on the surface at 33% H_2O, and no voids are seen at

the equiaxed/columnar alumina grain boundaries in the TGO in Figure 4.52 (e), Figure 4.55 (e), Figure 4.58 (e), and Figure 4.61 (e). Li et al. propose that voids are annihilated in this condition as oxygen transport through the scale reacts with evaporated aluminum inside the void, forming new alumina to fill the void. Internal oxidation increased with humidity as found by Li et al. [17] and was identified by an increase in oxide peg formation.

5.2 Effect of Composition on Oxidation

5.2.1 Base Composition

The base composition (sample A) spinel coverage is high (Figure 4.51 (a)) and increases with extended exposure time (Figure 4.52 (a)) in dry air oxidation. The TGO growth rate is largest in the dry air condition and the aluminum consumption rate is large for all humidity conditions compared to the other compositions indicating that the TGO is not protective, and alumina continues to quickly diffuse to the surface. Surface voids increase with humidity and oxidation time, while voids at the equiaxed/columnar alumina grain boundaries decrease with increasing humidity as seen by Li et al. [20]. In extended oxidation exposure, spinel coverage decreases with increasing humidity, indicating that water vapor promotes alumina formation in early oxidation. Transient Ni_2Y is identified in both humidity conditions and is most prevalent in air + 18% H_2O. TGO adhesion is good in this composition, with no visible spallation in any of the oxidation conditions. Large aluminum consumption and thick oxide scale indicate that the TGO is not protective and alumina continues to quickly diffuse to the surface.

5.2.2 Effect of Cobalt

The inclusion of cobalt slows initial oxide nucleation (Figure 5.3 (a)) and promotes the formation of α-Al_2O_3 over spinel as proposed by Reed et al. [8], where a CoO scale forms before NiO and allows for the more uniform growth of alumina. Fewer voids are seen at the equiaxed/columnar alumina grain boundaries with extended exposure compared to the base composition in all humidity conditions. The TGO growth and aluminum depletion rates also reflect an improvement in oxide protection (Figure 5.3 (a), (b)) compared to the base composition. As in dry air, the inclusion of cobalt in air + 18% H_2O slows oxide nucleation on the surface (Figure 5.4 (a)). In air + 33% H_2O, the TGO growth rates mirror the base composition (Figure 5.5 (a)), however, the aluminum depletion rate in sample B is much lower (Figure 5.5 (b)), indicating that cobalt is

beneficial to the early formation of alumina on the alloy surface compared to the base composition. Fewer voids are seen on the surface compared to the base composition with extended exposure (Figure 4.55) in all humidity conditions.

5.2.3 Effect of Tantalum

In dry air, tantalum inclusion results in the slowest oxide nucleation rate and the slowest growth rate (Figure 5.3 (a)). However, a uniform oxide does not form after extended exposure for this composition (Figure 4.58 (a)), drawing more aluminum to the surface from the alloy (Figure 5.3 (b)). The oxide grown at this composition shows the lowest amount of spinel coverage as found by Hu et al. [30] (Figure 4.58) and the alloy has the least rumpling of the four compositions, indicating lower internal stresses, and slower upward diffusion of aluminum to the surface as reported by Huang et al. [33]. Tantalum results in the slowest oxide formation in all humidity conditions (Figure 5.3 (a), Figure 5.4 (a), Figure 5.5 (a)). In air + 18%H_2O, TGO growth and aluminum depletion in Figure 5.4 (a) and (b) show a small increase from the 2h exposure in dry air. In 20h oxidation, the aluminum depletion rate decreases in air + 18%H_2O (Figure 5.4 (b)) compared to dry air, indicating that the oxide scale is more protective of the alloy. TGO adhesion improves with humidity but is relatively poor compared to the other compositions as spall is seen in the 20h dry air and air + 18%H_2O exposures (Figure 4.58 (c). After 20h oxidation in air + 33% H_2O, the inclusion of tantalum results in the slowest growing oxide scale (Figure 5.5 (a)) with a small aluminum depletion increase once the protective oxide has formed (Figure 5.5 (b)). This is favourable and shows the best performance of the four compositions in high-temperature humid environment oxidation. Tantalum effectively reduces the upward diffusion of alumina in the bond coat alloy and favours α-Al_2O_3 growth in early oxidation. This composition consistently shows the least amount of spinels and voids on the sample surface (Figure 4.58 (a), (b), (c)), as well as the least rumpling and no intergranular voids in the cross-section (Figure 4.58 (d), (e), (f)), indicating homogenous oxidation.

5.2.4 Effect of Hafnium and Silicon

The inclusion of hafnium initially forms a hafnia rich layer (Figure 4.60 (a)) on the surface over which alumina grows with extended exposure as reported by Li et al. [17]. Silicon has also been reported to form silica on the surface in early oxidation by Huang et al. [33]. From the XRD results in Table 12 we see that hafnia is the more abundant oxide found in 2h and 20h oxidation. Silica

was only identified in the 20h dry air condition, though the volume fraction may be very low or the phase may be amorphous in the other specimens. Both oxides are reported to be beneficial to oxidation resistance by forming an initial oxide scale, slowing the upward diffusion of aluminum through the alloy. In Figure 5.3 (a), Figure 5.4 (a), and Figure 5.5 (a) the inclusions of hafnium and silicon result in fast oxide scale formation, however the TGO growth rate of this composition is the highest of the four compositions, indicating that a dense and protective α-Al_2O_3 layer is not quick to form in early oxidation. Figure 5.3 (b), Figure 5.4 (b) show that the aluminum depletion rates for dry air and air + 18% H_2O are highest of all four compositions for these oxidation conditions. Li et al. [17] and Shuting et al. [34] report that when HfO_2 and SiO_2 appear in large quantities, they can create internal stresses in the TGO that promote cracking. This is seen in Figure 4.61 (a) and (b) where spallation of the TGO is seen in air and air + 18% H_2O after 20h oxidation. Alloy rumpling is improved compared to the base and cobalt compositions (Figure 4.61 (d), (e), (f)), and fewer voids are seen at the equiaxed/columnar alumina grain boundaries. Spinel coverage of the surface and surface voids are also fewer compared to the base compositions (Figure 4.61 (a), (b), (c)). Sample D grows the thickest oxide in air + 18% H_2O of the four compositions in the three humidity conditions. The inclusion of silicon did increase the volume fraction of the β-phase, as reported by Shuting et al. [34], but was not as active in the TGO formation as hafnium.

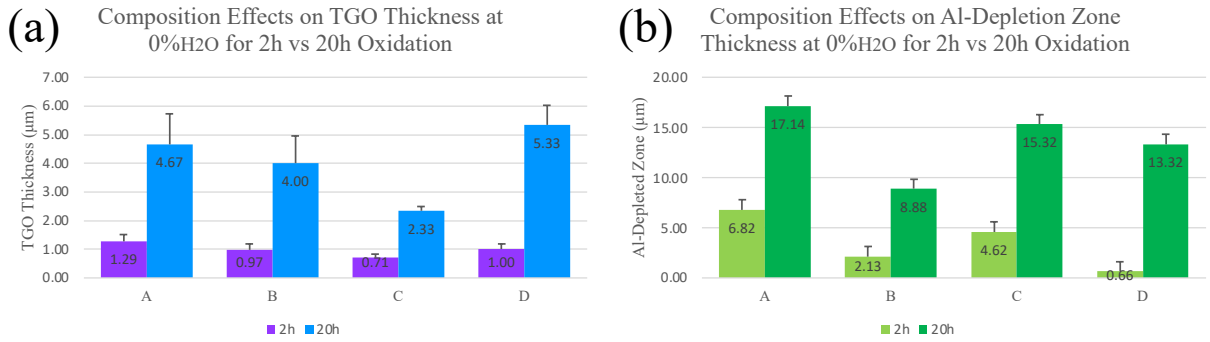

Figure 5.3 Composition Effects on TGO Thickness (a) and Al-depletion (b) at 0% H_2O for 2h and 20h oxidation

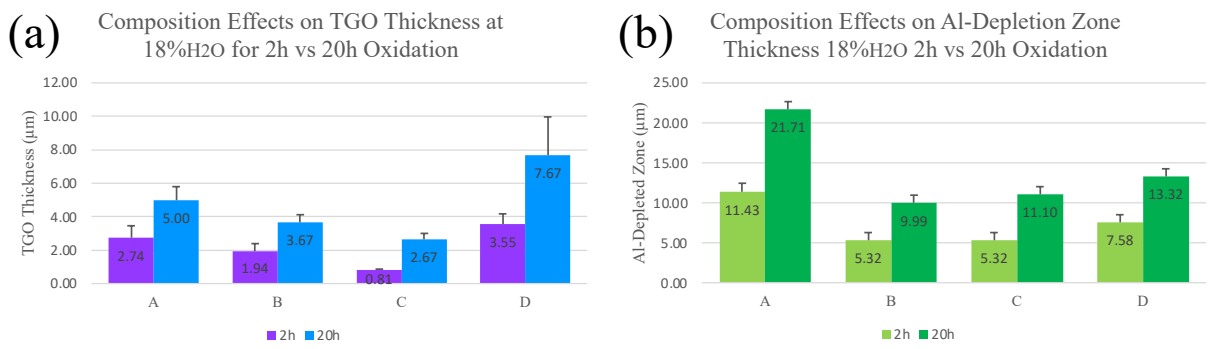

Figure 5.4 Composition Effects on TGO Thickness (a) and Al-depletion (b) at 18% H_2O for 2h and 20h oxidation

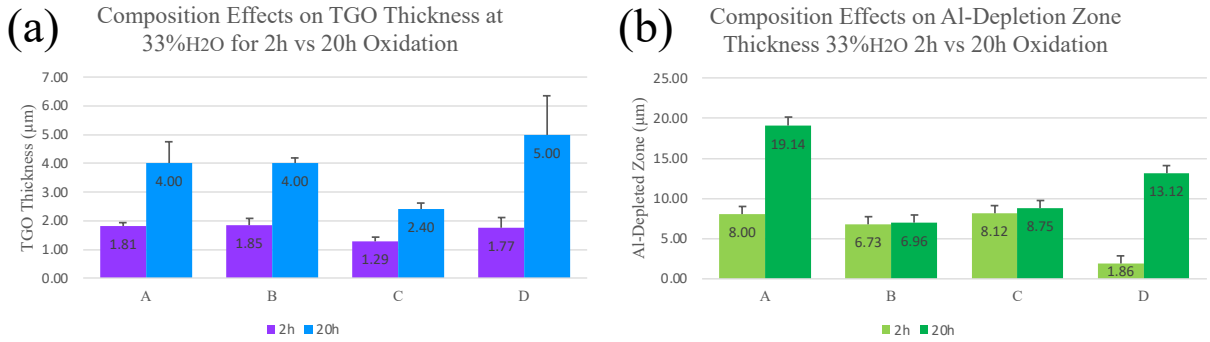

Figure 5.5 Composition Effects on TGO Thickness(a) and Al-depletion (b) at 33% H_2O for 2h and 20h oxidation

Chapter 6 Conclusions

6.1 Novelty

Previous investigations on the effects of water vapor on high-temperature oxidation behaviour in MCrAlY bond coat materials have reported conflicting results due to variability in bond coat alloy composition and experimental conditions. For instance, Sullivan et al. [13] reported that spinel coverage increases with humidity for 0-5h isothermal exposures on NiCoCrAlY and CoNiCrAlY alloys, while Li et al. [17] reported that air + 25% H_2O resulted in less surface spinel on CoNiCrAlHf than dry air after 300h and 600h cyclic oxidation. Table 5 in section 2.2.2 summarizes the materials and oxidation parameters found in literature. Temperature, water vapor content, and oxidation time are not consistent across the studies making it difficult to compare and understand the effects of each alloying element and the overall oxidation mechanisms at work.

A comparative study under the same oxidation conditions, focusing on the bulk alloy oxidation behaviour, has not been conducted in the literature. In this work, substrate and top coat interface effects are negated, as well as the effect of the alloy deposition method. This allows for better understanding of the alloy oxidation behaviour and the influence of the reactive elements. In varying one to two elements in each composition, a comparison of performance can be more confidently made than what is seen in the literature. Studying humidities that represent the conditions found in application when using high-hydrogen fuels such as syngas and steam injection better represents the behaviour expected in-situ, and provides more relevant data to the application context. The 2h oxidation exposure time was chosen to more closely study the transient TGO formation and the effect of water in oxide and spinel nucleation. This may act as a basis to investigate the validity of implementing steam pre-treatments to the alloy to form a dense alumina before thermal cycling. 20h isothermal oxidation is used to study the ongoing oxidation behaviour of the four compositions and draw conclusions pertaining to performance.

6.2 Main Conclusions

In this study, NiCrAlY, NiCoCrAlY, NiCoCrAlTaY, and NiCoCrAlHfSiY were oxidized at 1100°C in dry air + 0%, 18%, and 33% water by volume in a 1atm environment to simulate conditions expected in engines using high hydrogen fuels. Oxidation was done for 2h and 20h to observe transient oxide formation behaviour.

From this study, we see that the air + 18% H_2O presents the worst oxidation conditions for MCrAlY bond coat alloys as the presence of water vapor promotes oxide formation in early oxidation, resulting in a thicker, non-protective TGO. Oxide nucleation was delayed, allowing for the formation of more spinels and a faster aluminum diffusion flux to the surface. This increase in diffusion flux led to rumpling of the alloy which is detrimental to TBC lifetime in application, and to the formation of vacancies and voids at the alloy-oxide interface that act as fast diffusion paths for oxygen ingress, leading to heightened internal oxidation. The phase transformation from transient θ and γ to α-Al_2O_3 is delayed, resulting in a thicker TGO and increase in internal oxidation. The thicker TGO also undergoes a 14.3% volume reduction during phase transition, leading to cracks and spall of the TGO.

The inclusions of tantalum, hafnium, and silicon are found to be beneficial to oxidation resistance in MCrAlY bond coat alloys in the presence of water vapour. Of the four compositions, tantalum slowed the aluminum consumption in the formation of the TGO. Tantalum inclusion proved the most effective at promoting the formation of α-Al_2O_3 in early oxidation, producing an oxide scale with no voids and minimal rumpling, however, TGO adhesion was lowest in this composition at 18% H_2O . In the presence of water vapour, the inclusion of tantalum in bond coat composition effectively forms a protective TGO with prolonged exposure, and adhesion is improved by the presence of 33% H_2O in 20h oxidation compared to the 0% and 18% H_2O humidity oxidation exposures.

Hafnium and silicon were less effective at reducing internal oxidation in the alloy and produced thick, less protective oxide scales with a large number of voids. Hafnia and silica formation in the TGO did reduce internal oxidation compared to NiCrAlY and NiCoCrAlY, however, the oxides also increased internal stresses in the TGO, resulting in spallation of the oxide scale.

6.3 Future Work

The mechanisms by which tantalum inclusion slows the upward diffusion of aluminum should be studied in more detail. Future investigation would include study of oxidation behaviour without first removing the yttrium-oxide layer after vacuum heat treatment. This has been found in literature to be beneficial to alumina formation in early oxidation, and the formation of larger alumina grains, reducing the diffusion paths for elements during oxidation. Measuring the oxide grain sizes would give a more complete picture of the oxidation mechanisms and resistance, and

how they differ by alloy composition and humidity condition [48]. Initial steam pre-treatment of the alloys before isothermal and cyclic oxidation should also be investigated as an air + 18% H_2O atmosphere has been found to promote α-Al_2O_3 formation in the initial stages of oxidation, that would aide in the continued oxidation resistance of the alloy [20]. Longer isothermal oxidation of 200h would allow further study of the TGO progression. Cyclic oxidation tests of the bond coat alloys would ultimately better simulate the lifetime of bond coat materials in service. Isothermal and cyclic oxidation tests on complete TBC systems with substrate alloy and ceramic top coat would allow for a better understanding of how TGO growth and interdiffusion affect the lifetime of the system in the presence of water vapor. Comparative study of the differences in oxidation behaviour on bond coats deposited onto a substrate with EB-PVD, APS, and cold spray is also required as these coatings might behave differently depending on the deposition method. First principle and molecular dynamics simulations of interdiffusion would enable a better understanding of the differences in oxidation behaviour between the four samples and is not found in the literature. The use of hydrogen fuel in jet turbine engines would produce higher water content in the engine exhaust compared to using syngas which usually has water content of only up to 18% and was the focus of the present study. Further studies at higher humidities would give a better understanding of how these bond coat material systems would react to the very high humidities encountered when using hydrogen fuels.

References

[1] *2030 emissions reduction plan: Canada's next steps to clean air and a strong economy*. Gatineau, QC: Environment and Climate Change Canada = Environnement et changement climatique Canada, 2022.

[2] R. Darolia, "Thermal barrier coatings technology: critical review, progress update, remaining challenges and prospects," *International Materials Reviews*, vol. 58, no. 6, pp. 315–348, Aug. 2013, doi: 10.1179/1743280413Y.0000000019.

[3] "The role of a gas turbine engine in aircraft | Digitash." Accessed: May 08, 2023. [Online]. Available: https://digitash.com/engineering/aerospace/the-role-of-a-gas-turbine-engine-in-aircraft/

[4] T. K. Ibrahim and M. M. Rahman, "Effect of Compression Ratio on Performance of Combined Cycle Gas Turbine," *IJEE*, vol. 2, no. 1, pp. 9–14, Aug. 2012, doi: 10.5923/j.ijee.20120201.02.

[5] J. R. Nicholls, "Advances in Coating Design for High-Performance Gas Turbines," *MRS Bull.*, vol. 28, no. 9, pp. 659–670, Sep. 2003, doi: 10.1557/mrs2003.194.

[6] "Gas Turbines breaking the 60% efficiency barrier," Power Engineering International. Accessed: Feb. 26, 2020. [Online]. Available: https://www.powerengineeringint.com/coal-fired/equipment-coal-fired/gas-turbines-breaking/

[7] S. Bose, *High temperature coatings*. Amsterdam ; Boston: Elsevier Butterworth-Heinemann, 2007.

[8] R. C. Reed, *The Superalloys: Fundamentals and Applications*.

[9] K. von Fieandt *et al.*, "Multi-component (Al,Cr,Nb,Y,Zr)N thin films by reactive magnetron sputter deposition for increased hardness and corrosion resistance," *Thin Solid Films*, vol. 693, p. 137685, Jan. 2020, doi: 10.1016/j.tsf.2019.137685.

[10] Z. Feng, Z. Wen, M. Li, Y. Zhao, and Z. Yue, "Effect of aging heat treatment on microstructure of Ni-based single crystal superalloys," *AIP Advances*, vol. 11, no. 12, p. 125233, Dec. 2021, doi: 10.1063/5.0077845.

[11] M. C. Galetz, "Coatings for Superalloys," 2015. doi: 10.5772/61141.

[12] B. Gleeson, “Thermal Barrier Coatings for Aeroengine Applications,” *Journal of Propulsion and Power*, vol. 22, no. 2, pp. 375–383, Mar. 2006, doi: 10.2514/1.20734.

[13] M. H. Sullivan and D. R. Mumm, “Transient stage oxidation of MCrAlY bond coat alloys in high temperature, high water vapor content environments,” *Surface and Coatings Technology*, vol. 258, pp. 963–972, Nov. 2014, doi: 10.1016/j.surfcoat.2014.07.048.

[14] B. Wang, J. Gong, A. Y. Wang, C. Sun, R. F. Huang, and L. S. Wen, “Oxidation behaviour of NiCrAlY coatings on Ni-based superalloy,” *Surface and Coatings Technology*, vol. 149, no. 1, pp. 70–75, Jan. 2002, doi: 10.1016/S0257-8972(01)01427-X.

[15] A. G. Evans, D. R. Clarke, and C. G. Levi, “The influence of oxides on the performance of advanced gas turbines,” *Journal of the European Ceramic Society*, vol. 28, no. 7, pp. 1405–1419, Jan. 2008, doi: 10.1016/j.jeurceramsoc.2007.12.023.

[16] M. Elsaß, M. Frommherz, A. Scholz, and M. Oechsner, “Interdiffusion in MCrAlY coated nickel-base superalloys,” *Surface and Coatings Technology*, vol. 307, pp. 565–573, Dec. 2016, doi: 10.1016/j.surfcoat.2016.09.049.

[17] C. Li *et al.*, “Influence of water vapour on the HfO2 distribution within the oxide layer on CoNiCrAlHf alloys,” *Journal of Alloys and Compounds*, vol. 739, pp. 690–699, Mar. 2018, doi: 10.1016/j.jallcom.2017.12.334.

[18] C. Viazzi, J.-P. Bonino, F. Ansart, and A. Barnabé, “Structural study of metastable tetragonal YSZ powders produced via a sol–gel route,” *Journal of Alloys and Compounds*, vol. 452, no. 2, pp. 377–383, Mar. 2008, doi: 10.1016/j.jallcom.2006.10.155.

[19] G. Witz, V. Shklover, W. Steurer, S. Bachegowda, and H.-P. Bossmann, “Phase Evolution in Yttria-Stabilized Zirconia Thermal Barrier Coatings Studied by Rietveld Refinement of X-Ray Powder Diffraction Patterns,” *J American Ceramic Society*, vol. 90, no. 9, pp. 2935–2940, Sep. 2007, doi: 10.1111/j.1551-2916.2007.01785.x.

[20] C. Li *et al.*, “Test atmospheres affecting voids distribution on MCrAlY-bond coats for TBCs at 1050 °C,” *Corrosion Science*, vol. 195, p. 109967, Feb. 2022, doi: 10.1016/j.corsci.2021.109967.

[21] C. M. Koller *et al.*, “Selective phase formation in substoichiometric Al-Cr-based oxides,” *Scripta Materialia*, vol. 139, pp. 144–147, Oct. 2017, doi: 10.1016/j.scriptamat.2017.06.039.

[22] D. A. Porter, K. E. Easterling, and M. Y. Sherif, *Phase Transformations in Metals and Alloys Third Edition*, 3rd ed.

[23] D. Strauss *et al.*, "Oxide scale growth on MCrAlY bond coatings after pulsed electron beam treatment and deposition of EBPVD-TBC," *Surface and Coatings Technology*, vol. 135, no. 2–3, pp. 196–201, Jan. 2001, doi: 10.1016/S0257-8972(00)00916-6.

[24] Y. Hongzhi, W. Di, Z. Jianpeng, S. Qian, L. Songsheng, and D. Mingjiang, "Recent Advances for Interface Diffusion Behavior in MCrAlY Coatings at Elevated Temperature Oxidation," *Rare Metal Materials and Engineering*, 2020.

[25] M. H. Sullivan and D. R. Mumm, "Transient stage oxidation of MCrAlY bond coat alloys in high temperature, high water vapor content environments," *Surface and Coatings Technology*, vol. 258, pp. 963–972, Nov. 2014, doi: 10.1016/j.surfcoat.2014.07.048.

[26] M. J. Lance, K. A. Unocic, J. A. Haynes, and B. A. Pint, "Effect of water vapor on thermally-grown alumina scales on Pt-modified and simple aluminide bond coatings," *Surface and Coatings Technology*, vol. 237, pp. 2–7, Dec. 2013, doi: 10.1016/j.surfcoat.2013.06.041.

[27] S. Fontana, S. Chevalier, and G. Caboche, "Metallic interconnects for solid oxide fuel cell: Effect of water vapour on oxidation resistance of differently coated alloys," *Journal of Power Sources*, vol. 193, no. 1, pp. 136–145, Aug. 2009, doi: 10.1016/j.jpowsour.2008.11.041.

[28] B. Gleeson, "Thermal Barrier Coatings for Aeroengine Applications," *Journal of Propulsion and Power*, vol. 22, no. 2, pp. 375–383, Mar. 2006, doi: 10.2514/1.20734.

[29] Z. Zhou, H. Guo, M. Abbas, and S. Gong, "Effect of water vapor on the phase transformation of alumina grown on NiAl at 950°C," *Corrosion Science*, vol. 53, no. 9, pp. 2943–2947, Sep. 2011, doi: 10.1016/j.corsci.2011.05.029.

[30] J. Hu, C. Gu, J. Li, C. Li, J. Feng, and Y. Jiang, "Microstructure and oxidation behavior of the Y/Ta/Hf co-doped AlCoCrFeNi high-entropy alloys in air at 1100 ℃," *Corrosion Science*, vol. 212, p. 110930, Mar. 2023, doi: 10.1016/j.corsci.2022.110930.

[31] J. A. Haynes, K. A. Unocic, and B. A. Pint, "Effect of water vapor on the 1100°C oxidation behavior of plasma-sprayed TBCs with HVOF NiCoCrAlX bond coatings," *Surface and Coatings Technology*, vol. 215, pp. 39–45, Jan. 2013, doi: 10.1016/j.surfcoat.2012.07.099.

[32] S. Fontana, S. Chevalier, and G. Caboche, “Metallic interconnects for solid oxide fuel cell: Effect of water vapour on oxidation resistance of differently coated alloys,” *Journal of Power Sources*, vol. 193, no. 1, pp. 136–145, Aug. 2009, doi: 10.1016/j.jpowsour.2008.11.041.

[33] Y. Huang, Y. He, B. Yang, A. Khan, X. Zhao, and P. Song, “Effect of YSZ/TaSi2-MCrAlY thermal barrier coatings on oxidation resistance in air and water vapor,” *Ceramics International*, vol. 49, no. 9, pp. 14551–14562, May 2023, doi: 10.1016/j.ceramint.2023.01.045.

[34] Z. Shuting, D. Kaiping, R. Xianjing, and S. Ji, “Influence of Si on Microstructures and High-Temperature Properties of MCrAlY Type Coating,” *Rare Metal Materials and Engineering*, vol. 47, no. 9, pp. 2652–2656, Sep. 2018, doi: 10.1016/S1875-5372(18)30204-2.

[35] V. Déneux, Y. Cadoret, S. Hervier, and D. Monceau, “Effect of Water Vapor on the Spallation of Thermal Barrier Coating Systems During Laboratory Cyclic Oxidation Testing,” *Oxid Met*, vol. 73, no. 1–2, pp. 83–93, Feb. 2010, doi: 10.1007/s11085-009-9170-1.

[36] K. Chen, D. Seo, and P. Canteenwalla, “The Effect of High-Temperature Water Vapour on Degradation and Failure of Hot Section Components of Gas Turbine Engines,” *Coatings*, vol. 11, no. 9, p. 1061, Sep. 2021, doi: 10.3390/coatings11091061.

[37] V. Provenzano, K. Sadananda, N. P. Louat, and J. R. Reed, “Void formation and suppression during high temperature oxidation of MCrAlY-type coatings,” *Surface and Coatings Technology*, vol. 36, no. 1–2, pp. 61–74, Dec. 1988, doi: 10.1016/0257-8972(88)90136-3.

[38] B. A. Pint, G. W. Garner, T. M. Lowe, J. A. Haynes, and Y. Zhang, “Effect of increased water vapor levels on TBC lifetime with Pt-containing bond coatings,” *Surface and Coatings Technology*, vol. 206, no. 7, pp. 1566–1570, Dec. 2011, doi: 10.1016/j.surfcoat.2011.06.008.

[39] K. A. Unocic and B. A. Pint, “Effect of water vapor on thermally grown alumina scales on bond coatings,” *Surface and Coatings Technology*, vol. 215, pp. 30–38, Jan. 2013, doi: 10.1016/j.surfcoat.2012.08.100.

[40] C. Li *et al.*, “Effect of water vapour on morphology of the Si/Ti-rich phase at the interface between oxide layer and aluminide coating,” *Corrosion Science*, vol. 163, p. 108240, Feb. 2020, doi: 10.1016/j.corsci.2019.108240.

[41] Y. He *et al.*, “Effects of Stepped Heating on the Initial Growth of Oxide Scales on NiCrAlHf Bond Coat Alloy under Air and Water Vapor Atmospheres,” *Materials*, vol. 15, no. 8, p. 2914, Apr. 2022, doi: 10.3390/ma15082914.

[42] F. Cernuschi *et al.*, “Thermo-physical properties of as deposited and aged thermal barrier coatings (TBC) for gas turbines: State-of-the art and advanced TBCs,” *Journal of the European Ceramic Society*, vol. 38, no. 11, pp. 3945–3961, Sep. 2018, doi: 10.1016/j.jeurceramsoc.2018.04.044.

[43] J. A. Haynes, K. A. Unocic, M. J. Lance, and B. A. Pint, “Impact of superalloy composition, bond coat roughness and water vapor on TBC lifetime with HVOF NiCoCrAlYHfSi bond coatings,” *Surface and Coatings Technology*, vol. 237, pp. 65–70, Dec. 2013, doi: 10.1016/j.surfcoat.2013.09.062.

[44] Oerlikon Metco, “Material Product Data Sheet.” Accessed: Jan. 23, 2023. [Online]. Available: https://mymetco.oerlikon.com/en-us/category/powders

[45] “Messer Laboratory Equipment Catalogue.” Accessed: Jun. 21, 2023. [Online]. Available: https://www.messer-ca.com/wp-content/uploads/catalog/lab/en/6/

[46] C. Borgnakke, R. E. Sonntag, G. J. Van Wylen, and R. E. Sonntag, *Fundamentals of thermodynamics*, 7th ed. Hoboken, NJ: Wiley, 2009.

[47] M. H. Sullivan and D. R. Mumm, “Transient stage oxidation of MCrAlY bond coat alloys in high temperature, high water vapor content environments,” *Surface and Coatings Technology*, vol. 258, pp. 963–972, Nov. 2014, doi: 10.1016/j.surfcoat.2014.07.048.

[48] G.-H. Meng *et al.*, “Superior oxidation resistant MCrAlY bond coats prepared by controlled atmosphere heat treatment,” *Corrosion Science*, vol. 170, p. 108653, Jul. 2020, doi: 10.1016/j.corsci.2020.108653.

Appendix A: EDS Cross-Section Element Maps and Line Scans

A.1 0% 2h

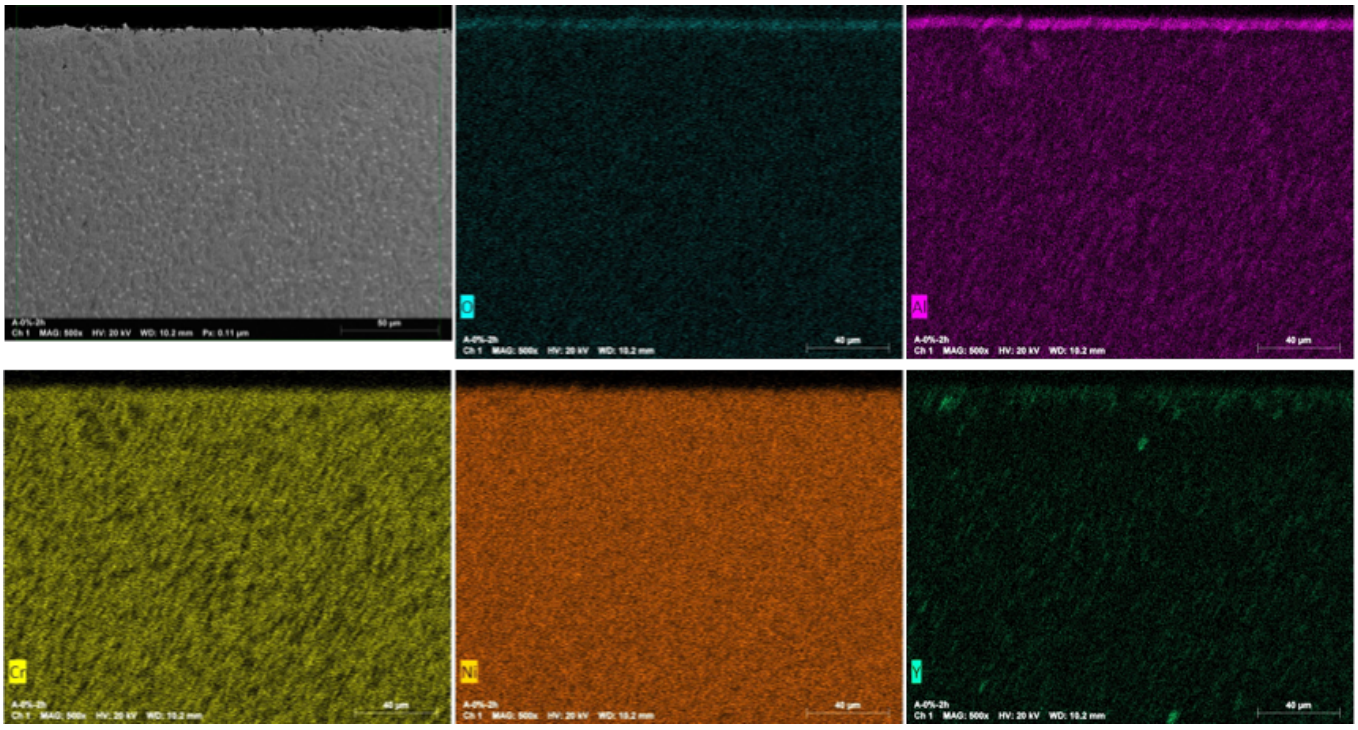

Figure 0.1 EDS Element Map A-0%-2h

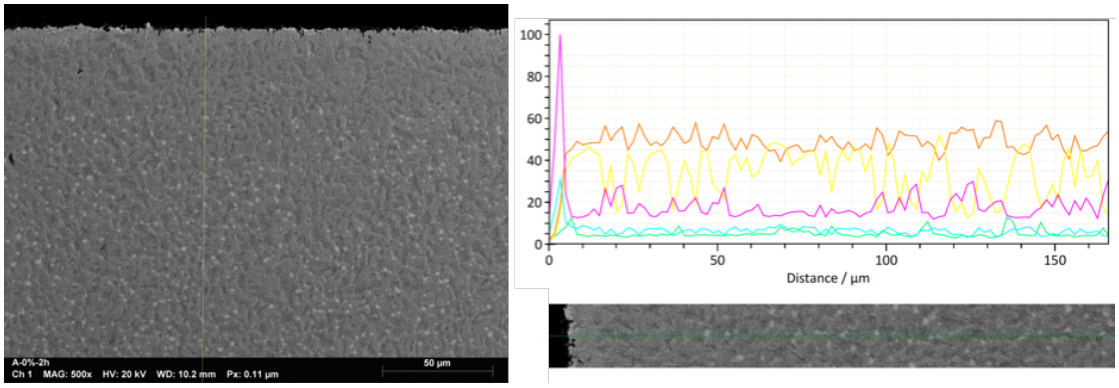

Figure 0.2 EDS Element Line Scan A-0%-2h

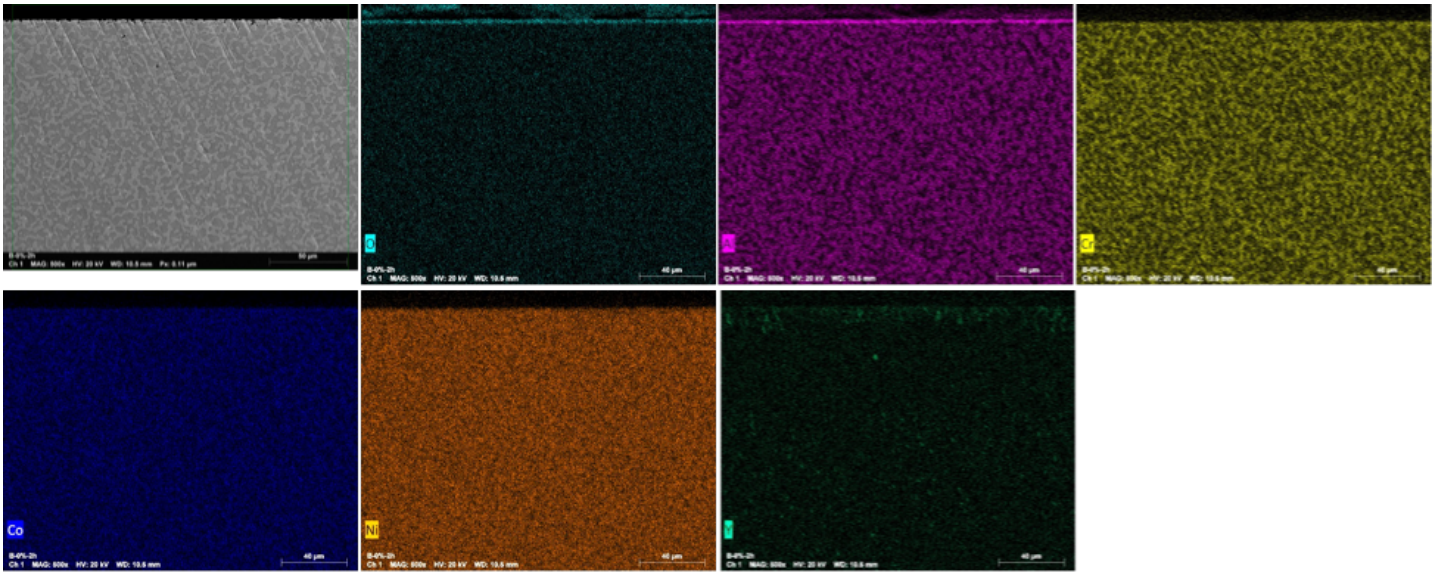

Figure 0.3 EDS Element Map B-0%-2h

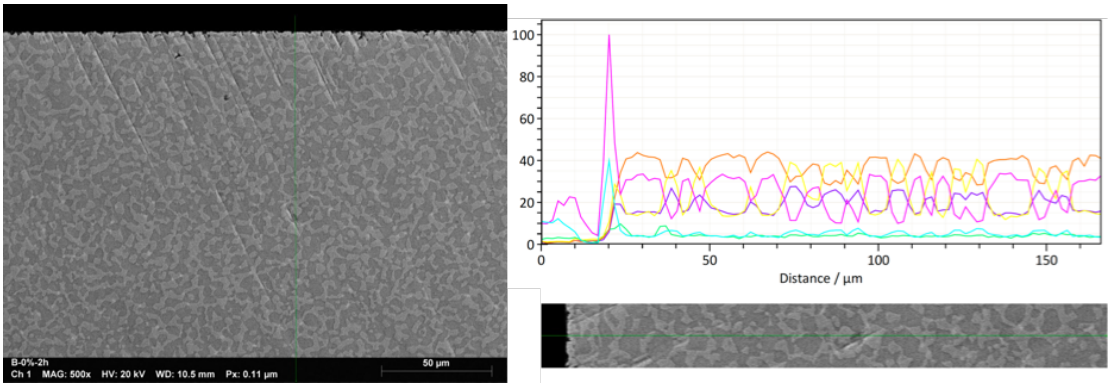

Figure 0.4 EDS Element Line Scan B-0%-2h

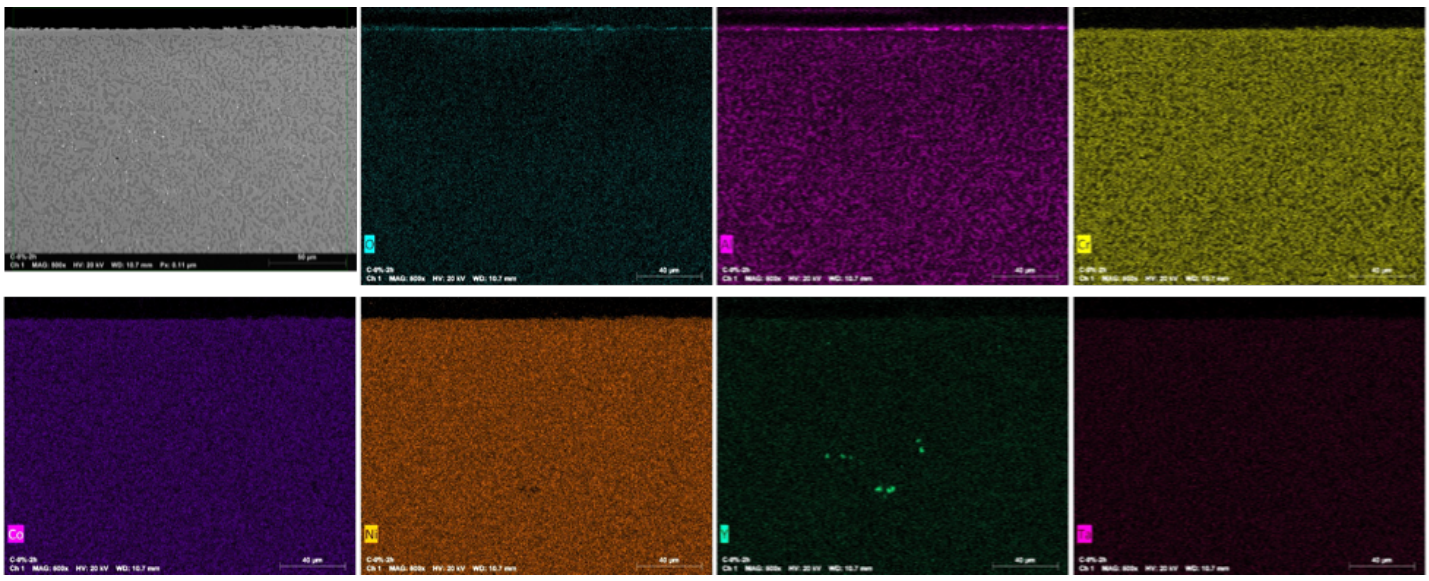

Figure 0.5 EDS Element Map C-0%-2h

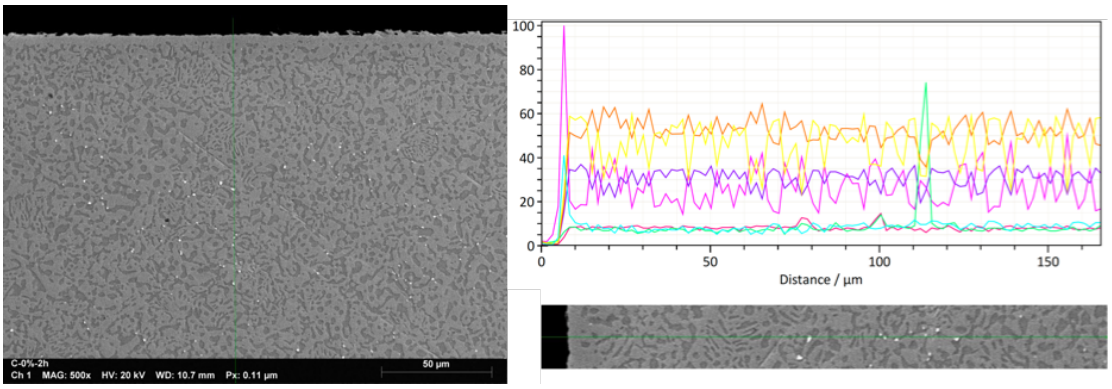

Figure 0.6 EDS Element Line Scan C-0%-2h

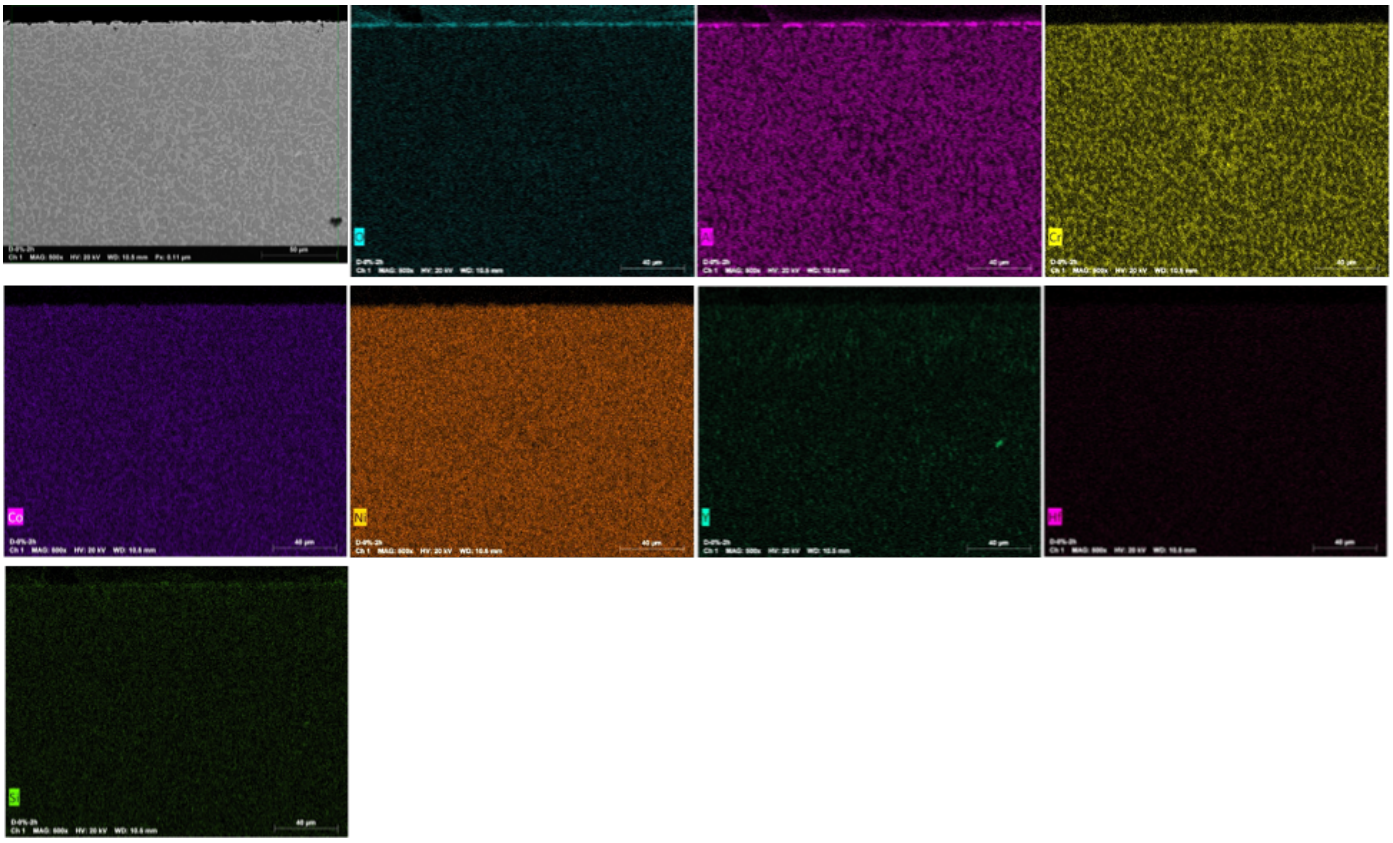

Figure 0.7 EDS Element Map D-0%-2h

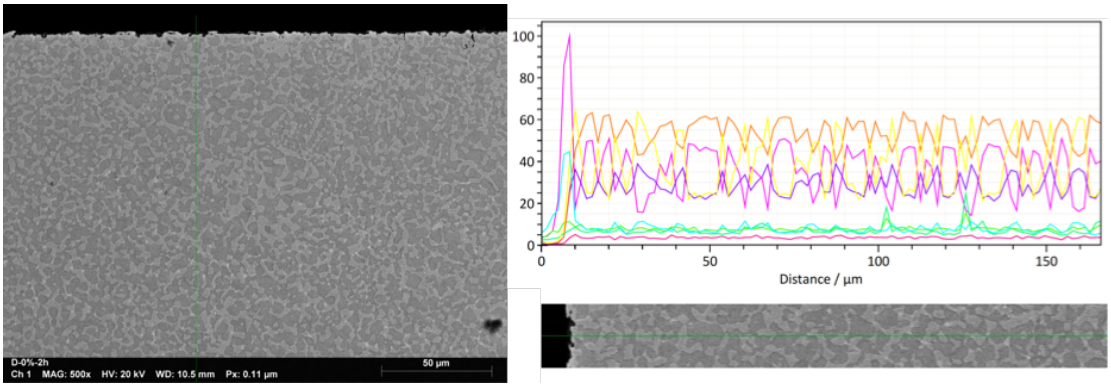

Figure 0.8 EDS Element Line Scan D-0%-2h

A.2 0%-20h

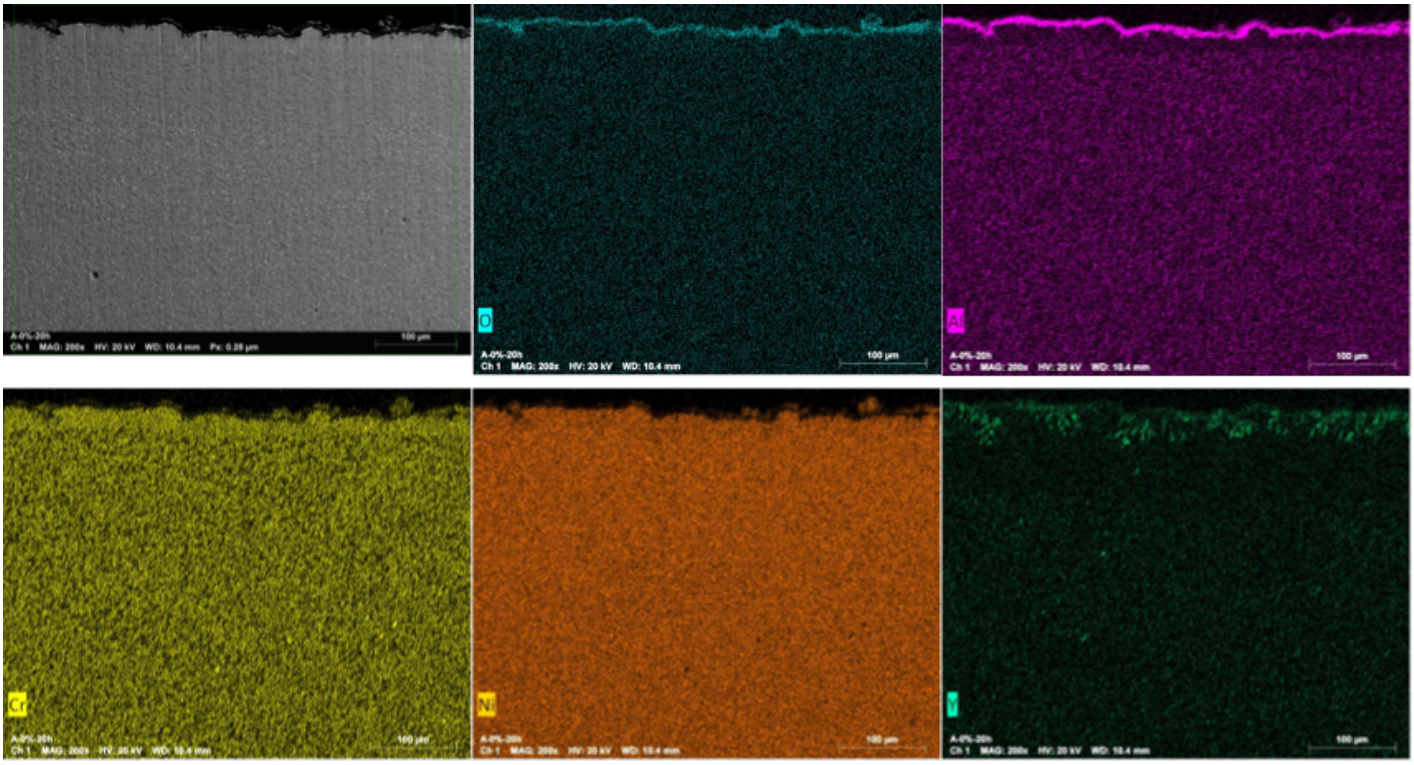

Figure 0.9 EDS Element Map A-0%-20h

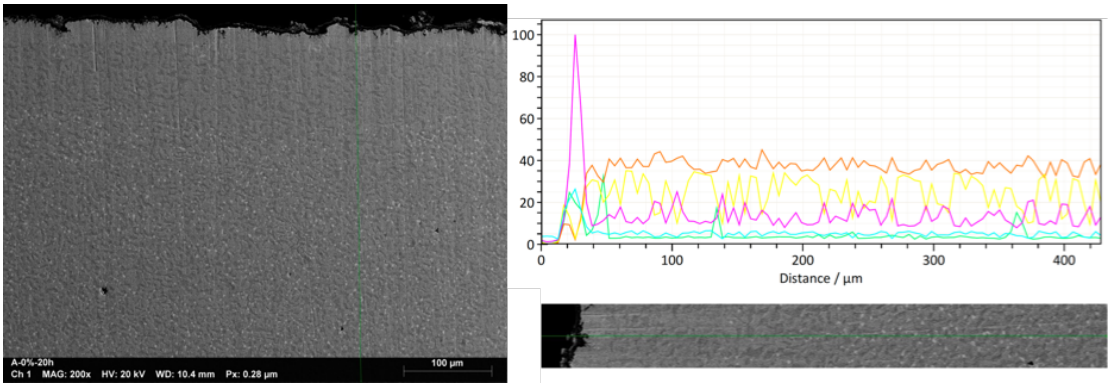

Figure 0.10 EDS Element Line Scan A-0%-20h

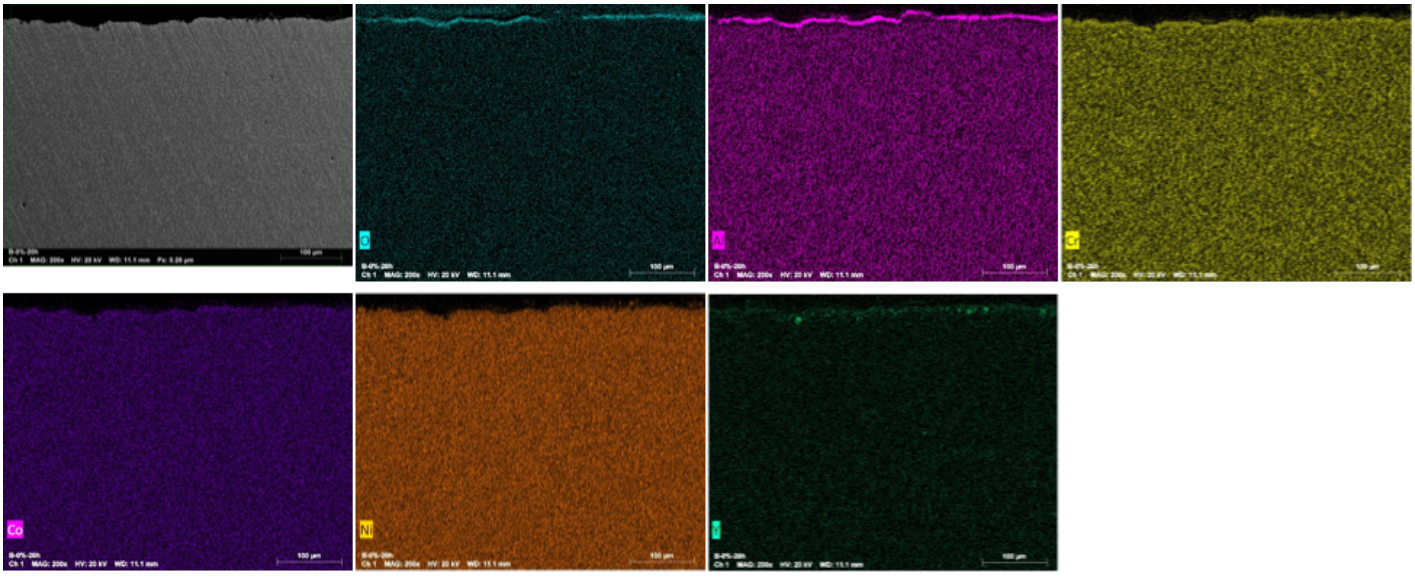

Figure 0.11 EDS Element Map B-0%-20h

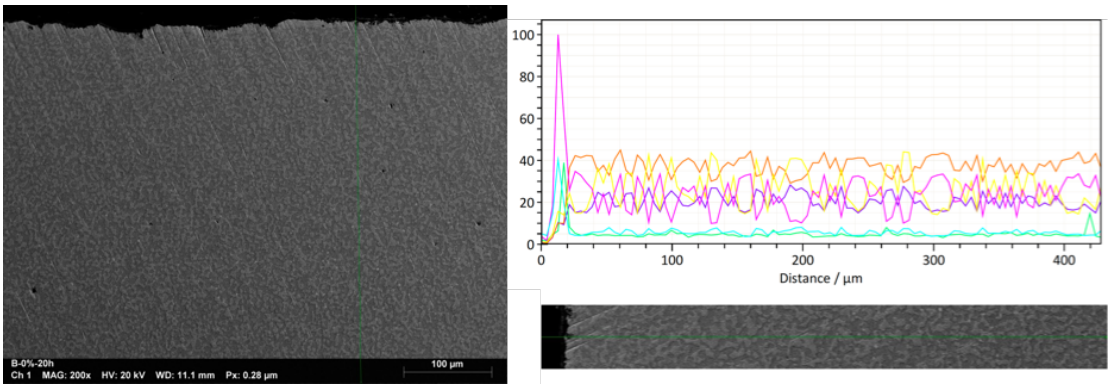

Figure 0.12 EDS Element Line Scan B-0%-20h

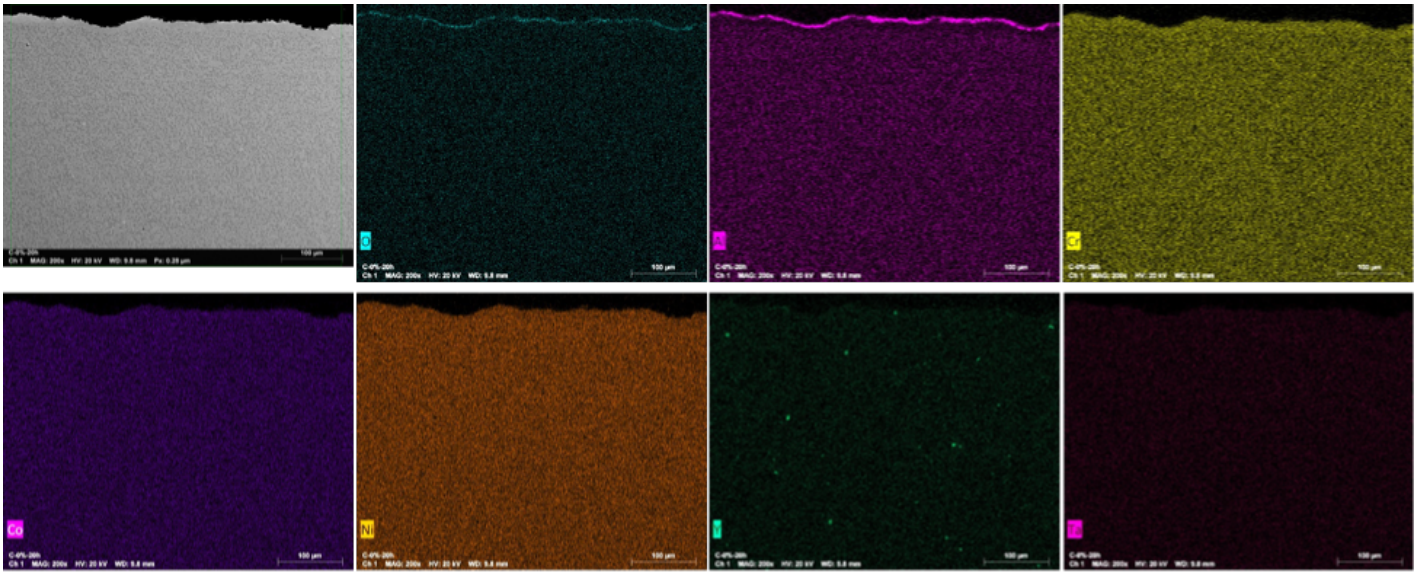

Figure 0.13 EDS Element Map C-0%-20h

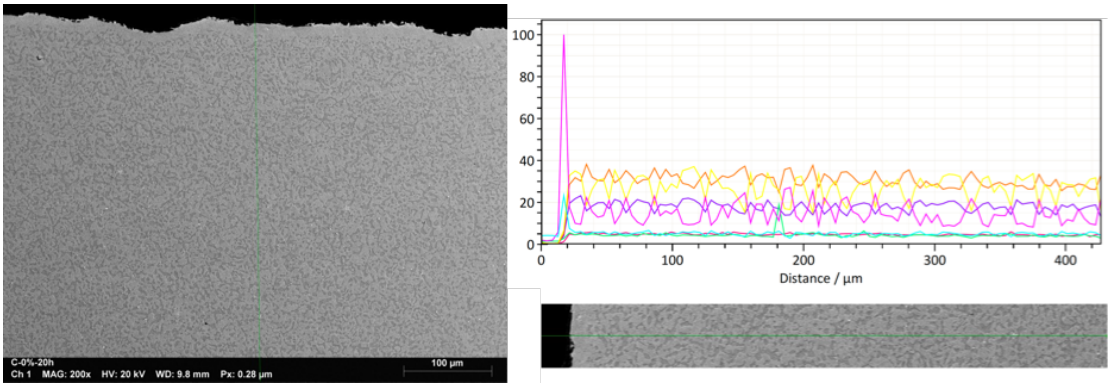

Figure 0.14 EDS Element Line Scan C-0%-20h

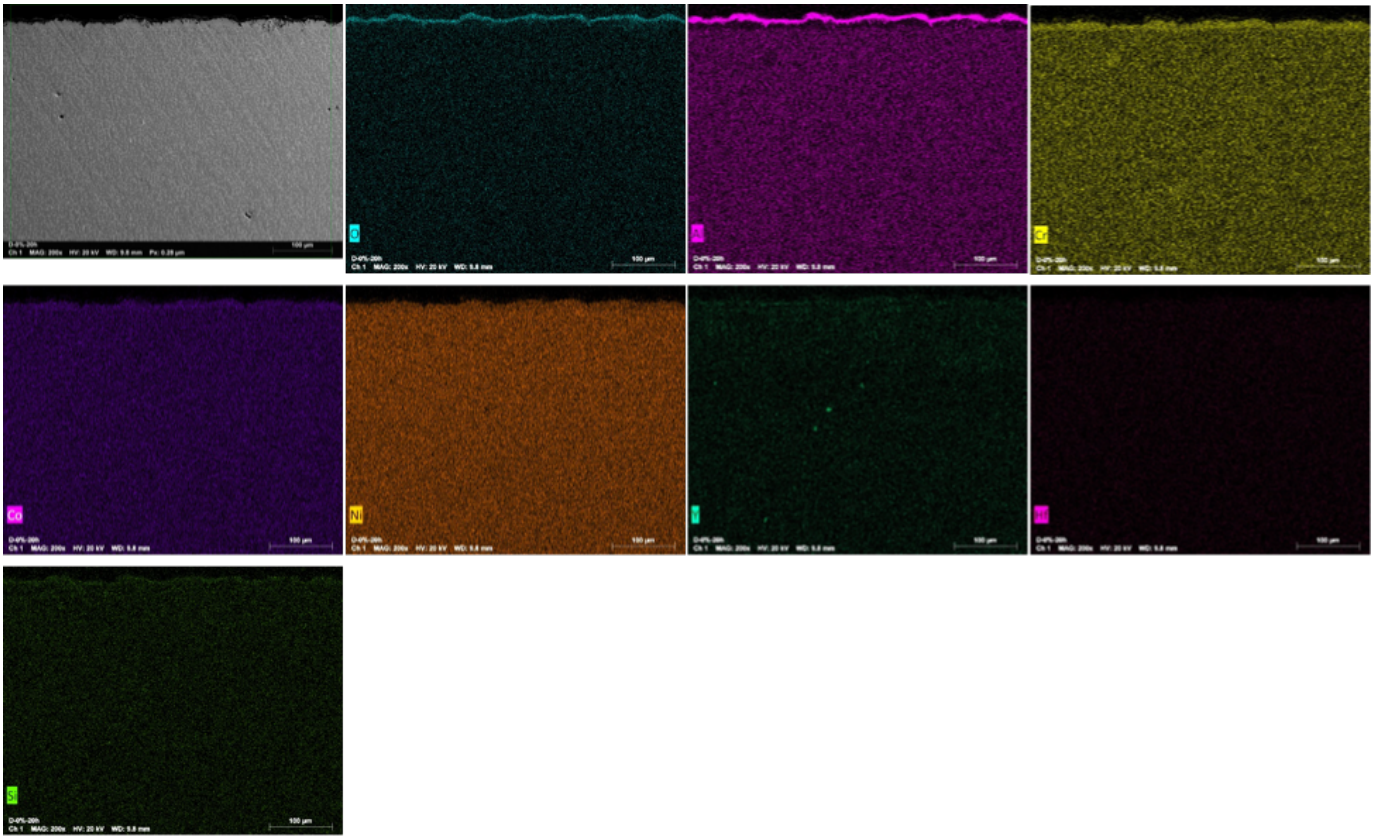

Figure 0.15 EDS Element Map D-0%-20h

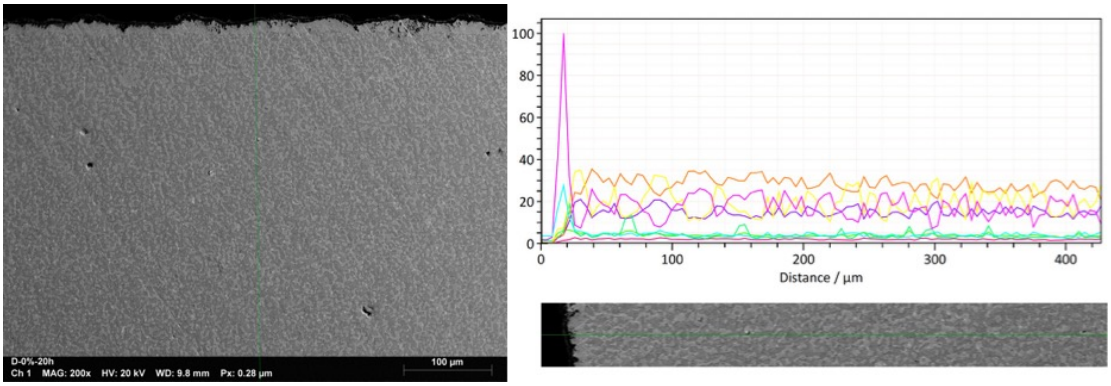

Figure 0.16 EDS Element Line Scan D-0%-20h

A.3 18%-2h

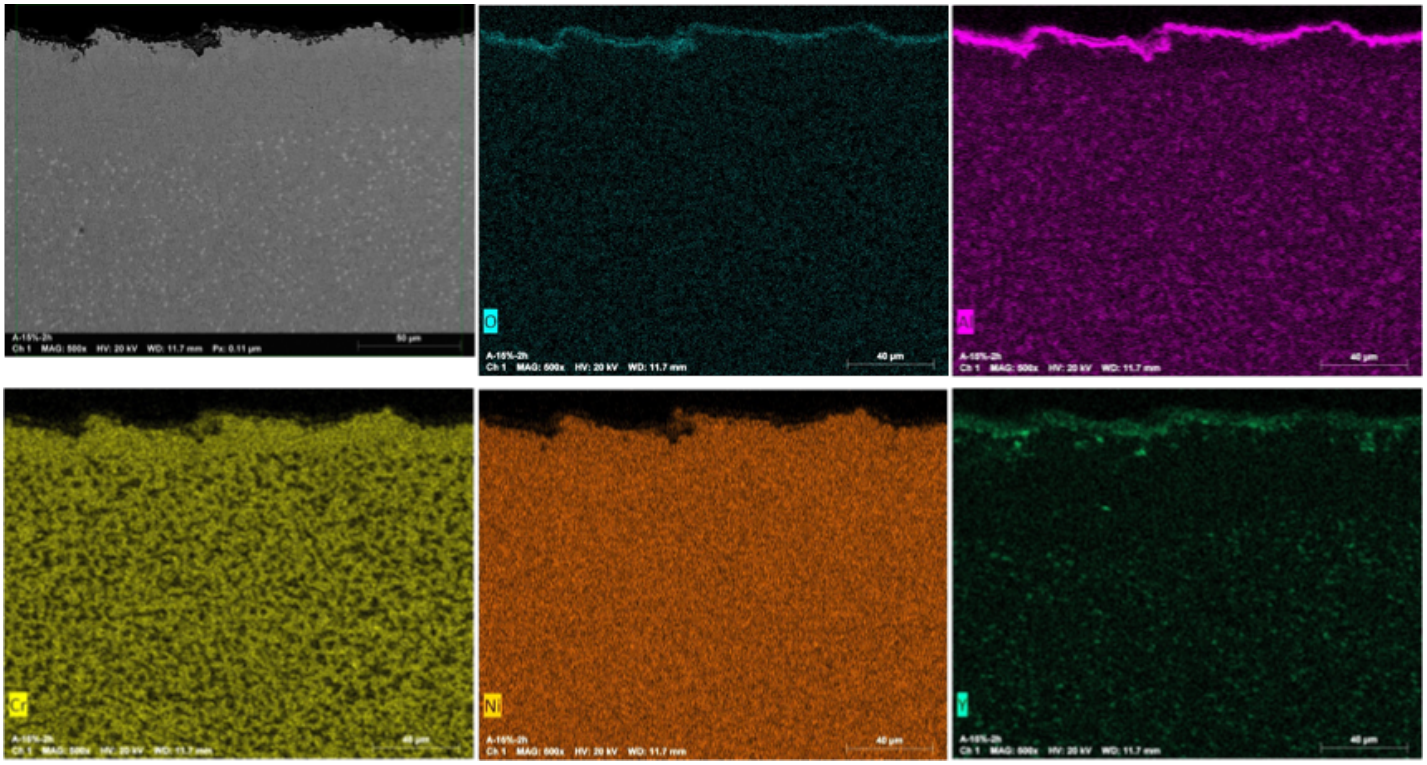

Figure 0.17 EDS Element Map A-18%-2h

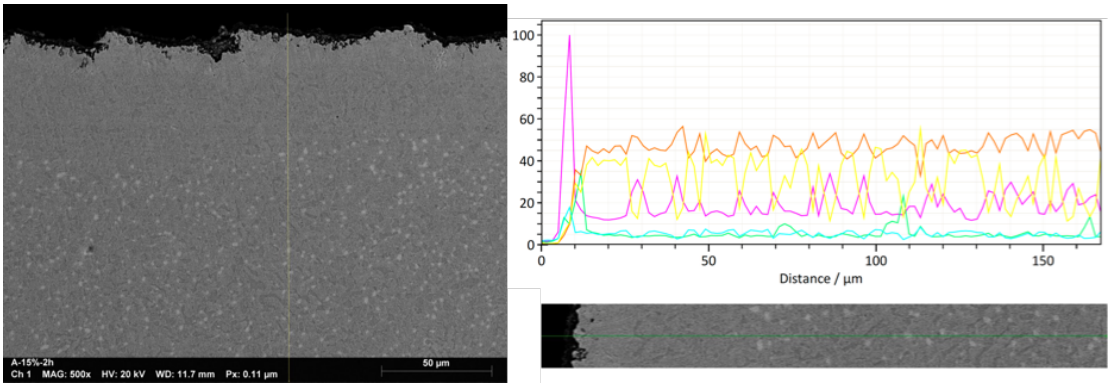

Figure 0.18 EDS Element Line Scan A-18%-2h

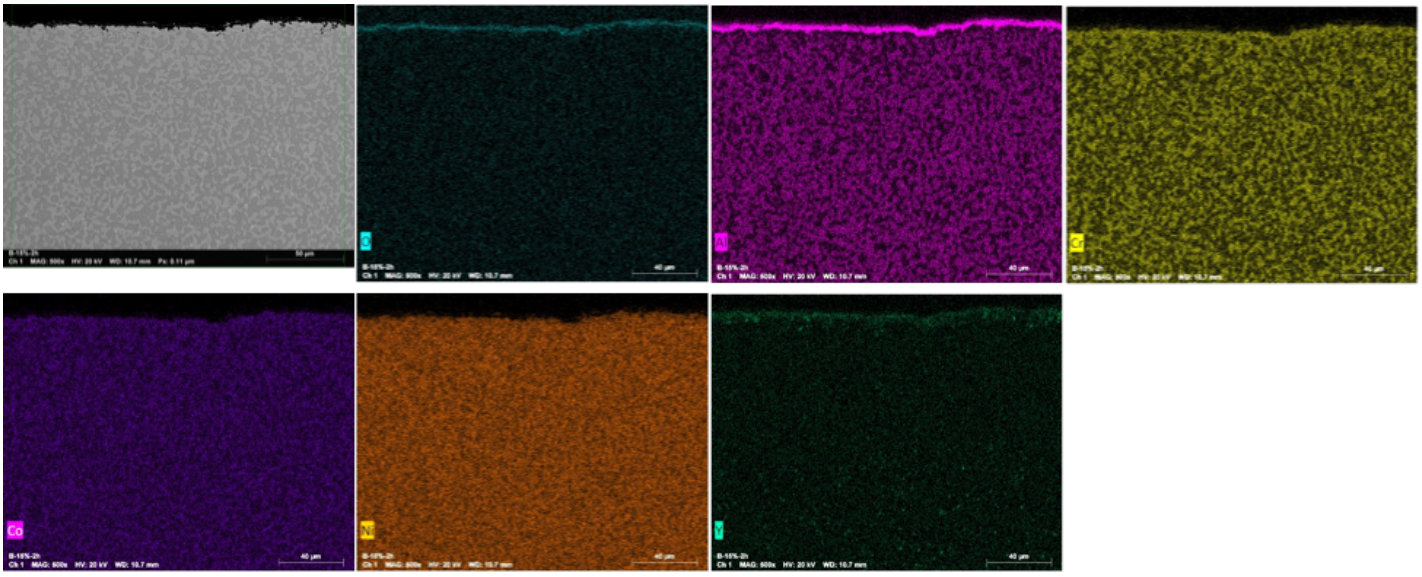

Figure 0.19 EDS Element Map B-18%-2h

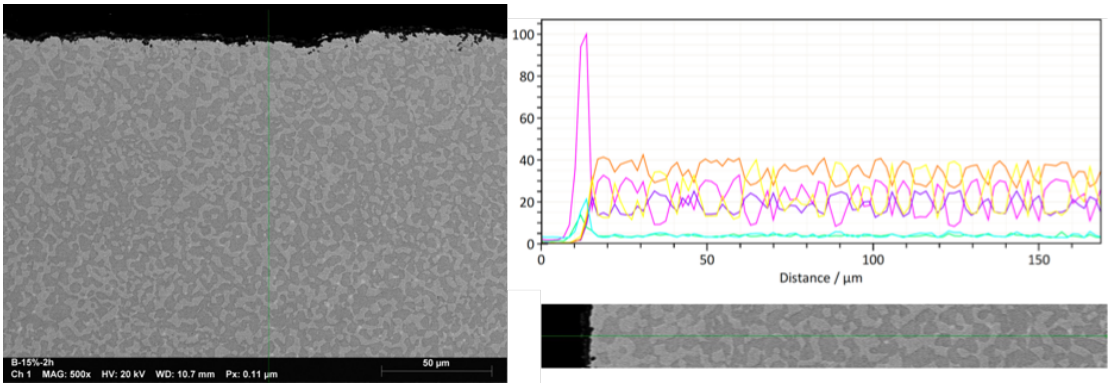

Figure 0.20 EDS Element Line Scan B-18%-2h

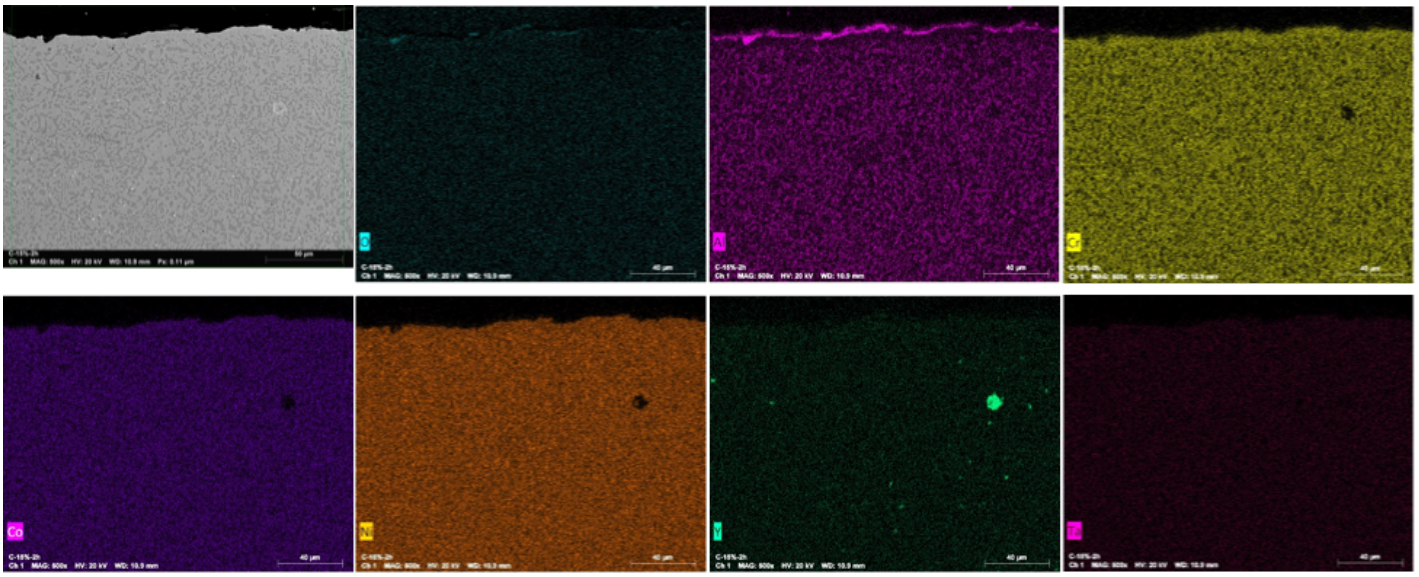

Figure 0.21 EDS Element Map C-18%-2h

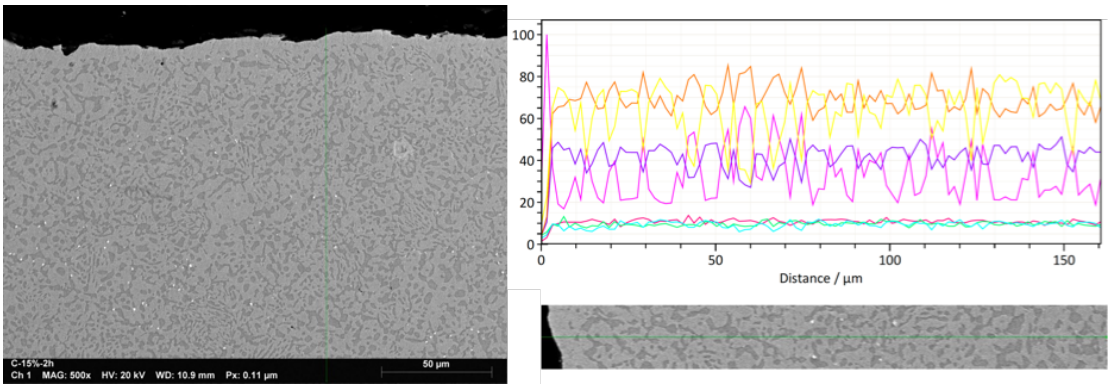

Figure 0.22 EDS Element Line Scan C-18%-2h

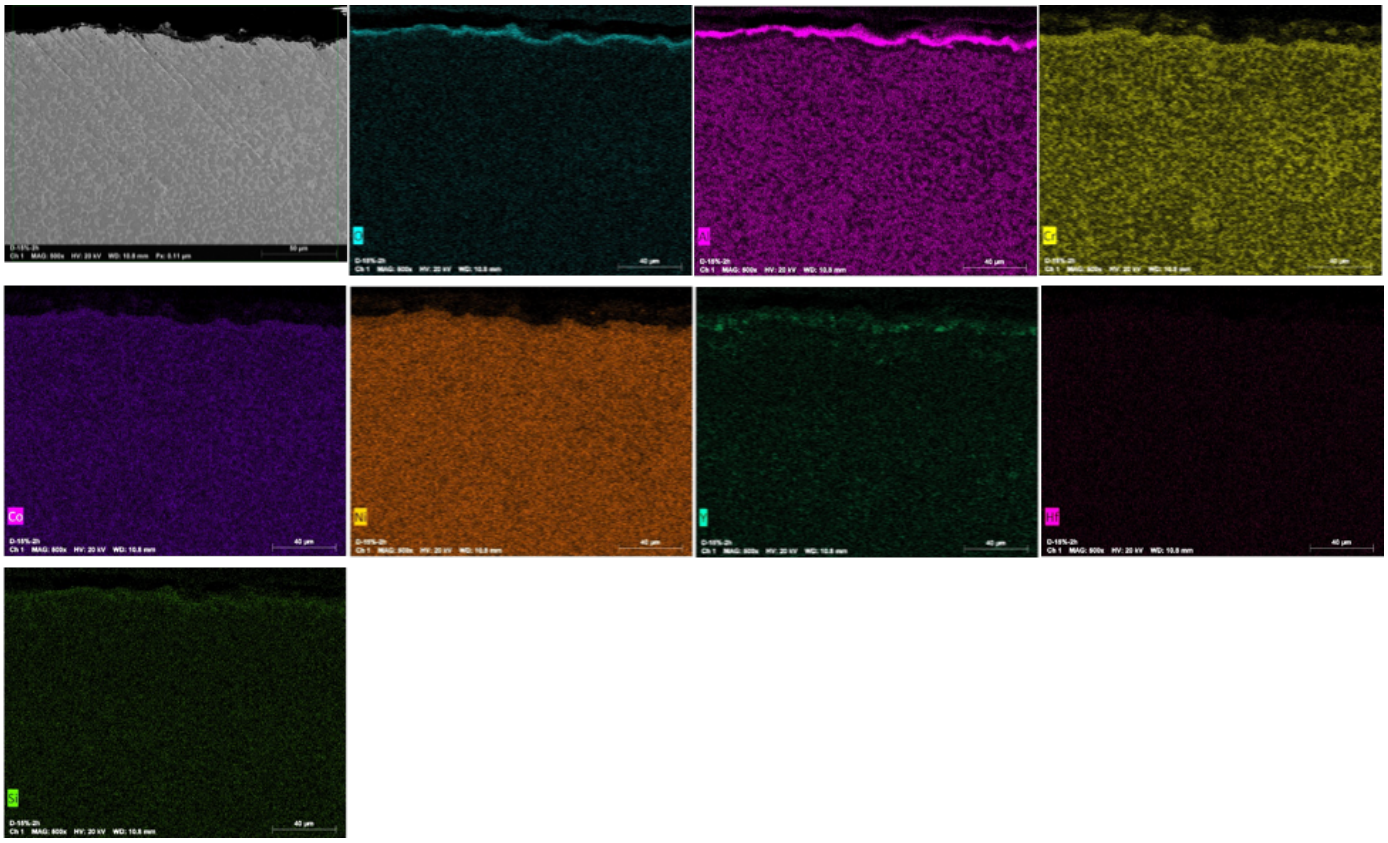

Figure 0.23 EDS Element Map D-18%-2h

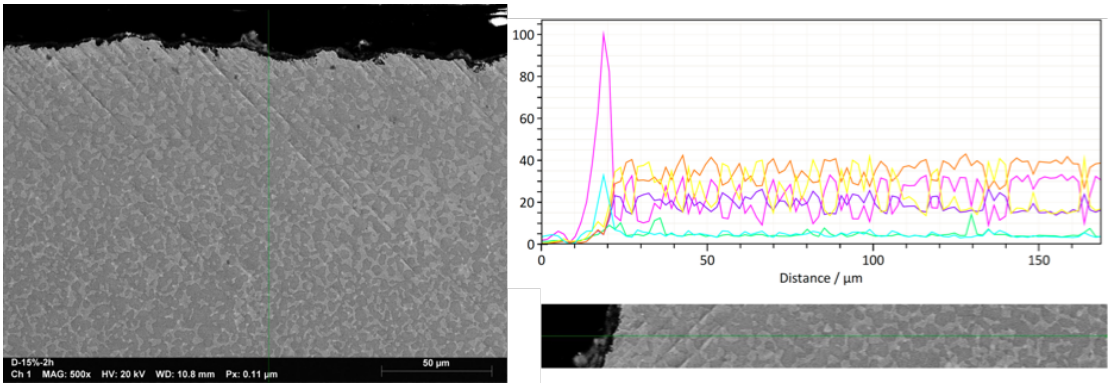

Figure 0.24 EDS Element Line Scan D-18%-2h

A.4 15%-20h

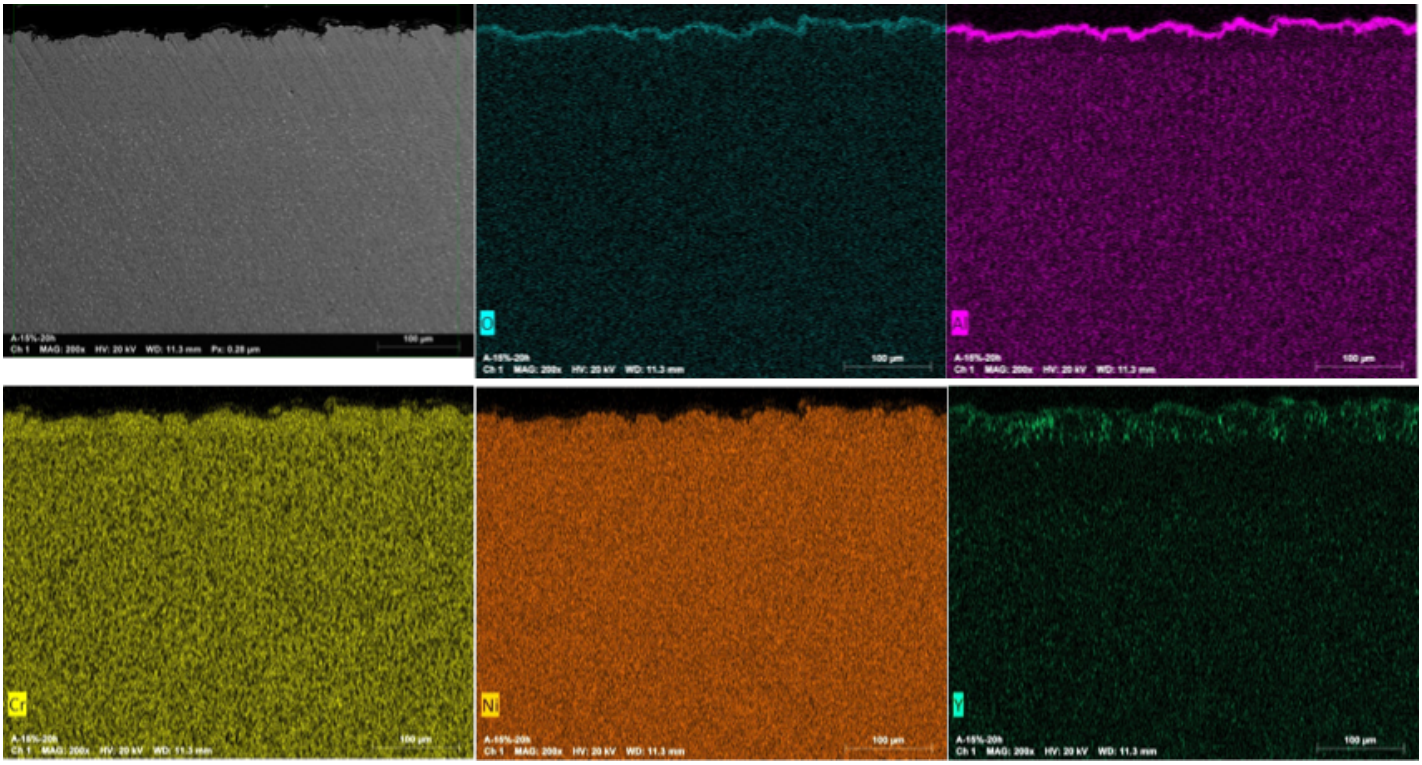

Figure 0.25 EDS Element Map A-18%-20h

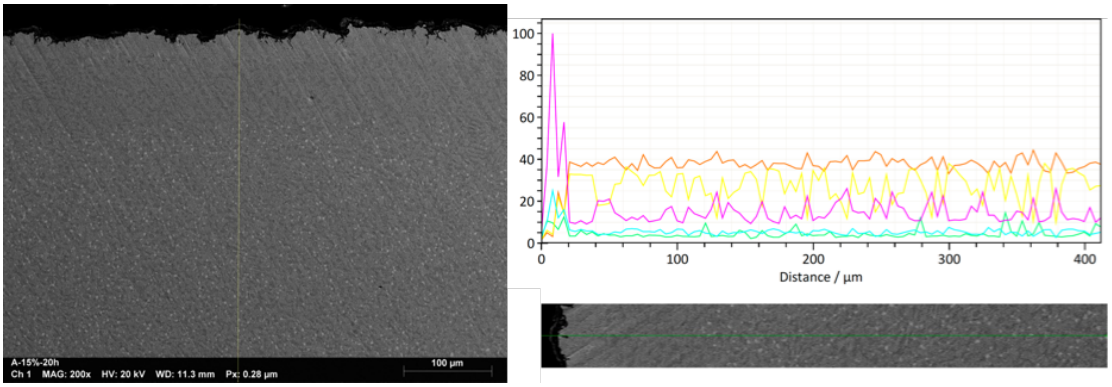

Figure 0.26 EDS Element Line Scan A-18%-20h

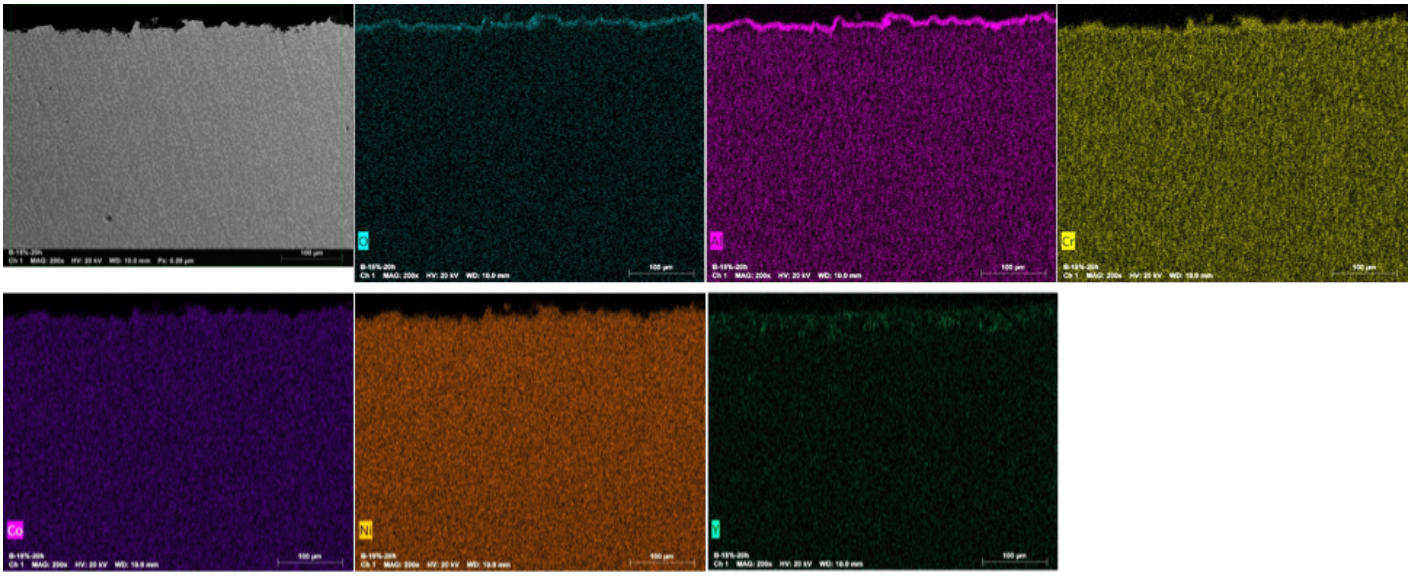

Figure 0.27 EDS Element Map B-18%-20h

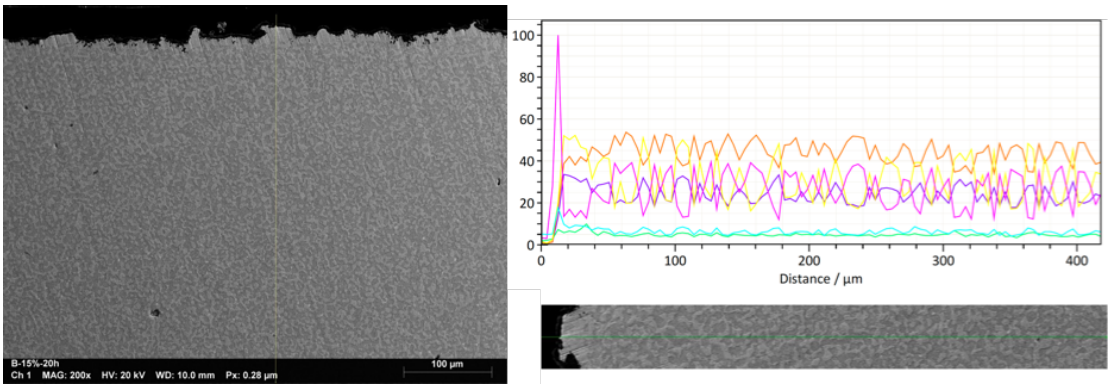

Figure 0.28 EDS Element Line Scan B-18%-20h

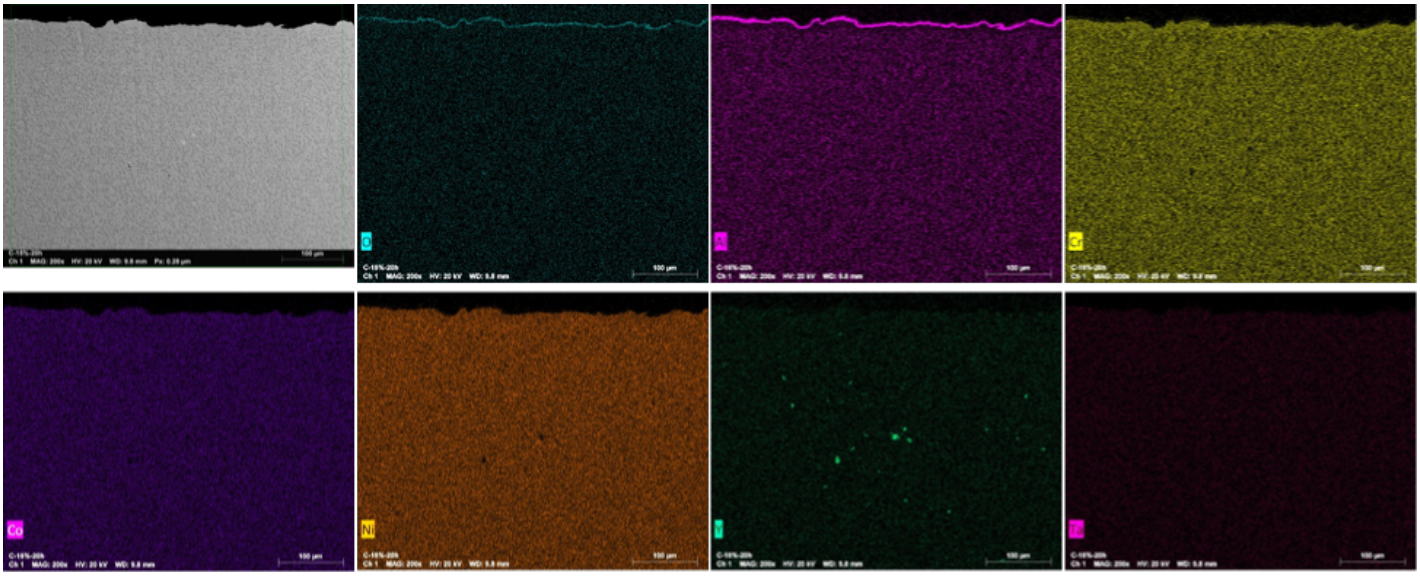

Figure 0.29 EDS Element Map C-18%-20h

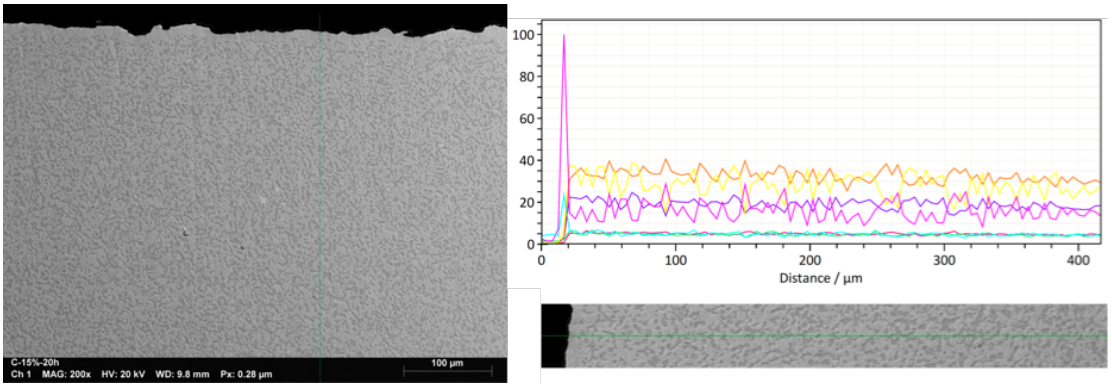

Figure 0.30 EDS Element Line Scan C-18%-20h

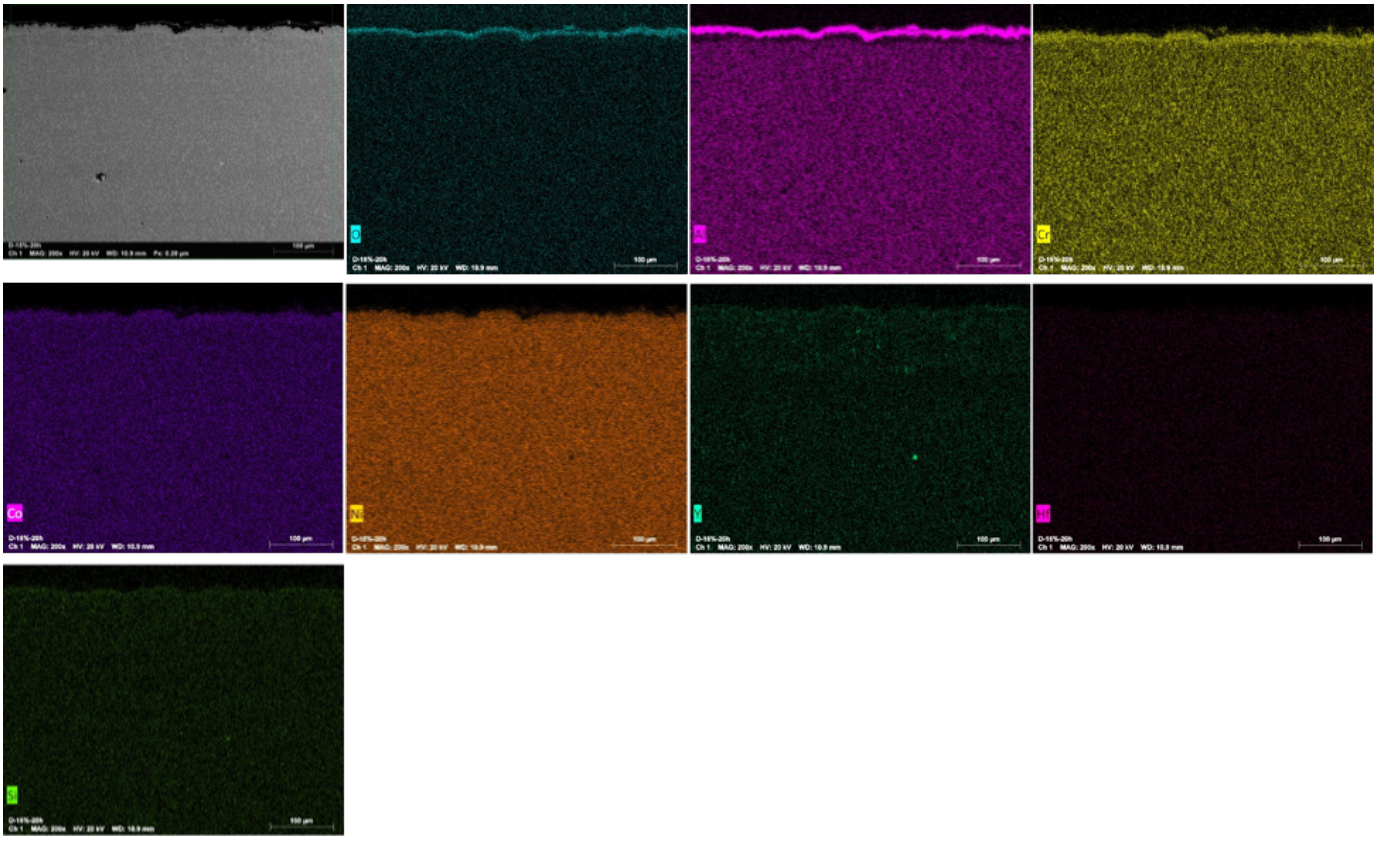

Figure 0.31 EDS Element Map D-18%-20h

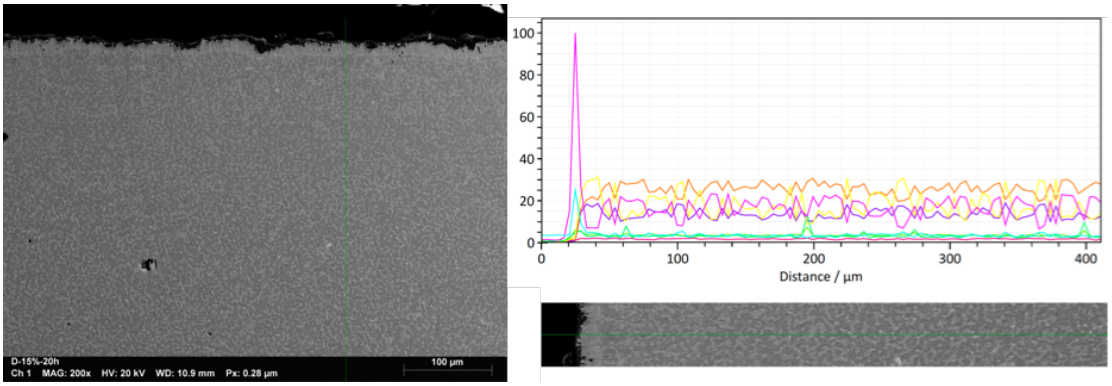

Figure 0.32 EDS Element Line Scan D-18%-20h

A.5 33%-2h

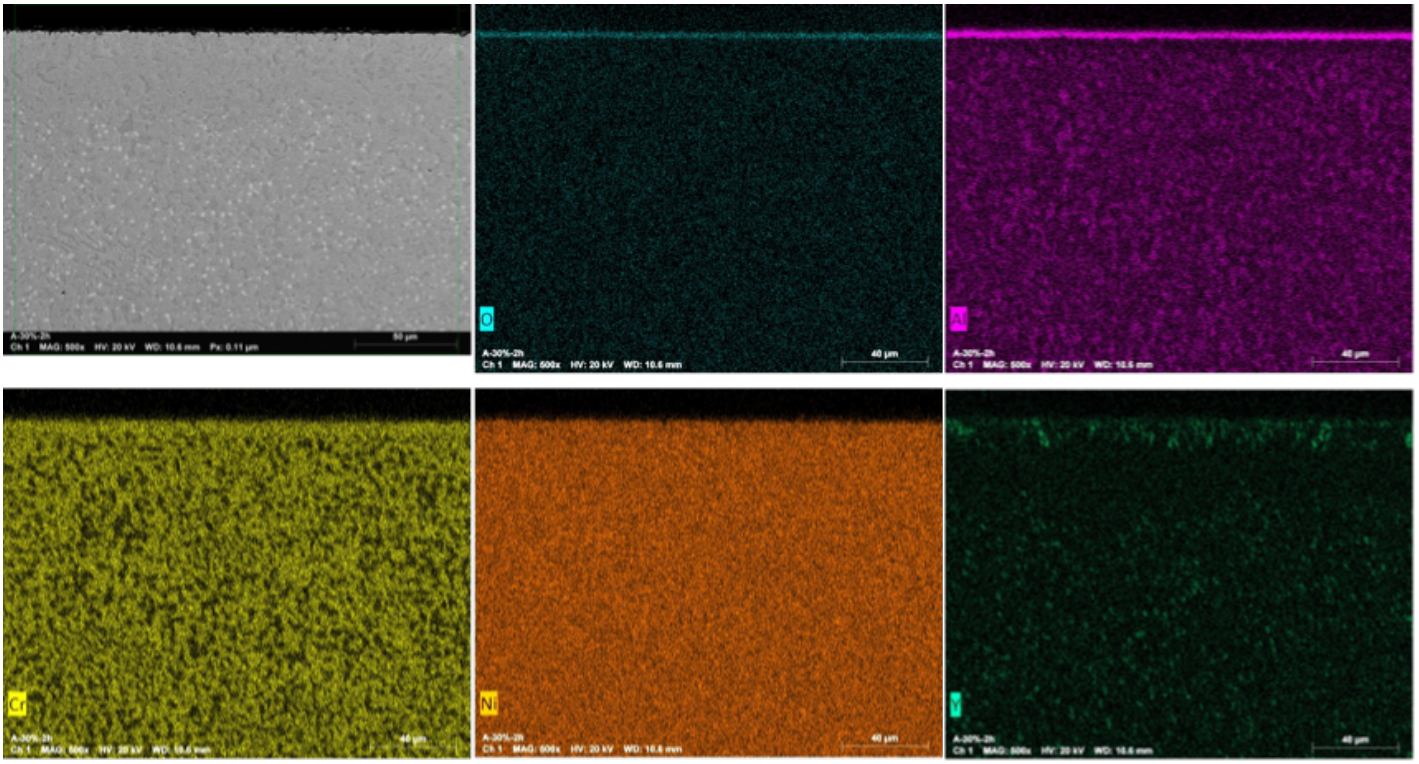

Figure 0.33 EDS Element Map A-33%-2h

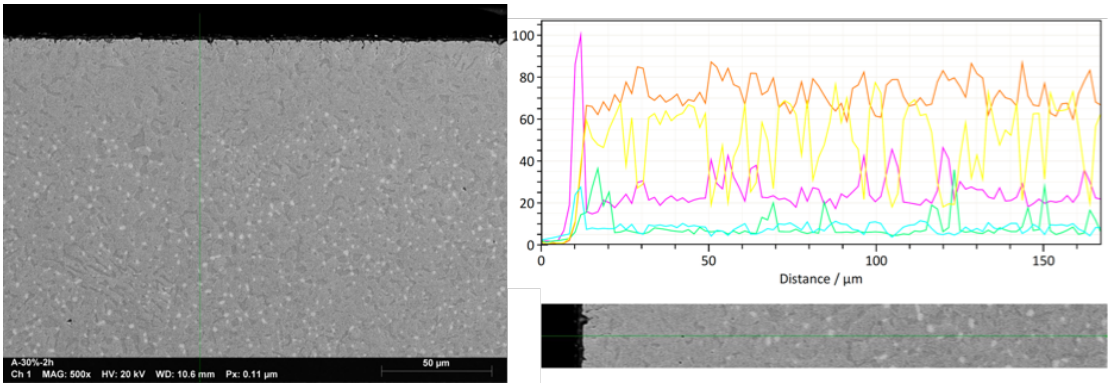

Figure 0.34 EDS Element Line Scan A-33%-2h

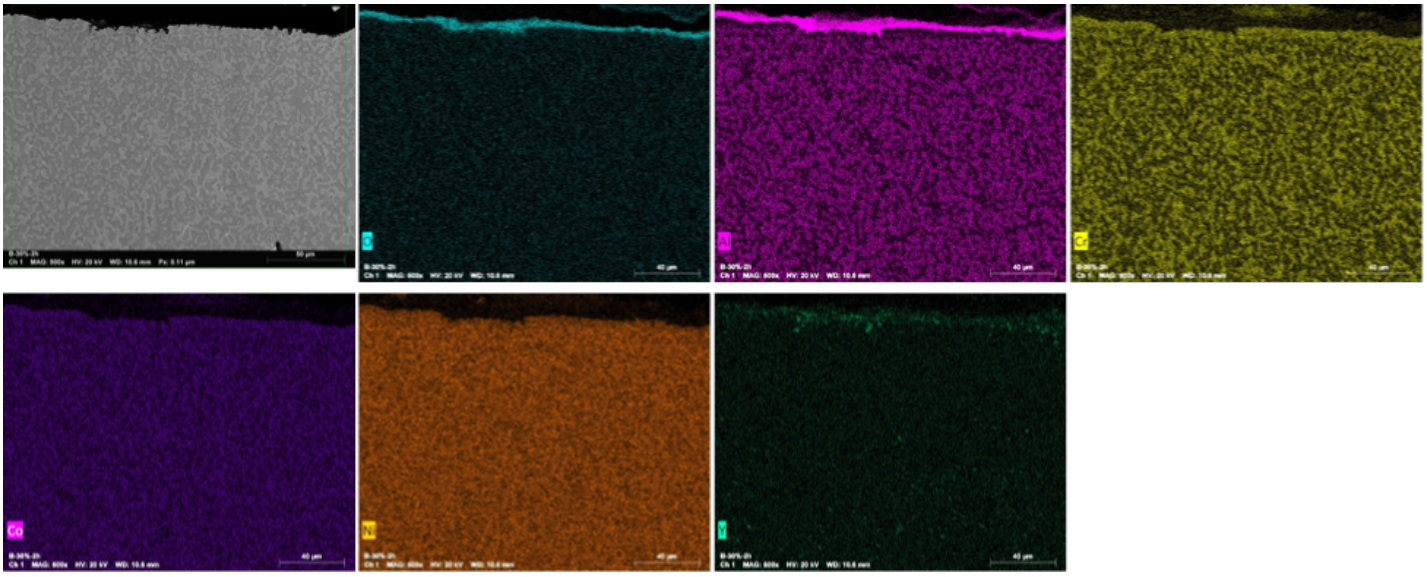

Figure 0.35 EDS Element Map B-33%-2h

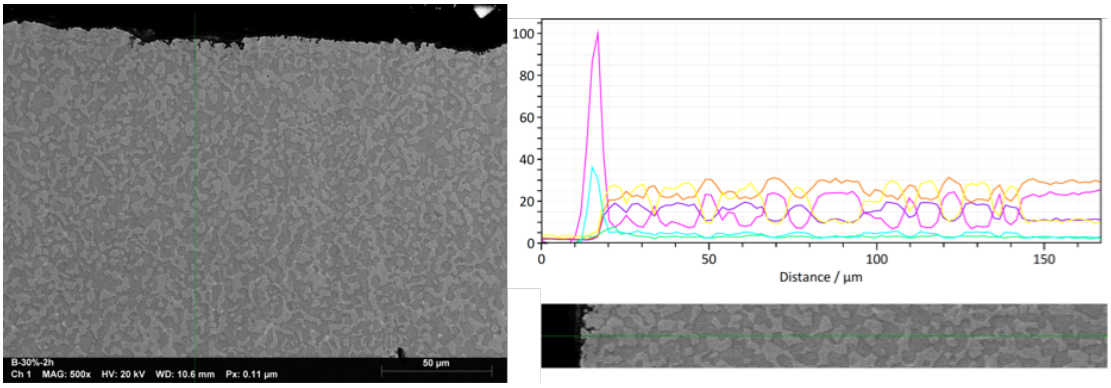

Figure 0.36 EDS Element Line Scan B-33%-2h

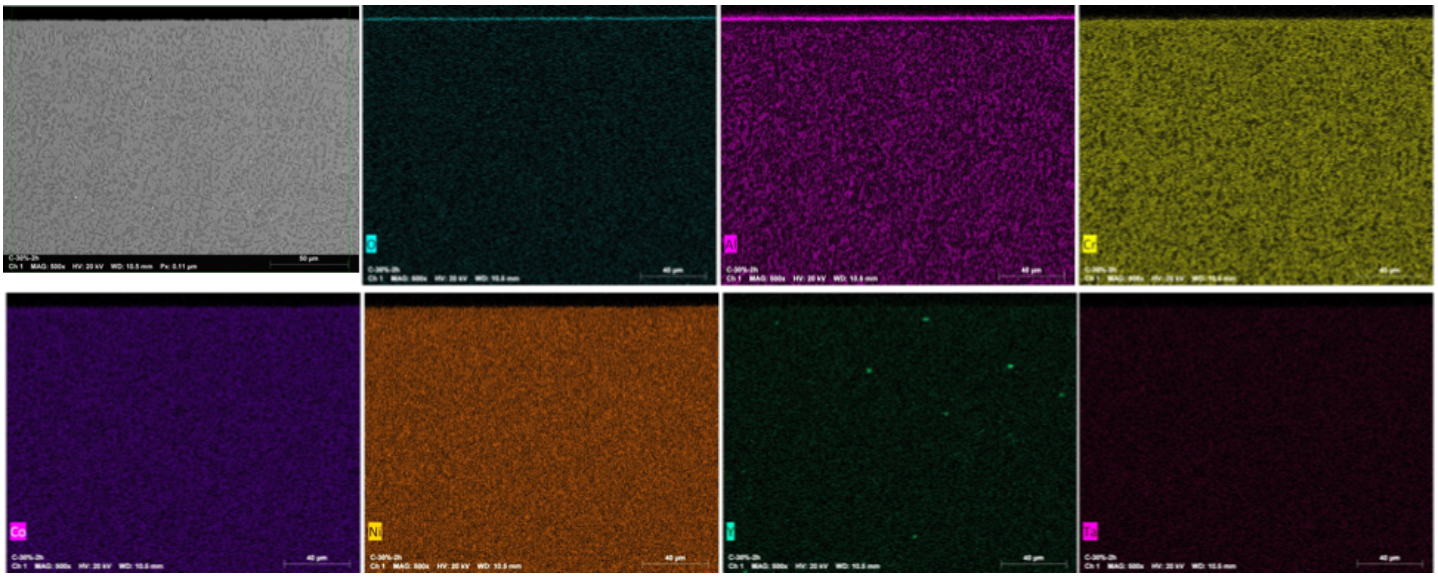

Figure 0.37 EDS Element Map C-33%-2h

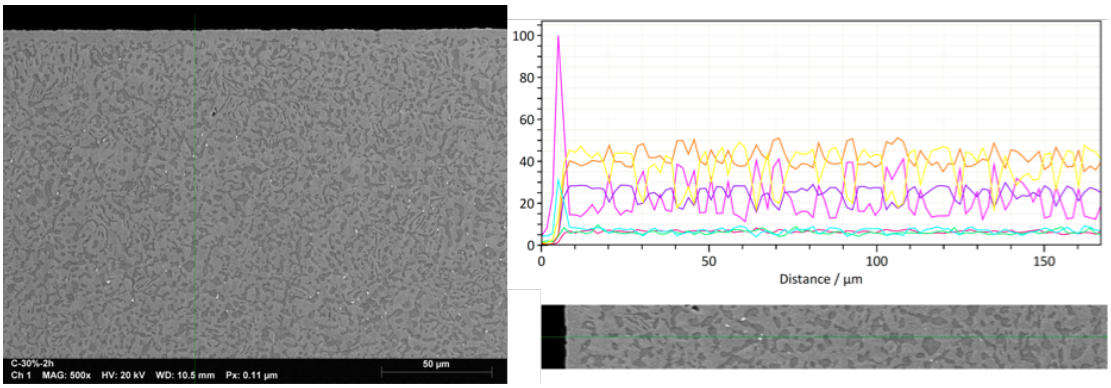

Figure 0.38 EDS Element Line Scan C-33%-2h

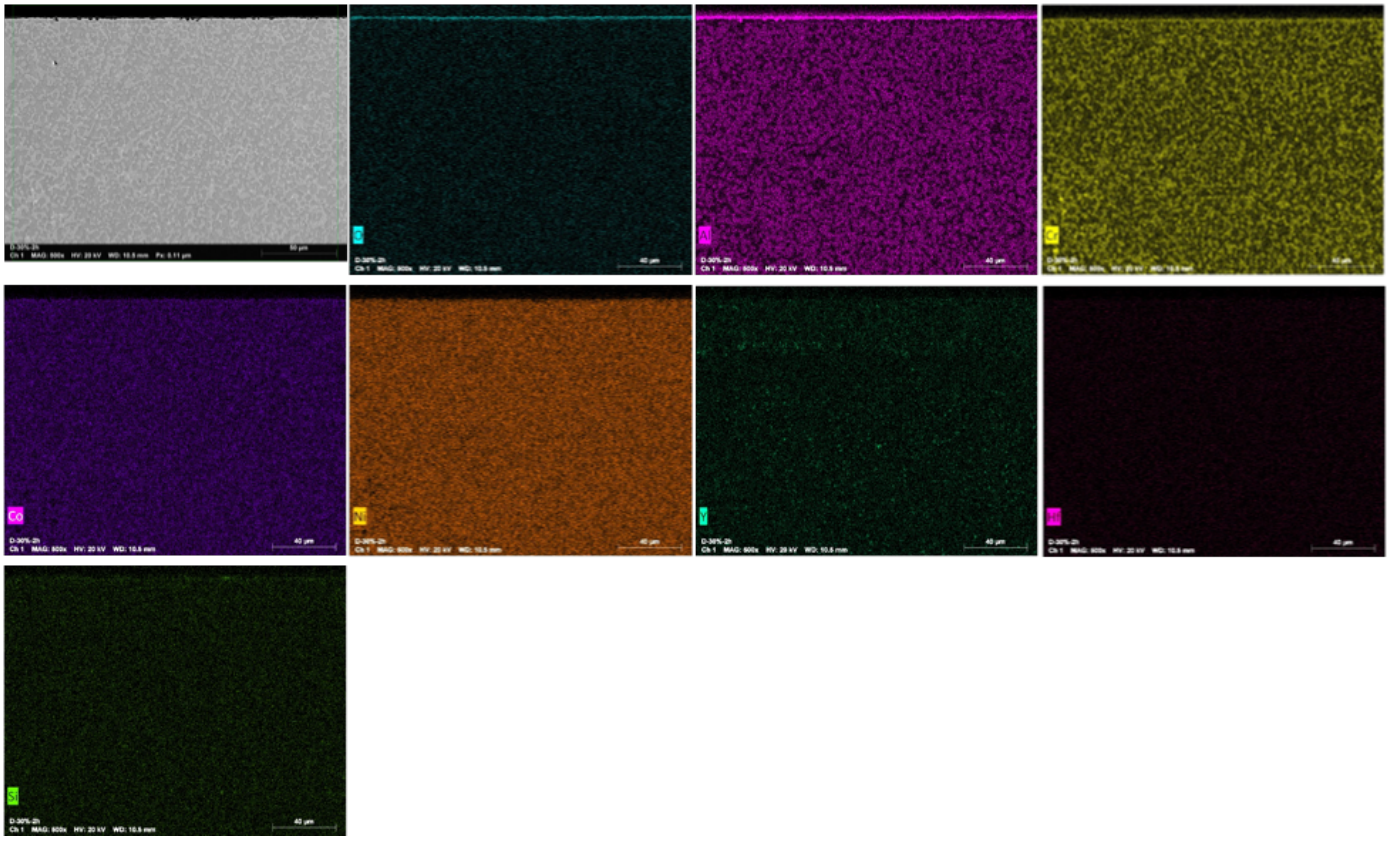

Figure 0.39 EDS Element Map D-33%-2h

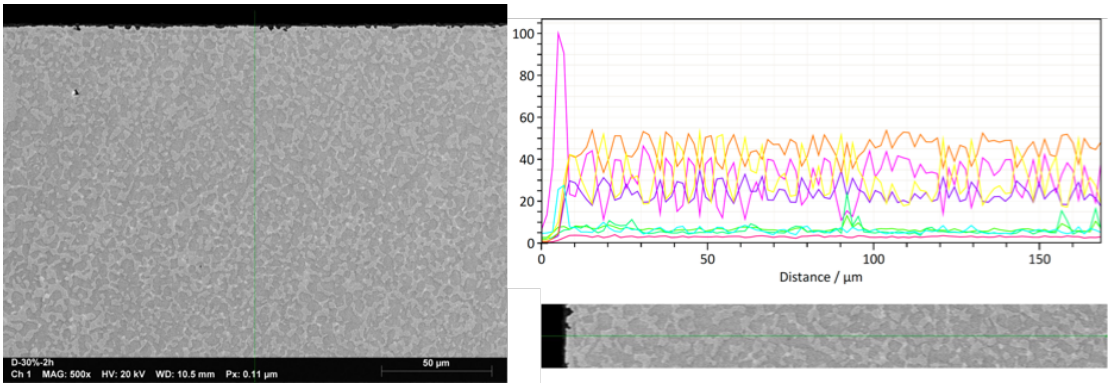

Figure 0.40 EDS Element Line Scan D-33%-2h

A.6 30%-20h

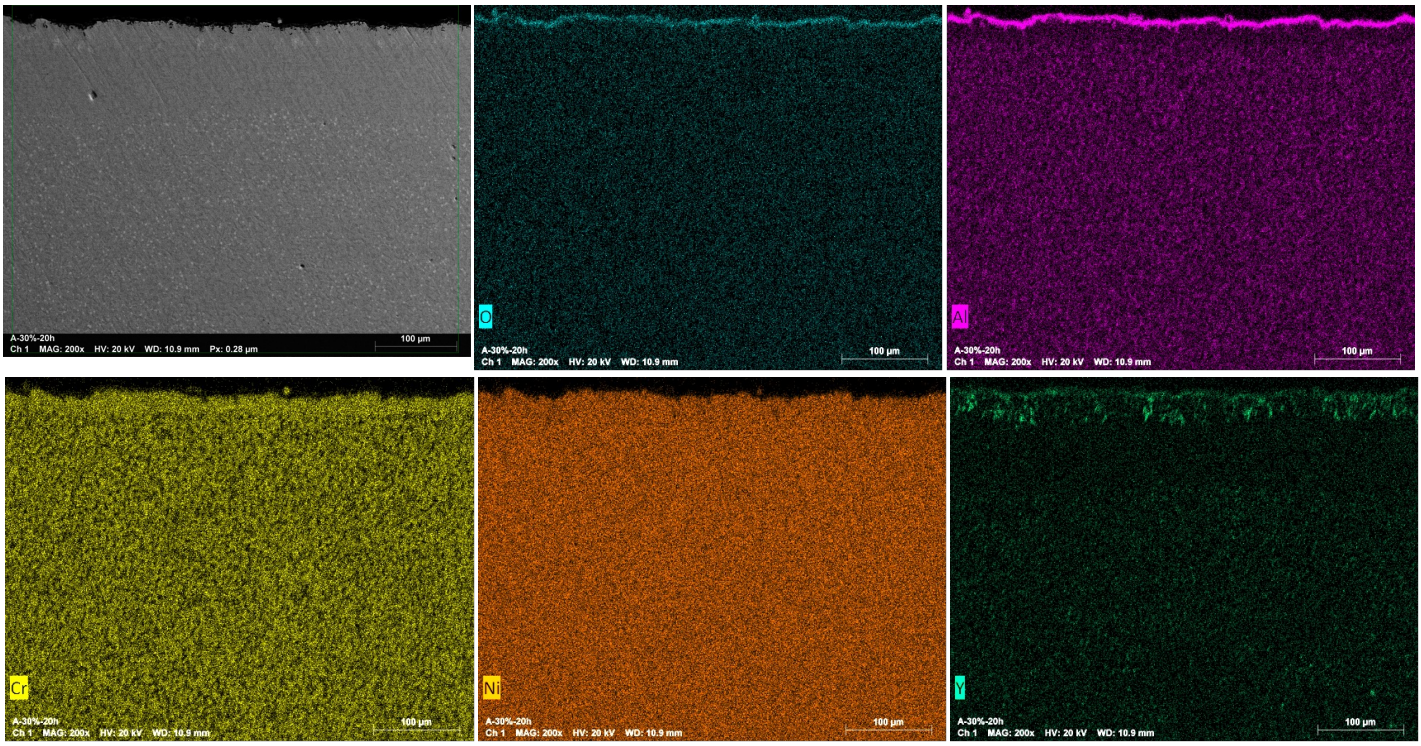

Figure 0.41 EDS Element Map A-33%-20h

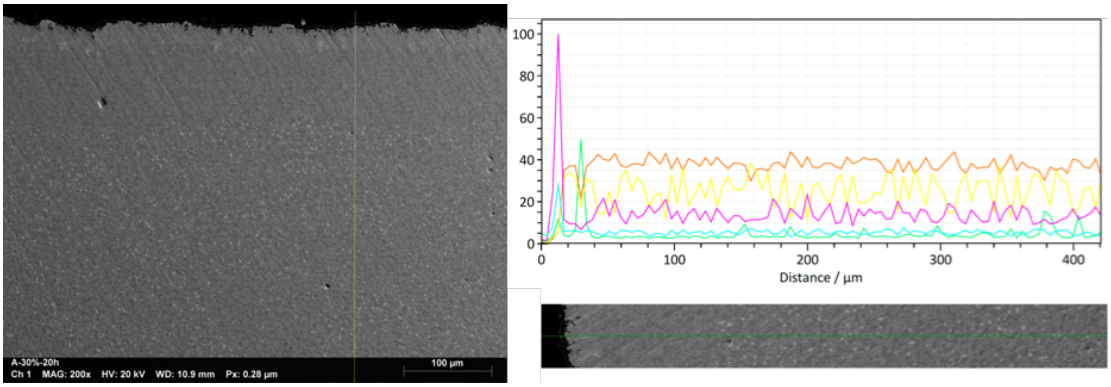

Figure 0.42 EDS Element Line Scan A-33%-20h

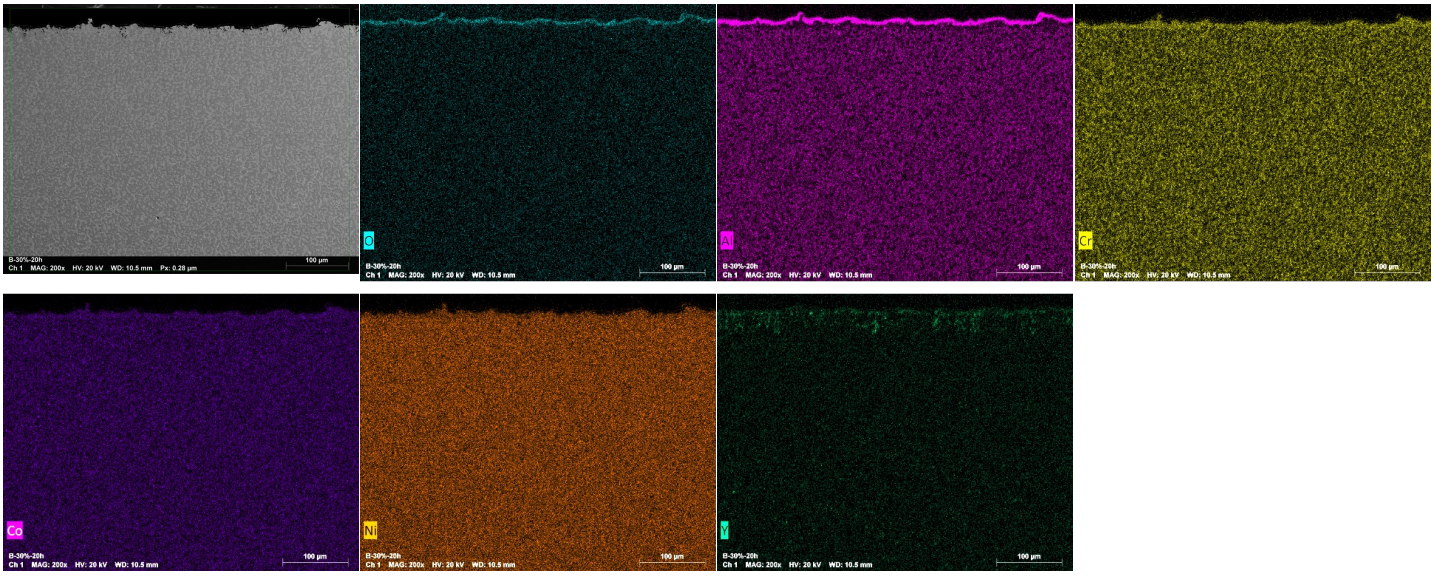

Figure 0.43 EDS Element Map B-33%-20h

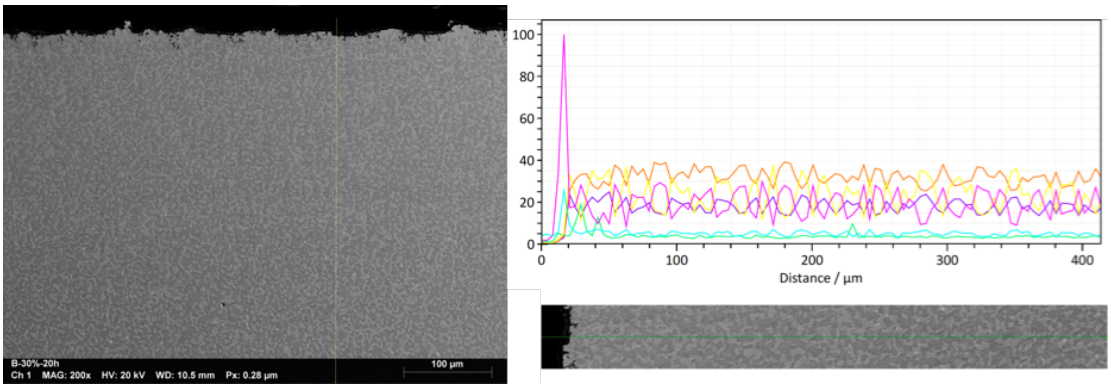

Figure 0.44 EDS Element Line Scan B-33%-20h

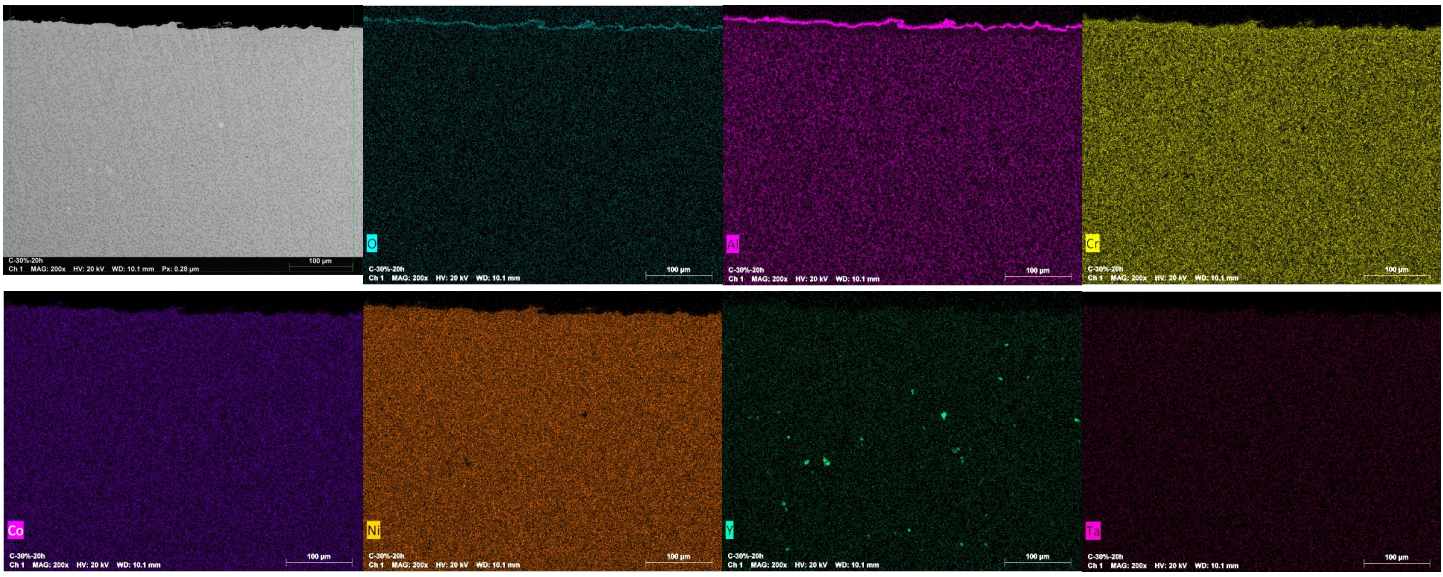

Figure 0.45 EDS Element Map C-33%-20h

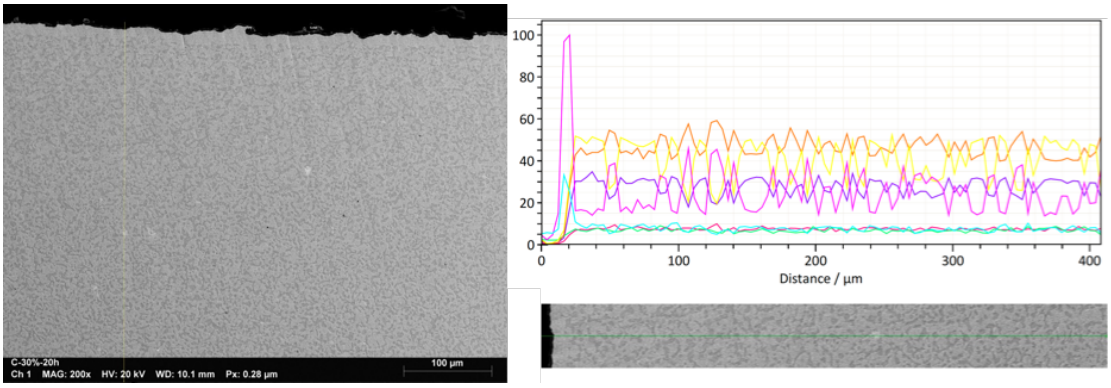

Figure 0.46 EDS Element Line Scan C-33%-20h

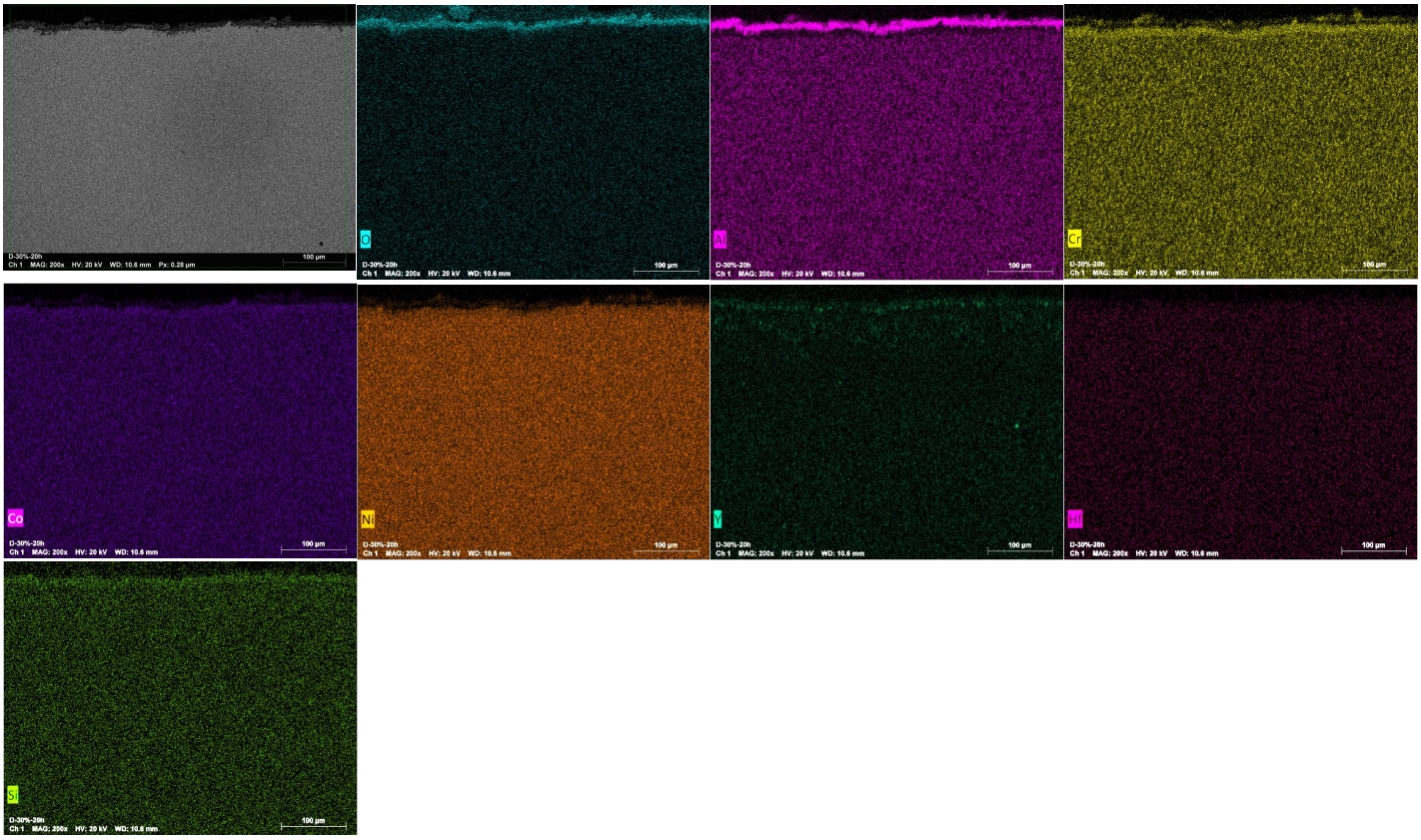

Figure 0.47 EDS Element Map D-33%-20h

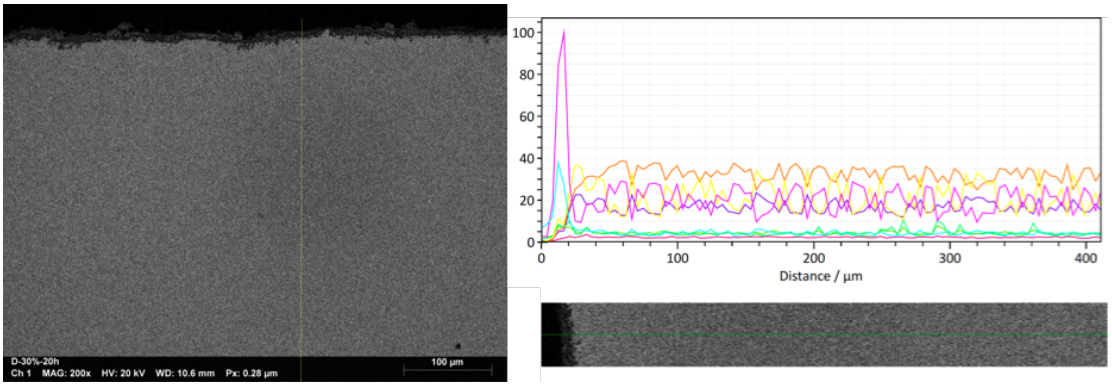

Figure 0.48 EDS Element Line Scan D-33%-20h

Appendix B: Thermodynamic Tables for Saturated Water

Table 13 Thermodynamic properties of Water Temperature Entry

Saturated Water

		Enthalpy, kJ/kg			Entropy, kJ/kg-K		
Temp. (°C)	**Press. (kPa)**	**Sat. Liquid h_f**	**Evap. h_{fg}**	**Sat. Vapor h_g**	**Sat. Liquid s_f**	**Evap. s_{fg}**	**Sat. Vapor s_g**
0.01	0.6113	0.00	2501.35	2501.35	0	9.1562	9.1562
5	0.8721	20.98	2489.57	2510.54	0.0761	8.9496	9.0257
10	1.2276	41.99	2477.75	2519.74	0.1510	8.7498	8.9007
15	1.705	62.98	2465.93	2528.91	0.2245	8.5569	8.7813
20	2.339	83.94	2454.12	2538.06	0.2966	8.3706	8.6671
25	3.169	104.87	2442.30	2547.17	0.3673	8.1905	8.5579
30	4.246	125.77	2430.48	2556.25	0.4369	8.0164	8.4533
35	5.628	146.66	2418.62	2565.28	0.5052	7.8478	8.3530
40	7.384	167.54	2406.72	2574.26	0.5724	7.6845	8.2569
45	9.593	188.42	2394.77	2583.19	0.6386	7.5261	8.1647
50	12.350	209.31	2382.75	2592.06	0.7037	7.3725	8.0762
55	15.758	230.20	2370.66	2600.86	0.7679	7.2234	7.9912
60	19.941	251.11	2358.48	2609.59	0.8311	7.0784	7.9095
65	25.03	272.03	2346.21	2618.24	0.8934	6.9375	7.8309
70	31.19	292.96	2333.85	2626.80	0.9548	6.8004	7.7552
75	38.58	313.91	2321.37	2635.28	1.0154	6.6670	7.6824
80	47.39	334.88	2308.77	2643.66	1.0752	6.5369	7.6121
85	57.83	355.88	2296.05	2651.93	1.1342	6.4102	7.5444
90	70.14	376.90	2283.19	2660.09	1.1924	6.2866	7.4790
95	84.55	397.94	2270.19	2668.13	1.2500	6.1659	7.4158
100	101.3	419.02	2257.03	2676.05	1.3068	6.0480	7.3548
105	120.8	440.13	2243.70	2683.83	1.3629	5.9328	7.2958
110	143.3	461.27	2230.20	2691.47	1.4184	5.8202	7.2386
115	169.1	482.46	2216.50	2698.96	1.4733	5.7100	7.1832
120	198.5	503.69	2202.61	2706.30	1.5275	5.6020	7.1295
125	232.1	524.96	2188.50	2713.46	1.5812	5.4962	7.0774
130	270.1	546.29	2174.16	2720.46	1.6343	5.3925	7.0269
135	313.0	567.67	2159.59	2727.26	1.6869	5.2907	6.9777
140	361.3	589.11	2144.75	2733.87	1.7390	5.1908	6.9298
145	415.4	610.61	2129.65	2740.26	1.7906	5.0926	6.8832
150	475.9	632.18	2114.26	2746.44	1.8417	4.9960	6.8378
155	543.1	653.82	2098.56	2752.39	1.8924	4.9010	6.7934
160	617.8	675.53	2082.55	2758.09	1.9426	4.8075	6.7501
165	700.5	697.32	2066.20	2763.53	1.9924	4.7153	6.7078
170	791.7	719.20	2049.50	2768.70	2.0418	4.6244	6.6663
175	892.0	741.16	2032.42	2773.58	2.0909	4.5347	6.6256
180	1002.2	763.21	2014.96	2778.16	2.1395	4.4461	6.5857
185	1122.7	785.36	1997.07	2782.43	2.1878	4.3586	6.5464
190	1254.4	807.61	1978.76	2786.37	2.2358	4.2720	6.5078

Table 14 Thermodynamic Properties of Water Pressure Entry

Saturated Water Pressure Entry

		Specific Volume, m^3/kg			Internal Energy, kJ/kg		
Press. (kPa)	**Temp. (°C)**	**Sat. Liquid v_f**	**Evap. u_{fg}**	**Sat. Vapor v_g**	**Sat. Liquid u_f**	**Evap. u_{fg}**	**Sat. Vapor u_g**
0.6113	0.01	0.001000	206.131	206.132	0	2375.3	2375.3
1	6.98	0.001000	129.20702	129.20802	29.29	2355.69	2384.98
1.5	13.03	0.001001	87.97913	87.98013	54.70	2338.63	2393.32
2	17.50	0.001001	67.00285	67.00385	73.47	2326.02	2399.48
2.5	21.08	0.001002	54.25285	54.25385	88.47	2315.93	2404.40
3	24.08	0.001003	45.66402	45.66502	101.03	2307.48	2408.51
4	28.96	0.001004	34.79915	34.80015	121.44	2293.73	2415.17
5	32.88	0.001005	28.19150	28.19251	137.79	2282.70	2420.49
7.5	40.29	0.001008	19.23674	19.23775	168.76	2261.74	2430.50
10	45.81	0.001010	14.67254	14.67355	191.79	2246.10	2437.89
15	53.97	0.001014	10.02117	10.02218	225.90	2222.83	2448.73
20	60.06	0.001017	7.64835	7.64937	251.35	2205.36	2456.71
25	64.97	0.001020	6.20322	6.20424	271.88	2191.21	2463.08
30	69.10	0.001022	5.22816	5.22918	289.18	2179.22	2468.40
40	75.87	0.001026	3.99243	3.99345	317.51	2159.49	2477.00
50	81.33	0.001030	3.23931	3.24034	340.42	2143.43	2483.85
75	91.77	0.001037	2.21607	2.21711	394.29	2112.39	2496.67
100	99.62	0.001043	1.69296	1.69400	417.33	2088.72	2506.06
125	105.99	0.001048	1.37385	1.37490	444.16	2069.32	2513.48
150	111.37	0.001053	1.15828	1.15933	466.92	2052.72	2519.64
175	116.06	0.001057	1.00257	1.00363	486.78	2038.12	2524.90
200	120.23	0.001061	0.88467	0.88573	504.47	2025.02	2529.49
225	124.00	0.001064	0.79219	0.79325	520.45	2013.10	2533.56
250	127.43	0.001067	0.71765	0.71871	535.08	2002.14	2537.21
275	130.60	0.001070	0.65624	0.65731	548.57	1991.95	2540.53
300	133.55	0.001073	0.60475	0.60582	561.13	1982.43	2543.55
325	136.30	0.001076	0.56093	0.56201	572.88	1973.46	2546.34
350	138.88	0.001079	0.52317	0.52425	583.93	1964.98	2548.92
375	141.32	0.001081	0.49029	0.49137	594.38	1956.93	2551.31
400	143.63	0.001084	0.46138	0.46246	604.29	1949.26	2553.55
450	147.93	0.001088	0.41289	0.41398	622.75	1934.87	2557.62
500	151.86	0.001093	0.37380	0.37489	639.66	1921.57	2561.23
550	155.48	0.001097	0.34159	0.34268	655.30	1909.17	2564.47
600	158.85	0.001101	0.31457	0.31567	669.88	1897.52	2567.40
650	162.01	0.001104	0.29158	0.29268	683.55	1886.51	2570.06
700	164.97	0.001108	0.27176	0.27286	696.43	1876.07	2572.49
750	167.77	0.001111	0.25449	0.25560	708.62	1866.11	2574.73
800	170.43	0.001115	0.23931	0.24043	720.20	1856.58	2576.79